Swirl-Stabilised Turbulent Spray Flames in an Axisymmetric Model Combustor

by

Sheen, Dong-Hyon

A dissertation submitted for the degree of
Doctor of Philosophy
in the Faculty of Engineering
University of London
and for the
Diploma of Membership of Imperial College

Department of Chemical Engineering and Chemical Technology
Imperial College of Science, Technology and Medicine
London

May 1993

Acknowledgements

It is my great pleasure to have the opportunity to acknowledge all the support I have received from my friends, colleagues and my family during the course of this work.

First of all, I would like to express my gratitude to my supervisor, Dr. W.P. Jones, for his guidance and advice from the beginning to the very end of this project. Often his immense patience and optimism gave me great encouragements and kept me afloat when the progress was delayed and work seemed to be in the doldrums.

My employer, Yukong Limited, Korea, allowed me the leave and financially supported me, which is gratefully acknowledged.

I am much obliged to Messrs. A. Tober and M. Wille for their ever willingness to help. Their friendly discussions on matters arising from experiments and computations were very helpful. Other colleagues, Messrs. S. Ledin, J.Alvarez, M. Kakhi, M. Uhlmann, Y. Prasetyo and M. Distelhoff helped to make life in London more enjoyable.

Finally, I express my gratitude and love to my wife, Sunhee, and my son, Yonghoon, whose devotion, encouragement and full support made the experience of writing this dissertation possible and worthwhile.

Abstract

Measurements and computational predictions have been made for the turbulent flames of hollow-cone kerosene spray in a swirl-stabilised axisymmetric model combustor.

A high degree of circumferrential uniformity of the air flow has been achieved by withdrawing the aerodynamic swirler from the combustor inlet plane by 50 mm which, combined with a carefully selected spray nozzle, produced an axisymmetric flame structure.

Velocity, temperature and species concentrations of O_2, CO, CO_2, H_2 and UHC have been measured by a single component LDV, a fine bare wire (40μm) thermocouple and the relevant gas analysers. Particular effort has been made to determine the inlet flow conditions, thus eliminating the uncertainties in specifying the inlet boundary conditions in the subsequent computation.

The recirculation on the axis has been confined inside the combustor and the overall turbulence intensities have been found to be significantly reduced when compared with those of cold flow at comparable inlet flow conditions, suggesting the spray droplets reduces the turbulence. Two separate high temperature regions have been observed. One, very narrow and occurring close to the fuel injection nozzle, appears to play a role in flame stabilisation. The other, corresponding to the main flame region, is much broader and develops down stream. O_2 and CO_2 concentrations on the combustor axis have been found to be good indicators of the overall input AFR's. Going from the axis to the wall of the combustor, a definite sequence of the maxima of mean temperature, CO/H_2, UHC and O_2/mean axial velocity has been observed.

Computational predictions have been performed modelling the gas phase turbulence with both the $k-\varepsilon$ model and a full second moment closure. The combustion was approximated by the laminar flamelet approach. A discrete Lagrangian stochastic particles approach has been adopted to describe the two-phase character of the flow while the turbulent dispersion of the droplets is modelled by the Wiener process.

In general the agreements between the measuremens and the predictions are good particularly with the second moment closure. Although there are only small differences in the mean velocity fields predicted by the two turbulence models, the second moment closure produced considerably more accurate results for all other quantities. This appears to be due to fact that the turbulence mixing is more properly represented in the higher order scheme. However, both models overpredicted the stream wise expansion of the main air flow and as a result the maximum velocities were underpredicted.

The temperature field has been systematically overpredicted but this appears to be due to the adiabatic flow assumption with the consequent neglect of radiative heat loss in the combustion model. However, the prediction with the second moment closure was qualitatively accurate enough to reproduce two separate high temperature regions as indicated by measurements. These were not predicted by the $k-\varepsilon$ model due to the strong overprediction of the mixing processes.

The scalar fields have also been predicted reasonably well, but the concentrations of the intermediate species, CO and H_2, have been overpredicted by a factor of about two close to the nozzle whilst they are underpredicted in the down stream region.

Table of Contents

List of Illustrations

Nomenclature

A	Amplitude of velocity fluctuation,
	Drift vector,
	Surface area
a	Crossectional area
B	Diffusion vector
b	Diffusion coefficient
C	Constant
Cp	Specific heat
c	Proportionality constant
D	Droplet diameter,
	Molecular diffusivity,
	Drag force function,
	Spacing between two parallel beams
d	Diameter
e	Electro-motive force
F	Force on a particle by external forces
f	Spray function,
	Mixture fraction
g	Accelleration due to gravity
h	Enthalpy,
	Heat transfer coefficient
ΔH_f^o	Standard heat of formation
J	Molecular diffusion flux
K	Number of droplet size classes
k	Thermal conductivity,
	Turbulence kinetic energy
L	Latent heat of vaporisation of fuel
Le	Lewis number
l	Length scale
M	Total number of chemical elements
$\dot{m}$	Mass flow rate
Δm	Mass change
N	Number of droplets,
	Number of sample,
	Total number of species
Nu	Nusselt number
p	Probability density,
	Pressure
Pr	Prandtl number
$\dot{q}$	Rate of heat transfer
R	Rate of droplet vaporisation
Re	Reynolds number
r	Droplet radius,
	Radial position
$\dot{r}$	Rate of formation of species

S	Swirl number, Source
Sc	Schmidt number
T	Temperature, Sampling Time
t	Time
u	Instantaneous (axial) velocity
U	Mean (axial) velocity
V	Volume
ΔV	Volume change
v	Velocity
W	Wiener process
w	Swirl velocity
X	Axial distance
X	Random vector, Stochastic force
x	Axial coordinate, Relative intensity of velocity fluctuation to the mean velocity
Δx	Grid spacing in x-direction
Y	Mean mass fraction
y	Instantaneous mass fraction
Δy	Grid spacing in y-direction
z	Mass fraction

Superscripts

'	Fluctuating part of unweighted average
"	Fluctuating part of density-weighted average
¬	Unweighted average
~	Density-weighted average
i	Time-level index
n	Time-level index
*	Estimation

Subscripts

b	Thermocouple junction bead
C	Control cell
g	Gas phase
h	Enthalpy
i, j, l	Coordinate index
inj	Injection nozzle
int	Intermediate cell
k	Droplet size class index
m	Mass
mv	Measurement volume
new	New cell

old	Old cell
p	Particle, or droplet phase
T	Turbulence
x, r, θ	Axes in cylindrical coordinate
x, y, z	Axes in Cartesian coordinates
w	Thermocouple wire
α	Element index
ε	Eddy

Greeks

Γ	Gamma function
α	Thermal Diffusivity, Exponent of β-pdf, Exponent of DSD
β	Exponent of β-pdf, Exponent of DSD, Beam crossing angle
$\dot{\gamma}_D$	Data rate
δ_{ij}	Kronecker delta function
δt	Time interval for digital sampling
ε	Dissipation rate of turbulence kinetic energy
θ	Discharge angle of swirl vanes
μ	Viscosity
μ_T	Turbulent Viscosity
ν	Kinematic Viscosity
ξ	Normal random variable
ρ	Density, instantaneous
σ	Stefan-Boltzmann constant
σ_k	Model constant
σ_T	Turbulent Prandtl number
σ_ε	Model constant
τ	Relaxation time of droplet, Shear stress, Viscous stress tensor
ϕ	Instantaneous value
φ	Instantaneous value
ω	Frequency of velocity fluctuation

List of Abbreviation

AFR	Air-to-fuel ratio

CDM	Continuum droplet model
DDM	Discrete droplet model
DSD	Droplet size distributio
emf	Electro-motive force
FID	Flame ionisation detector
IBP	Initial boiling point
LDV	Laser Doppler velocimetry
LHF	Locally-homogeneous flow
PDA	Phase Doppler anemometry
PDF	Probability distribution function
RHS	Right hand side
RMS, rms	Root-mean-square
SMD	Sauter mean diameter
TPF	Two-phase flow
UHC	Unburned hydrocarbon

Chapter 1.

Introduction

1.1 Turbulent Spray Flames

Spray combustion has been used for more than a century as a powerful method of exploiting the chemical energy stored in the liquid fossil fuels, and the applications range from gas turbine combustors, through diesel engines, industrial furnaces, steam-raising boilers, to liquid-fuelled rockets. It's effectiveness comes from the atomisation process which disintegrates the bulk of liquid fuel into a cloud of many tiny droplets. Thus, the total surface area of fuel is much increased so that the rates of heat and mass transfer between the fuel and air are also greatly enhanced.

The flow inside the practical combustors involving spray flames is invariably turbulent. Turbulence is another mechanism by which the inter- and intra-phase mixing is further enhanced. Every aspect of transport processes and the chemical reactions involved is influenced by the turbulence. And in many cases, swirl is introduced to stabilise the flame inside the combustor. Swirl in the flow increases the mixing and reduces the flame length. It also affects the formation of pollutants. The fuel droplets, mostly polydisperse with different velocities, move in different directions from the main gas flow. Thus, the fuel distribution in spray flames is non uniform and the boundary of the flame zone is rather irregular and poorly defined, making the situation much different from the gaseous flames. Turbulent spray flame is such a complex reactive flow system where all of these features come in to play their roles. The extent of the success of the spray combustion process and it's performance, such as combustion efficiency and pollutant emission levels, are determined by these factors all combined. Therefore, to meet the nowadays growing demand of efficient and at the same time environmentally-acceptable use of fuels in combustors, a more general understanding is required for all of the above-mentioned aspects of spray combustion.

There have been both experimental and computational efforts made to advance understanding of turbulent spray combustion. With the development of non-intrusive measurement techniques such as laser Doppler velocimetry (LDV) and

phase Doppler anemometry (PDA) over the last decade or so, a considerable amount of valuable information has been provided for the improvement of the general knowledge of turbulent spray flames. Other optical measurement methods and imaging techniques have also contributed significantly to an increased understanding of the subject. With these advanced measuring techniques, both time- and space-resolved information of turbulent spray flames has become available for analyses. On the other hand, the computational approach has been also much facilitated by the improvement of computer capacity. With the ever-growing computing speed and memory capacity, more and more complex problems are analysed with even more sophisticated method than before. This is reflected on the fact that the majority of spray combustion modelling works nowadays adopts heterogeneous, or two-phase flow approaches with discrete droplets representations.

Obviously, not every property of potentially important implications can readily be measured, which could be a limitation imposed upon the experimental investigations. Whereas, the computational method, once developed, can provide some insights for the properties that can not be measured. However, it is very often the case that measurement provides a unique way of testing our understanding advanced through computational works. Therefore, both experimental and computational methods are complimentary to each other for the advancement of understanding of the turbulent spray flames.

1.2 Motivations and Objectives

There have been quite a number of experimental investigations carried out into turbulent spray flames in model combustors. However, rarely do these studies provide a complete picture of the spray flames concerned, and often only one or two of the field variables of practical importance, such as, velocities, temperature, species concentrations, or some spray characteristics, are presented. This, together with uncertainties in the relevant inlet boundary conditions, represents a major difficulty for modelling works aimed at the prediction of spray flame characteristics. Further, while most of the previous work has been performed with axisymmetric model combustion, often insufficient measurements have been made to check the axisymmetry of the flame structure.

In view of these, some of the main objectives of present work are, for swirl-stabilised spray flames in a model combustor;

- to test effect of inlet air flow condition on the flame structure to establish the flame structure with acceptable axisymmetry;
- to provide the proper inlet boundary conditions;
- to provide a complete set of velocity, temperature and concentrations of major species (CO, CO_2, O_2, H_2 and UHC);

and thereby

- to obtain an improved understanding of liquid fuelled combustion systems.

Based on this experimental work, computational predictions are also made of the flames. For these purposes, computer codes developed earlier by Jones and Marquis (1985), and Jones and Pascau (1989), at Imperial College, London, are used. These codes have been successfully employed in varieties of complex flow problems including the combustion reaction. However, the application has been limited so far to the gaseous flames. Thus, the other main objectives of the present work are:

- to develop and implement the spray combustion model;

and

- to evaluate its performance by comparisons with measurements.

For this, a new approach is introduced to model the turbulent dispersion of spray droplets, which employs the Wiener process.

Chapter 2.

Experimental Measurements of Turbulent Spray Flames

2.1. Introduction

Velocity, temperature, and concentrations of gaseous species of major interest have been measured for turbulent spray flames inside a swirl-stabilised axisymmetric quartz combustor fuelled by kerosene. A hollow cone spray has been produced by a pressure-jet type simplex atomiser. Laser-Doppler velocimetry (LDV) has been employed to measure the mean and root-mean-square (rms) velocities of the gas phase; mean and rms temperatures have been measured by a Pt vs. Pt-13% Rd thermocouple with the diameter of 40 μm; various gas analysers have been used to determine the mean species concentrations. The data will provide the relevant input data for inlet boundary conditions to computational modelling and also form the basis by which the performance of the computational prediction is evaluated. Some results, such as flow visualisations, are qualitative in nature.

No attempt has been made, in this work, to measure the spray behaviour such as droplet size distribution, velocity distribution, and size-velocity correlation, which would of course make the experimental part of this work more complete. However, in an area close to the fuel injection nozzle, the mean velocities of droplets have been measured, the mean values being independent of the droplet sizes due to the limitation of the LDV's capability.

First, a critical review is made, in the next section 2.2, for experimental works in the related area. The next Section explains the experimental facilities employed in this work, with detailed descriptions of the inlet conditions of air and fuel spray into the combustor. The measures taken to make the inlet flow reasonably axisymmetric with negligible circumferrential variation are described, and the results are explained later. Together with the axisymmetry of spray structure, the measures taken resulted in a reasonable axisymmetric flame structure, without which a two dimensional mapping of the three dimensionally structured flames is not justified. Two test conditions are chosen for this work, one being fuel-richer than the other, with the fuel injection rates being kept the same. The overall flame shapes at each conditions

are briefly described. Experimental methods, with some evaluations of errors associated with, where deemed necessary, are described in the following section 2.4. Characteristics of mean values measured are analysed in detail, for velocity, temperature, and species concentrations. These analyses have great importance when the results of computational predictions are interpreted and compared with experimental results. Section 2.5 describes the experimental results. Cold flows without spray are presented with their mean and rms velocities. These provide a reference against which to compare the combusting flows, whereby the change in the flow field in general due to the combustion can be evaluated. Details of the inlet boundary conditions for the air are presented also. The effect of the presence of spray droplets on the LDV measurements are discussed. This is followed by the presentations of the flow fields under burning conditions, starting with the axial component, then radial and swirl component velocities, and ending with the temperature and species concentration fields, with discussions in detail on each of these measurements. The last section summarises important features related with and the major findings from the experimental measurements.

2.2 Review of Experimental Works

The previous experimental works on the spray flames are reviewed. Attention is limited to experiments with general flame properties (size and shape) not too far different from those investigated in the present work; namely axisymmetric, swirl-stabilised, hollow-cone jet flames inside the combustor of rather simple geometry, without dilution holes in the wall. Although the main concern in the present wok is the spray flames, experiments on the flames fuelled by conical jet of gas are also included in this review. This is done on the grounds that, the flow fields are often not much different when the mode of fuel injection (solid cone vs. hollow cone) is similar to spray flames, and consequently there are common features between the gaseous and spray flames.

Khalil, et al.(1976) investigated kerosene spray flames in a cylindrical water-cooled combustor of diameter 200 mm, at various swirl numbers, ranging from 0.721 to 1.98. They measured the axial and tangential velocity with a water-cooled 3-hole pitot tube and found that the size and strength of the central recirculation zone and the recirculated mass flow increased almost linearly as the swirl number

increases. Temperature was measured by a water-cooled suction pyrometer with 0.2 mm diameter thermocouple wires of 6%Rd-Pt vs. 30%Rd-Pt, and was found to be almost uniform throughout the reverse flow zone. Their measurements provide useful information on the global features of the flame, particularly the effect of swirl number on the size and extent of recirculation zone. However, their measurements start at an axial stage of 100 mm, which appears to be too far away from the fuel injection plane to reveal the detailed *near-field* information about how the flame develops. Furthermore, no information is provided on the spray characteristics, for example, the mean droplet size (either estimated or measured) and the shape of the spray (solid- or hollow-cone).

Hollow cone spray flames stabilised in the wake of a disc were studied by Tuttle, et al.(1976). The fuel they used was liquid propane. The simplex pressure jet type atomiser with a nominal spray cone angle of 90° was placed on the centre of the flame holder disc of diameter 114 mm, which was in turn placed at the centre of the combustor of diameter 146 mm, allowing the swirling air to enter through the annulus extending from the wall. Mean temperature and species concentrations of CO, CO_2, UHC, and NO_x were measured. The recirculation behind the flame holder disc was characterised by high and nearly constant concentrations of CO (4 ~ 7 %) and UHC (above 2 % methane equivalent). They found the heterogeneous processes (i.e., the interactions between spray droplets and gas phase) to be of increasing importance as the air flow increases. The velocity field was not measured and their interpretation of flow field, for example, the size of recirculation zone and shear layer mixing region, was based on the shape of the contour lines of CO and UHC. Like Khalil, et al's.(1976), no measured or estimated droplet size is given in this work, either.

Owen, et al.(1978) investigated the effect of fuel volatility and air swirl on the spray flame characteristics. They measured the mean temperature, UHC concentration, and axial velocity of droplets and gas. They used the pressure-atomising swirl-type fuel injector, which appears to have produced hollow cone sprays. The combustor was of diameter 122 mm and was water-cooled. The blockage ratio was relatively small (0.25) and the air was introduced through the annulus extending from the wall, and resulted in only one small torroidal recirculation zone close to the fuel injector plane. They found that for the light hydrocarbon fuels selected in their study, namely iso-octane and no. 2 fuel oil with the initial boiling points (IBP's) of 373 and 454 K, respectively, the flame structure

resemble that of the gaseous fuel diffusion flame investigated previously in the combustor of similar geometry (Owen, et al., 1976). They also found that the smaller droplets are entrained into a torroidal recirculation zone surrounding the fuel spray, and these recirculated droplets appear to play a role in flame stabilisation. Their measurements of gas phase velocity were of the axial component only and were not detailed enough to analyse appropriately the flow field and it's effect on the flame structure with confidence. Only UHC concentrations (as % methane equivalent) are presented, although other species (O, CO_2 and O_2) were claimed to have been measured.

The influence of the mean spray droplet diameter on flame characteristics was explored by El Banhawy and Whitelaw (1981). They employed a rotating cup atomiser which is claimed to be capable of producing sprays with near monodisperse droplet size, approximately 90 % of droplets in the quoted size range with the remainder being of smaller diameter. This allowed control over the mean droplet diameter without the need to alter the fuel and air operating conditions. The kerosene spray was produced at the tip of the rotating cup, which protruded by 50 mm into the combustor of diameter 157 mm. The spray droplets were released virtually radially and subsequently were subject to the in-coming swirling air. CO_2 concentration of as high as 11 % was measured upstream of main flame area, where similar level of CO_2 concentrations were also measured. The mean droplet size was varied from 33 to 96 μm and it was found that the combustion intensity was reduced as the mean droplet size increases, indicated by the reduced temperature in the initial part of the flame. Attya and Whitelaw (1984) carried out nearly the same experiments, this time with less protrusion (22 mm) of the rotating cup into the combustor of a slightly larger diameter (200 mm). They observed again that the combustion intensity increases with the reduction of mean droplet diameter. Furthermore, they estimated that, for mean droplet diameters less than about 50 μm, the fuel will behave in a manner close to gaseous. The velocity fields were not measured in these two works, and their analysis of the effect of swirl is consequently rather indirect, being inferred from the temperature and species concentration data. Nevertheless, the latter work was employed in validating their computational prediction and the agreement between the measurements and the prediction was in general very good.

Time-resolved temperature and velocity field have been measured by LaRue, et al. (1984) for swirl-stabilised propane flame in an axisymmetric combustor of

diameter 80 mm. The propane fuel was delivered through a conical annulus of width 1 mm and total angle 40°, to emulate the directional momentum flux of a hollow-cone liquid spray nozzle. 25 μm diameter thermocouple wires of Pt. vs. Pt 10% Rd. were used to measure the instantaneous temperature. The mean temperature was found to be nearly constant in the recirculation zone with the instantaneous peak temperatures approaching the maximum adiabatic flame temperature. In the region where turbulent mixing of hot and cold gas streams was vigorous, temperature fluctuations of the order of 1100 °C were observed. The cross correlation of the fluctuating axial and azimuthal velocities was measured for the same flame fuelled by a conical annular jet of gaseous propane by Brum and Samuelsen (1987). The peak value of the correlation coefficient, i.e. $C = \overline{u' w'} / \sqrt{\overline{u^2}} \sqrt{\overline{w^2}}$, was higher in the reacting flow (0.2) than in the non-reacting flow and an increase in the fuel loading increased the correlation coefficient to about 0.25. The recirculation zone was found to be shorter, radially wider, and stronger (with higher negative axial velocities) in the reacting flows. McDonnell, et al. (1988) employed phase Doppler interferometry to measure the droplet size and velocity of the spray flame of JP-4 fuel oil in the same combustor as LaRue, et al's. (1984) and Brum and Samuelsen's (1987). An air-assist atomiser was used, which produced a hollow-cone spray. However, their work was mainly concerned with measurement of the spray droplet phase. Gas phase temperature and velocity fields were treated only qualitatively. In none of these three works were the species concentrations measured.

The works reviewed so far are rather fragmentary in the sense that not all of the major field properties (velocity, temperature and species concentrations of major species) are reported. Only one or two of these properties are measured and do not provide the basis of full perspective view of the flames involved. In contrast, in the work of Jones and Tober (1988), a more complete description is provided for the swirl-stabilised axisymmetric flames. The three major field variables were measured of the swirl-stabilised flame fuelled by a conical annular jet of gaseous propane, with the half cone angle of 45^{o}, in a 196 mm diameter quartz combustor. There was a torroidal corner recirculation zone created by the sudden expansion from the swirler of diameter 42 mm into the combustor. Another recirculation zone, induced by the swirling motion of the air was along the axis of combustor, extending from the bluff hub of the swirler to about 1.7 combustor diameter downstream. The mixture fractions in both two recirculation zone were nearly constant. However, it was higher and lower than the overall mixture fraction in the central and corner recirculation zones, respectively. The locally stoichiometric and near stochiomentric

conditions, on a mean basis, occurred on both the inner and outer side of the expanding annular fuel-air jet. While the flame developed near the interface between the central recirculating flow and the annular swirling air jet, on the outer side of the annular jet it did not in spite of the near stoichiometric condition, indicating that the burning there was not mixing-controlled. The maximum CO concentrations of about 2.5 % and 4 % were measured for overall fuel lean and stoichiometric flames, respectively (i.e. the overall equivalence ratios of 0.8 and 1.0, respectively). The reverse flow velocity in the central recirculation zone was typically 10 m/sec. The same set of data with more species concentrations was presented by Jones and Wilhelmi (1989) in the similar combustor but with smaller diameter of 100 mm. The swirl vanes had 45° angle to the combustor axis and the diameter was the same as Jones and Tober (1988). The central recirculation zone had a length of about one combustor diameter and the estimated reverse mass flow was about 15 to 20 % of the total air flow. They observed three maxima of turbulent kinetic energies. Two of them were on both sides of the expanding annular jet and the other one was found at roughly downstream end of the central recirculation zone, probably developed by the reaction. Two peaks in the circumferrential velocity profiles were observed at the earlier axial stages. This was attributed to the angular momentum being transported around both the central and corner recirculation zones. They compared the measured CO and UHC concentration as functions of the mixture fraction to those calculated from strained laminar flamelet, and found that the calculated flamelet CO concentrations were much higher than the measured values irrespective of the strain rate, in the fuel rich side of the stoichiometric. Based on this observation, they pointed that the conserved scalar type combustion model may not be appropriate for modelling the flames measured.

2.3. Experimental Facilities

2.3.1. Test Rig

Figure 2.1 shows the test rig used in this work. Air is taken from the ambient outside the laboratory and fed into the combustor by a fan blower, without being preheated. The air temperature at the inlet to the combustor is, slightly higher than the ambient by about 15 ^{o}C., due to the compression effect of the fan blower. Thus the inlet air temperature is in the range of 25 - 35 ^{o}C throughout this work. Air flow

rate is measured by an orifice flow meter. Kerosene fuel is stored in a cylinder and then pressurised by high pressure nitrogen gas to be delivered to the combustor through the injection nozzle. Fuel flow rate, being regulated by adjusting the pressure applied to the fuel cylinder, is measured by turbine-type flow meter (Litre Meter[@] , Type LM D 30). Fuel flow rate has been found stable, with the fluctuations less than ± 1 % of the set value, throughout this work.

The hot gas from the combustor is cooled down by the curtain of water spray, before being ventilated out of the room via the exhaust fan. To prevent the quartz combustor from being overheated, 16 small holes with diameters of 2 mm are provided around just outside the combustor wall, at the front plate, for the compressed air jets to come out of them and blow along the outside of combustor. Not shown in Figure 2.1 are the traversing mechanisms for moving the optics of LDV and the probes for temperature and species concentration measurements.

2.3.2. Combustor and Swirler

Combustor is made of a quartz tube the internal diameter and wall thickness of which are 200 and 2.0 mm, respectively, and is 500 mm long, Figure 2.2. Front end of the tube is fitted in the front metal plate through which combustion air and fuel are introduced. Also provided is the electric spark ignitor at the inner surface of this plate to ignite the fuel spray. Electricity of 24 volts DC is provided by a spark generator commonly used in passenger cars. The other end of the tube is open to the atmosphere, through which the probes are inserted for temperature measurements and sampling the gas.

The swirler has 20 equally spaced *aerodynamically* curved swirl vanes with the discharge angle of 30^{o} to the axis (Figure 2.3). The swirl number of this swirler is 0.91, based on the definition (Beer and Chigier, 1972; Mather and McCallum, 1967) of;

$$S = \frac{2}{3}\,\frac{1-(d_i/d_o)^2}{1-(d_i/d_o)^2}\tan\theta \qquad (2.3\text{-}1)$$

[@] Litre Meter, Aylesbury, Bucks., HP19 3RS, UK.

where d_i and d_o are the inside and outside diameters of the swirler, respectively, and θ is the discharge angle of swirler vanes.

As is to be explained in more detail later in section 2.3.4, the swirler is set back from the front plate by 50 mm to minimise the circumferrential variations in the air flow entering the combustor. The tip of the fuel injection nozzle is flush with the surface of the front plate of combustor.

2.3.3 Spray Characteristics

The fuel injection nozzle used in this work is a pressure-jet type simplex atomiser manufactured by Lechler GmbH@ (model no. 212.085). The nozzle has been modified to allow it to be fitted into the combustor used in the present work and sketch of it is shown in Figure 2.4.

A flow visualisations study serves to determine the spray quality in terms of the spatial distribution of spray droplets. A sheet of laser light has been illuminated in a plane perpendicular to the axis of the nozzle to visualise the spray structure at desired axial distances (X) from the nozzle. Similarly a sheet of light has been cast in the plane containing the nozzle axis to obtain a side view of the spray. The Figures 2.5 to 2.8 are the results with fuel flow rate of 51 ml/min. Since the intensity of light scattered by spray droplets becomes minimal at a right angle of view (AOV), (which is the angle between the line of sight and the plane of sheet of laser light), all of these pictures have been taken at other AOV than 90^o.

The axisymmetry and circumferrential uniformity of the spray appears to be excellent, at least as it appears to the eye. However, as will be seen in other figures of flame shapes in section 2.2.6, even with this seemingly good axisymmetry of the spray structure, the resulting flame itself is not so axisymmetric as expected. This implies of course that the spray structure, particularly the circumferrential variation of spray distribution, are not revealed in sufficient detail by flow visualisations. The effect of swirling air on the spray structure is clearly seen by comparing Figures 2.5 and 2.7 to Figures 2.6 and 2.8, where the latter ones have been taken with the air flow rate of 31 g/sec in the unconfined space. Most of the droplets (perhaps of

@ Lechler GmbH & Co. KG, Hohenstrasse 24, Postfach 1709, W-7012 Fellbach, Germany.

smaller sizes) near the axis of thespray in Figures 2.5 and 2.7 are driven outward by the action of swirling air, as could be seen in Figures 2.6 and 2.8.

Although the nozzle used in the present work is designed to generate a hollow cone spray, the hollow feature is not that clear when fuel is sprayed into a quiescent air. The spray appears to be reasonably hollow initially very close to nozzle, but this feature is lost almost completely rather soon at farther downstream distances. The spray structure becomes definitely hollow, however, when the spray is subject to a surrounding swirling air flow, as is clearly seen in Figures 2.6 and 2.8.

2.3.4. Axisymmetry of Air Flow

It is most desirable that the flame structure is axisymmetric without circumferrential variation, since attempting to measure or predict a truly 3-dimensional structures would be a considerably increased effort. An axisymmetric flame with negligible circumferrential variation can be treated as a 2-dimensional structure, which is obviously far more economic for both measurements and computations.

To obtain an ideal structure of the flame, both spray and flow structure should be maintained as axisymmetric and circumferrentially even as possible. Spray structure has been found to be fairly ideal as has been previously discussed in section 2.3.3, and in this section, the structure of air flow into the combustor is assessed.

Swirl is generated by the aerodynamic force induced by 20 equally spaced curved swirl vanes in the swirler. As a consequence, vortices are bound to develop at the end of each swirl vane, and this makes the air flow circumferrentially uneven. This is illustrated in Figure 2.9 which shows the contours of mean axial velocity of the air measured just in front of the swirler and which covers a quarter of the cross section of swirler annulus. What is apparent from this figure is that the circumferrential variation of the axial velocity is so high that, along the circle at r = 13 mm, for example, the maximum velocity reaches over 40 m/sec, while the minimum value is about 12 m/sec. As a consequence, the flow is far from axisymmetric. Figure 2.10 shows radial profiles of mean axial velocity measured along the radii at several orientation angles. They are not similar each other at different angles, again indicating the lack of symmetry. Figure 2.11 shows the radial profiles of rms velocity and, as with mean velocity profiles, they are not axisymmetric, either.

To achieve an axisymmetry and negligible circumferrential variation of air flow, it has been found that moving back the swirler from the front plate of the combustor is an effective measure. All the previous problems of poor symmetry and large circumferrential variations have been resolved out with the swirler located upstream of the nozzle. The following Figure 2.12 shows the result obtained when this measure was taken and clearly to be seen is the much reduced, indeed negligible circumferrential variation when compared with Figure 2.9. Axisymmetry has been remarkably improved as can also be seen in Figures. 2.13 and 2.14. The radial profiles of both the mean and rms of axial velocity at different orientation angles are almost identical.

2.3.5 Test Conditions

Fuel used in this work is aviation gas turbine fuel Jet A-1 typical properties of which are shown in Table 2.1. The data included in this table are taken from the literature, with the exception of specific gravity which was measured during the present work.

Table 2.1 Selected Physico-Chemical Properties of Fuel

Specific gravity, g/g at 15 ^{o}C	0.7925
Viscosity, cP	3.18
C/H ratio	1.9185
Calorific value, net, MJ/kg	42.8

The operation of the combustor is restricted by two limits. One is set by the blow-off of the flame at high air-to-fuel ratios (AFR) and the other is set by excessive noise and instability at lower AFR's, as is shown in Figure 2.15.

Table 2.2 Test Conditions

Flame	Fuel rate, f g/sec	Air rate, *a* g/sec	AFR *a/f*	Equivalence ratio
A	0.951	26.51	27.88	0.53
B	0.951	20.75	21.82	0.67

The operability range between these two limits has been found to be fairly narrow, being from 0.55 to 0.65 in terms of equivalence ratios for fuel flow rates in the range of 50 to 100 ml/min. Also shown in this figure are two points, A and B, designating the two test conditions selected for the present work. The flames at these two conditions are hereinafter referred to as Flame A and Flame B, respectively.

2.3.6 Overall Flame Shapes

Figure 2.16 shows the side views of two Flames A and B. As can be clearly seen in these pictures, there is quite a difference in luminosities between two flames. Flame B has yellow luminous flamelets very close to the injection nozzle and becomes completely yellow further away from nozzle, whereas Flame A has virtually no such yellow luminous flamelets throughout the whole region of the combustor. In both cases, the flames can be observed from around X = 10 mm and downstream, which suggests, by the time the fuel reaches that station, either the fuel injected has not been sufficiently disintegrated yet into fine droplets, or not enough time has elapsed for the droplets to be vaporised and subsequently be burnt out, or both.

Sheets of laser light have been used to illuminate the axial plane close to the nozzle to observe the spray behaviour in the flame and the photographs are shown in Figure 2.17. It appears that the flame develops just inside of the hollow spray cone close to the nozzle. At this AOV of 90^{o}, no spray droplets could be observed in the far downstream region, due to a much reduced intensity of light scattered by droplets. This intensity of scattered light is, obviously, dependent upon the direction of observation and it is the maximum at 0^{o} observation angle, which is the orientation for forward scattering. Spray behaviour in the flame, away from the nozzle, could be seen at other AOV than 90^{o}. Figure 2.18 is the photograph taken with AOV of about 32^{o}. It is noted that, due to this AOV of 32^{o}, while the side views of the flames are taken at right angles, the tracing planes of flying droplets superimposed have an angle of 32^{o} with the normal to the plane of picture, thus the trace of droplets having been projected as such on these pictures.

It has to be mentioned that the traces visualised this way do not represent all of the fuel droplets present in the flames. Rather, they correspond to the larger droplets from which the scattered light intensities are high enough to be detected by the

human eye, in the background light of flames. These larger droplets are found from the photographs to maintain their initial trajectory until they are vaporised and disappear, and they are not much deflected by the swirling air. Thus, the trajectories of the larger droplets appear to be virtually the same for the two flames which are different only in the air flow rates. Most of the droplet traces are slightly out of focus in these photographs since they are focused on the middle of the field.

Figure 2.19 shows front views of the two flames and, as has been mentioned previously in Section 2.3.3, even with the apparently negligible circumferrential variation in the spray shape observed by flow visualisation, the actual flames are not so entirely symmetric. The deviations from axisymmetry of the flame structures are evident in the field measurements of velocity and temperature, which are discussed later in Section 2.5. However, the flames do not have such features as separated flame regions which are typical of those resulting from spray nozzles of poor design or finish where the circumferrential variation of flame properties are extremely large.

While the flames studied in the present work may not be perfectly axisymmetric, the circumferrential variations are very smooth, as can be typically observed in Flame A, and the degree of symmetry achieved is probably close to the best which can be achieved in combusts of the present size and geometry.

2.4 Experimental Methods

2.4.1 Laser-Doppler Velocimetry

The velocities are measured by a dual-beam, or differential Doppler technique (Drain, 1980; Durst, et al., 1981), in forward scattering mode. The frequency of one of the two beams is shifted by 40 MHz by being passed through a Bragg cell, in order to eliminate problems of directional ambiguity. Two parallel beams, one unshifted and the other shifted by 40 MHz, are focused by a transmitting lens with a focal length of 310 mm and made cross to form a measurement volume inside the combustor. Light scattered by seeding particles moving through the measurement volume is collected by a lens (collecting lens) with a focal length of 500 mm and is focused into a tiny pinhole of the photomultiplier (RCA4526).

The modulation of light intensity produced by seeding particles moving across the fringes formed inside the measurement volume is converted into a voltage modulation by the photo multiplier. The electric signal, amplified if necessary, is fed into the frequency counter where the Doppler frequency is determined for each of the Doppler bursts. This frequency data is passed on to a micro computer and collected until the total number of frequency data reaches a specified number, using between 500 and 1500, but normally taken to be 1000, following which the statistics are calculated to produce mean and rms values. In addition, the probability density function (pdf) of velocity is displayed on the monitor as a histogram of the number of events vs. velocity. Occasionally, noise which was not rejected properly by the electronic filters of the counter appears as either an unusually long tail on one side of the pdf or some small spikes separated from the main pdf. This noise can be removed by restricting the range of frequencies over which the statistical analysis is performed. Normally, however, this was necessary only occasionally and most of the pdf's measured displayed negligible noise.

The light source is an Argon ion laser (Spectra Physics) with a nominal power of 2W. A single line of green colour with wavelength of 514.5 nm is selected and when the transverse mode of the beam is adjusted to TEM_{00}, which is the ideal mode for LDV measurements, the intensity of green light is about 180 mW, only a fraction of the nominal power but still high enough to produce good signal-to noise ratios throughout this work. The LDV system used in this work is basically the same as those used by Altgeld, et al. (1983), Wilhelmi (1984), and Jones and Tober (1988). The layout of the system is shown schematically in Figure 2.20 and the operational characteristics are listed in Table 2.3

Table 2.3 Operational Characteristics of LDV System

Light source	Ar^+, 2W
Wavelength of light	514.5 nm, green
Focal length, transmitting lens	310 mm
collecting lens	500 mm
Half angle of beam crossing	5.53^o
Fringe spacing	2.67 μm
Frequency shift (Bragg cell)	40 MHz
Beam spacing	60 mm
Probe volume (diameters of main axes of ellipsoid)	0.11x1.14 mm

Titanium oxide (TiO_2) powder with nominal size of 1 μm is used to provide seeding particles in the present work. The nominal size of seeding particle is considered to be small enough to provide a good response to turbulent fluctuation frequencies in excess of 1 kHz which should be high enough in most cases of turbulent gas flow. It has been observed that the seeding particles are somehow consumed by combustion reactions resulting in a much reduced data rate, by about two orders of magnitude in some cases. This is probably due to the reduction of particle numbers caused by conglomeration of the seeding particles. Thus, titanium oxide powder appears not to be an ideal material for seeding particles in combusting flows. This has also been observed by Witze and Baritaud(1986), who showed that titanium oxide was indeed the worst amongst others tested, as far as the data rate reduction is concerned. Other seeding particles of Zirconium oxide (ZrO_2), zirconium fluoride (ZrF_4), or alumina (Al_2O_3) were found to be far better, in the sense that the data rate is not reduced by combustion. This fact was not known to the author at the time of measurements and no attempt was made to test the performance of the other materials than titanium oxide for seeding particles. However, the selection of the material for seeding particles does not likely to affect the velocity measurements by LDV, in the combustor of the present work.

When the two beams and the axis of cylindrical combustor are all in the same plane and the movement of the two beams is confined in that plane, as is the case for the axial velocity measurements, the position of the measurement volume inside the combustor will be determined almost entirely by the positioning of the optics. However, if the plane containing the two beams is normal to the axis of the combustor and the two beams are traversed vertically for radial velocity measurements or horizontally for swirl velocity measurements, then the measurement volume may not correspond exactly to the traverse of the two beams, because at different altitude, for example, the incident angles and the effective wall thickness over which the beams have to travel are different for the two beams. This could be analysed by applying the geometrical optics to the geometry considered, and the results are shown in Figures 2.21 and 2.22. Details of the analysis are included in the Appendix A.

The trajectory of the measurement volume follows virtually the same path as the optics unless the measurement volume gets very close to the combustor wall. For example, with the beams arranged for radial velocity measurements, Figure 2.21, the measurement volume is formed at (1.4 mm, 93.8 mm), rather than at (0.0 mm, 95

mm) when the beams are traversed vertically upwards by 95 mm from a reference point in the present case of γ=0.025. Fringe lines, or fringe planes more precisely, become inclined from the horizontal axis of the combustor as the two beams are traversed vertically. Once again this angle of inclination of fringe lines is hardly significant, with the maximum being only about 1^{o} close to the wall. A similar problem, but of less significance, is observed for swirl velocity measurements, as shown in Figure 2.22, where the movement of the measurement volume falls slightly short of the movement of optics. For example, the measurement volume is formed at (94.2 mm, 0.0 mm) rather than at (95 mm, 0.0 mm) as the beams are traversed horizontally by 95 mm from the reference point. In this case, the fringe lines remain horizontal at all time.

All in all, the effect of the beam refraction at the inside and outside surfaces of combustor wall is quite small, and no correction for this effect is applied to the measured data in the present work. However, as is obvious from these figures, the effect of beam refraction at the interfaces of the combustor wall becomes more significant as the wall thickness becomes larger, in which case the measurements should be corrected for the effect.

2.4.2 Thermometry by Fine Wire Thermocouple

Temperature is measured by a fine bare wire thermocouple of Pt vs. Pt-13%Rd. The diameters of the wires of both elements are the same and are 40 μm. The thermocouple junction is made by butt-welding the two wire elements with an electric spark and the two legs are connected to supporting wires of the same materials by tightly winding up several turns around the supports. The supporting wires, both with the same diameters of 0.5 mm, are separated by about 20 mm, with the thermocouple junction placed in the middle, as shown Figure 2.23. These two supports are inserted separately into twin-bore alumina tube of diameter 3.5 mm. This twin-bore tube is in turn sleeved into two successively larger tubes to retain mechanical rigidity over the length of the probe.

There are three major sources of error in temperature measurements by a fine bare wire thermocouple, namely the errors due to conduction, radiation, and the finite speed of response to temperature change. First, the conduction error refers to the effect of conductive heat loss from the junction bead to both legs and eventually to both supports. This type of error was analysed by Scadron and Warshawsky (1952)

and was subsequently adopted by many workers (Bradley and Mathews, 1968; Ballantyne and Moss, 1977; Attya and Whitelaw, 1981; Jones and Toral, 1983;, Heitor, 1985; and Jones and Wilhelmi, 1989) to estimate the error in their measurements. Based on their analysis, the conduction error for thermocouple used in the present work is negligibly small, being less than 0.2 %. This low level of error is possible only because the aspect ratio is so large, about 250 in the present case, and thus allows only a small temperature gradient along the length of both legs.

Secondly, the radiative heat loss from the junction bead also affects the accuracy of temperature measurements by a bare wire thermocouple. The influence of radiation was experimentally investigated by Attya (1983) and Heitor (1985) with several thermocouples of different sizes, following the procedure suggested by Holderness, et al.(1969). They found that the mean temperature was underestimated by 35 ^{o}C at 1000 ^{o}C for 40 μm wire. It is expected, based on their work, that the error due to radiation would be less than 5% in the present work.

Thirdly, since the thermocouple junction has a bead of finite physical size, there is bound to be a time lag and dampening in the thermocouple response to a temperature change of gas. This point is important when time-resolved measurements are attempted for fluctuating temperatures. Mathematically, after neglecting the above-mentioned conduction and radiation effects, thermocouple response to gas temperature is a quasi-first order damping system which can be expressed as:

$$T_g = T_w + \tau \frac{dT_w}{dt} \qquad (2.4\text{-}1)$$

where, T_g, T_w, and τ are gas temperature, wire temperature, and time constant or time of rise, respectively. Thus, to get the correct value of gas temperature, T_g, the wire temperature, T_w, should be compensated according to this relationship, and this can be done either electronically or digitally. Digital compensation is used in the present work. Electric compensation (Lockwood and Moneib, 1980) involves the application of an electric circuit which performs the operation of $(1 + \tau\ d/dt)\ e_w$ on the emf signal, e_w, from the wire with the resultant signal, say e_g, being the emf corresponding to the gas temperature. Digital compensation and corresponding error analysis is explained in detail by Heitor(1985), and similar procedure is adopted in

the present work. The continuous analogue signal of emf from the thermocouple is digitised by an analogue-to-digital converter at the rate of upto 5 kHz. The digital signal is converted into corresponding wire temperature by a micro-computer dedicated for temperature measurements. The compensation is then just a matter of finding a value for the time constant and a time rate change of wire temperature. A linear variation of time constant is assumed, from 6 to 2 milli seconds as temperature changes from 300 to 2000 K. The time rate of wire temperature change is approximated by central time differencing on the time series of sampled wire temperatures as follows:

$$T_g^i = T_w^i + \tau(T_w^{i+1} - T_w^{i-1}) / 2\delta t \qquad (2.4\text{-}2)$$

where superscripts denote the time steps and δt is the interval between each digital data, which depends on the sampling rate of the system. Total number of 4096 samples compensated this way are collected and the mean and rms values are calculated from them.

The error associated with this procedure comes largely from the uncertainty in estimating the time constant values which depend on the local gas velocity as well as temperature. This dependence of time constant on both temperature and velocity of gas can be seen from the following definition;

$$\tau = \rho_w C_{P_w} d_b^2 / 2k_g h \qquad (2.4\text{-}3)$$

where, amongst others, the convection heat transfer coefficient, h, is a function of fluid temperature and velocity. Therefore, some error is expected as the velocity dependence of the time constant has been neglected. The magnitude of the resulting error is, however, not readily quantified, but is expected to be small.

The mean temperature measurements are expected not to be much influenced by the finite time response of the thermocouple to the change in gas temperature. Therefore, the uncertainty in time constant estimation will not then affect the mean temperature measurements.

Catalytic effects are also known to interfere with the accuracy of mean temperature measurements obtained by a bare-wire thermocouples. Bicen, et

al.(1986) showed that this effect could be significant when UHC concentration is high, where the mean temperature may be overestimated by up to 70 K. The thermocouple junction could be coated with ceramic paste, for example, to prevent catalysis effects on the surface of the thermocouple junction, but coating the thermocouple inevitably increases the time constant by up to 3 times as has been shown by Heitor(1985).

Common to every probe technique is the error associated with the flow disturbance caused by inserting a probe into a test Section. Differences of up to 100 % in the flow field, caused by the presence of a thermocouple probe in the recirculation zone, have been reported (LaRue, 1984). However, the error in temperature measurement is not as readily quantified as the flow disturbance could be measured. The effect of flow perturbation caused by the presence of probe is not measured in the present work though, this point should be considered in interpreting the measured data.

The actual position of thermocouple junction is guided by two crossed laser beams. Only when the junction bead is placed at the beam crossing properly, the interference images made by the bead will appear at the same time. Once the probe is properly positioned, the bead has been found to remain quite stable, leaving the probe positioning error of less than ± 1 mm in most cases. Since the bead is positioned at the beam crossing, it is heated up by the laser lights. The extent of heating has been found to be up to about 20 and 10 K at temperatures of 300 and 1300 K, respectively.

No flame stabilisation has been observed at the thermocouple junction throughout this work, up to the axial distance of 10 mm from the nozzle.

2.4.3 Species Concentration Measurements

The concentrations of five species of major interest, namely O_2, CO, CO_2, H_2, and UHC, are measured, using a sampling probe. The gas sampling probe is made of stainless steel tubes of several diameters, and the design is shown in Figure 2.24. The outer diameter of the probe is 6 mm (1/4" tube) and the probe is cooled by water to reduce the gas temperature so that the chemical reaction is frozen as the gas sample is taken into the probe. However, at the same time, the probe should be kept at a high enough temperature to keep the sample fully vaporised and homogeneous.

The distribution of sample to different gas analysers will not be identical, otherwise. To achieve this, pressurised hot water of about 160 ^{o}C and 15 bar is used to cool the probe, according to SAE ARP 1256A.

Because the probe stem has to span over a distance of about 600 mm through the region where the temperature is non-uniform, the probe stem may distort quite significantly and , moreover, may not be stable, and consequently the probe tip may move around by up to = 20 mm. To improve the probe positioning accuracy, a sheath of copper tube is sleeved on the probe up to within 20 mm to the tip, whereby the positioning accuracy is much improved, being better than ± 2 mm, throughout the combustor. As with positioning of the thermocouple probe, the gas sampling probe is also guided by two crossed laser beams.

Infrared gas analysers, ADC[@] Model 336 and 483, are used to measure CO and CO_2 concentrations, respectively. O_2 concentration is measured by a Beckman[&] Oxygen Analyser Model E2, the operation of which is based on the fact that the paramagnetic susceptibility of virtually all gases except NO and NO_2, relative to that of oxygen, is negligible. Gas chromatography is used for H_2 concentration measurement. The chromatograph column is packed with "molecular sieve 13X" and argon gas at the rate of about 0.06 l/min is used as a carrier gas. A fixed amount, 5 ml, of gas is injected each time for measurement and the total recovery time is about 7 min. All the species mentioned so far are measured on a dry basis; that is, the gas sample taken by sampling probe is passed through a series of cooler/condensers, a drier, and a filter, to dry up completely all the condensable components, mostly water vapour and some unburned fuel. In contrast, UHC concentration is measured in wet basis. The sample gas, completely in vapour phase, is fed directly into a UHC analyser, AAL[£] Model 520 Series II Hydrocarbon Analyser. Basically, this instrument is the flame ionisation detector (FID) and is equivalent to a carbon number counter. Each concentration measured is represented as a methane equivalent concentration. Therefore, a sample of 5 % propane, for example, would give an analyser reading of 15 %.

[@] Analytical Development Co., Ltd., Pindar Road, Hoddesdon, Hertfordshire, UK.

[&] Beckman Instrument Co., Fullerton, CA 02634, USA.

[£] Analysis Automation Ltd., now under the control of Rotork Analysis, Ltd., Regal Way, Farringdon, Oxon, SN7 7BX, UK.

The linear response of all the instruments have been checked before starting the measurements, and all were found to be satisfactory over the span ranges relevant to the present work. Among the analysers used, only CO_2 analyser has been found to be sensitive to sample flow rate. The instrument has been calibrated at the sample rate of 400 ml/min and particular care has been exercised to keep the sample rate constant at this value throughout the study. The sample flow has been maintained within the range from 300 to 500 ml/min, which corresponds to an error of around ± 5 % in CO_2 concentration.

No flame stabilisation has been observed at the tip of gas sampling probe downstream of an axial distance of 10 mm from the nozzle. When the probe is moved closer to the nozzle, the flame becomes much distorted and is noticeably unstable.

Isokinetic sampling is very difficult if not impossible to achieve in highly turbulent and swirling, or recirculating flows, and departure by varying degrees from the isokinetic sampling is thus unavoidable in the present work. However, the error due to non-isokinetic sampling cannot be readily estimated, though it is generally felt to be small.

2.4.4 Characteristics of Mean Values Measured

2.4.4.1 Mean Velocities by LDV

The mean velocity measured by LDV is, basically, a particle-average, which means the average is taken for the particle velocities detected and collected. The rate at which the signal for particle velocities are detected, called the data rate, $\dot{\gamma}_D$, is dependent upon various factors such as the light intensity, particle size (distribution), size of measurement volume, arrangement of optics, particle number density, particle velocity, and so on. If the seeding comprises of monodispersed particles and the overall particle number density is not so high that the occurrence of two or more panicles occupying the measurement volume at the same time can be excluded, then the data rate becomes dependent largely upon the particle density and velocity only as;

$$\begin{aligned}\dot{\gamma}_D(t) &= k'_p \rho_p(t) V_p(t) a_{mv} \\ &= k_p \rho_p(t) V_p(t)\end{aligned} \qquad (2.4\text{-}4)$$

where, k'_p = a proportionality constant,

a_{mv} = the cross sectional area of measurement volume,

$\rho_p(t)$ = the instantaneous particle density,

$V_p(t)$ = the instantaneous particle velocity,

and $k_p = k'_p a_{mv}$.

Then the particle mean velocity is calculated by;

$$\overline{V}_p = \frac{\int_0^T \dot{\gamma}_D(t) V_p(t) dt}{\int_0^T \dot{\gamma}_D(t) dt} = \int_0^T \rho_p(t) V_p^2(t) dt \Big/ \int_0^T \rho_p(t) V_p(t) dt \qquad (2.4\text{-}5)$$

where, T is the sampling time which is set by specifying the number of samples to collect, N, so that:

$$N = \int_0^T \dot{\gamma}_D(t) dt \qquad (2.4\text{-}6)$$

If the air has been initially homogeneously seeded, then the instantaneous particle density will be proportional to the instantaneous gas density, $\rho_g(t)$. Thus, the Equation (2.4-5) is expressed in terms of gas phase density as follows:

$$\overline{V}_p = \int_0^T [\rho_g(t) V_p(t)] V(t) dt \Big/ \int_0^T [\rho_g(t) V_p(t)] dt \qquad (2.4\text{-}7)$$

The terms in the brackets in the Equation (2.4-7) represent the instantaneous mass flux. This equation implies that the mean velocity measured in this way is the mass-flux-weighted average.

In isothermal flow, the Equation (2.4-7) becomes as;

$$\overline{V}_{isothermal} = \int_0^T V_p(t)^2 dt \Big/ \int_0^T V_p(t) dt \qquad (2.4\text{-}8)$$

which shows the mean velocity is *velocity-weighted*, or *biased* by velocity. Now, if it is assumed that the fluctuating gas velocity could be expressed as follows, ;

$$V(t) = < V > + A\cos\omega t \tag{2.4-9}$$

where, <V> = the unweighted average, or Reynolds' mean velocity,
A = the amplitude of velocity fluctuation,
and ω = the frequency of velocity fluctuation.

Then the Equation(2.4-8) becomes:

$$\begin{aligned}\overline{V} &= \int_0^T (< V > + A\cos\omega t)^2 dt \,/\, \int_0^T (< V > + A\cos\omega t) dt \\ &= \int_0^T (< V >^2 + 2A < V > \cos\omega t + A^2\cos^2\omega t) dt \,/\, \int_0^T (< V > + A\cos\omega t) dt\end{aligned} \tag{2.4-10}$$

Upon rearrangement, and after employing the following trigonometric identity relationship;

$$\cos^2 x = (1 + \cos 2x)/2 \tag{2.4-11}$$

the Equation (2.4-10) results in:

$$\overline{V} = \frac{< V >^2 T + \frac{2A}{\omega} < V > \sin\omega T + \frac{A^2}{2} T + \frac{A^2}{4\omega}\sin 2\omega T}{< V > T + \frac{A}{\omega}\sin\omega T} \tag{2.4-12}$$

As ω increases, the Equation (2.4-12) may be simplified to:

$$\overline{V} = < V > + \frac{A^2}{2} < V > \tag{2.4-13}$$

The second term on the right hand side of this equation represents the effect of *velocity bias* for highly turbulent flow. The relative intensity of velocity fluctuation, x, which is loosely related with turbulence intensity, can be defined as:

$$x = A / < V > \tag{2.4-14}$$

Then the Equation (2.4-13) may be rewritten as;

$$\overline{V} = < V > (1 + x^2 / 2) \tag{2.4-15}$$

which shows that the velocity bias effect is proportional to the square of the relative intensity of velocity fluctuation. Thus for modest intensity of fluctuation, say x = 0.3, velocity bias results in the measurement overestimating the gas velocity by about 4.5 % Therefore, unless the relative intensity of fluctuation is significantly high, say x > 0.5, the effect of velocity bias is small and Equation (2.4-15) simplifies into:

$$\overline{V} = < V > \tag{2.4-16}$$

Now, if the effect of velocity bias neglected, then the data rate becomes simply a function of gas density alone, as ;

$$\dot{\gamma}_D = c\rho_g(t) \tag{2.4-17}$$

where c is a proportionality constant. Then the Equation (2.4-5) for the mean velocity can be expressed as;

$$\overline{V} = \int_0^T \rho_g(t) V(t) dt \, / \int_0^T \rho_g(t) dt \tag{2.4-18}$$

which is exactly the expression for a density-weighted, or Favre, average velocity.

However, in practice, it is difficult to ensure that the seeding particles are homogeneously dispersed and remains so throughout the period of measurement. Unless a homogeneous and strictly steady dispersion of seeding particles is achieved, the measured mean velocity will be something *close to*, and not exactly equal to, a density-weighted average.

2.4.4.2 Mean Temperature

The time constant of a thermocouple is related, by the definition of Equation (2.4-3), to the convective heat transfer coefficient which is a function of gas density as well as flow properties such as velocity and temperature. Therefore, the density change of gas could affect the temperature measurements in as much as it could cause a change to the time constant. However, the way in which the gas density enters the averaging process in temperature measurements by a bare-wire thermocouple is indirect and not as clear as for velocity measurements by LDV.

Although the displacement of mean measured temperature relative to actual mean gas temperature, due to pulsation of heat transfer coefficient and therefore time constant, in turbulent flow, was identified by Chomiak and Niedzialek(1967), it is still not clear at all in general whether or how, the measured mean temperature is weighted by fluctuating gas density. Attya and Whitelaw(1981) tried to explain that the mean measured temperature is close to the 'true averaged', by which they appear to mean the unweighted, or Reynolds' mean, gas temperature by a heat balance around the thermocouple junction as follows:

$$\overline{T}_w = \overline{T}_g - (\overline{T}_w^4 - \overline{T}_g^4) - \frac{\sigma\varepsilon}{\overline{h}}\overline{T}\left[6\left(\frac{\overline{T_w'^2}}{\overline{T}_w^2}\right) + 4\left(\frac{\overline{T_w'^2}}{\overline{T}_w^3}\right) + \left(\frac{\overline{T_w'^2}}{\overline{T}_w^4}\right)\right] + (\overline{h'T_g'} - \overline{h'T_w'}) - \text{conduction} \qquad (2.4\text{-}18)$$

Alternatively, if the thermocouple bead size is infinitely small, the time constant is accordingly small via the relationship of Equation (2.4-3). Then the Equation (2.4-1) simply becomes;

$$T_g = T_w \qquad (2.4\text{-}20)$$

which means the wire temperature represents, faithfully and independently of any change in gas density, the fluctuation of gas temperature without any time lag or attenuation. In this case, the measured mean temperature is close to unweighted, or Reynolds', average, as long as the rate of sampling the emf signal from thermocouple junction is sufficiently higher than the frequency of temperature fluctuations.

In addition, Moneib (1980) and Attya and Whitelaw (1981) has shown that the unweighted mean temperature could be measured by fine wire thermocouples of wire diameters up to 80 μm, by comparing the temperature measurements with those obtained with 15 μm wire which is considered to be small enough to give an unweighted average temperature. The mean temperatures measured by thermocouple with a wire diameter of 40 μm in the present work is therefore expected to be close to unweighted, or Reynolds' averaged, mean temperature.

2.4.4.3 Mean Species Concentration

The instantaneous mass rate of species α sampled through the probe can be expressed as;

$$\dot{m}_\alpha = \rho u a_{probe} Y_\alpha \tag{2.4-21}$$

where, ρ = instantaneous gas density,

u = instantaneous gas velocity normal to cross section of probe tip,

a_{probe} = cross area of probe tip,

and Y_α = instantaneous mass fraction of species α.

The time mean sampling rate of species α is then obtained by taking the time-average of Equation (2.4-21);

$$\bar{\dot{m}}_\alpha = a_{probe} \overline{\rho u Y_\alpha} \tag{2.4-22}$$

since a_{probe} is a constant. Now, if the instantaneous velocity and concentration are decomposed into density-weighted means and their fluctuating counter parts, i.e.;

$$u = \tilde{U} + u'' \tag{2.4-23}$$

$$y_\alpha = \tilde{Y}_\alpha + y''_\alpha \tag{2.4-24}$$

the time mean sampling rate of species α is represented by following equation.

$$\bar{\dot{m}}_\alpha / a_{probe} = \bar{\rho} \tilde{U} \tilde{Y}_\alpha + \overline{\rho u''} \tilde{Y}_\alpha + \overline{\rho y''_\alpha} \tilde{U} + \bar{\rho} \widetilde{u'' y''_\alpha} \tag{2.4-25}$$

The second and third terms of this equation vanish, since, from the definition of density-weighted mean:

$$\overline{\rho u''} = 0 \tag{2.4-26}$$

$$\overline{\rho y_\alpha''} = 0 \tag{2.4-27}$$

Thus, the Equation(2.4-25) becomes:

$$\overline{\dot{m}}_\alpha / a_{probe} = \overline{\rho}\,\tilde{U}\tilde{Y}_\alpha + \overline{\rho}\,\widetilde{u''y_\alpha''} \tag{2.4-28}$$

Now, if the following can be assumed;

$$\left|\widetilde{u''y_\alpha''}\right| << \left|\tilde{U}\tilde{Y}_\alpha\right| \tag{2.4-29}$$

which is very often the case, then the time mean sampling rate of species α is represented by;

$$\overline{\dot{m}}_\alpha = a_{probe}\ \overline{\rho}\,\tilde{U}\tilde{Y}_\alpha \tag{2.4-30}$$

which shows that the mean sampling rate of species α corresponds to a density-weighted, or Favre, mean concentration, $\tilde{Y}_\alpha$. Indeed, the above-mentioned assumption, Equation (2.4-29), is well satisfied in the experimental results of Starner(1983), where it has been shown that the second order velocity-scalar correlations were at most a few percent of the products of means of velocity and scalars in their magnitudes. Similar conditions are likely to prevail over most of the combustor used in the present study.

Alternatively, if an unweighted, Reynolds decomposition is applied, viz.;

$$u = \overline{U} + u' \tag{2.4-31}$$

$$y_\alpha = \bar{Y}_\alpha + y'_\alpha \tag{2.4-32}$$

then the time mean sampling rate of species α is:

$$\overline{\dot{m}}_\alpha / a_{probe} = \overline{\rho}\,\overline{U}\,\overline{Y}_\alpha + \overline{U}\,\overline{\rho' y'_\alpha} + \overline{Y}_\alpha\,\overline{\rho' u'} + \overline{\rho}\,\overline{u' y'_\alpha} + \overline{\rho' u' y'_\alpha} \qquad (2.4\text{-}33)$$

If, similar to Equation (2.4-29), it is assumed that;

$$\left|\overline{u' y'_\alpha}\right| << \left|\overline{U}\,\overline{Y}_\alpha\right| \qquad (2.4\text{-}34)$$

then the Equation (2.4-32) could be rewritten as:

$$\overline{\dot{m}}_\alpha / a_{probe} = \overline{\rho}\,\overline{U}\,\overline{Y}_\alpha + \overline{U}\,\overline{\rho' y'_\alpha} + \overline{\rho' u' y'_\alpha} \qquad (2.4\text{-}35)$$

Here, neither the second or third terms on the right hand side of Equation (2.4-35) vanish as before. The advantage of Favre averaging which allows the second order correlation involving density to drop does not apply here and the mean sampling rate of species α, $\overline{\dot{m}}_\alpha$, does not correspond to the unweighted mean concentration, $\overline{Y}_\alpha$, alone.

It is noted that, from the definition of density-weighted mean, it follows that:

$$\tilde{Y}_\alpha - \overline{Y}_\alpha = \overline{\rho' y'_\alpha} / \overline{\rho} \qquad (2.4\text{-}36)$$

That is, the two mean values become identical when the second order correlation, $\overline{\rho' y'_\alpha}$, vanishes; i.e., density fluctuations are negligibly small.

Thus, the mean species concentration measured is expected to be close to the density-weighted average, which in turn may be identical to the unweighted average depending on the situation. Kennedy and Kent (1981) were able to measure the instantaneous mixture fraction and gas density at the centre line of an axisymmetric turbulent hydrogen diffusion flame, by light scattering technique, and determined both unweighted and density-weighted mean mixture fractions. They compared their results with probe measurements and found that the concentrations measured by sampling probe fell in-between the unweighted and density-weighted mean values measured by optical method, whilst those three values were basically the same in some area where the density fluctuations were expected to be relatively small.

2.5 Experimental Results and Discussions

2.5.1 Flow Fields

2.5.1.1. Cold Flows

To provide a reference for the combusting case, the velocity fields have been measured for inert flow inside the combustor. The air flow rate was the same for Flame A, that is, 26 g/sec. The results are shown in Figures 2.25 through 2.31.

The main air flow is stretching from the inlet along the straight line with an angle of about 30^{o} to the axis of the combustor, which reflects the discharge angle (30^{o}) of the *aerodynamically curved* swirl vanes used in the present work. Clearly seen from the Figure 2.25 (a) are two recirculation zones. One is the smaller, torroidal, corner recirculation which is induced by a sudden expansion of flow and the other is the larger, located along the combustor axis and extends all the way to the exit of the combustor. This on-axis recirculation is generated by the swirl of the air flow, obviously. A slight accelleration in the axial velocity is observed close to the wall at the axial distance of about 150 mm, which appears to be due to the *blockage effect* of the on-axis recirculation.

RMS contours show a single-peaked turbulence structure, Figure 2.25 (b). The maximum of rms value is ovserved just inside of the maximum mean values. From about 1.5 combustor diameter downstream, i.e., X = 150 mm, the rms values become more or less uniform, indicating the turbulence is *homogeneous*.

The radial profiles of mean and rms axial velocities are shown in Figure 2.26. Close to the inlet plane, e.g., X = 10 mm, the rms profile show two peaks, each being located on both inner and outer side of the peak mean velocity, where the gradient of the mean velocity is higher, which is quite as expected. However, the rms peak on the outer edge of the forward flowing main air stream becomes only marginally discernable as the axial distance increases, and as a consequence the rms profiles appear to be single-peaked. Flow reattachment point appears at the axial distance of about 120 mm. From X = 150 mm on, the profiles remain virtually the same.

Profiles of mean and rms velocities are ahown in Figures 2.27 and 2.28, for radial and swirl components, respectively. Close to the inlet plane, e.g., X = 10 mm for

radial velocity, Figure 2.27 (a), and X < 30 mm for swirl velocity, Figure 2.28 (a) to (c), the rms values are higher on the axis than the rest. This is again due to high gradient of mean velocity around the combustor axis. In this region, the rms peaks which would have been observed on inner side of the peak mean velocities, as have been the case with axial component, appear to have been overshadowed by even higher rms values on the axis. Due to this point, the contours of rms velocities, Figures 2.29 (b) for radial velocity and 2.30 (b) for swirl velocity, appear to be slightly more complicated than those of axial velocity, Figure 2.25 (b). From X = 120 mm, the radial profiles of mean radial velocities are almost flat around zero, and as a result, the flow is more or less *unidirectional.* From X = 150 mm, mean and rms profiles of three component velocities remain virtually the same, indicating the flow is *fully-developed.*

The rms values of three component velocities are shown in Figure 2.31. The turbulence is highly *anisotropic*, close to the inlet plane, particularly around the main air stream, whereas the flow in both on-axis and corner recirculation zones are more or less *isotropic.* From X = 150 mm, the profiles are nearly flat and the difference in the rms values of three components are small, indicating the turbulence is almost *homogeneous* and *isotropic.*

2.5.1.2 Inlet Velocity Profiles

Inlet profiles of the three components of velocity at two flow conditions, corresponding to Flames A and B, have been measured for both cold and burning flows. To do this, one of the two laser beams had to be aligned parallel to or slightly tilted toward the front wall of combustor for the axial component velocity measurements. Thus the angle between the bisector plane of two crossed beams and the front wall is about 6^{o}, the angle of beam crossing being about 11^{o}. For radial and swirl velocities, the plane containing two laser beams is tilted slightly (by about 5^{o}) toward the front wall of the combustor. Because of these angles of beam orientation, the velocity measured in this way is slightly underestimated. However, the degree of underestimation is small ($\cos^{-1} 6^{o}$ = 1.0055, or 0.6 %) and can be safely ignored.

Figure 2.32 shows the inlet profiles for the non-reacting flows measured in this way. It is observed that the mean radial velocity is very small when compared to the other components. This 'is quite understandable when the inlet geometry is

considered. The geometry of the air flow into the combustor is a straight cylindrical annulus and no radial velocity is developed until the air exits from it. It is worth noting that, in spite of large differences in mean velocity levels between three velocity components, the rms levels are remarkably similar, indicating the turbulence at the inlet to the combustor is quite *isotropic*, if not *homogeneous*, though.

Figure 2.33 shows the inlet profiles of the three velocity components for burning flows. The most striking differences when compared with those of the non-reacting flows are; firstly, the rms levels are much reduced for all components whilst the *isotropic* nature is maintained. The reductions are by a factor of 2 to 5. Secondly, while the mean axial and swirl velocity profiles remain virtually the same in the non-burning and burning flows, the radial velocity profiles are very much different in the two cases. The mean radial velocities for the burning flows are about 3 times higher than those of cold flows. However, they are still very low compared with the other two components. Also worth noting is that the burning flows appear to give rise to a more homogeneous turbulence than the cold flow, at least at the inlet to the combustor.

The difference in the inlet flow conditions between cold and burning flows, while not so striking, can also be observed by comparing the streak lines. Figures 2.34 and 2.35 are the streak lines plotted in U-V and V-W planes, respectively. Here, once again, it can be easily seen that the difference in the inlet flows between the cold and burning flows is restricted mostly to the radial velocity and this is almost certainly due to the flow expansion caused by combustion.

2.5.1.3 Effect of Presence of Spray Droplets on LDV

The quantities measured by LDV is, basically, the velocity of whatever particles that scatter the laser light in the probe volume; gas phase velocity measurement is always biased by the presence, if any, of spray droplets at the point of measurement, as has been observed by previous workers (Owen, et al., 1978; Wood, et al. 1984; and Thiele and Brodbeck, 1986). A typical example is illustrated in Figure 2.36, where two velocity pdf's are shown as observed at the same position and flow conditions, in the presence and absence of seeding particles.

As is apparent from this example, when there are two sets of particles of different origins, namely seeding particles and spray droplets, then the measured velocity pdf

may be bimodal as in Figure 2.36(b), if the mean velocities associated with each set of particles are significantly different; for example, if the spray droplets are injected into recirculation zone where the mean axial gas phase velocity is negative. In passing, however, it has to be mentioned that bimodal velocity pdf's are possible not only in the two phase flow but also in single phase flows in situations where there is a high shear between two groups of fluids having distinct flow properties. In the present case, the gas phase velocity measurements are affected, i.e. biased, depending on the relative number of spray droplets to seeding particles moving across the fringes in the measurement volume.

When the mean velocities are so different that the resultant pdf is composed of two separable pdf's each representing the seeding particles and spray droplets, then unbiased information concerning the two different phases can be obtained by treating each pdf's separately. This is done straightforwardly in the present case by specifying the velocity, or frequency, range from which the statistics are to be extracted. However, when the mean and rms velocities of the two phases are distinct but not too different from each other, then the contributing pdf's for each phases will overlap and the resultant pdf becomes bimodal, the mean and rms of which represent neither phases correctly. This is bound to happen in some parts of the flow whenever LDV is employed to measure the gas phase velocity field of spray flames.

There are some ways of relieving this problem of lack of phase discrimination of LDV's ability. Firstly, the threshold levels of the Doppler signals can be adjusted so that the signals with too high amplitudes, probably generated by large spray droplets rather than the seeding particles, can be filtered out electronically. In this way the degree of bias in the gas phase velocity can be reduced and the method is easy to implement. However, partly because the size distribution of spray droplets is so wide extending continuously and quite frequently from sub microns to a few hundred microns, and also because no electric filter has a perfect cut-off frequency, the result obtained by this technique can not be significantly free from any bias due to spray droplets.

Another method of alleviating the problem is by subtracting the pdf measured without seeding particles, the pdf of spray droplets only, e.g., Figure 2.36 (a), from another pdf obtained for the same period of time with seeding particles included, e.g., Figure 2.36(b). This method is applicable only when both the spray properties and the seeding particle density remain the same during the measurement period.

Only a small change of particle density in either phase could cause difficulty in subtracting the pdf's, since it becomes then quite possible that the result has negative frequencies at some points in the velocity spectrum, which is obviously physically not sound.

The optimum method to overcome the problem of velocity measurement of two-phase flow appears to be phase Doppler anemometry (PDA) which allows simultaneous measurements of the velocity and size of particles. Such measurements would allow the gas phase velocity, unbiased by spray droplets, to be obtained, alongside the relevant statistics of the spray droplets, by selecting the velocities associated with particles smaller than a certain size, commonly 5 microns, which is regarded small enough to follow the turbulent fluctuations with high fidelity, then processing them to get the statistics required. However, a PDA system was not available for use during the present work and this could not be done.

2.5.1.4. U-Velocities

Figure 2.37 shows the radial profiles of mean and rms axial velocities at several axial stages for Flame A. To test the axisymmetry of the flow field, velocity profiles have been measured along a complete diameter of the combustor and the profiles along the radii on both sides around the axis of combustor are shown at each axial stages. Overall, the axisymmetry of flow appears to be excellent in most part of the combustor. The profiles of rms velocities are also represented in these graphs but are only plotted for one radius so as not to make the graphs too crowded to be legible.

At the axial positions close to the nozzle, say X = 10 mm for example, the radial profile has two peaks. One is associated with the spray droplets at around r = 8 mm whereas the other corresponds to the gas phase, at around r = 20 mm. Because of the LDV's lack of ability to discriminate between phases, it is not possible to obtain unbiased information of gas phase flow in the region where there are spray droplets, i.e., $0 < r < 20$ mm, in this case. The largest bias error is expected to occur in the range where the contributions from both spray droplets and seeding particles are of comparable order, say $10 < r < 18$ mm. In this region, the measured values are representative of neither spray droplets nor gas phase. Whereas in other parts the profiles can be regarded to be reasonably representative of the appropriate phases. In the latter case, an estimate could be made of the mean velocity of the spray droplets,

which is about 20 m/sec at X = 10 mm. However, it should be noted that the mean and rms velocities measured this way at best represent the averages over the entire droplet size range and thus provide only limited information. By comparison with the profiles measured in the cold flows, a reasonable estimation for the gas phase velocity can be made in the region where the spray droplets are dominant, This is indicated by dotted lines where applicable in the Figures 2.37 (a) and (b).

As the axial distance increases, the spray droplets loose their initial momenta and the velocity difference between them and surrounding gas phase decreases. In addition, the total number of droplets is much reduced due to the evaporation and burning of the fuel. Thus, the bias caused by the presence of spray droplets, accordingly, become less .

One of the main features of burning flow is, compared with cold flow, that the on-axis recirculation zone is much shortened by combustion and is confined within the combustor, as has also been observed by Wilhelmi (1984), with the propane gas fuelled flames in a combustor of similar geometry to that of the present work. This can readily be seen in Figure 2.38 where contours of axial velocities are shown.

Another big difference in similar flow features between cold and burning flows is that the intensity of the off-axis torroidal recirculation near the front corner of combustor, generated basically by a sudden expansion of the flow, is much increased by combustion. The maximum negative mean axial velocity is about 10 m/sec in burning flow compared with about 3 m/sec in the cold flow, whereas the magnitude of the recirculating velocity of the on-axis recirculation zone is less in burning flow (about 7 m/sec) than in cold flow (10 m/sec).

The flow reattachment point appears at X = 100 ~ 120 mm. From half a diameter downstream of this point, i.e., from X = 200 mm, most of the radial variations is evened out and from another half a diameter downstream, X = 300 mm, the radial profiles are essentially uniform and the velocities are positive everywhere inside the combustor, indicating the flow is essentially *unidirectional.*

The velocity increases monotonically slowly from just below 1 m/sec at the centre of the combustor to about 4 m/sec at close to the combustor wall, near the exit of the combustor.

The flow behaviour of Flame B is virtually the same as that of Flame A with the mean velocity levels of Flame B being slightly lower than those of Flame A. This is simply because the air flow rate is lower in Flame B than in Flame A. Therefore, the foregoing description of the flow features of Flame A apply similarly to Flame B. The radial profiles of mean axial velocities at several axial stages are shown in Figure 2.39, together with the profiles of rms values. Contours plots for Flame B are shown in Figure 2.40.

2.5.1.5 V-Velocities

Radial profiles of mean and rms values of radial velocities are shown in Figures 2.41 and 2.42 for Flames A and B, respectively. As with axial velocities, the overall features are the same for both two flames, except that the velocity levels of Flame B are slightly lower than those of Flame A, due to lower air flow rate.

As in the case of the axial velocity profiles, the spray droplets are detected in the region close to the nozzle. For example, at X = 3 mm, the region around r = 5 mm with high peak represents the thick cloud of spray droplets. However the remaining part of the profile is considered to represent the gas phase flow fairly well. This contribution of spray droplets to the measured profiles becomes smaller as the axial distance increases. That is, the maximum of about 30 m/sec at X = 3 mm is reduced down to about 20 m/sec at X = 10 mm, and is further reduced to about 8 m/sec at X = 20 mm where the contribution from the spray droplets is now too small and the central position of the spray is too close to the position of the main air stream to form a distinct maximum. At X = 30 mm, the contribution of spray droplets is hardly distinguishable. It is noted that both mean axial and radial velocities have similar values of about 20 m/sec and is observed at the similar radial position at about r = 10 mm, at the axial stage of X = 10 mm, indicating the total (or inclusive) angle of the spray is about 90^{o}.

In those regions where the contribution of spray droplets to the measurements is significant, the gas phase flow could only be estimated from the measurements because of the LDV's lack of ability to discriminate between the phases. An estimate can be made based on the reasoning that the radial velocity approaches zero monotonically as the axis of combustor is approached, and is represented by the dotted lines in these profiles, Figures 2.41 (a), (b), (c) and Figures 2.42 (a), (b), (c).

The maximum in the mean velocity is not so high initially, being about 6 m/sec at X = 3 mm, obviously due to the low inlet levels of radial velocity. As the axial distance from the nozzle increases, the maximum values rise up to about 22 and 17 m/sec in Flames A and B, respectively, at X = 30 mm, which is apparently due to volumetric expansion generated by combustion. These maximum values are only slightly reduced until the flow reattachment point is reached at around X = 100 mm, from where the profiles become almost uniform rapidly. Inside the maxima, the profiles are also uniform around zero velocities. This part of profiles represent the on-axis recirculation zone, together with the negative parts of the axial velocity profiles extending from the axis of the combustor. The negative velocities arising beyond the maxima in the region of the combustor wall are associated with the off-axis recirculation zone which extends up to X = 60 mm, approximately.

The rms profiles have two maxima around the point where the mean velocity gradients are highest, which is most typically observed at X = 30 mm for both two flames. This feature is not so apparent at other axial stages due to either the complexities of the profiles induced by the spray droplets at upstream locations, or the reduced turbulence levels overall in downstream regions.

From the axial and radial mean velocities, streak lines plot is constructed and is shown in Figure 2.43. Two major groups of streak lines are observed close to the nozzle, say at X = 10 mm. One group, originating from the nozzle which is placed at the axis, represent the movements of spray droplets with the average divergence angle of 45^{o} to the combustor axis while the other, representing the air flow, issues from just in front of the annulus inlet for air and has smaller divergence angle than the other group. This distinction between different phases disappears quickly as the axial distance increases.

These streak lines can be compared with those of cold flow, shown in Figure 2.44, although this is for an air flow rate higher than that of the flames. One major difference is that the relative intensities of recirculation velocities are reversed between on- and off-axis recirculation zones. That is, while the on-axis recirculation of the burning flow has been reduced in intensity and size, the off-axis recirculation zone has been significantly intensified when compared with cold flow. This has also been observed previously in section 2.4.1.4 where the contours of axial velocities have been compared between cold and burning flows at the same air flow rates.

2.5.1.6 W-Velocities

Although the fuel injector has a swirl chamber just located behind the injection nozzle (a characteristic feature of a pressure-jet type atomisers designed to generate a hollow cone spray), the swirling action is restricted only up to the very tip of the nozzle. Once the fuel, broken into spray droplets or not, leaves the injector body, it has little or no swirling motion imposed upon it. The measurement of swirl velocities of gas flow is hence not much hampered by the presence of spray droplets. Since the droplets have virtually no swirl velocity initially, they do not contribute to the resultant swirl velocity pdf measured by LDV. Thus, the swirl velocity profiles measured by LDV represent the gas phase flow faithfully enough in most cases.

Figures 2.45 and 2.47 show the radial profiles of mean and rms swirl velocities at several axial stages for Flames A and B, respectively. A slight positive mean velocity at the axis of combustor at X = 3 mm appears to indicate that the aerodynamic centre does not precisely coincide with the geometrical centre of the combustor. It should otherwise be zero, or close to zero at least.

Once again, as was the case for the axial and radial velocities, the basic features of the swirl velocity profiles are the same for both Flames A and B. The overall levels of mean swirl velocity are slightly lower in Flame B than in Flame A, simply because of the lower air flow rate.

The mean swirl velocities of the inflowing air are about 21 and 17 m/sec for Flames A and B, respectively, as indicated by the maxima in the profiles at X = 3 mm. These peak values drop rather quickly as the axial distance increases. As early as X = 30 mm, the maxima are not so apparent any more, and, at further downstream, the radial variations of mean swirl velocity become negligible except in the region where solid body rotation is observed where the swirl velocity increases monotonically with radius. The solid-body rotation can be observed at around X = 30 mm, and persists further downstream but is limited within a radius of about 40 mm at most towards the exit of the combustor.

It is noted that twin peaks start to develop in the mean swirl velocity profiles from about X = 30 mm, Figure 2.45 (d), in Flame A and from about X = 40 mm, Figure 2.47 (e), in Flame B. In contrast, there are only one peaks observed in the cold flow, Figure 2.28. The development of these twin peaks in mean swirl velocity was

explained by Jones and Wilhelmi (1989) to be due to the angular momentum transported around the recirculating vortex.

However, there is no recirculating flow, as can be seen in the mean axial velocity profiles, Figures 2.37 and 2.38, in those region where the twin peaks of mean swilr velocity are observed. Thus, their argument of the angular momentum transported around the vortex is not supported in the present case. More plausible explanation of why the two peaks are developed in the mean swirl velocity profiles is not yet found. The presence of these two peaks is reflected in the contours, Figures 2.46 and 2.48, of mean swirl velocity, where the contoursof high mean velocities are forked into two *ridges* as the axial distance increases.

Small negative mean velocities on the axis, measured in the downstream region, say X > 100 mm, appear to be due again to the difference between the aerodynamic centre of the flow and the geometrical centre of the combustor.

Just as with the other velocity components, the maximum rms values are observed to arise on both sides of the mean velocity maxima , where the gradients of mean velocity are the highest.

It would be worth mentioning that the overall turbulence level is significantly reduced in burning flows, Figures 2.49 and 2.50, compared to that of cold flow, Figure 2.31. This appears to be due to the turbulence being modulated by the presence of many small spray droplets. Indeed, dispersed particles can either reduce or enhance the turbulence in the gas flow, Yuan and Michaelides (1992), depending upon the Reynolds number based on the particle diameter. That is, small particles consumes the energy via works done by the eddies to accellerate the particles with negligible wakes behind them, for $Re_p < 20$ and as a result the turbulence intensity is reduced. Whereas larger particles shed the vortices behind them with wakes behind and contribute to the production of turbulence at $Re_p > 400$, Clift, et al. (1978).

2.5.2 Temperature Fields

For Flames A and B, radial profiles of mean and rms temperatures have been measured, across the complete diameter of the combustor at several selected axial stages to test the axisymmetry of flame structure in terms of temperature. Overall

flame structure can be assessed from the contours plots of the mean temperature fields shown in Figure 2.51.

The axisymmetry appears to be excellent in the area where most of the spray droplets are expected. Asymmetry becomes identifiable at axial stages beyond about X = 40 mm, and in the outer region of the combustor, r > 40 mm. This can be explained in terms of the spatial, or more properly, the circumferrential variations of either size or number density, or perhaps both, of spray droplets, which can not be easily detected by the flow visualisation technique adopted in the initial stages of nozzle selection for the present work. The region on the one side of the combustor where the temperature is relatively higher is, thus, probably due to more fuel burning there than on the other side where temperature is relatively lower.

A more detailed picture of the temperature fields is provided by the radial profiles of mean and rms temperatures shown in Figures 2.52 and 2.53 for Flames A and B, respectively. Two radial profiles of mean temperatures measured on both sides of the combustor axis are shown in the same graph at each axial stages. Radial profiles of rms temperatures for one side only of the combustor axis are included simply so as not to make the graphs too crowded to read.

Although as has been noted previously the axisymmetry of the flame structure in terms of mean temperatures is not perfect, since the temperatures have been measured across the diameter of the combustor, the two radial profiles represent something close to the upper and lower bounds of the temperature, with circumferrentially averaged temperature profiles being expected to fall between them. It has to be mentioned here that, at the axial stations closest to the nozzle, X = 10 mm, the temperatures could only be measured on one side of thecentreline because of the difficulty of focussing the two crossed laser beams used for positioning the thermocouple junction at desired points.

The asymmetry, observed in the photographs for front views of the flames (Figure 2.19), is detected in terms of temperature profiles. Thus, the radial profiles measured on the opposite sides of the combustor axis at the same axial stages are not identical and differences up to 250 K are evident. From the observation that the radial positions of the maximum and minimum temperatures at each axial stations are almost identical, it follows the asymmetry of flame structure is almost certainly

due to an uneven circumferrential droplet size distribution while the spatial positioning of the spray is closely axisymmetric.

Close to the nozzle, say at X = 10 mm, the profiles are slightly complicated in two respects. One is that a *shoulder* appears at a radial position beyond that of the maximum temperature profile at X = 10 mm. This *shoulder* is probably associated with the presence at this position of spray droplets which hit and cool the thermocouple junction, thereby lowering the mean temperature locally. This is evidenced by very high levels of rms temperatures around the point, suggesting the presence of many droplets. Further evidence of this comes from the axial and radial mean velocities where the maxima associated with the spray droplets are found at around the same position.

Another aspect of the mean temperatures at X = 10 mm is the cut-flat troughs in the profiles at r = 17 ~ 22 mm, which indicates fresh air virtually unmitigated by combustion with a temperature of 289 K, close to the ambient temperature of the inflowing air. This is also consistent with the measured maxima in the axial velocity profiles at the same radal position, which represent the incoming air. The cut-flat troughs in the mean temperature profiles disappear rather quickly, and cannot be observed at other downstream axial stations.

It is interesting to note, from Figure 2.51, that the mean temperature fields have two maxima in both flames. One occurs at about X = 60 mm and covers a wide area , whereas the other one is close to the nozzle, at around X = 15 mm, and covers a narrow region just inside the fuel spray cone. The maximum temperatures associated with the latter region are remarkably similar in both flames, being 1743 and 1746 K in A and B, respectively. However, the maximum temperatures arrising at about X = 60 mm have significantly different values, being 1626 and 1817 K in Flames A and B, respectively.

The mean temperatures on the centre line remain almost constant, being about 1300 and 1450 K in Flames A and B, respectively. The profiles are nearly uniform from the axis to just inside of the mean temperature maxima and this is due to the on-axis recirculation. Other regions of near uniform temperature arise in the outer part of the combustor between the air inlet stream and the combustor wall and upstream of X = 30 mm and are related to the off-axis recirculation region.

The radial variations in mean temperature become gradually reduced as the axial distance increases and, from about X = 150 mm, the profiles bocome almost uniform, indicating that most of the fuel has burned out. Beyond this point, the mean temperature drops slightly as the axial distance increases until the exit of combustor but this is obviously due to heat losses by radiation and convection from the combustor wall to the ambient.

The rms temperatures are largest approximately at the point where the gradients of mean temperature appear to be highest. The maximum rms temperature recorded is about 220 K for Flames A and around 250 K for Flames B. Relatively high values of rms temperatures, say above 50 K, are observed at axial stations of up to about X = 100 mm.

The rms temperature profiles of the two flames do display important differences around the point where the spray droplet densities are expected to be highest. For example, at X = 10 mm, the rms temperature profile of Flame A has a single maximum at r = 8 mm, while that for Flame B has two maxima at r = 6 and 12 mm. The reason why the rms temperature profiles for the two flames should be so different is not clear. A realistic explanation requires more information about the details of the spray behaviour around and inside the flame region but this cannot be obtained by conventional LDV.

2.5.3 Species Concentrations

All the species concentrations have been measured on a dry basis, with the sole exception being the UHC which has been measured wet. Radial profiles of all the species concentrations measured are shown in Figure 2.54 for Flame A and Figure 2.55, for Flame B. To facilitate the analysis and interpretation of the data, the radial profiles of different species concentrations measured are plotted on a single figure for each axial stages.

Since the FID analyser for UHC concentration measurements gives methane (CH_4) equivalent concentrations, these values have to be divided by a factor of 12 to convert them into $C_{12}H_X$ equivalent concentrations, which should represent the unburned liquid kerosene approximately. However, to be precise, measured concentration of UHC should comprise of methane equivalent concentrations from various hydrocarbon species with a certain distribution between them.

It can be observed that O_2 and CO_2 concentrations on the axis of combustor remain almost the same from very close to nozzle to the exit of combustor and they are good indicators of the overall input AFR's. From the overall AFR's, the O_2 and CO_2 concentrations are 10.3 and 7.7 % for Flame A and 7.3 and 10 % for Flame B. These concentrations compare well with the measurements of 10.5 and 7.3 % for Flame A and 7.0 and 9.7 % for Flame B, suggesting small errors of less than 5 % in measurements of these concentrations. Of course, these constant concentrations on the axis are maintained by the on-axis recirculation of hot combustion product gas, which should be more or less homogeneous; thus, the radial profiles over the on-axis recirculation zone are nearly uniform. The O_2 and CO_2 profiles are also uniform in the outer region of the combustor due to the off-axis recirculation.

Most of the change in the radial profiles is confined within the area around the fuel spray which is represented by peaks of UHC concentrations. Thus, where the fuel has been consumed completely, say from X = 100 mm on, the radial profiles are almost flat and remain so all the way down to the exit of combustor.

In the region close to the nozzle, say at X = 10 mm, the measured maximum UHC concentration is about 12 % $C_{12}H_X$ equivalent. Because of this high UHC concentration, relative minima are observed on the CO and H_2 concentration profiles at X = 10 mm. That is, the point where UHC concentration is very high is occupied predominantly by spray droplets and the concentrations of minor species like CO and H_2 are much diluted thereby bringing about a reduction of their concentrations, where otherwise maxima would be expected. This *dilution effect* is observed only very close to the nozzle, at X = 10 mm.

The peak concentrations of UHC fall rather quickly, which is of course due to evaporation and subsequent combustion of spray droplets, as the axial distance increases; for example in Flame A from 12 % at X = 10 mm, through 2.4 % at X = 20 mm, and 0.6 % at X = 30 mm to 0.2 % at X = 50 mm, and so on. Along with this reduction in the peak UHC concentrations, broadening of the spray is also observed with increasing axial distance until the most of spray droplets disappear and the remaining droplets impinge on the combustor wall at around X = 100 mm.

The intermediate species CO and H_2 reflect the changes in UHC concentrations, though the maxima of these species concentrations tend to lie just inside the maximum UHC concentrations at corresponding axial stations. In contrast the

maxima of O_2 and troughs of CO_2 concentration profiles are positioned just outside the maximum UHC concentrations at each axial stages.

CO_2 profiles drop fast across the spray region manifested by UHC peak, as the radial distance increases, to a minimum or trough just outside of the spray. As the radial distance increases further they rise up quickly to the concentration level maintained rather uniform by the off-axis recirculation of combustion product gases.

O_2 profiles behave exactly the other way round. That is, as the radial position inreases, the O_2 concentration rises quickly across the spray region, reaching a maximum just outside the spray and drops down back to the level of the off axis recirculation zone.

The difference between two flames are mainly in the concentration levels of O_2 and CO_2 and the other species concentrations are more or less the same for the two flames. In most part of the combustor, for example in the two recirculation zones and in the far downstream region ($z > 100$ mm), Flame B has higher CO_2 concentration by about 2 % and lower O_2 concentration by 3% when compared with Flame A. The CO, UHC and H_2 concentrations are only slightly higher in Flame B which is fuel-richer than in Flame A.

Contours of species concentrations measured are shown in Figures 2.56 through 2.57, for Flames A and B, respectively. Common to all of these contour plots are the divergence angle of *ridge* contours of each properties, which is about 45^{o} against the axis of combustor and is conforming to visual observation of flame shapes.

It may be worth mentioning that the maximum concentrations of CO and H_2 for both flames are observed at somewhat delayed axial station, say X = 20 mm, rather than earlier position of X = 10 mm. This position of global maxima of CO and H_2 concentrations coincide with the point of global maximum temperature.

A peculiarity is observed with regard to the UHC concentration profiles for the two flames at X = 20 mm. While the concentration levels are quite similar everywhere else, a large difference in peak UHC concentrations is observed at this axial position with about 2 % being measured for Flame A compared with 10 % for Flame B.

Given the differences in overall AFR then comparable differences in UHC concentrations are to be expected at the axial station close to the nozzle, X = 10 mm. However this was not observed to arise. The profiles at X = 10 and 20 mm were remeasured and found to be closely repeatable. The most likely reason why no such difference was observed at X = 10 mm seems to be due to the *ceiling effect* of the FID instrument used in this work. That is, the UHC concentrations arising at X = 10 mm are too high for the instrument to measure, and instead the FID registered a *saturation* concentration which appears to be about 140 % CH_4 equivalent, or 12 % $C_{12}H_X$ equivalent concentration. The instrument has the upper range of 140 % CH_4 equivalent concentration and cannot be used to give reliable results close to the nozzle. The response of the instrument was linear upto about 120 % CH_4 equivalent concentration but above this appreciable errors arose. Consequently the maximum concentration of $C_{12}H_X$ which could be measured reliably was around 10 %.

In the region near the nozzle, say up to X = 80 mm, the relative positions of the maxima of the different species are found to be in a definite sequence, as can be seen in Figure 2.58. That is, going from the centre to the wall of combustor, the maxima appear in the sequence of mean temperature, H_2/CO, UHC and O_2/mean axial velocity. It can be observed from this figure that the trajectories of the spray, indicated by UHC curve, starts from the centre of the combustor and spreads initially almost straight with an inclusive angle of 90^o, indicating a hollow cone spray, and is then deflected slightly inward by the surrounding swirling air, in conformity with the visual observation of flame shapes shown in Figure 2.16.

It is worth noting that the positions of maximum H_2 and CO concentrations do not coincide with those of temperature, except at the early stage of combustion, around X = 10 ~ 20 mm. This can be explained by the intermediate nature of these species, the concentrations of which are determined by a balance between formation and consumption. As the temperature goes up, it appears that the consumption rates are faster than formation rates with the consequence that the maximum concentrations of these species are not coincident with the maximum temperatures.

2.6. Summary

Velocity vectors and scalar properties of turbulent spray flames have been measured inside a swirl-stabilised axisymmetric model combustor made of quartz cylinder. Swirl is induced in the inflowing air stream by an aerodynamic swirler

made of 20 equi-spaced curved swirl vanes, with a resulting swirl number of 0.91. Flames have been maintained by a kerosene hollow cone sprays generated by a pressure-jet type atomiser operated at 16 bars. Two flames have been measured with the same fuel injection rate of 0.951 g/sec, differing only in the air flow rates, 26.51 and 20.75 g/sec, for which the corresponding equivalence ratios are 0.53 and 0.67.

The atomiser nozzle was selected from a number of candidates by observing the spray pattern and then selecting the one which gave to closest axisymmetric distribution. To achieve negligible circumferrential variation of the inlet air flow, the swirler was pulled back from the nozzle by 50 mm. The axisymmetry and circumferrential uniformity of the air flow have been made excellent by this measure.

Three component velocities have been measured at the inlet to the combustor, to provide the relevant set of inlet boundary conditions for computational modelling work. At the inlet to the combustor, the axial and swirl velocities of the burning case are virtually the same as the cold flow, while the radial velocity is higher in burning flow than in cold flow.

The recirculation zone on the axis is shortened in burning flows, extending only up to about X = 300 mm, when compared with that of cold flow, which extends all the way down to the exit of the combustor. The extent of recirculation is increased, by combustion, in the off-axis recirculation zone, while it is reduced in the on-axis recirculation zone. The flow reattachment point to the combustor wall is at about X = 100 mm, downstream of which the radial variation of the mean velocity is monotonic and eventually, close to the exit, the radial profiles of mean axial and radial velocities are nearly uniform. A solid body rotation starts to be seen from about X = 30 mm and it's size increases with axial distance, but covers only up to about the inner half of the combustor radius.

While the maxima of the mean axial and swirl velocities (about 33 and 22 m/sec) set by the inlet conditions both decrease with the axial distance, the peaks of mean radial velocity increase initially from the inlet value of 7.5 m/sec in Flame A, for example, to about 17 m/sec at X = 50 ~ 80 mm, then, after the flow reattachment point at about X = 100 mm, fall rather quickly to zero. This implies that the effect of the volumetric expansion due to combustion is restricted mainly to the radial velocity.

The flame structure is better represented by temperature than velocity. Axisymmetry of the flame structure is excellent close to the nozzle, up to a quarter diameter downstream. Asymmetry develops later and is due to the possible circumferrentially uneven distribution of the spray droplet size or number density, rather than due to any asymmetry of the background gas flow.

There are two temperature maxima in both flames. One occurs close to the nozzle, around X = 20 mm, and the peak is very sharp with both flames having similar maximum temperatures of about 1750 K. The other one develops later, at X = 60 ~ 70 mm, and the peak is much broader than the former one.

A peculiarity has been observed with regard to the rms temperature profiles of the fuel richer (Flame B) of the two flames investigated in this work. The rms temperature profiles have two peaks, and the minimum between them appears to be placed at around the point where the maximum spray droplet density is expected. No realistic explanation for this has been yet found.

The presence of fuel droplets has been sensed by the thermocouple and is indicated by high levels of rms temperatures. The maximum rms temperature recorded was about 250 K in the fuel-richer flame.

O_2 and CO_2 concentrations on the axis of the combustor remain the same from very close to the nozzle to the exit of combustor and are excellent indicators of overall AFR's. In most parts of the combustor , the CO_2 concentration is higher by about 2 % and the O_2 concentration is lower by about 3 % in the fuel-rich flame (Flame B) than in the leaner counterpart. Other species concentrations are more or less the same for the two flames, with CO, UHC, and H_2 concentrations being only very slightly higher in the fuel-rich one. The maximum concentrations observed are about 2 and 1.1 % for CO and H_2, respectively. These maximum concentrations are observed at X = 20 mm, which coincides roughly with the position of global maximum mean temperature.

Chapter 3.

Computational Modelling of Turbulent Spray Flames

3.1 Introduction

Computational modelling is attempted to predict the properties of turbulent flames fuelled by hollow-cone sprays of kerosene, as have been studied experimentally and described in Chapter 2. The main task of the present work is to properly predict the behaviour of spray droplets in turbulent flames. The spray droplets are viewed as the passive particles whose histories (position, velocity, and acceleration, for example) is influenced by the gas phase flow and turbulence. They are regarded as the source of fuel and provide the gaseous fuel through the evaporation of the liquid fuel droplets along their trajectories.

While the gas phase flow field is represented by the Navier-Stokes equations , the spray droplets are represented by discrete Lagrangian stochastic particles. Turbulence in the gas phase flow field is modelled by a second moment closure. The effect of the gas phase turbulence on the spray droplets (turbulent dispersion), which is the main issue of spray modelling in the present work, is modelled by a Wiener process.

The governing equations for the gas phase properties are stated in the section 3.2, followed by the description of the Reynolds averaging process. The next section covers turbulence modelling, where the second moment closure approximation for the Reynolds stress is described. Previous approaches to spray modelling are reviewed in section 3.4 where attention is restricted mainly to two-phase flow approaches, stochastic or deterministic. The Wiener process, employed to model the turbulent dispersion of spray droplets, is explained in section 3.5. Various transport processes relevant to droplets are outlined in section 3.6. The laminar flamelet approach adopted to model the combustion reaction is explained in the Section 3.7. Some numerical aspects relevant to the present work are covered in the last section.

3.2 Governing Equations of Gas Phase

The transport processes in the gas phase can be described by a set of partial differential equations based on the conservation of mass, momentum, energy, and species concentrations as follows:

$$\frac{\partial}{\partial t}\rho + \frac{\partial}{\partial x_j}\rho u_j = S_m \tag{3.2-1}$$

$$\frac{\partial}{\partial t}\rho u_i + \frac{\partial}{\partial x_j}\rho u_j u_i = -\frac{\partial p}{\partial x_i} + \frac{\partial}{\partial x_j}[\mu(\frac{\partial u_i}{\partial x_j} + \frac{\partial u_j}{\partial x_i} - \frac{2}{3}\delta_{ij}\frac{\partial u_l}{\partial x_l})] + \rho g_i + S_i \tag{3.2-2}$$

$$\frac{\partial}{\partial t}\rho h + \frac{\partial}{\partial x_j}\rho u_j h = \frac{\partial p}{\partial t} + \frac{\partial}{\partial x_j}[\frac{\mu}{Pr}\frac{\partial h}{\partial x_j} + \mu(\frac{1}{Sc} - \frac{1}{Pr})\sum_{\alpha=1}^{N} h_\alpha \frac{\partial Y_\alpha}{\partial x_j}] + S_h \tag{3.2-3}$$

$$\frac{\partial}{\partial t}\rho Y_\alpha + \frac{\partial}{\partial x_j}\rho u_j Y_\alpha = \frac{\partial}{\partial x_j}[\frac{\mu}{Sc_\alpha}\frac{\partial Y_\alpha}{\partial x_j}] + \rho \dot{r}_\alpha \ , \quad \alpha = 1, N \tag{3.2-4}$$

Here, u_i is the velocity in the $x_i (i = 1,2,3)$ direction at time t and ρ, μ, p and Y_α are the gas density, viscosity, pressure and mass fraction of species α amongst a total of N species. h is the total enthalpy contributed by all the species present, and is given by;

$$h = \sum_{\alpha=1}^{N} Y_\alpha h_\alpha \tag{3.2-5}$$

where h_α is the enthalpy of species α, defined by;

$$h_\alpha = (C_P T)_\alpha + (\Delta H_f^\circ)_\alpha \tag{3.2-6}$$

with $(\Delta H_f^\circ)_\alpha$ being the standard heat of formation of species α and Y_α is the mass of the species α. Pr and Sc are the Prandtl and Schmidt numbers defined as;

$$Pr = \frac{\nu}{\alpha} \tag{3.2-7}$$

$$Sc = \frac{\nu}{D} \tag{3.2-8}$$

where ν is the kinematic viscosity, μ/ρ, α is the thermal diffusivity, $k/\rho Cp$, with k being the thermal conductivity, and D is the molecular diffusivity.

The various source terms are denoted by S_m, S_i, S_h, and $\dot{r}_\alpha$, for mass, momentum in x_i direction, enthalpy, and the rate of formation of species α, respectively.

3.2.1 Averaging Process

The governing equations (3.2-1) to (3.1-4) hold for the instantaneous values of the properties concerned. The direct solution to these equations for turbulent flow problems requires both the computational time and length scales to be smaller than the smallest expected eddy time and length scales, and this is not feasible in most cases even with nowadays improved computer resources. Furthermore, in many engineering applications, the set of mean values are sufficient to describe the problem adequately enough. Therefore, the common approach to the solution of turbulent flow problem is to transform the instantaneous base equations into the averaged ones. This is usually done by decomposing the instantaneous value, φ, into it's mean, $\overline{\varphi}$, and the fluctuating component, φ', as below;

$$\varphi(x_i,t) = \overline{\varphi}(x_i) + \varphi'(x_i,t) \tag{3.2-9}$$

inserting this into the equations and averiging the results, the Reynolds averaging process.

The instantaneous value can also be decomposed into a density-weighted, or Favre, mean, $\tilde{\varphi}$, and a fluctuation, φ'', about that mean (Favre, 1969);

$$\varphi(x_i,t) = \tilde{\varphi}(x_i) + \varphi''(x_i,t) \tag{3.2-10}$$

where the mean is defined by:

$$\tilde{\varphi} = \frac{\overline{\rho\varphi}}{\overline{\rho}} \tag{3.2-11}$$

The averaged equations which may be derived may thus be either unweighted or density-weighted, depending upon the type of mean used to decompose the instantaneous value. Whenever necessary, the unweighted averages can be deduced from the density-weighted ones, or vice-versa, by making use of the following relationships:

$$\tilde{\varphi} - \overline{\varphi} = \frac{\overline{\rho'\varphi'}}{\overline{\rho}} = \frac{\widetilde{\rho'\varphi''}}{\overline{\rho}} \tag{3.2-12}$$

Obviously, when there is no density fluctuation, the distinction between two averages vanishes.

3.2.2 Density-Weighted Averaged Equations

The averaged governing equations become simpler when the density weighted means are used in decomposing the instantaneous values. For example, the average of the momentum flux are written either with the unweighted mean as;

$$\overline{\rho u_i u_j} = \overline{\rho}\,\overline{u}_i\overline{u}_j + \overline{\rho}\,\overline{u_i'u_j'} + \overline{u}_i\overline{\rho'u_j'} + \overline{u}_j\overline{\rho'u_i'} + \overline{\rho' u_i'u_j'} \tag{3.2-13}$$

or with the density weighted mean as:

$$\overline{\rho u_i u_j} = \overline{\rho}\,\tilde{u}_i\tilde{u}_j + \overline{\rho}\,\widetilde{u_i''u_j''} \tag{3.2-14}$$

As is observed from this example, the Equation (3.2-14) contains no correlations involving density fluctuations, which is a major advantage of the Favre average over the unweighted average. Since it involves fewer unknown correlation terms, it relieves much of the computational work that might otherwise be necessary for modelling.

With density-weighted averaging, the governing equations can be written for high Reynolds number flow as:

$$\frac{\partial}{\partial t}\bar{\rho} + \frac{\partial}{\partial x_i}\bar{\rho}\tilde{u}_j = \bar{S}_m \tag{3.2-15}$$

$$\frac{\partial}{\partial t}\bar{\rho}\tilde{u}_i + \frac{\partial}{\partial x_j}(\bar{\rho}\tilde{u}_i\tilde{u}_j + \bar{\rho}\widetilde{u_i''u_j''}) = -\frac{\partial \bar{p}}{\partial x_i} + \bar{S}_i \tag{3.2-16}$$

$$\frac{\partial}{\partial t}\bar{\rho}\tilde{h} + \frac{\partial}{\partial x_j}(\bar{\rho}\tilde{u}_j\tilde{h} + \bar{\rho}\widetilde{u_j''h''}) = \frac{\partial \bar{p}}{\partial t} + \bar{S}_h \tag{3.2-17}$$

$$\frac{\partial}{\partial t}\bar{\rho}\tilde{Y}_\alpha + \frac{\partial}{\partial x_j}(\bar{\rho}\tilde{u}_j\tilde{Y}_\alpha + \bar{\rho}\widetilde{u_j''Y''}) = \bar{\rho}\tilde{r}_\alpha\ ,\ \ \alpha = 1,N \tag{3.2-18}$$

There are three extra unknown correlations, $\widetilde{u_i''u_j''}$, $\widetilde{u_j''h''}$, and $\widetilde{u_j''Y_\alpha''}$, corresponding to the Reynolds stress, enthalpy flux, and scalar flux respectively. To close the problem, proximations for these must be provided and methods of achieving this is described in the next section on turbulence model.

3.3 Turbulence Model

There have been many models proposed to approximate the extra unknown correlation terms that arise as a result of the Reynolds or Favre averaging process. One of the most popular is the k-ε model. In this model, the Boussinesque eddy viscosity concept is invoked to relate the turbulent stress to the mean rate of strain via a turbulent, or eddy viscosity, and the gradient diffusion hypothesis is used to model the scalar flux:

$$\bar{\rho}\widetilde{u_i''u_j''} = -\mu_T\left(\frac{\partial \tilde{u}_i}{\partial x_j} + \frac{\partial \tilde{u}_j}{\partial x_i} - \frac{2}{3}\delta_{ij}\frac{\partial \tilde{u}_l}{\partial x_l}\right) + \frac{2}{3}\delta_{ij}\bar{\rho}\tilde{k} \tag{3.3-1}$$

$$\bar{\rho}\widetilde{u_j''\varphi''} = -\frac{\mu_T}{\sigma_T}\frac{\partial \tilde{\varphi}}{\partial x_j} \tag{3.3-2}$$

where σ_T is a turbulent Prandtl number and μ_T is the turbulent viscosity, determined from the local values of turbulence kinetic energy k and it's dissipation rate ε:

$$\mu_T = C_\mu \rho \tilde{k}^2 / \tilde{\varepsilon} \tag{3.3-3}$$

The turbulence kinetic energy and it's dissipation rate are obtained from the solution of the modelled transport equations:

$$\frac{\partial}{\partial t}\bar{\rho}\tilde{k}+\frac{\partial}{\partial x_j}\bar{\rho}\tilde{u}_j\tilde{k}=\frac{\partial}{\partial x_j}(\frac{\mu_T}{\sigma_k}\frac{\partial \tilde{k}}{\partial x_j})+G-\bar{\rho}\tilde{\varepsilon} \tag{3.3-4}$$

$$\frac{\partial}{\partial t}\bar{\rho}\tilde{\varepsilon}+\frac{\partial}{\partial x_j}\bar{\rho}\tilde{u}_j\tilde{\varepsilon}=\frac{\partial}{\partial x_j}(\frac{\mu_T}{\sigma_\varepsilon}\frac{\partial \tilde{\varepsilon}}{\partial x_j})+C_1\bar{\rho}\frac{\tilde{\varepsilon}}{\tilde{k}}G-C_2\bar{\rho}\frac{\tilde{\varepsilon}^2}{\tilde{k}} \tag{3.3-5}$$

where

$$G=[\mu_T(\frac{\partial \tilde{u}_i}{\partial x_j}+\frac{\partial \tilde{u}_j}{\partial x_i}-\frac{2}{3}\delta_{ij}\frac{\partial \tilde{u}_l}{\partial x_l})-\frac{2}{3}\delta_{ij}\bar{\rho}\tilde{k}]\frac{\partial \tilde{u}_i}{\partial x_j} \tag{3.3-6}$$

where the model constants, C_μ, C_1, C_2, σ_k, and σ_ε are assigned with the values as in Table 3.1

Table 3.1 Model Constants for k-ε Model

C_μ	C_1	C_2	σ_k	σ_ε
0.09	1.44	1.92	0.433	4.82

This model is relatively simple and has been applied successfully to many diverse flow problems including combustion. However, it has been reported (Attya and Whitelaw, 1984; Nikjooy, et al., 1988; and Pascau, 1989) that this model performs poorly, particularly for swirling flows. Nevertheless, it is still one of the most widely used model (Crowe, et al., 1977; Jones and Priddin, 1978; Gosman and Johns, 1981; Watkins, et al., 1986; Reitz and Diwakar, 1986; and Wild, et al., 1988) and is employed in the present work for the purpose of comparison with a higher order model.

In the second order moment closure model, the turbulent stress and the scalar flux are obtained from solution of their modelled transport equations, which can be written as;

$$\frac{\partial}{\partial t}\overline{\rho}\,\widetilde{u_i''u''} + \frac{\partial}{\partial x_l}\overline{\rho}\,\tilde{u}_l\widetilde{u_i''u_j''} = -\left[\overline{\rho}\,\widetilde{u_i''u_j''}\frac{\partial \tilde{u}_i}{\partial x_l} + \overline{\rho}\,\widetilde{u_l''u_i''}\frac{\partial \tilde{u}_j}{\partial x_l} + \frac{\partial}{\partial x_l}\overline{\rho}\,\widetilde{u_i''u_j''u_l''}\right]$$
$$-\left[\overline{u_i''}\frac{\partial \overline{p}}{\partial x_j} + \overline{u_j''}\frac{\partial \overline{p}}{\partial x_i} + \overline{u_i''\frac{\partial p'}{\partial x_j}} + \overline{u_j''\frac{\partial p'}{\partial x_i}}\right] - \left[\overline{\tau'_{li}\frac{\partial u_j''}{\partial x_l}} + \overline{\tau'_{lj}\frac{\partial u_i''}{\partial x_l}}\right] \qquad (3.3\text{-}7)$$

$$\frac{\partial}{\partial x_l}\overline{\rho}\,\tilde{u}_l\widetilde{u_i''f''} = -\left[\overline{\rho}\,\widetilde{u_j''f''}\frac{\partial \tilde{u}_i}{\partial x_j} + \overline{\rho}\,\widetilde{u_i''f''}\frac{\partial \tilde{u}_j}{\partial x_i} + \frac{\partial}{\partial x_l}\overline{\rho}\,\widetilde{u_i''u''f''}\right]$$
$$-\left[\overline{f''}\frac{\partial \overline{p}}{\partial x_i} + \overline{f''\frac{\partial p'}{\partial x_i}}\right] - \left[\overline{\tau'_{ij}\frac{\partial f''}{\partial x_j}} - \overline{J_{fj}\frac{\partial u_i''}{\partial x_j}}\right] \qquad (3.3\text{-}8)$$

where τ_{ij} and J_{fj} are the viscous stress tensor and the molecular diffusion flux, respectively.

To solve these equations (3.3-7) and (3.3-8) requires further modelling of the many terms involved on the right hand sides of them. In the present work the closure formulated by Jones and Musonge (1988) recast in density weighted form is used. The model is summarized in Appendix B.

The computer code developed earlier (Jones and Marquis, 1985; and Jones and Pascau, 1989) is employed for the present study. It solves the equations appropriate to axisymmetric flow problems and has been successfully applied to predict various flow problems including the combustion with gaseous fuels injected.

3.4 Review of Approaches to Spray Modelling

There are two major groups of spray models, namely the locally homogenous-flow (LHF) model and the two-phase-flow (TPF) model. In the LHF model, the two phases of the spray system are assumed to be in dynamic and thermodynamic equilibrium. That is the spray droplets are assumed to behave as if they are a gaseous jet with equal momentum. This is also called the simulated gaseous flame model (Khalil and Whitelaw, 1976). This model can be a useful tool for the limiting

case of a spray consisting of very small droplets, where at the instant of spraying, all the liquid is vaporised into vapour without delay; a rather rare occurrence to expect. It has been observed (Styles and Chigier, 1973; Onuma and Ogasawara, 1974; Komiyama, et al., 1976; and Onuma, et al., 1976) that for sprays well atomised with Sauter mean diameters in the range of 10 to 20 μm, the model predicts flame structure satisfactorily. However, according to Khalil and Whitelaw(1976), the predicted length of the flame is shorter than the measured ones, and the model is not a good approximation to spray flames. Also, it has been reported (Shuen, et al., 1983) that this model always overestimates droplet dispersion. Nonetheless, the model can provide a reasonable first estimate of the extent and character of spray flames.

The TPF model can be further classified into two groups. One is the continuum droplet model (CDM) and the other is the discrete droplet model (DDM). The CDM represents two phases as two superimposed continua occupying the same volume. That is, the two phases are described as two interpenetrating continua which interact with each other, and the droplets are treated as a continuous fluid, not a discrete one, differing only by the phase from the background gaseous fluid. Therefore, the governing equations for the phases are similar. This idea originates from early investigations of heterogeneous reacting systems and in the 1970's this approach was used by a number of workers, e.g., Harlow and Amsden (1975), and Travis, et al. (1976) to study safety problems related to nuclear reactor cooling systems. The continuity and the momentum equations, for example, are written as follows for the droplet phase:

$$\frac{\partial \rho_p}{\partial t} + \nabla \bullet (\rho \mathbf{u}) = S_m \qquad (3.4\text{-}1)$$

$$\frac{\partial}{\partial t}\rho \mathbf{u} + \nabla \bullet (\rho \mathbf{uu}) = S_i - \nabla p + \rho \mathbf{g} + D(\mathbf{u}) \qquad (3.4\text{-}2)$$

where S_m and S_i are sources (or sinks) to the mass and momentum of each phase, and $D(\mathbf{u})$ is the drag force term.

This approach yields a particular concise formulation when a single fluid is adequate to describe the process. However, for sprays, which are invariably polydispersed, multiple "*phases*" must be considered based on droplet size ranges, and this can only be represented by defining discrete size ranges. A polydisperse

spray system can only be realistically represented, in this model, by the introduction of a large number of transport equations, one for each discrete size of droplets, with the consequence that the approach becomes too costly in terms of computer time and storage requirements. Also, the model requires small computational grids for all phases near the injector in order to resolve the flow and reduce numerical diffusion.

The spray equation, developed by Williams (1958, 1959, and 1985), is the stochastic version of the CDM. The droplet field is described by a continuous statistical distribution function defined at all positions in the flow field. The distribution function, or the density function, f(r, **x**, **v**, t) is defined to represent the probable number of droplets as a function of droplet size, r, the spatial position, **x**, and the velocity, **v**, at an instant t. An equation governing the time rate change of this function has been derived as;

$$\frac{\partial f}{\partial t} + \frac{\partial}{\partial r}(Rf) + \nabla_x \bullet (\mathbf{x}f) + \nabla_v \bullet (\mathbf{F}f) = S \qquad (3.4\text{-}3)$$

where R is the vaporisation rate of droplet dr/dt, **F** is the force per unit mass acting on a particle exerted by external forces, such as gravity and the aerodynamic drag force, and S is the generalised source including droplet interaction terms such as coalescence and collisions.

Bracco (1974) adopted this equation to study the combustion of sprays of ethanol droplets in oxygen in a constant cross-sectional area rocket motor. The steady state spray equation was solved for monodisperse and distributed initial droplet radii with various drag and vaporisation rate equations. Westbrook (1976) applied this equation to thin sprays injected into a satisfied charge internal combustion engine. Chemical reactions were not included and the properties of the gas flow field were assumed to be not affected by the presence of droplets during the penetration and vaporisation of the spray.

The spray equation may be expressed in terms of the probable mass fraction, instead to the probable number density, of droplets. Under the following assumptions that:

- there is no relative velocity between the phases (no-slip),
- any forces acting on a particle does not change the distribution,

- there is no droplet collision and break-up, and
- the flow is steady,

it can be expressed as;

$$\nabla \bullet (\rho \mathbf{u} m) = -r^3 \frac{\partial}{\partial r}(R\rho m / r^3) \qquad (3.4\text{-}4)$$

where m is the probable mass of droplets of size r in position x. This equation was employed by Jones and Priddin(1978) and Jones and McGuirk(1979) for a liquid kerosene spray fuelled gas turbine combustor without swirl.

The spray equation model is most easily applied to simplified problems, for example, where the droplets of pure component are evaporating at a steady wet-bulb condition. Even in this case the number of dimensions required to specify the distribution function is eight. For more complex problems the number of independent dimensions should be further increased when additional factors, such as temperature and composition variations of the droplets are to be considered, leading to serious computer storage problems. Furthermore, the droplet densities, velocities, sizes, etc. vary rapidly in the region close to the nozzle, which would require closely spaced multidimensional grids if the problem is to be solved without serious numerical diffusion. Consequently solution of the spray equation by finite difference techniques is intractable for most practical problems. For this reason, the DDM is becoming more widely adopted nowadays for most of the spray problems (Faeth, 1983).

In the DDM, the spray is normally statistically represented by a finite selected number of discrete droplets. This amounts to statistical (or Monte Carlo) formulation of the problem. Each computational (or stochastic) particle is considered to represent a group of particles possessing the same characteristics such as size, composition, temperature, velocity, and position. The main difference between this model and the others is that two different viewpoints are used for each phase. While the Eulerian viewpoint is employed for the equation of motion for the continuum gas phase, the Lagranigian viewpoint is used to describe the motion of the discrete phase, i.e. droplets. The Lagrangian formulation of the equations for droplet motion are as follows;

$$m_p \frac{dv_p}{dt} = m_p g + D(v_g, v_p)(v_g - v_p) \tag{3.4-5}$$

$$\frac{dx_p}{dt} = v_p \tag{3.4-6}$$

where m_p,v_p, and x_p are the mass, velocity vector and the position vector of droplet, respectively; D is the drag force function, **g** is the gravity vector and v_g is the gas velocity vector.

Gauvin, et al. (1975) used the Lagrangian equation to calculate the droplet trajectories in three-dimensional motion with the application corresponding to a spray dryer. The forces due to centrifugal, Coriolis, and lift were accounted for in the equations. They used the predetermined velocity field for the gas phase and assumed no change in the gas flow field by the presence of spray droplets. Therefore, the interaction between the phases was *one-way*.

The model developed by Crowe (1974) accounted for *two-way coupling* of mass and momentum between the phases, and was used for swirling flow in an axisymmetric combustor where it was found that the on-axis recirculation velocity was attenuated by the spray and that the droplet penetration was increased over that predicted with the gas-droplet interaction neglected. The model was developed further by Crowe, et al. (1977) and Crowe (1978) to include all three modes, mass, momentum, and energy, of two-way coupling. The model is founded on the idea that the droplets are treated as sources of mass, momentum, and energy to the gas phase, and is thus called the particle-source-in-cell (PSIC) model. Actually, this concept of regarding the condensed (i.e. discrete) phase as a source to a continuum phase was proposed first by Migdal and Agosta (1967). However, the approach was used in a continuum representation of the droplet phase.

Many works up to the early 1980's were deterministic ones in the sense that only the mean trajectories of droplets, with different initial conditions, were considered. The stochastic DDM, where turbulent dispersion of droplets is accounted for, was proposed only recently by Dukowicz (1980). In this work the random instantaneous turbulent velocity of the gas was selected according to the equation:

$$v_g = \sqrt{k}\, sign(\mathbf{X}) \mathrm{erf}^{-1}(|\mathbf{X}|) \tag{3.4-7}$$

where $\mathbf{X}$ is the random vector with uniform distribution in the range of $-1 < \mathbf{X} < 1$. The initial particle size and the injection velocities were selected independently of each other from the uniform random distributions in the ranges of:

$$0 \le r_p \le r_{p,max} \tag{3.4-8}$$

$$0 \le v_p \le v_{p,max} \tag{3.4-9}$$

Then particles are assumed to be acted on by this instantaneous velocity for a time period equal to τ_t, a turbulence time scale with the values of k and τ_t being estimated from turbulence modelling. Amsden, et al. (1985) employed this approach to predict the spray combustion inside the cylinder of an internal combustion engine and calculations were made for 2- and 3-dimensional problems.

Dukowicz's method was subsequently slightly modified by Gosman and Ioannides (1983) and has since been adopted by many researchers (Beshay, et al., 1986; Reitz and Diwakar, 1986; Watkins, et al., 1986; Wild, et al., 1988) in dealing with turbulent dispersion of spray droplets. Their method was different from Dukowicz's only in the selection of the time scale over which the random velocity is presumed to act. They assumed the flow field comprises turbulent eddies with the characteristic time scale, τ_ε, and the length scale, l_ε, whose velocity probability distribution function (pdf) is Gaussian with standard deviation $(2k/3)^{1/2}$. The characteristic time and length scales are related to the turbulent kinetic energy and it's dissipation rate by:

$$\tau_\varepsilon = (\frac{3}{2} C_\mu)^{1/2} k / \varepsilon \tag{3.4-10}$$

$$l_\varepsilon = C_\mu^{1/2} k^{3/2} / \varepsilon \tag{3.4-11}$$

As a droplet traverses an eddy, it is assumed to experience an instantaneous velocity obtained by randomly sampling from the afore-mentioned pdf, and the time over which this act is taken to be the smaller of the eddy life time, τ_ε, and the time required for the droplet to traverse the eddy, i.e.,

$$\tau_{int} = \min(\tau_\varepsilon, \tau_t) \tag{3.4-12}$$

where τ_t is the traverse time for the droplet through the eddy, determined by:

$$\tau_t = l_\varepsilon / \left| \mathbf{u}_g - \mathbf{u}_p \right| \qquad (3.4\text{-}13)$$

The corresponding predictions were compared with the measurements in a quiescent bomb of Yule, et al. (1985) and satisfactory agreement with measured penetration data was reported.

A similar method was employed by Watkins, et al. (1986) who calculated the multidimensional behaviour of sprays injected into the combustion chamber of motored reciprocating engines. Droplet sizes were randomly selected from a prescribed inlet size distribution function with a Sauter mean diameter of 25 μm. Wild, et al. (1988) reported a slight variation of the approach in which, based on the analysis by Hinze (1975), Equation (3.4-10) was replaced by:

$$\tau_\varepsilon = 0.16k / \varepsilon \qquad (3.4\text{-}14)$$

3.5 Wiener Process for Turbulent Dispersion

The turbulent dispersion of spray droplets is basically a random process, where the movement of droplets is determined not only by the deterministic but also by the stochastic, or fluctuating, forces arising from the turbulent motions of the gas phase. If only viscous drag forces are considered (with gravity, Magnussen and Basset forces neglected), then the equation of motion of droplets undergoing a random dispersion can be written as:

$$m_p \frac{dv_p}{dt} = C_D a_p (v_g - v_p) + \mathbf{X} \qquad (3.5\text{-}1)$$

where $\mathbf{v}_g$ is the mean gas phase velocity vectors and m_p, C_D and a_p are the droplet mass, the drag coefficient and the cross-section area, respectively. The last term, $\mathbf{X}$, denotes the stochastic force which gives rise to the dispersion of the droplets in turbulent flow.

In fact, this equation is just one example of Langevin's equation, which originates from Langevin's work in describing mathematically the extremely irregular motion of pollen particles suspended in water, as was observed microscopically by Brown and hence named Brownian motion. Langevin was the first to develop this type of stochastic differential equation to analyse particle trajectories and the problem is clearly analogous to the task of determining possible trajectories of spray droplets.

The solution to this Equation (3.5-1) can be readily obtained only if the random force term, **X** is expressed in such a way that it can be integrated with respect to time. The Wiener process (Chandrasekhar, 1954; Cox and Miller, 1965; and Papoulis, 1965) is a very useful and widely used stochastic process for representing the random force corresponding to a diffusion process, although, to the best knowledge of the author, it has not been used so far in modelling the turbulent dispersion of spray droplets. The Wiener process is defined as the following process involving the random variable ξ_i;

$$\mathbf{W}(t_n) \equiv \delta t^{1/2} \sum_{i=1}^{n} \xi_i \tag{3.5-2}$$

where $t_n = n(\delta t)$ and ξ_i is the sequence of n independent normal random variables whose mean is zero and the variance is unity. The increment of this process, $\mathbf{W}(t_n)$, written as;

$$\Delta\mathbf{W}(t_n) = \mathbf{W}(t_n) - \mathbf{W}(t_{n-1}) \tag{3.5-3}$$

has following properties:

$$\langle \Delta\mathbf{W}(t_n) \rangle = \delta t^{1/2} \langle \xi_n \rangle = 0 \tag{3.5-4}$$

$$\langle \Delta\mathbf{W}^2(t_n) \rangle = \delta t^{1/2} \langle \xi_n{}^2 \rangle = \delta t \tag{3.5-5}$$

That is, the increment of the Wiener process is a Gaussian random variable with zero mean and the variance equal to the time step δt. The Equation (3.5-3) shows that the Wiener process is a continuous process, since $\Delta\mathbf{W}(t_n) \rightarrow 0$, that is $\mathbf{W}(t_n) \rightarrow \mathbf{W}(t_{n-1})$ as δt goes to zero. It also shows that the Wiener process is not differentiable because, as δt becomes infinitely small, the derivative of the process, $\Delta\mathbf{W}(t_n)/\delta t$

becomes infinite. These are, together with the properties described by equations (3.5-4) and (3.5-5), the most important features of the Wiener process.

The use of the Wiener process in analysing random, or Brownian motion, and thus dispersion, is justified by the fact that it is a solution to the Fokker-Planck equation. The Fokker-Planck equation is a reduced example of the differential Chapman-Kolmogorov equation which is the most general probabilistic differential equation for a diffusion process and which can be written:

$$\frac{\partial}{\partial t}p(\mathbf{z},t;\mathbf{y},t') = -\sum_i \frac{\partial}{\partial z_i}A_i(\mathbf{z},t)p(\mathbf{x},t;\mathbf{y},t') + \frac{1}{2}\sum_{i,j}\frac{\partial^2}{\partial z_i \partial z_j}B_{ij}(\mathbf{z},t)p(\mathbf{x},t;\mathbf{y},t') \tag{3.5-6}$$

In this equation, $p(\mathbf{x},t;\mathbf{y},t')$ denotes the conditional probability density at $\mathbf{z}$ and t provided that the probability density at $\mathbf{y}$ and t is given. $\mathbf{z}$ and $\mathbf{y}$ are each a different point in random vector space $\mathbf{X}(\mathbf{x})$. $A_i(\mathbf{z},t)$ is called the drift vector and $B_{ij}(\mathbf{z},t)$ the diffusion matrix. A process whose evolution of probability is governed by this equation, is called a diffusion process. If there is no drift and the diffusion coefficient is unity, Equation (3.5-6) reduces to:

$$\frac{\partial}{\partial t}p(\mathbf{w},t;\mathbf{w}_o,t_o) = \frac{1}{2}\sum_i \frac{\partial^2}{\partial w_i{}^2}p(\mathbf{w},t;\mathbf{w}_o,t_o) \tag{3.5-7}$$

Given the initial condition:

$$p(\mathbf{w},t_o;\mathbf{w}_o,t_o) = \delta(\mathbf{w}-\mathbf{w}_o) \tag{3.5-8}$$

the solution to the Equation (3.5-7) is:

$$p(\mathbf{w},t;\mathbf{w}_o,t_o) = \frac{1}{\sqrt{2\pi(t-t_o)}}\exp[-(\mathbf{w}-\mathbf{w}_o)^2/2(t-t_o)] \tag{3.5-9}$$

Thus, the probability, initially a sharp distribution, spreads in time and is a Gaussian pdf whose mean and variance are;

$$\langle \mathbf{W}(t) \rangle = \mathbf{w}_o \tag{3.5-10}$$

$$\left\langle [\mathbf{W}(t) - \mathbf{w}_o]^2 \right\rangle = t - t_o \qquad (3.5\text{-}11)$$

which are basically the same properties as described by the equations (3.5-4) and (3.5-5) with $\mathbf{w}_o=\mathbf{0}$ and $\delta t = t - t_o$.

It is the increment of the Wiener process, Equation (3.5-3), which is commonly used in specifying the stochastic term of Equation (3.5-1). The Equation (3.5-1) can be written as;

$$dv_p = \frac{1}{\tau_p}(v_g - v_p)dt + \mathbf{X}dt \qquad (3.5\text{-}12)$$

where $\tau_p = C_D A_p / m_p$ is the relaxation time of the droplet.

To employ the Wiener process for turbulent dispersion the second term on the RHS of the Equation (3.5-12) is written as the product of the diffusion coefficient matrix **B** and the increment of the Wiener process, **dW**:

$$dv_p = \frac{1}{\tau_p}(v_g - v_p)dt + \mathbf{B}d\mathbf{W} \qquad (3.5\text{-}13)$$

The diffusion matrix **B** should be distinguished from the turbulent diffusivity since the former has dimensions of $l / t^{3/2}$, whereas the latter has dimensions of l / t^2. If the dispersion is presumed isotropic, then the diffusion matrix can be reduced to a scalar coefficient and the Equation (3.5-13) can be written:

$$dv_p = \frac{1}{\tau_p}(v_g - v_p)dt + b\,d\mathbf{W} \qquad (3.5\text{-}14)$$

Now the droplet trajectory, or sample path, described by this equation will be continuous but extremely irregular and variable because of the properties of the Wiener process. In addition and more importantly, the variance of the droplet trajectories of many samples (a measure of diffusion) spreads as time increases from the initially sharp distribution as is prescribed by the Wiener process. Furthermore, this variance is a continuous function of time and is independent of the time step, δt, selected for the integration of the equation.

It is noted that the basic assumption underlying the Langevin's equation (a probabilistic expression for Brownian motion) is that the evolution of the process in question, $v_p(t)$ in this work, is solely dependent upon present values and not upon the past value. Such a process involving only the present value is called a Markov process.

Langevin's equation and the Wiener process have been used to describe *mixing* in turbulent motion of a single gaseous phase, Pope (1983). In this approach the diffusion coefficient, b, is represented by:

$$b = \sqrt{C_o \varepsilon} \tag{3.5-15}$$

where C_o is a presumed universal constant and ε is the dissipation rate of turbulent kinetic energy. Alternatively it can be expressed (Luhar and Britter, 1989) as:

$$b = \sqrt{2k/\tau_t} \tag{3.5-16}$$

where k is the turbulent kinetic energy and $\tau_t = k/\varepsilon$ is a turbulent time scale, characteristic of the energy containing turbulent eddies.

In the present work which is concerned with dispersion of a liquid droplet phase, the diffusion coefficient is modelled as;

$$b = \sqrt{k/\tau_p} \tag{3.5-17}$$

where τ_p is the relaxation or aerodynamic response time of the droplet. The use of this new model for diffusion coefficient is motivated by following points:

Strictly speaking, the forms represented by Equations (3.5-15) and (3.5-16) are only appropriate to dissipation processes arising in turbulent motions of a single fluid phase. However, the expession (3.5-16) has been applied with reasonable success to represent the dispersion of *pollutant* particles in cases where the particles are essentially *passive* and thus do not change their size or properties as they disperse. Examples include the works of Gifford (1982); Gaffen, et al. (1987); Segal (1988); Turfus (1988); Luhar and Britter (1989, 1990, and 1992); Sawford (1991); and

Kaplan and Dinar (1992) in dealing with pollutants dispersion in the atmosphere. However, for the fuel sprays and flames, it appears that the turbulent time scale, τ_t, should be replaced by the droplet response time, τ_p, to account for the time scales associated with the evolution of droplet size.

With this new model, the Langevin equation for droplet movement can be written in terms of the Wiener process as:

$$dv_p = (v_g - v_p)\frac{dt}{\tau} + \sqrt{C_o k/\tau_p}\, dt^{1/2}\xi \qquad (3.5\text{-}18)$$

where ξ is the random variable vector and C_O is an empirical constant whose value has been provisionally arranged to unity.

In cylindrical polar coordinates, the equations for three components of velocity are written as follows:

$$du_p = \frac{1}{\tau_p}(u_g - u_p)dt + \sqrt{\frac{k}{\tau_p}}\, dt^{1/2}\xi_x \qquad (3.5\text{-}20)$$

$$dv_p = \frac{1}{\tau_p}(v_g - v_p)dt + \frac{w_p^2}{r_p}dt + \sqrt{\frac{k}{\tau_p}}\, dt^{1/2}\xi_r \qquad (3.5\text{-}20)$$

$$dw_p = \frac{1}{\tau_p}(w_g - w_p)dt + \frac{v_p w_p}{r_p}dt + \sqrt{\frac{k}{\tau_p}}\, dt^{1/2}\xi_\theta \qquad (3.5\text{-}21)$$

The second terms on the RHS of the equations (3.4-20) and (3.5-21) are the centrifugal and the Coriolis forces, which arise due to the tangential movement of the droplet. The relationships between the three Cartesian and cylindrical polar components of the random number vectors are;

$$\xi_x = \xi'_x \qquad (3.5\text{-}22)$$

$$\xi_r = \xi'_y \cos\theta + \xi'_z \sin\theta \qquad (3.5\text{-}23)$$

$$\xi_\theta = \xi'_z \cos\theta - \xi'_y \sin\theta \qquad (3.5\text{-}24)$$

where ξ_x', ξ_y' and ξ_z' are the three components of the random variable vector ξ in Cartesian coordinates.

3.6 Spray Submodels

A turbulent spray flame is achieved and sustained by many important physical processes such as the atomisation of liquid fuel into individual droplets, heating-up and vaporisation of the droplets, and various modes of inter-phase exchange processes. Droplet events such as collision, coalescence, and breakups of droplets are also important aspects in determining the spray behaviour. However, accounting for all of these processes would require a prohibitively large amount of storage and time even with the todays advanced computers. Therefore, to make the problem of predicting the turbulent spray flames computationally manageable, the following is assumed:

- the spray is already fully developed into individual droplets at the point where the fuel leaves the injection nozzle body.
- the droplet number density is low enough throughout the combustor so that the collision, coalescence, and secondary atomisation of the droplets are all negligible.
- the volume fraction occupied by the droplets is negligible and consequently the void fraction is unity throughout the combustor.
- there is no internal movement of liquid inside the droplets.
- the temperature is uniform inside the droplet.
- the heat exchange due to radiation is negligible.

The tasks then remaining are to determine the evolution of droplet size and temperature along droplet trajectories. The governing equations for the droplet histories can be written as balances of droplet fuel mass and energy together with the momentum balance:

$$m_p \frac{dv_p}{dt} = C_D A_p (v_g - v_p) + \mathbf{X} \qquad (3.5\text{-}1)$$

$$\frac{dm_p}{dt} = -\pi \rho_p D_p^2 \dot{r} \qquad (3.6\text{-}1)$$

$$m_p C_P \frac{dT_p}{dt} = L\frac{dm_p}{dt} + \dot{q} \qquad (3.6\text{-}2)$$

where m_p, ρ_p, C_P, D_p, T_p, L and $\dot{q}$ are the mass, liquid fuel density, specific heat of liquid fuel, droplet diameter, droplet temperature, latent heat of vaporisation and the rate of heat transfer to droplet, respectively. $\dot{r}$ is the evaporation rate, or size reduction rate, of the droplet.

3.6.1 Droplet Trajectories

The trajectories are calculated form the relationship;

$$\mathbf{v}_p = d\mathbf{x}_p / dt \qquad (3.6\text{-}3)$$

where $\mathbf{x}_p$ is the position vector and $\mathbf{v}_p$ is the droplet velocity, the solution of the Equation (3.5-1). In cylindrical coordinates, the three components of this position vector are related to the velocities as follow:

$$dx_p = u_p dt \qquad (3.6\text{-}4)$$

$$dr_p = v_p dt \qquad (3.6\text{-}5)$$

$$d\theta_p = (w_p / r_p)dt \qquad (3.6\text{-}6)$$

The following expression is used for the drag coefficient, C_D, (Clift, et al., 1978) :

$$C_D = \frac{24}{Re_p}(1 + 0.15Re_p) \quad for\ Re_p \le 1000$$
$$C_D = 0.44 \qquad for\ Re_p > 1000 \qquad (3.6\text{-}7)$$

where Re_p is the Reynolds number based on the droplet diameter and the relative velocity of the droplet to gas phase.

3.6.2 Droplet size

To solve Equation (3.6-1) for droplet size evolution, the evaporation rate, $\dot{r}$, should be defined. The equation developed experimentally by Agoston, et al. (1957) has been used by El Banhawy and Whitelaw (1980) and Attya and Whitelaw(1981), and is written as;

$$\dot{r} = \frac{dD_p}{dt} = \frac{4k_g}{\rho C_{P_g} D_p}(1 + 0.24Re_p^{1/2}) \ln[1 + C_P(T_g - T_p)/L] \qquad (3.6\text{-}8)$$

where k_g and C_{P_g} are the thermal conductivity and the specific heat of the surrounding gaseous phase.

It appears to be a common practice to assume either that the evaporation starts only when the droplet temperature reaches the boiling point of the fuel or that the droplet instantly flashes out as soon as the droplet temperature reaches the boiling point, or both. However, these assumptions seem to be unnecessary and are relaxed in the present work, though the droplet temperature is not allowed to increase beyond the boiling point of the fuel.

3.6.3 Droplet Temperatures

In the absence of radiative heat transfer between the droplets and the surroundings, heat transfer is mainly by convection. The rate of heat transfer from the surrounding gas to the droplet by convection, $\dot{q}$, is expressed as;

$$\dot{q} = \pi D_p k_p (T_g - T_p) Nu \qquad (3.6\text{-}9)$$

where Nu is the Nusselt number for convective heat transfer. For forced convection the Nusselt number is expressed in terms of Reynolds and Prandtl numbers as;

$$Nu = 2 + 0.6Re_p^{1/2}Pr^{1/3} \qquad (3.6\text{-}10)$$

which is the well-known Ranz-Marshall expression. Thus, the equation for the evolution of droplet temperature is written as:

$$\frac{dT_p}{dt} = \frac{6k_p}{\rho_p C_{P_p} D_p^2}(2 + 0.6Re_p^{1/2}Pr^{1/3})(T_g - T_p) + \frac{L}{\rho_p C_{P_p}}\frac{dm_p}{dt} \qquad (3.6\text{-}11)$$

where k_p and C_{P_p} are the thermal conductivity and the specific heat of the fuel liquid.

3.7 Combustion Model

To approximate the turbulent flame, the following assumptions are often made:

- adiabatic process,
- the molecular Schmidt numbers are equal for all species,
- Le = 1 (or Pr = Sc),
- the pressure is thermodynamically constant.

The first assumption is based on the reasoning that the rate of heat loss to the surrounding is in general negligible when compared to the rate of heat generation by combustion. The second and third assumptions are based on the fact that in turbulent flames the mixing process is dominated by turbulence, therefore, the effect of the difference in molecular diffusivities between the species is negligible. The last assumption is valid if the Mach number is small compared to unity and the flow is statistically stationary.

Under these assumptions, the instantaneous thermochemical state of the gas (temperature, pressure, species concentrations, and density) can be uniquely determined as a function of a conserved scalar (Bilger, 1977 and Libby and Williams, 1980). When the combustor is fed by two separate streams of fluid, all the conserved scalars are linearly interrelated. Therefore, any one of them may be selected to obtain the other conserved scalars, and a common choice is the mixture fraction f which is defined as;

$$f = \frac{z_\beta - z_{\beta_O}}{z_{\beta_F} - z_{\beta_O}} \quad \text{for } \beta = 1, \text{M and h} \qquad (3.7\text{-}1)$$

where M is the number of chemical elements involved; z_β is the mass fraction of β^{th} element; and the subscripts F and O refer to the values in the fuel and oxidant (commonly the air) streams, respectively. The instantaneous scalar properties as a function of the mixture fraction can be provided by the chemical equilibrium approach. In this approach, the reaction rate is assumed to be fast enough for the mixture of fuel and oxidant to reach chemical equilibrium, hence the precise reaction mechanisms need not to be specified. Although the concentrations of major species (O_2, N_2, and CO_2) and the temperature are predicted realistically with this approach, it has been reported (Jones and Whitelaw, 1982, 1984) that CO concentrations are overpredicted by a factor of up to four in fuel-rich hydrocarbon flames.

The laminar flamelet approach is an alternative to the chemical equilibrium approach. In this approach, the same instantaneous relationships between the instantaneous scalar properties and the mixture fraction, with the strain rate as parameter, are assumed to prevail in a laminar counter-flow diffusion flame and in turbulent non-premixed flames. That is, the turbulent flame properties are determined from the laminar flamelet properties, based on either the measurements or the computed results.

In the present work, the laminar flamelet approach is adopted and the state relationships between temperature,density, and composition and mixture fraction are obtained using the four step mechanism of Jones and Lindstedt(1988):

$$C_nH_{2n+2} + n/2\,O_2 \rightarrow nCO + (n+1)H_2 \qquad (3.7\text{-}2)$$

$$C_nH_{2n+2} + nH_2O \rightarrow nCO + (2n+1)H_2 \qquad (3.7\text{-}3)$$

$$H_2 + 1/2\,O_2 \Leftrightarrow H_2O \qquad (3.7\text{-}4)$$

$$CO + H_2O \Leftrightarrow CO_2 + H_2 \qquad (3.7\text{-}5)$$

The results of computations of a laminar propane-air counter-flow diffusion flame at a negligible strain rate were expressed as polynomial functions of mixture fraction and are shown in Figure 3.1. The laminar flame results were provided by Lindstedt (1992). Propane was used in place of the kerosene burnt in the present study as a suitable kinetic mechanismwas not available at the time the computations were completed.

As is apparent from these figures, the relationship between the scalars and the mixture fraction is highly non-linear, hence the mean mixture fraction is not

sufficient to determine the mean scalar properties, and fluctuations in the mixture fraction must be taken into account. This problem is conveniently overcome by making use of the probability density function (pdf) for mixture fraction, p(f,**x**,t). The common approach is to presume the shape of the pdf in terms of the mean and variance of the mixture fraction. It is known (Jones and Whitelaw, 1982, 1984) that results are relatively insensitive to the choice of the particular shape of pdf, provided that it is a continuous function with possibly Dirac delta functions at the bounds of the mixture fraction. In the present work, a β-pdf is presumed;

$$p(f,\mathbf{x},t) = \frac{f^{\alpha-1}(1-f)^{\beta-1}}{\int_0^1 f^{\alpha-1}(1-f)^{\beta-1}df} \qquad 0 \le f \le 1 \tag{3.7-6}$$

and where the exponents α and β are given by;

$$\begin{aligned} \alpha &= \tilde{f}\left[\frac{\tilde{f}(1-\tilde{f})}{\widetilde{f''^2}} - 1\right] \\ \beta &= (1-\tilde{f})\left[\frac{\tilde{f}(1-\tilde{f})}{\widetilde{f''^2}} - 1\right] \end{aligned} \tag{3.7-7}$$

where the mean and the variance of the mixture fraction are determined from the solution of their respective transport equations which can be written in the Favre-averaged form;

$$\bar{\rho}\tilde{u}_j \frac{\partial \tilde{f}}{\partial x_j} = \frac{\partial}{\partial x_j}\left(\frac{\mu_t}{\sigma_t}\frac{\partial \tilde{f}}{\partial x_j}\right) + \tilde{S}_f \tag{3.7-8}$$

$$\bar{\rho}\tilde{u}_j \frac{\partial \widetilde{f''^2}}{\partial x_j} = \frac{\partial}{\partial x_j}\left(\frac{\mu_t}{\sigma_t}\frac{\partial \widetilde{f''^2}}{\partial x_j}\right) + 2\frac{\mu_t}{\sigma_t}\left(\frac{\partial \tilde{f}}{\partial x_j}\right)^2 - C_D\bar{\rho}\frac{\varepsilon}{k}\widetilde{f''^2} \tag{3.7-9}$$

where C_D is a constant equal to 2.0 and μ_t, σ_t, ε are the turbulent viscosity, turbulent Prandtl number, and dissipation rate of turbulence kinetic energy k, respectively. The last term, $\tilde{S}_f$, on the RHS of quation (3.7-8) is the mean source term for the mean mixture fraction equation.

With the pdf determined by the above procedure, the mean scalar properties are calculated from:

$$\tilde{\phi} = \int_0^1 \phi(f)\, p(f,\mathbf{x},t)\, df \tag{3.7-10}$$

$$\overline{\phi} = \overline{\rho} \int_0^1 \frac{\phi(f)}{\rho(f)}\, p(f,\mathbf{x},t)\, df \tag{3.7-11}$$

where the mean density $\overline{\rho}$ is given by:

$$\overline{\rho} = \left[\int_0^1 \frac{p(f,\mathbf{x},t)}{\rho(f)} df \right]^{-1} \tag{3.7-12}$$

3.8 Numerical Schemes

3.8.1 Initial Conditions for Droplet Injection

One of the major uncertainties in predicting spray flames is the specification of the initial spray characteristics. The difficulty comes from the assumption that the fuel is already fully atomised into a stable spray at the tip of the injection nozzle. In reality this cannot happen and instead the fuel goes through a series of deformation, collision, breakup, and coalescence processes as it leaves the injection nozzle until it is fully atomised into a stable spray. As this atomisation process is not simulated in the present work assumptions must be made concerning the initial spray characteristics, namely the size and velocity distributions of the spray droplets at the point of injection.

A convenient way to represent the spray characteristics is to express it by a model equation describing the size distribution in terms of a few parameters that can be readily determined from the experiments; the Nukiyana-Tanasawa Equation (Lefebvre, 1989; Williams, 1990) is one example;

$$\frac{dN}{dD_p} = a D_p^{\alpha} \exp(-b D_p^{\beta}) \tag{3.8-1}$$

where α, β, a, and b are all empirical constants and dN is the number of droplets in the size range from D_p to $D_p + d\,D_p$.

The coefficients a and b can be expressed in terms of V_{SMD} and ΔV_{inj}, the volume of the droplet with the Sauter mean diameter and the volume of total liquid injected over a time step selected, respectively, as;

$$a = \beta \frac{\Delta V_{inj}}{V_{SMD}} \frac{\Gamma_4^{\alpha+3}}{\Gamma_3^{\alpha+4}} \tag{3.8-2}$$

$$b = (\Gamma_4 / \Gamma_3)^{\beta} \tag{3.8-3}$$

where Γ_4 and Γ_3 are defined, in terms of gamma function, Γ, as:

$$\Gamma_3 = \Gamma(\frac{\alpha+3}{\beta}) \tag{3.8-4}$$

$$\Gamma_4 = \Gamma(\frac{\alpha+4}{\beta}) \tag{3.8-5}$$

More details are included in Appendix C.

In the present work, it is assumed that all the droplets are injected with the same injection velocity, irrespective of their sizes. While this may be a rather too bold assumption there is no direct measurement of velocity distribution available at the very tip of the nozzle on which to base alternative specifications. Furthermore, a slight variation in the injection velocities either with different droplet sizes or at different times will probably be overshadowed very quickly by the effect of turbulent dispersion.

The size distribution function is discretized into a specified number of droplet size classes and for each class, the droplet number density, N_k, is calculated according to the distribution function. This number density is assumed to remain unchanged throughout the life of the stochastic droplet in question, i.e., there is no droplet breakup or coallescence. The size and the number density of the droplets selected from K representative droplets, called the computational droplet, or the stochastic parcel, satisfy the following relationship;

$$\sum_{k=1}^{K} \frac{\pi}{6} D_k^3 \rho_p N_k = \dot{m}_f \Delta t \tag{3.8-6}$$

where K is the class number of droplet sizes, $\dot{m}_f$ is the mass rate of fuel injection and Δt is the time interval between the injection of new set of droplets (stochastic parcels).

The droplet velocities are assumed to be independent of the size distribution as in the present work no reliable method was available to measure directly the droplet injection velocities. Thus the ordinary LDV measurements made the closest to the front wall of combustor have been used to estimate the spray injection velocities as:

$$\mathbf{v}_{p,inj} = (u_{p,inj}, v_{p,inj}, w_{p,inj}) = (30, 30, 0) \text{ m/sec} \tag{3.8-7}$$

3.8.2 Calculation of Source Terms

The mass source for the gas phase arising from the evaporating spray is calculated for each control volume. It is expressed as the rate of fuel mass addition to the control volume per unit volume, and is determined from the increment of the mass of fuel vapour contributed by all the droplets that traverse the control volume in question over the time step, viz:

$$\dot{f}_C = \frac{\sum_{i=1}^{N_C} \Delta V_{p,i}}{V_C \Delta t} \tag{3.8-8}$$

where $\Delta V_{p,i}$ is the volume change (decrease) of the i^{-th} droplet among N_C droplets that visited the control volume , the volume of which is V_C. Δt is the time interval between the injection of each new set of droplets.

Because of the turbulent dispersion and the finite number of stochastic particles, the rate of mass addition, $\dot{f}_C$, will fluctuate with time, whereas the average rate of mass source is required to calculate the gas phase properties, for example the mixture fraction. Therefore, the mass rate per unit volume calculated by the above equation is transformed into an averaged one. In the present work, the following expression is used for the average of $\dot{f}_C$;

$$\langle \dot{f}_C \rangle^{n+1} = \frac{t_n}{t_{n+1}} \langle \dot{f}_C \rangle^n + \frac{\Delta t}{t_{n+1}} \dot{f}_C \tag{3.8-9}$$

where $\langle \dot{f}_C \rangle^n$ is the time average of $\dot{f}_C$ up to the time t_n and $t_{n+1} = t_n + \Delta t$. This gives the average of source term converged within a short time range.

In any time step δt an individual droplet travels at most to one of the eight control volumes bordering the current one, as show in the Figure 3.2. Illustrated are the five cases of droplet translation into a new control volume for the positive axial and radial velocities of the droplet in question. The new position of the droplet is collectively denoted by, $\mathbf{x}(x,y)$ while the original position is by $\mathbf{x}_o(x_o,y_o)$, for all of the five cases. The total mass of the fuel vaporised over the time step between the positions $\mathbf{x}_o$ and $\mathbf{x}$ is calculated, for the j-th droplet, as;

$$\Delta m_j = \frac{\pi}{6}(D^o_{p,j}{}^3 \rho^o_{p,j} - D_{p,j}{}^3 \rho_{p,j}) N_j \qquad (3.8\text{-}10)$$

where D^o_p and D_p are the old and new droplet diameters and ρ^o_p and ρ_p are the old and new fuel liquid densities, respectively. The density of fuel droplets ρ_p is determined as a function of droplet temperature, taken from a reference (API, 1981):

$$\rho_p = 0.9443 - 0.2782 \times 10^{-4} T^{1.5}, \quad g / ml$$

The amount of fuel vaporised over the time period is divided between each of the cells which the droplet visited in travelling along one of the five trajectories shown in Figure 3.2, as follow:

$$\Delta V_{old} = \sum_{j=1}^{N_{old}} f_{old,j} \Delta m_j \qquad (3.8\text{-}11)$$

$$\Delta V_{int} = \sum_{j=1}^{N_{int}} f_{int,j} \Delta m_j \qquad (3.8\text{-}12)$$

$$\Delta V_{new} = \sum_{j=1}^{N_{new}} f_{new,j} \Delta m_j \qquad (3.8\text{-}13)$$

N_{old}, N_{int}, and N_{new} are the numbers of droplets that visited the old, the intermediate, and the new control cells, respectively. The three factors, f_{old}, f_{int},

and f_{new} are the fractions of the time, δt, spent by the droplet in the old, the intermediate, and the new control cells, respectively. They are determined from the old and the new positions, $\mathbf{x}_o$ and $\mathbf{x}$, of the droplet relative to the position of the north east corner, $\mathbf{x}^*$, of the old control cell, assuming the vaporisation and the trajectory of the droplet are linear to the time over the time step in question. The following relationship is satisfied:

$$f_{old,j} + f_{int,j} + f_{new,j} = 1 \tag{3.8-14}$$

This complete procedure applies equally to the other possible combinations of the axial and radial velocities of the droplet. Of course, if the droplet does not translate out of the current control cell, then the total amount of fuel mass vaporised from it is wholly assigned to the old control cell, with $f_{old,j} = 1$.

3.8.3 Numerical Integration of the Langevin Equations

The set of stochastic differential equations for the droplet velocities are integrated numerically with the implicit, or forward-time, first-order Euler method:

$$\mathbf{v}_p^{n+1} - \mathbf{v}_p^n = (\mathbf{v}_g - \mathbf{v}_p^{n+1}) + b\xi \tag{3.8-15}$$

Upon the rearrangements, this can be written:

$$\mathbf{v}_p^{n+1} = (\mathbf{v}_p^n + \frac{\delta t}{\tau_p}\mathbf{v}_g + b\xi) / (1 + \frac{\delta t}{\tau_p}) \tag{3.8-16}$$

With this method, the particle velocity $\mathbf{v}_p^{n+1}$ correctly approaches the gas phase velocity $\mathbf{v}_g$ as τ_p tends to zero due to the evaporation. This is to be compared with the explicit method as:

$$\mathbf{v}_p^{n+1} = \mathbf{v}_p^n + \frac{\delta t}{\tau_p}(\mathbf{v}_g - \mathbf{v}_p^n) + b\xi \tag{3.8-17}$$

where the particle velocity becomes infinite as $\tau_p \rightarrow 0$, which is clearly unrealistic.

The time step, δt, for integrating the droplet equation is determined from;

$$\delta t = \min(\delta t_x, \delta t_y) \tag{3.8-18}$$

where δt_x and δt_y are the time steps chosen so that the following Courant number criteria are satisfied;

$$u_p^* \delta t_x / \Delta x_{max} < 1 \tag{3.8-19}$$

$$v_p^* \delta t_y / \Delta y_{max} < 1 \tag{3.8-20}$$

where u_p^* and v_p^* are the estimated droplet velocities;

$$u_p^* = u_p + \sqrt{k}\xi_x \tag{3.8-21}$$

$$v_p^* = v_p + \sqrt{k}\xi_y \tag{3.8-22}$$

and Δx_{max} and Δy_{max} are the local grid spacings which are the maximum distances the droplet is allowed to travel.

This method is compared with the approach taken by Gosman and Ioannides (1981) and subsequently by others (Beshay, et al., 1986; Reitz and Diwakar, 1986; Watkins, et al., 1985; and Wild, et al., 1988), Equation (3.4-12). In their approach, the time step could be selected unnecessarily too small if either the eddy length scale or the turbulence time scale is very small, which is not beneficial for the droplets to march forward in time. Whereas, in the present work, the time step can be as large as possible in so far as the droplet velocity and the grid spacing satisfy the Courant number criteria, equations (3.8-20) and (3.8-21). Obviously, this is possible because the turbulent dispersion in the present work is modelled by the Wiener process, according to which the dispersion, or the variance of the process, does not depend upon the particular time step selected, Equation (3,5-11).

The use of low order integration method is justified providing the grid spacing is small enough. In the present work droplets are not permitted to travel more than one cell spacing in one time step. Thus the time step for the integration of the Langevin equation is kept small enough throughout.

Chapter 4.

Results and Discussions

The computational results of spray flame predictions are presented in this chapter and analysed by comparison with the relevant sets of experimental data discussed in Chapter 2.

A second moment closure has been used for modelling the gas phase turbulence and it's superiority in predicting the turbulence mixing processes is demonstrated by comparison with the results obtained by the k - ε model. The two-phase flow feature of the spray has been dealt with the discrete Lagrangian stochastic particles with the turbulent dispersion of which being modelled by the Wiener process. The combustion reaction has been modelled by the laminar flamelet approach.

The spray behaviour, such as the droplet trajectories and size, temperature, and velocity histories, are tested, first in nonreacting flows then in the reacting flows with swirl. The side and front views of the spray are also presented in the first section. Gas phase properties of velocity, temperature, and species concentrations are presented and discussed in the section 4.2, followed by the summary of the major findings from the computational predictions of turbulent spray flames, in the section 4.3.

4.1 Spray Behaviour

The trajectories of droplets with different sizes are shown in Figure 4.1(a). The air temperature is maintained artificially at 1000 K throughout the domain to see the changes of droplets size and temperature. The slight bend of the trajectories off the 45° line is due to the air flow through the inlet annulus located at a radial position between 10.5 and 21.5 mm. The slightly "*wiggly*" trajectories reflect the influence of the gas flow turbulence on the movement of droplets. The largest droplet of 95 μ m diameter shown in the figure, vanishes before it impinges on the combustor wall

and it takes about 10 milli seconds to evaporate, as can be seen from the accompanying Figure 4.1(b).

The temperature change plotted in Figure 4.1(c) shows the way the heat transfer from the hot environment to the droplet is modelled. In the present work the droplet temperature is allowed to increase only up to the boiling point of the fuel, which is estimated 475 K. Although it was not specified as such, the droplet size changes resembles the conventional d^2-law, as shown in Figure 4.1(d).

The side and front cut views are shown in Figure 4.2 and 4.3, respectively. Although the present problem is axisymmetric, all three components of the velocities for both phases are calculated. The effect of the swirling air is clearly shown in the front cut view of the spray, Figure 4.3.

The size-velocity correlations at X = 50 mm are shown in Figure 4.4. At this particular position, some positive correlations are observed between the size and velocity of droplets, which is in conformity with the PDA measurements in cold sprays (Bachalo and Houser, 1984; Presser, et al., 1990).

4.2 Gas Phase Properties

4.2.1 Preliminary Tests

One of the major uncertainties of predicting the cold or reacting turbulent flows is in the specification of the inlet boundary conditions. This has been in most cases due to the lack of relevant directly measured data at the inlet to the combustor. In many previously published works, be it for gaseous flames (Jones and McGuirk, 1979 and Soong, et al., 1992) or the spray flames (El Banhawy and Whitelaw, 1980; Boysan, et al., 1981; Gosman and Ioannides, 1981; Attya and Whitelaw, 1984; and Wild, et al., 1988), it appears that uniform profiles of mean and fluctuating velocities have been assumed. In the present work, the velocity profiles were measured very close to the inlet to the combustor and were found to be slightly different in the cold and burning flows, as was discussed in Chapter 2. These measured velocity profiles are used as inlet boundary conditions for the present computational works.

It was initially reasoned that there would be zero mean radial velocity at the inlet of the combustor, since the air flows through a straight annulus before reaching the inlet plane. The measured inlet profiles of radial velocities indeed seemed to support this point. Thus, the mean radial velocities were rather set to zero at the inlet to the combustor. However, this was found to be not favourable for computation, as the residuals oscillated with a large amplitude and the speed of convergence was slow. However, this behaviour did not arise when the measured (and non-zero) radial velocities were used to provide boundary conditions at the inlet plane.

As has been discussed in Section 2.5.1.2, two major differences have been observed in the inlet profiles of cold and burning flows. One is that the mean radial velocity increases in the reacting flow with the maximum positioned in the middle of the annulus, while there is virtually no difference in the other velocity components. In addition the turbulence is significantly reduced in it's intensity and becomes far more homogeneous and isotropic in burning flows. In cold flow, the rms velocities are higher at both the inner and outer edges of the annulus.

To see the effect of inlet conditions on flame calculations, two sets of inlet boundary conditions were tested, one taken from the cold the other from the burning flow measurements. The results are shown for the mean axial velocities in Figure 4.5. Some slight differences are observed between the two different specifications of inlet boundary conditions.

First, the recirculation velocity at the axis of the combustor is predicted to be lower with the hot inlet profiles - close to the inlet plane at X = 10 mm, for example.

Secondly, the change in the direction of recirculating flow across the boundary of the central recirculation zone is much more abrupt with the hot inlet profiles, and this is more realistic when compared with the measured profiles at the axial stations up to X = 80 mm. Thirdly, the position of the maximum velocities is better predicted with the cold inlet profiles. The positions of the velocity maxima are predicted radially slightly outward with the hot inlet profiles when compared with the measurements. This is possibly due to the higher mean radial velocities (with the maximum of about 7 m/sec) with the hot inlet profiles compared with the much lower values of around 1 m/sec with the cold inlet profiles. The latter two effects are also evident in the other velocity components as well, Figures 4.6 and 4.7.

A similar effect of the inlet boundary conditions was also observed with the k - ε model. Thus, it appears that care should be exercised in selecting the proper inlet boundary conditions. In the present work, the cold inlet profiles are taken for the boundary condtions at the inlet, as these were felt to be the most realistic.

The other major uncertainty in predicting spray flames is the specification of the initial spray characteristics, as has been discussed in Section 3.8.1. Since the fuel is assumed to have been fully atomised into spray droplets at the very tip of the fuel injection nozzle, the initial spray characteristics have to be assumed at the point of injection. Thus, to see the effect of the specifications of the spray characteristics on the calculations, several sprays with different characteristics have been tested. The results are shown in Figures 4.8 and 4.9, expressed in terms of mean temperature and mixture fraction, respectively.

For the purpose of the test, monodisperse sprays with different sizes are tested and the results are compared with the measurements, Figure 2.52 for mean temperature contours and Figures 2.56 and 2.57 for species concentration contours. From this test, the estimated SMD of 60 μm, according to the equation by Hiroyasu and Katoda (1974), appears to be representative of the actual value reasonably well.

The effect of the spread of the size distribution assumed was also tested, as shown in Figures 4.10 and 4.11. From these tests, SMD of 60 μm was selected and the coefficients of $\alpha = 20$ and $\beta = 3$ of the Nukiyama-Tanasawa representation have been taken in the present work as they appeared to represent a reasonable fit to the measurements.

4.2.2 Velocity Fields

The radial profiles of the predicted mean velocities are shown in Figures 4.12, 4.13, and 4.14 for the axial, radial and tangential components, respectively. Measurements are also shown for comparison. As shown in these graphs, the position of the maxima in the axial and radial velocities are well predicted, and the general shapes of the curves are reasonably well represented by the prediction.

However, the maximum velocities are significantly underestimated and are less than 50% of the measured values at X = 80 mm, for example. This appears to be related to the fact that the stream wise expansion of the flow is overpredicted. The

extent of the recirculation velocities are also underestimated for both the central and the corner recirculation zones.

The discrepancies in the predictions persist throughout the combustor upto the axial station where the recirculation disappears, at about X = 300 mm. It is noted here, as has been mentioned in Chapter 2, that the presence of two maxima in the measurements of velocities at X = 10 mm is clearly due to the spray droplet influence on the LDV. Thus, the maximum at about r = 10 mm is associated with the liquid fuel spray and the second maximum at about r = 20 mm is a result of the gas phase velocity. The effect of the presence of spray droplets on the profile, though of much reduced extent, is still slightly evident at X = 20 mm.

The overprediction of the stream wise expansion is also evident in the radial profiles, as early as from X = 10 mm. The peak radial velocities are again underpredicted by about 30 % when compared with the measurements. At the first axial station, X = 3 mm, an extra small maximum in the profile is predicted at about r = 5 mm. An explanation for this is not found easily, particularly because no gas phase velocity measurement was possible at this location because of the presence of spray droplets.

As has been discussed in Sections 2.5.1.4 and 2.5.1.5, some complications in the measured profiles at the axial stations close to the fuel injection nozzle, say up to X = 20 mm, are obviously due to the presence of spray droplets. The area and the extent of converging flow (i.e. negative radial velocities) towards the combustor wall are underpredicted at all the axial positions.

In contrast to both the axial and radial velocities predictions, the maximum mean tangential velocities are overpredicted at X = 20, 30, and 40 mm. The positions of the maxima are also not well predicted and they are calculated to occur to close to the centreline at most stations along the combustor. Solid-body rotation is predicted to start at around X = 10 mm, whereas the measurements show it starts to develop from about X = 30 mm, before which the tangential velocities in the region close to the combustor axis are nearly uniform and zero.

The computational method seems not able to represent the two peaks of mean tangential velocity profiles, as observed in the measurements at X = 30 ~ 60 mm.

Although, it is obviously desirable to be able to predict such a detail, it is not clear what the influence of the failiure to do so will be on the overall predictions.

The rms velocities predicted are compared with the measurement in Figures 4.15, 4.16, and 4.17 for axial, radial and tangential components, respectively. Overall, the rms levels predicted are in good agreements with the measured values and the general features of the profiles measured are reasonably well represented by the predictions.

One of the major discrepancies in the predictions, however, appears to be that the maximum rms values at the outer edge of the main air stream is underpredicted. This appears to be coincident with the less steep profiles of the predicted mean axial velocity at the outer edge of the main air stream. The discrepancies between predicted and measured rms velocities are greatest in the axial component, where predicted values are around half of those measured at X = 30, 40, and 50 mm.

4.2.3 Temperature Fields

In general, the temperature field is reasonably well predicted, at least qualitatively, throughout the combustor, Figure 4.18 The one outstanding discrepancy between the measurement and the prediction is that the temperature levels predicted are systematically significantly higher than the measurements throughout the combustor by up to about 450 K.

This can, in part, be ascribed to the fact that the laminar flamelet adopted in the present work is based on propane as a fuel and no laminar flamelet data was available with kerosene fuel. For example, the calorific value of kerosene is typically 10,286 kcal/kg, whereas that of propane is 11,079 kcal/kg, i.e., about 8 % higher. Furthermore, in the present work adiabatic flow and consequently no radiative heat transfer to the surroundings was assumed and this may also contribute to the discrepancy between measured and predicted temperatures. For example, if the combustor wall temperature is assumed to be uniform, then the rate of heat loss due to radiation can be roughly estimated as;

$$q = -\sigma \varepsilon A_{wall} (T_{wall}^4 - T_{air}^4) \qquad (4.2\text{-}1)$$

where σ is the Stefan-Boltzmann constant, 5.6697×10^{-8} W/m^2 K^4 and ε is the emissivity of the quartz with a value of 0.9, taken from Eckert and Drake (1972). For a wall temperature of 900 K, the estimated radiation loss is about 2500 cal/sec, which amounts to about 24 % of the oveall heat release rate of 10286 cal/sec. This together with convective heat loss, which is also ignored in the calculations, is sufficient to account for the differences between the measured and the predicted temperatures.

The *dimple* at about r = 10 mm in the profile predicted at the axial stage of X = 10 mm indicates the presence of large amount of liquid fuel, which is manifested by a small shoulder in the measured profile at around the same point. The mean temperature rises, as the radial distance increases, sharply from the value of about 1400 K at the combustor axis, and falls rapidly due to the presence of cold incoming air, which contributes to a small isolated high temperature region in the contours of both measured (Figure 2.51) and predicted (Figure 4.19) mean temperatures. The height of this peak is reduced and it moves radially outward as the axial distance increases and contributes to the second high temperature region, which is observed in the measurements and predictions.

The temperature profiles are virtually flat at axial positions greater than 100 mm, indicating that most of the spray droplet evaporation and subsequent combustion has been completed. Contrary to the measurements, which show the temperature along the axis of the combustor to be almost constant with a value around 1300 K, the predicted centreline temperature initially falls slightly as the axial distance increases and then starts to rise from around 1550 K at X = 30 mm to about 1700 K at X = 70 mm after which it remains constant.

The two localised high temperature regimes measured and predicted by the second order moment closure are not reproduced by the $k-\varepsilon$ model calculations, Figure 4.20, suggesting that this model does not give an accurate representation of the mixing process.

4.2.4 Species Concentration Fields

The mixture fraction contours predicted are presented in Figure 4.21. The *ridge* of the contour is initially oriented at 45° to the centreline, consistent with a 45° hollow cone spray. It is subsequently deflected by the strong inlet air stream.

Further downstream, the original hollow cone shape is recovered with the divergence angle of about 45° but displaced a little away from the injection plane. Finally, due to the effect of the presence of the wall, at further down stream of about X = 75 mm, the *ridge* of mixture fraction contour is bent parallel to the wall. The region of high mixture fraction area close to the combustor wall between X = 130 and 200 mm is due to the larger droplets impinging on the hot combustor wall then evaporating to produce fuel vapour. Some of the fuel vapour is transported back towards the inlet plane by the reverse flow of the corner recirculation zone. At axial stations larger than 150 mm, the mixture fraction field is more or less homogeneous, indicating that most of the mixing process is complete by at about 3/4 diameter downstream and this is consistent with the nearly uniform temperature profiles for X > 100 mm.

The superiority of the second moment closure to the k - ε model in predicting the present turbulent non-premixed flame appears to be associated with it's capability to predict the scalar field mixing process far more accurately. The mixture fraction contours predicted by the k - ε model are shown in Figure 4.22. The mixture fraction contours predicted by the second moment closure are much more localised than those of the k - ε model and compares far more favourably with the measurements. This is perhaps not surprising since in the second moment closure method the Reynolds stresses and the scalar fluxes and hence the turbulent mixing processes are described in a much more detailed fashion than is the case with the k - ε model.

The contours of predicted concentrations of the 5 species measured are shown in Figure 4.23. They compare quite favourably with the contours of measured concentrations, Figure 2.56, for example. However, closer examinations reveal some of the shortfalls of the predictions, which can be anaysed by comparing the profiles of predicted and measured concentrations.

O_2 concentration profiles predicted are compared with the measurements in Figure 4.24. General feature of the profiles measured are reasonably well represented. The minima in the profiles of both measurement and prediction just inside the peaks, at about r = 10 mm and r = 15 mm in Figures 4.24 (a) and (b), respectively, are due to the presence of high concentration of liquid fuels. As the axial distance increases, the peak values are underpredicted, which appears to be related with the streamwise expansion of the main air stream being overpredicted. In general, the concentrations are underpredicted by about 2 %.

CO_2 concentration profiles predicted tend to have peak just inside the main stream of incoming fresh air, while the measurements indicate only a small or no peak being observed, Figure 4.25. The *dimple* in the predicted profile at abou r = 10 mm in Figure 4.25 (a) is due to presence of thick fuel spray. The minimum values are always overpredicted at every stages, indicating that the mixing is slightly overprdicted in general. CO_2 concentration predicted on the axis falls slightly, as the axial stage increases, then rises back and remains nearly constant at X > 70 mm. Whereas the measured concentrations are almost the same along the combustor axis. Final overall CO_2 concentration is reasonably predicted, for example at X = 100 mm.

Mean CO concentration profiles are presented in Figure 4.26. The maximum CO concentration is overpredicted by upto 100 %, e.g. about 3.8 % compared with 1.5 %, at X = 10 mm. As the axial distance increases, this discrepancy decreases and from X = 50 mm the maximum concentration is underpredicted. Farther down stream at X = 100 mm and beyond no CO at all is predicted whilst the measurements show some low concentrations of CO. The CO concentration on the combustor axis is extremely overpredicted by a factor of about 2 close to the inlet plane, say up to X = 30 mm. This appears to be due to the underpredicted recirculation velocity along the combustor axis which allows too much of the fuel to be transported towards the exit plane of the combustor in the prediction.

The behaviour of the H_2 and UHC predictions is almost the same as that of the predicted CO concentration and they are compared with the measurements in Figures 4.27 and 4.28. The maximum concentrations are initially overpredicted by a factor of about two but from X = 30 mm, they are underpredicted. As has been observed with the CO concentration profiles, this is perhaps due to an underestimation of the recirculation velocity along the combustor axis. At far down stream, the concentrations of both H_2 and UHC are significantly underpredicted. For example, while the measurements shows about 0.1 and 0.07 % of H_2 and UHC concentrations at the axial stage of X = 70 mm, virtually none of these components are predicted existent at the same axial stage.

4.3 Summary

The swirl-stabilised turbulent spray flames have been reasonably well predicted through three main areas of modelling works; namely, turbulence, combustion, and spray modelling. For each of these modellings, a second moment closure, the laminar flamelet, and stochastic Lagrangian particle approaches have been adopted.

With regard to turbulence modelling, the second moment approach's superiority to the $k-\varepsilon$ model is typically in it's ability to predict the turbulent mixing processes more accurately and is apparent in the scalar fields predictions, such as the mixture fraction. In contrast there is very little qualitative difference in the mean velocity fields predicted by the $k-\varepsilon$ model and the second moment closure . Both methods have the same failings and incorrectly reproduce the magnitude of the recirculation velocity along the combustor axis. In general, the stream wise expansion is overpredicted, leading to the underprediction of maximum velocities for both axial and radial components.

The velocity fluctuations were reasonably represented by the second moment closure, though the method does not reproduce the double maxima that have been measured around the mean velocity maxima.

The temperature field is systematically overpredicted but this appears to be mainly due to the assumption of the adiabatic flow process combined with the fact that propane with slightly higher calorific value than kerosene was used for the laminar flamelet prescription. However, the general features of temperature field have been reasonably well predicted. In particular, the prediction was accurate enough to represent the two separate high temperature regimes at the same positions as have been measured. This could not be predicted with the $k-\varepsilon$ model presumably due to its limited representation of mixing processes.

The species concentration fields have also been reasonably predicted and this is mainly due to again the turbulent mixing process being properly predicted with the second moment closure. However, closer examination shows two major shortfalls in the prediction of the intermediate species, CO and H_2.

First, the maximum values are overpredicted near the fuel injection nozzle by a factor of about two, whereas they are underpredicted in the down stream region.

Secondly, the concentrations inside the cone of spray (or flame) are also overpredicted close to the nozzle; the measurements show that the concentrations of these species fall quickly to zero away from the flame towards the axis of the combustor. This appears to be due to the underprediction of the magnitude of the velocity within the recirculation region particularly close to the nozzle.

Chapter 5.

Closure

An experimental investigation and computational study have been carried out on a swirl-stabilised turbulent spray flame in an axisymmetric model combustor.

In the experimental works, particular care has been exercised to keep the flame structure axisymmetric, by both careful selection of the spray nozzle and by setting back the swirler from the combustor inlet plane. A comprehensive set of measurements have been made of the gas phase velocity, temperature and concentrations of the major species (CO, CO_2, O_2, UHC and H_2). In the computational study the spray droplets were represented by a discrete set of Lagrangian stochastic particles undergoing turbulent dispersion due to the turbulence in the gas phase. A new and novel approach, based on a Wiener process, has been adopted to model the turbulent dispersion of the spray droplets, and incorporated in an existing computer code developed as a result of earlier research.

The major findings of the present work are summarised in the following section and are followed by some recommendations for future works in the area.

5.1 Conclusions

5.1.1 Experimental

The overall flame structure, particularly the axisymmetry, is very sensitive to both the initial conditions of the inlet air flow and the fuel spray structure. Whilst the spray structure depends mainly on the selection of the spray nozzle, an excellent circumferential uniformity in the inlet air flow has been achieved by recessing the swirler upstream of the combustor inlet plane by 50 mm. This measure can be easily adopted in other future experimental programs where swirl is generated by swirl vanes.

The effect of the combustion on the flow field is observed mainly in the radial velocity. While the maxima in the other components decrease as the axial distance increases, the maximum radial velocity rises to a aximum of about 17 m/sec at around the flow reattachment point after which it falls rapdly. The central recirculation zone extends up to about 1.5 diameter downstream, i.e. up to X = 300 mm beyond which the flow becomes essentially unidirectional.

Two separate high temperature regions, of similar maximum temperature but with different sizes, have been observed. The smaller one occurs very close to the nozzle, at about X = 25 mm and appears to play a role in stabilising the flame. The position of the other high temperature region corresponds to the main flame and is at about X = 60 mm.

The O_2 and CO_2 concentrations along the combustor axis are almost constant and are excellent indicators of the overall AFR's. The maximum concentrations of CO and H_2 (about 2 % and 1 % respectively) have been observed around the point of maximum temperature.

5.1.2 Computational

The velocity, temperature and species concentration fields have been reasonably well predicted. In particular, the predictions have been accurate enough to capture the two separate high temperature regions at the same positions as have been measured. The turbulent mixing of scalar properties is reasonably represented by the second moment method whereas in the $k-\varepsilon$ model calculations they were grossly overpredicted.

However, in spite of the generally reasonable performances, there have been some shortcomings observed in the predictions. First, the streamwise expansion of the axial and radial velocities have been overpredicted significantly, leading to underprediction of maximum velocities. The extent of recirculating flow along the combustor axis was also underpredicted. Secondly, the temperatures have been systematically overpredicted by up to 450 K. This appears to be related to the neglect of radiative heat loss in the flame calculations. Thirdly, the peak concentrations of the intermediate species, CO and H_2, have been overpredicted by a factor of about two, close to the nozzle. The concentrations of these species on the combustor axis are also overpredicted. These discrepancies between measured and

predicted values appear to be related to the underprediction of the extent of recirculating flow along the combustor axis, particularly close to the nozzle.

5.2 Recommendations for Future Work

The axisymmetry of the flame structure is very much dependent upon the conditions of the inlet air flow and the fuel injector. As has been demonstrated in the present work the flow field could be made axisymmetric relatively easily, by recessing the swirler appropriately from the combustor inlet plane. However, the spray structure was almost totally dependent upon the selection of the spray nozzle. Thus, a significant a amount of effort and care should be made in selecting the spray nozzle in order to obtain good axisymmetry in spray field. Flow visualisation of the cold spray could be an efficient and effective method in many cases for this purpose.

In the present work, no direct measurement of the spray could be made with conventional LDV and only indirect and limited information on the spray could be deduced from the LDV measurements. For the direct information on the spray, phase Doppler anemometry could be best employed for both cold and burning sprays. Such information could very much reduce the uncertainty in specifying the initial spray characteristics as is required in the present type of spray modelling work.

The swirl-stabilised spray flame can be predicted reasonably realistically with the present method. The agreement with the measurements is very good, qualitatively in general and quantitatively in many cases. Nevertheless, two major areas were identified which need further improvements.

First, the temperature has been systematically overpredicted. This could be improved by accounting for radiative heat loss in the gas phase energy equation possibly accompanied by combustor wall temperature measurements.

Secondly, the combustion modelling might be improved by replacing the propane fuel with kerosene in the laminar flamelet prescription. However this would require a reaction mechanism for kerosene combustion to be available and its subsequent application to laminar counerflow diffusion flames in order to construct suitable

flamelet. It is likely that both may contribute to reducing the extent of overprediction of temperature and it might also improve the prediction of the concentrations of the intermediate species.

REFERENCES

G.A.Agoston, H.Wise, and W.Rosser, Dynamic Forces Affecting the Combustion of Liquid Spheres, 6th Symp. (Int'l.) on Comb., 708-717 (1957).

H.Altgeld, W.P.Jones, and J.Wilhelmi, Velocity Measurements in a Confined Swirl Driven Recirculating Flow, Exp. in Fluids, **1**, 73-78 (1983).

API, *Technical Data Book-Petroleum Refining*, American Petroleum Institute, New York, 1981.

A.E.M.A.Attya, Kerosene Spray Flames, PhD Thesis, Univ. London (1983).

A.M.Attya and J.H.Whitelaw, Velocity, Temperature, and Species Concentrations in Unconfined Kerosene Spray Flames, ASME Paper No. 81-WA/HT-47 (1981).

A.M.Attya and J.H.Whitelaw, Measurements and Calculations of Preheated and Unpreheated Confined Kerosene Spray Flames,Comb.Sci.&Technol., **40**, 193-215 (1984).

W.D.Bachalo and M.J.Houser, Development of the Phase/Doppler Spray Analyzer for Liquid Drop Size and Velocity Characterizations, AIAA-84-1199 (1984).

R.J.Baker, P.Hutchinson, E.E.Khalil, and J.H.Whitelaw, Measurements of Three Velocity Components in a Model Furnace with and without Combustion, 15th Symp. (Int'l.) on Comb., 553-559 (1974).

A.Ballantyne and J.B.Moss, Fine Wire Thermocouple Measurements of Fluctuating Temperature, Comb. Sci. & Technol., **17**, 63-72 (1977).

R.S.Barlow and C.Q.Morrison, Two-Phase Velocity Measurements in Dense Particle-Laden Jets, Exp. in Fluids, **9**, 93-104 (1990).

J.M.Beer and N.A.Chigier, "*Combustion Aerodynamics*," Applied Science, London, 1972.

A.P.Benito, The Application of Second Order Turbulence Closures to Isothermal and Combusting Swirling Flows, PhD Thesis, Univ.London (1989).

K.R.Beshay, A.D.Gosman, and A.P.Watkins, Assessments of Multidimensional Diesel Spray Predictions, SAE Paper No. 861570 (1986).

A.F.Bicen, M.Heitor, and J.H.Whitelaw, Velocity and Temperature Measurements in a Can Type Gas Turbine Combustor, AGARD, CP-399, Paper 14 (1986).

A.F.Bicen and W.P.Jones, Velocity Characteristcs of Isothermal and Combusting Flows in a Model Combustor, Comb. Sci. & Technol., **49**, 1-15 (1986).

R.W.Bilger, Turbulent Jet Diffusion Flames, Prog. Energy & Comb. Sci., **1**, 87-109 (1976).

R.W.Bilger, The Structure of Diffusion Flames, Comb. Sci. & Technol., **13**, 155-170 (1976).

R.W.Bilger, Reaction Rates in Diffusion Flames, Combustion and Flame, **30**, 277-284 (1977).

F.Boysan, W.H.Ayers, J.Swithenbank, and Z.Pan, Three Dimensional Model of Spray Combustion in Gas Turbine Combustors, AIAA Paper No. 81-0324 (1981).

F.V.Bracco, Applications of Steady-State Spray Equation to Combustion MOdelling, AIAA J., **12**(11), 1534-1540 (1974).

L.J.S.Bradbury and I.P.Castro, Some Comments on Heat-Transfer Laws for Fine Wires, J. Fluid Mech., **51**(3), 487-495 (1972).

D.Bradley and K.J.Mathews, Measurements of High Temperature with Fine Wire Thermocouple, J.Mech.Eng.Sci., **10**(4), 299-305 (1968).

R.D.Brum and G.S.Samuelsen, Two-Component Laser Anemometry Measurements of Non-Reacting and Reacting Complex Flows in a Swirl-Stabilised Model Combustor, Exp. in Fluids, **5**, 95-102 (1987).

S.Chandrasekhar, Stochastic Problems in Physics and Astronomy, Reviews of Modern Physics, **15**(1), (in N.Wax, ed., *Selected Papers on Noise and Stochastic Processes*, Dover Publications, Inc., New York, 1954).

J.Chomiak and B.Niedzialek, Measurement of Rapidly Varying Gas Temperatures in an Unsteady Flows, Int'l. J. Heat & Mass Transfer, **10**, 1571-1579 (1967).

R.Clift, J.R.Grace, and M.E.Weber, *Bubbles, Drops and Particles*, Academic Press, Inc.,New York, 1978.

D.C.Collins and M.J. Williams, Two-Dimensional Convection from Heated Wires at Low Reynolds Numbers, J. Fluid Mech., **6**, 357-389 (1959).

D.R Cox and H.D.Miller, *The Theory of Stochastic Processes*, Methuen & Co. Ltd.,London, 1965.

C.T.Crowe, A Computational Model for the Gas-Droplet Flow Field in the Vicinity of an Atomizer, Paper No. 74-23, Western States Section/The Combustion Institute (1974).

C.T.Crowe, A Numerical Model for the Gas-Droplet Flow Field Near an Atomizer, 1st Int'l. Conf. on Liq. Atomiz. and Spray System, 377-383, Tokyo, August, 1978.

C.T.Crowe, M.P.Sharma, and D.E.Stock, The Particle-Source-in Cell (PSI-CELL) Model for Gas-Droplet Flows, Trans. ASME, J.Fluids Eng., **99**, 325-332 (1977).

B.J.Daly and F.H.Harlow, Transport Equations in Turbulence, Phys. Fluids, **13**, 2634-2649 (1970).

R.Diwakar, Multidimensional Modelling Applied to the Direct-Injection Stratified Charge Engine-Calculation versus Experiment, SAE Paper No. 810225 (1981).

J.L.Doob, The Brownian Movement and Stochastic Equations, Annals of Mathematics, **43**(2), 351-369 (1942) (in N.Wax, ed., *Selected Papers on Noise and Stochastic Processes*, Dover Publications, Inc., New York, 1954)

L.Drain, *The Laser Dopper Technique*, John Wiley & Sons, Chichester (1980).

J.K.Dukowicz, A Particle-Fluid Numerical Model for Liquid Sprays, J. Comput. Phys., **35**, 229-253 (1980).

F.Durst, A.Melling, and J.H.Whitelaw, *Principles and Practice of Laser Doppler Anemometry*, Academic Press, London (1981).

E.R.G Eckert and R.M.Drake, *Analysis of Heat and Mass Transfer*, McGraw-Hill Books, New York (1972).

Y.El Banhawy and J.H.Whitelaw, Calculation of the Flow Properties of a Confined Kerosene-Spray Flame, AIAA J., **18**(12), 1503-1510 (1980).

Y.El Banhawy and J.H.Whitelaw, Experimental Study of the Interaction Between a Fuel Spray and Surrounding Combustion Air, Combustion and Flame, **42**, 253-275 (1981).

G.M.Faeth, Evaporation and Combustion of Sprays, Progr. Energy & Comb. Sci., **9**(1), 1-76 (1983).

A.Favre, Statistical Equations of Turbulent Gases, in *Problems of Hydrodynamics and Continuum Mechanics*, SIAM, Philadelphia, 231-266, 1969.

D.J.Gaffen, C.Benocci, and D.Olivari, Numerical Modeling Buoyancy Dominated Dispersal Using a Lagrangian Approach, Atmospheric Environment, **21**(6), 1285-1293 (1987).

W.H.Gauvin, S.Katta, and F.H.Knelman, Droplet Trajectory Predictions and Their Importance in the Design of Spray Dryers, Int'l. J. Multiphase Flow, **1**, 793-816 (1975).

F.A.Gifford, Horizontal Diffusion in the Atmosphere: A Lagrangian-Dynamical Theory, Atmospheric Environment, **16**(3), 505-512 (1982).

G.A.E.Godsave, Studies of the Combustion of Drops in a Fuel Spray-The Burning of Single Drops of Fuel, 4th Symp. (Int'l.) on Comb., 818-830 (1953).

A.D.Gosman and E.Ioannides, Aspects of Computer Simulation of Liquid Fueled Combustors, J. Energy, **7**(6), 482-490 (1983).

A.D.Gosman and R.J.R.Johns, Computer Analysis of Fuel-Air Mixing in Direct-Injection Engines, SAE Paper No. 800091 (1981).

F.H.Harlow and A.A.Amsden, Flow of Interpenetrating Material Phases, J. Comput. Phys., **18**(4), 440-464 (1975).

M.Heitor, Experiments in Turbulent Reacting Flows, PhD Thesis, Univ. London (1985).

J.O.Hinze, *Turbulence*, 2nd ed., McGraw-Hill, Inc., New York, 1975.

H.Hiroyasu and T.Katoda, Fuel Droplet Size Distribution in Diesel Combustion Chamber, SAE Paper No. 740715 (1974).

F.G.Holderness, J.R.Tilson and J.J.MacFarlane, Electrical Compensation for Radiation Loss in Thermocouples, NGTE Note No. 758 (1969).

W.P.Jones, Models for Turbulent Flows with Variable Density, VKI Lecture Series 79-2 (in W.Kollman, ed., *Prediction Methods for Turbulent Flows*, Hemisphere Publishing Corp., New York, 1979)

W.P.Jones and R.P.Lindstedt, The Calculation of the Structure of Laminar Counterflow Diffusion Flames Using a Global Reaction Mechanism, Comb. Sci. & Technol., **61**, 31-49 (1988).

W.P.Jones and A.J.Marquis, Calculation of Axisymmetric Recirculating Flows with a Second Order Turbulence Model, Proc. 5th Symp. Turbulent Shear Flows, Cornell Univ., 1985.

W.P.Jones and J.J.McGuirk, Mathematical Modelling of Gas-Turbine Combustion Chambers, AGARD Conf. Proceedings No. 275 (1979).

W.P.Jones and P.Musonge, Closure of the Reynolds Stress and Scalar Flux Equations, Phys. Fluids, **31**, 3589-3604 (1988).

W.P.Jones and A.Pascau, Calculation of Confined Swirling Flows with a Second Moment Closure, Trans. ASME, J. Fluids Eng., **111**, 248-255 (1989).

W.P.Jones and C.H. Priddin, Predictions of the Flow Field and Local Gas Composition in Gas Turbine Combustors, 17th Symp. (Int'l.) on Comb., 399-409 (1978).

W.P.Jones and A.Tober, Velocity, Composition, and Temperature Fields in an Axisymmetric Model Combustor, 4th Int'l. Symp. on Laser Applic. to Fluid Mechnics, Lisbon, July, 1988.

W.P.Jones and A. Tober, Measurements of Gas Composition and Temperature Inside a Can Type Model Combustor, IUTAM Symp. Taipei, 1991.

W.P.Jones and H. Toral, Tempeture and Composition Measurements in a Research Gas Turbine Combustion Chamber, Comb. Sci. & Technol., **31**, 249-275 (1983).

W.P.Jones and J.H.Whitelaw, Calculation Methods for Reacting Turbulent Flows: A Review, Combustion and Flame, **48**, 1-26 (1982).

W.P.Jones and J.H.Whitelaw, Modelling and Measurements in Turbulent Combustion, 20th Symp. (Int'l.) on Comb., 233-249 (1984).

W.P.Jones and J.Wilhelmi, Velocity, Temperature, and Composition Measurements in a Confined Swirl-Driven Recirculating Flow, Comb. Sci. & Technol., **63**, 13-31 (1989).

H.Kaplan and N.Dinar, A Stochastic Model for the Dispersion of a Non-Passive Scalar in a Turbulent Field, Atmospheric Environment, **26A**(13), 2413-2423 (1992)

I.M.Kennedy, Some Aspects of Seeding Flames with Refractory Oxide Particles, Comb. Sci. & Technol., **27**, 247-252 (1982).

I.M.Kennedy and J.H.Kent, Scalar Measurements in a Co-Flowing Turbulent Diffusion Flame, Comb. Sci. & Technol., **25**, 109-119 (1981).

E.E.Khalil and J.H.Whitelaw, Aerodynamic and Thermodynamic Charicteristics of Kerosene-Spray Flames, 16th Symp. (Int'l.) on Comb., 569-576 (1976).

K.H.Khalil, F.M.El-Mahallawy, and H.A.Moneib, Effect of Combustion Air Swirl on the Flow Pattern in a Cylindrical Oil Fired Furnace, 16th Symp. (Int'l.) on Comb., 135-143 (1977).

K.Komiyama, R.C.Flagan, and J.B.Heywood, The Influence of Droplet Evaporation on Fuel-Air Mixing Rate in a Burner, 16th Symp. (Int'l.) on Comb., 549-560 (1976).

J.C.LaRue, G.S.Samuelsen and E.T.Seiler, Momentum and Heat Flux in a Swirl-Stabilised Combustor, 20th Symp. (Int'l.) on Comb., 277-285 (1984).

A.H.Lefebvre, "*Atomization and Sprays*," Hemisphere Publishing Corp., New York, 1989.

P.A.Libby and F.A.Williams(eds.), "*Turbulent Reacting Flows*," Springer-Verlag, Berlin, 1980.

R.P.Lindstedt, Private Communication (1992).

F.C.Lockwood and H.A.Moneib, Fluctuating Temperature Measurements in a Heated Round Free Jet, Comb. Sci. & Technol., **22**, 63-81 (1980).

A.K.Luhar and R.E.Britter, A Random Walk Model for Dispersion in Inhomogeneous Turbulence in a Convective Boundary Layer, Atmospheric Environment, **23**(9), 1911-1924 (1989).

A.K.Luhar and R.E.Britter, An Application of Lagrangian Stochastic Modelling to Dispersion During Shoreline Fumigation, Atmospheric Environment, **24**(4), 871-881 (1990).

J.L.Lumley, Pressure-Strain Correlation, Phys. Fluids, **18**, 750-751 (1975).

M.L.Mather and N.R.L.McCallum, Swirling Air Jets Issuing from Vane Swirler, J. Inst. Fuel, **39**, 214-225 (1967).

V.G.McDonell, C.P.Wood, and G.S.Samuelsen, A Comparison of Spatially-Resolved Drop Size and Drop Velocity Measurements in an Isothermal Chamber and a Swirl-Stabilzed Combustor, 21th Symp. (Int'l.) on Comb., 685-694 (1986).

D.Migdal and V.D.Agosta, A Source Flow Model for Continuum Gas-Particle Flow, Trans. ASME, J. Appl. Mech., **34**, 860-865 (1967).

H.A.Moneib, Experimental Study of the Fluctuation Temperature in Inert and Reacting Turbulent Jets, PhD Thesis, Univ. London (1980).

M.Nikjooy, R.M.So, and R.E.Peck, Modelling of Jet- and Swirl-Stabilized Reacting Flows in Axisymmetric Combustors, Comb. Sci. & Technol., **58**, 135-153 (1988).

Y.Onuma and M.Ogasawara, Studies on the Structure of a Spray Combustion Flame, 15th Symp. (Int'l.) on Comb., 453-465 (1974).

Y.Onuma, M.Ogasawara, and T.Inoue, Further Experiments on the Structure of a Spray Combustion Flame, 16th Symp. (Int'l.) on Comb., 561-567 (1976).

F.K.Owen, L.J.Spadaccini, and C.T.Bowman, Pollutant Formation and Energy Release in Confined Turbulent Diffusion Flames, 16th Symp. (Int'l.) on Comb., 105-117 (1976).

F.K.Owen, L.J.Spadaccini,J.B.Kennedy, and C.T.Bowman, Effect of Inlet Air Swirl and Fuel Volatility on the Structure of Confined Spray Flames, 17th Symp.(Int'l.) on Comb., 467-473 (1978).

A.Papoulis, *Probability, Random Variables, and Stochastic Processes*, McGraw-Hill Inc., New York, 1965.

H.L.Petrie, M.Samimy, and A.L.Addy, Laser Doppler Velocity Bias in Separated Flows, Exp. on Fluids, **6**, 80-88 (1988).

S.B.Pope, A Lagrangian Two-Time Probability Density Function Equation for Inhomogeneous Turbulent Flows, Phys. Fluids, **26**, 3448-3450 (1983).

S.B.Pope, Application of the Velocity-Dispersion Probability Density Function Model to Inhomogeneous Turbulent Flows, Phys. Fluids A, **3**(8), 1947-1957 (1991).

S.B.Pope and Y.L.Chen, The Velocity-Dissipation Probability Density Function Model for Turbulent Flows, Phys.Fluids A, **2**(8), 1437-1449 (1990).

R.D.Reitz and R.D.Diwakar, Effect of Drop Breakup on Fuel Sprays, SAE Paper No. 860469 (1986).

H.C.Rodean, The Universal Constant for the Lagrangian Structure Function, Phys. Fluids, A**3**(6), 1479-1480 (1991).

B.L.Sawford, Reynolds Number Effects in Lagrangian Stochastic Models of Turbulent Dispersion, Phys. Fluids, A**3**(6), 1577-1586 (1991).

M.D.Scadron and I.Warshawsky, Experimental Determination of Time Constants and Nusselt Numbers for Bare-Wire Thermocouples in High-Velocity Air Streams and Analytic Approximation of Conduction and Radiation Errors, NACT TN 2599 (1952).

M.Segal,C.-H.Yu,R.W.Arritt, and R.A.Pielke, On the Impact of Valley/Ridge Thermally Induced Circulations on Regional Pollutant Transport, Atmospheric Environment, **22**(3), 471-486 (1988).

C.E.Shepard and I.Warshawsky, Electrical Techniques for Compensation of Thermal Time Lag of Thermocouples and Resistance Thermometer Elements, NACA TN No. 2703 (1952).

I.G.Shepherd and J.M.Moss, Characteristic Scales for Density Fluctuations in a Turbulent Premixed Flame, Comb. Sci. & Technol., **33**, 231-243 (1983).

J.S.Shuen, L.D.Chen, and G.M.Faeth, Evaluation of Stochastic Model of Particle Dispersion in a Turbulent Round Jet, AIChE J., **29**(1), 167-170 (1983).

H.C.Soong, H.W.Han, and K.C Chang, Comparative Numerical Studies on Reynolds and Favre Averigings of Turbulent Diffusion Flame, J. Propul. Power, **8**(2), 259-263 (1992).

S.H.Starner, Joint Measurements of Radial Velocity and Scalars in a Turbulent Diffusion Flame, Comb. Sci. & Technol., **30**, 145-169 (1983).

S.H.Starner and R.W.Bilger, Joint Measurements of Velocity and Scalars in a Turbulent Diffusion Flame with Moderate Swirl, 21th Symp. (Int'l.) on Comb., 1569-1577 (1986).

A.C.Styles and N.A.Chigier, Combustion of Air Blast Atomized Spray Flames, 16th Symp. (Int'l.) on Comb., 627-638 (1976).

T.Takagi and T.Okamoto, Characteristics of Combustion and Pollutant Formation in Swirling Flames, Combustion and Flame, **43**, 69-79 (1981).

K.Thiele and H.Brodbeck, Velocity and Turbulence Measurements by Two-Color-LDA in Light and Heavy Oil Flames, 3th Int'l. Symp. on Applic. of Laser Anemom. to Fluid Mechanics, Lisbon, 1986.

D.J.Thomson, Criteria for the Sellection of Stochastic Models of Particle Trajectories in Turbulent Flows, J. Fluid Mech., **180**, 529-556 (1987).

C.Turfus, Calculating Mean Concentrations for Steady Sources in Recirculating Wakes by a Particle Trajectory Method, Atmospheric Environment, **22**(7), 1271-1290 (1988).

Tuttle, R.A.Shisler, and A.M.Mellor, Investigation of Liquid Fueled Turbulent Diffusion Flames, Comb. Sci. & Technol., **14**, 229-241 (1976).

A.P.Watkins, A.D.Gosman, and B.S.Tabrizi, Calculation of Three Dimensional Spray Motion in Engines, SAE Paper No., 860468 (1986).

C.K.Westbrook,Three Dimensional Numerical Modelling of Liquid Fuel Sprays, 16th Symp. (Int'l.) on Comb., 1517-1526 (1976).

P.N.Wild, F.Boysan, and J.Swithenbank, Spray Combustor Modelling, J. Inst. Energy, March (1988).

J.Wilhelmi, Axisymmetric Swirl Stabilized Combustion, PhD Thesis, Univ, London (1984).

A.Williams, Combustion of Droplets of Liquid Fuels: A Review, Combustion and Flame, **21**, 1-31 (1973).

A.Williams, "*Combustion of Liquid Fuel Sprays*," Butterworths, London, 1990.

F.A.Williams, Spray Combustion and Atomization, Phys. Fluids, 1(6), 541-545 (1958).

F.A.Williams, Spray Combustion Theory, Comb. & Flame, **3**, 215-228 (1959).

F.A.Williams, *The Combustion Theory*, 2nd ed., The Benjamin/Cummings Publishing Co. Inc., Menlo Park, 446- , 1985.

H.Wise and G.A.Agoston, Burning of Liquid Droplet, in *Literautre of the Combustion of Petroleum*, 116-135, American Chemical Society, 1958.

P.O.Witze and T.A.Baritaud, Particle Seeding for the Mie Scattering Measurements in Combusting Flow, 3rd Int'l. Symp. on Applic. of Laser Anemom. to Fluid Mechanics, Lisbon, 1986.

C.P.Wood, R.A.Smith, and G.S.Samuelsen, Spatially-Resolved Measurements of Soot Size and Population in a Swirl-Stabilized Combustor, 20th Symp. (Int'l.) on Comb., 1083-1094 (1984).

Z.Yuan and E.E.Michaelides, Turbulence Modulation in Particulate Flows - A Theoretical Approach, Int. J. Multiphase Flow, **18**(5), 779-785 (1992).

A.J.Yule, S.L.Mo, Y.S.Tham, and S.M.Aval, Diesel Spray Structure, 3rd Int'l. Conf. on Liquid Atomiz. and Spray System, London, 1985.

Appendix A. Trajectories of Measurement Volume of LDV

Case 1 Arrangements for W Velocity Measurements

Consider the optics are moved horizontally by Δx away from the combustor, as shown in Figure 2.22 (a). α and D are the beam crossing angle and the spacing between the two parallel beams. β_A and β_B are the incident angles at points A and B, respectively. It is assumed, for simplicity, that the relative refractive index of the quartz glass is 3/2.

The coordinates of point A are determine from the quations for the line RA and the circle passing through R_o, as:

$$x_A = [-ab + (a^2 r_0^2 + r_0^2 - b^2)^{1/2}] / (1 + a^2) \; ; \; y_A = a x_A + b \qquad \text{(A-1)}$$

where a and b are the slope and the intercept of the line RA and given:

$$a = \tan(\alpha / 2) \; ; \; b = y_R - a x_R \qquad \text{(A-2)}$$

The coordinates of point B are determined form the equations for the lone AB, represented by y_{AB}, and the circle passing through the point R_i, represented by $x^2 + y^2 = r_i^2$,as:

$$x_B = [-a'b' + (a'^2 r_i^2 + r_i^2 - b'^2)^{1/2}] / (1 + a'^2) \; ; \; y_B = a' x_B + b' \qquad \text{(A-3)}$$

where a′ and b′ are determined as:

$$a' = \tan(\alpha / 2 - \beta_A / 3) \; ; \; b' = y_A - a' x_A \qquad \text{(A-4)}$$

Finally, the coordinates of point P are determined from the equation for line BP, represented by $y_{BP} = a''x + b''$, as:

$$x_P = -\frac{b''}{a''} \; ; \; y_P = 0 \qquad \text{(A-5)}$$

where a″ and b″ are given as:

$$a'' = \tan(\alpha/2 - \beta_A/3 + \beta_B/2) \; ; \quad b'' = y_B - a''x_B \tag{A-6}$$

The incident angles, β_A and β_B are given as:

$$\beta_A = \alpha/2 - \theta_A \; ; \quad \beta_B = \alpha/2 - \theta_A - \theta_B \tag{A-7}$$

where

$$\theta_A = \tan^{-1}(y_A / x_A) \; ; \quad \theta_B = \tan^{-1}(y_B / x_B). \tag{A-8}$$

Case 2 Arrangements for V Velocity Measurements

Consider the optics are moved vertically by h away from the combustor, as shown in Figure 2.21 (a). Here again α and D are the beam crossing angle and the spacing between two parallel beans. Then it follows, from geometrical consideration as in Case 1, that:

$$L(x_L, y_L) : x_L = r_O + s \; , \; y_L = h - D/2 \tag{A-9}$$

$$y_{LB} = -ax + b \; ; \; a = \tan(\alpha/2) \; , \; b = y_L + ax_L \tag{A-10}$$

$$B(x_B, y_B) \; ; \text{ from } y = -ax + b \text{ and } x^2 + y^2 = r_O^2 \tag{A-11}$$

$$x_B = [ab + (a^2 r_o^2 + r_o^2 - b^2)^{1/2}]/(1 + a^2) \; ; \; y_B = -ax_B + b \tag{A-12}$$

The incident angle at B : $\beta_L = \alpha/2 + \theta_B$ with $\theta_B = \tan^{-1}(y_B / x_B)$

$$y_{BD} = -a'x + b' \; ; \; a' = \tan(\alpha/2 - \beta_L/3) \; , \; b' = a'x_B + y_B \tag{A-13}$$

$D(x_D, y_D)$, from $y = -a'x + b'$ and $x^2 + y^2 = r_i^2$

$$x_D = [a'b' + (a'^2 r_i^2 + r_i^2 - b'^2)^{1/2}]/(1 + a'^2) \; ; \; y_D = -a'x + b' \tag{A-14}$$

The incident angle at D ; $\gamma_L = \alpha/2 - \beta_L/3 + \theta_D$ with $\theta_D = \tan^{-1}(y_D / x_D)$

$$y_{DP} = -a''x + b'' \; ; \quad a'' = \tan(\alpha/2 - \beta_L/3 + \gamma_L/2) \; , \quad b'' = a''x_D + y_D \tag{A-15}$$

Similarly for the upper beam, it follows that:

$$H(x_H, y_H) : \; x_H = r_O + s \; , \; y_H = h + D/2 \tag{A-16}$$

$$y_{HA} = px + q;\ \ p = \tan(\alpha/2)\ ,\ q = y_H - px_H \qquad \text{(A-17)}$$

A(x,y), from $y = px + q$ and $x^2 + y^2 = r_o^2$:

$$x_A = [-pq + (p^2 r_o^2 + r_o^2 - q^2)^{1/2}] / (1 + p^2)\ ;\ y_A = px_A + q \qquad \text{(A-18)}$$

The incident angle at A, $\beta_H = \theta_A - \alpha/2$ with $\theta_A = \tan^{-1}(y_A / x_A)$

$$y_{AC} = p'x + q'\ ;\ \ p' = \tan(\alpha/2 + \beta_H/3)\ ,\ \ q' = y_A - p'x_A \qquad \text{(A-19)}$$

C(x_C,y_C), from $y = p'x + q'$ and $x^2 + y^2 = r_i^2$:

$$x_C = [-p'q' + (p'^2 r_i^2 + r_i^2 - q'^2)^{1/2}] / (1 + p'^2)\ ;\ y_C = p'x_C + q' \qquad \text{(A-20)}$$

The incident angle at C, $\gamma_H = \theta_C - (\alpha/2 + \beta_H/3)$ with $\theta_C = \tan^{-1}(y_C / x_C)$

$$y_{CP} = p''x + q''\ ;\ \ p'' = \tan(\alpha/2 + \beta_H/3 - \gamma_H/2)\ ,\ q'' = y_C - p''x_C \qquad \text{(A-21)}$$

Thus, the coordinates of point P are determined from the intersection of two lines, (A-15) and (A-21), as:

$$x_P = \frac{b'' - q''}{a'' + p''}\ ,\ y = -a''x_P + b'' = p''x_P + q'' \qquad \text{(A-22)}$$

The inclination angle of the fringes in the control volume against the horizontal axis, θ, is:

$$\theta = [\tan^{-1}(p'') - \tan^{-1}(a'')] / 2 \qquad \text{(A-23)}$$

Appendix B. Reynolds Stress Model Equations

The averaged momentum equation (3.3-7) is rewritten as:

$$\frac{\partial}{\partial t}\overline{\rho}\,\tilde{u}_i + \frac{\partial}{\partial x_j}\overline{\rho}\,\tilde{u}_j\tilde{u}_i = -\frac{\partial p}{\partial x_i} + \frac{\partial}{\partial x_i}(\overline{\tau}_{ij} - \overline{\rho}\,\widetilde{u_i''u_j''}) \tag{B-1}$$

where τ_{ij} is the viscous stress tensor and the average of it can be written in terms of unweighted mean velocities:

$$\overline{\tau}_{ij} = \mu(\frac{\partial \overline{u}_i}{\partial x_j} + \frac{\partial \overline{u}_j}{\partial x_i} - \frac{2}{3}\delta_{ij}\frac{\partial \overline{u}_l}{\partial x_l}) \tag{B-2}$$

At high Reynolds numbers this term is, however, negligible.

The last term, $\overline{\rho}\,\widetilde{u_i''u_j''}$, on the right hand side of the equation (B-1), is obtained, in the second moment closure approach, from the evolution type transport equation of it. For high Reynolds number flows, the Reynolds stress transport equation can be written as follows:

$$\frac{\partial}{\partial t}\overline{\rho}\,\widetilde{u_i''u_j''} + \frac{\partial}{\partial x_l}\overline{\rho}\,\tilde{u}_l\widetilde{u_i''u_j''} = -\overline{\rho}[\widetilde{u_i''u_j''}\frac{\partial \tilde{u}_i}{\partial x_l} + \widetilde{u_i''u_i''}\frac{\partial \tilde{u}_j}{\partial x_l}] \qquad \text{(I)}$$

$$-[\overline{u}_i''\frac{\partial \overline{p}}{\partial x_j} + \overline{u}_j''\frac{\partial \overline{p}}{\partial x_i}] \qquad \text{(II)}$$

$$-\frac{\partial}{\partial x_l}\overline{\rho}\,\widetilde{u_i''u_j''u_l''} \qquad \text{(III)}$$

$$-[\overline{u_i''\frac{\partial p'}{\partial x_j}} + \overline{u_j''\frac{\partial p'}{\partial x_i}}] \qquad \text{(IV)}$$

$$-[\overline{\tau_{li}'\frac{\partial u_i''}{\partial x_l}} + \overline{\tau_{ij}'\frac{\partial u_i''}{\partial x_l}}] \qquad \text{(V)} \tag{B-3}$$

The term (IV) on the RHS of equation (B-3) is decomposed into the redistributive and non-redistributive terms (Lumley, 1979), as:

$$-[\overline{u_i''\frac{\partial p'}{\partial x_j}}+\overline{u_j''\frac{\partial p'}{\partial x_i}}]=-[\overline{u_i''\frac{\partial p'}{\partial x_j}}+\overline{u_j''\frac{\partial p'}{\partial x_i}}-\frac{2}{3}\delta_{ij}\overline{u_l''\frac{\partial p'}{\partial x_l}}]-\frac{2}{3}\delta_{ij}\overline{u_l''\frac{\partial p'}{\partial x_l}} \tag{B-4}$$

The term in the bracket on the RMS is the redistributive term, denoted by A_{ij}, and is collectively modelled (Jones and Musonge, 1988) as a linear function of the Reynolds stress and the mean velocity field.

$$\begin{aligned}-A_{ij} &= C_1\bar{\rho}\frac{\tilde{\varepsilon}}{\tilde{k}}(\widetilde{u_i''u_j''}-\frac{2}{3}\delta_{ij}\tilde{k})+C_2\delta_{ij}\bar{\rho}\widetilde{u_l''u_m''}\frac{\partial\tilde{u}_l}{\partial x_m}\\ &+C_3[\bar{\rho}\widetilde{u_i''u_j''}\frac{\partial\tilde{u}_i}{\partial x_l}+\bar{\rho}\widetilde{u_l''u_i''}\frac{\partial\tilde{u}_j}{\partial x_l}]+C_4\bar{\rho}\tilde{k}[\frac{\partial\tilde{u}_i}{\partial x_j}+\frac{\partial\tilde{u}_j}{\partial x_i}]\\ &-(\frac{3}{2}C_2+C_3)[\bar{\rho}\widetilde{u_l''u_j''}\frac{\partial\tilde{u}_l}{\partial x_i}+\bar{\rho}\widetilde{u_l''u_i''}\frac{\partial\tilde{u}_l}{\partial x_j}]+C_5\bar{\rho}\tilde{k}\delta_{ij}\frac{\partial\tilde{u}_l}{\partial x_l}\end{aligned} \tag{B-5}$$

The other term on the RHS of equation (B-4) is the non-redistributive term and can be written as:

$$\frac{2}{3}\delta_{ij}\overline{u_l''\frac{\partial p'}{\partial x_l}}=-\frac{2}{3}\delta_{ij}\overline{p'\frac{\partial u_l''}{\partial x_l}}+\frac{2}{3}\delta_{ij}\frac{\partial\overline{p'u_l''}}{\partial x_l} \tag{B-6}$$

The first term on the RHS is usually small in low speed flows (Bilger, 1976) thus neglected and the second term is combined with the term (III) of the equation (B-3) to form a total diffusion term as:

$$-T_{ijl}=\bar{\rho}\widetilde{u_i''u_j''u_l''}+\frac{2}{3}\delta_{ij}\widetilde{p'u_l''} \tag{B-7}$$

and is modelled, after Daly and Harlow(1970), as:

$$T_{ijl}=C_5\bar{\rho}\frac{k}{\varepsilon}\widetilde{u_l''u_m''}\frac{\partial\widetilde{u_i''u_j''}}{\partial x_m} \tag{B-8}$$

The last term (V) of the equation (B-3) is the viscous dissipative correlation, i.e.:

$$\overline{\tau'_{li}\frac{\partial u''_j}{\partial x_l}} + \overline{\tau'\frac{\partial u''_i}{\partial x_l}} = \bar{\rho}\varepsilon_{ij}$$
$$= \frac{2}{3}\delta_{ij}\varepsilon \quad (\because \varepsilon_{ij} = 0 \text{ if } i = j) \tag{B-9}$$

and ε is calculated it's transport equation as:

$$\frac{\partial}{\partial t}\bar{\rho}\tilde{\varepsilon} + \frac{\partial}{\partial x_j}\bar{\rho}\tilde{u}_j\tilde{\varepsilon} = \frac{\partial}{\partial x_j}[C_1\bar{\rho}\frac{\tilde{k}}{\tilde{\varepsilon}}\widetilde{u''_i u''_j}\frac{\partial\tilde{\varepsilon}}{\partial x_i}] - C_{\varepsilon_1}\frac{\tilde{\varepsilon}}{\tilde{k}}\bar{\rho}\widetilde{u''_i u''_j}\frac{\partial\tilde{u}_i}{\partial x_j}$$
$$- C_{\varepsilon_2}\bar{\rho}\frac{\tilde{\varepsilon}^2}{\tilde{k}} - C_{\varepsilon_3}\frac{\tilde{\varepsilon}}{\tilde{k}}\overline{u''_i}\frac{\partial p'}{\partial x_i} \tag{B-10}$$

The values of model constants in Equations (B-5) and (B-10) used in this work are listed in Table B.1.

Table B.1 Model Constants for Second Moment Closure

C_1	3.0
C_2	-0.44
C_3	0.46
C_4	-0.23
C_5	0.0
C_{ε_1}	1.4
C_{ε_2}	1.9
C_{ε_3}	0.0

For the scalar field the second moment closure assembled by Pascau (1989) was used and this can be summarised as:

$$\bar{\rho}\frac{\partial}{\partial t}\widetilde{u_i''\phi''}+\bar{\rho}\tilde{u}_j\frac{\partial\widetilde{u_i''\phi''}}{\partial x_j}+\bar{\rho}\widetilde{u_j''\phi''}\frac{\partial\tilde{u}_i}{\partial x_j}+\bar{\rho}\widetilde{u_i''u_j''}\frac{\partial\tilde{\phi}}{\partial x_j}$$

$$=\frac{\partial}{\partial x_j}\{C_S\bar{\rho}\frac{k}{\varepsilon}\widetilde{u_j''u_k''}\frac{\partial\widetilde{u_i''\phi''}}{\partial x_k}\}-C_{\phi_1}^{*}\bar{\rho}\frac{\varepsilon}{k}\widetilde{u_i''\phi''}+C_{\phi_2}\bar{\rho}\,b_{ij}k\frac{\partial\tilde{\phi}}{\partial x_j} \quad \text{(B-11)}$$

$$+C_{\phi_3}\bar{\rho}\widetilde{u_j''\phi''}\frac{\partial\tilde{u}_i}{\partial x_j}+C_{\phi_4}\bar{\rho}\widetilde{u_j''\phi''}\frac{\partial\tilde{u}_j}{\partial x_i}$$

with $C_{\phi_1}^{*}=\dfrac{3}{1+3(b^2)^{1/2}}$, $C_{\phi_2}=0.12$, $C_{\phi_3}=1.09$, $C_{\phi_4}=0.51$ *and* $C_S=0.2$

and where $b^2=b_{ij}b_{ij}$ with $b_{ij}=\widetilde{u_i''u_j''}/k-2/3\delta_{ij}$.

$$\bar{\rho}\frac{\partial\widetilde{\phi''^2}}{\partial t}+\bar{\rho}\tilde{u}_i\frac{\partial\widetilde{\phi''^2}}{\partial x_i}+2\bar{\rho}\widetilde{u_i''\phi''}\frac{\partial\tilde{\phi}}{\partial x_i}=\frac{\partial}{\partial x_j}\{C_S\bar{\rho}\frac{k}{\varepsilon}\widetilde{u_i''u_j''}\frac{\partial\phi''^2}{\partial x_i}\}-2\varepsilon_\phi \quad \text{(B-12)}$$

$$\bar{\rho}\frac{\partial\varepsilon_\phi}{\partial t}+\bar{\rho}\tilde{u}_i\frac{\partial\varepsilon_\phi}{\partial x_i}=\frac{\partial}{\partial x_j}\{C_\varepsilon\bar{\rho}\frac{k}{\varepsilon}\widetilde{u_i''u_j''}\frac{\partial\varepsilon_\phi}{\partial x_i}\}-C_{P_1}\bar{\rho}\frac{\varepsilon}{k}\widetilde{u_j''\phi''}\frac{\partial\tilde{\phi}}{\partial x_j}$$

$$-C_{P_2}\bar{\rho}\frac{\varepsilon_\phi}{k}\widetilde{u_i''u''}\frac{\partial\tilde{u}_i}{\partial x_j}-C_{D_1}\bar{\rho}\frac{\varepsilon}{k}\varepsilon_\phi-C_{D_2}\bar{\rho}\frac{\widetilde{\varepsilon_\phi''^2}}{\widetilde{\phi''^2}} \quad \text{(B-13)}$$

The recommended constants for Equation (B-13) are: C_{P_1} = 1.7, C_{P_2} = 1.4, C_{D_1} = 1.8 and C_{D_2} = 2.0.

Appendix C. Droplet Size Distribution Function

The Nukiyama-Tanasawa equation for size distribution takes the form:

$$\frac{dN}{dD} = aD^{\alpha}e^{-bD^{\beta}} \tag{C-1}$$

where a, b, α, and β are the constants selected to best fit the given size distribution; N is the number of droplets in the size range between D and D+dD.

From it's definition, the Sauter mean diameter (SMD) can be calculated as:

$$\begin{aligned} SMD &= \frac{\int_0^{\infty} D^3 dN}{\int_0^{\infty} D^2 dN} = \frac{\int_0^{\infty} D^{\alpha+3}e^{-bD^{\beta}} dD}{\int_0^{\infty} D^{\alpha+2}e^{-bD^{\beta}} dD} = \frac{b^{-(\alpha+4)/\beta}\Gamma(\frac{\alpha+4}{\beta})}{b^{-(\alpha+3)/\beta}\Gamma(\frac{\alpha+3}{\beta})} \\ &= b^{-1/\beta}\Gamma_{43} \end{aligned} \tag{C-2}$$

where $\Gamma_{43} = \Gamma(\frac{\alpha+4}{\beta}) / \Gamma(\frac{\alpha+3}{\beta})$

Thus, the coefficient b can be rewritten in terms of SMD, as:

$$b = (\Gamma_{43} / SMD)^{\beta} \tag{C-3}$$

It is noted that the following identity is employed in equation (C-2):

$$\int_0^{\infty} x^{p-1}e^{-\mu x^q} dx = \frac{1}{q}\mu^{-p/q}\Gamma(p/q) \tag{C-4}$$

where Γ denotes the gammer function.

The total volume of the droplets, injected over a fixed time period in the present work, is determined as:

$$V_T = \frac{\pi}{6}\int_0^\infty D^3 dN = \frac{\pi}{6} a \int_0^\infty D^{\alpha+3} e^{-bD^\beta} dD = \frac{\pi}{6}\frac{a}{\beta} b^{-(\alpha+4)/\beta}\Gamma(\frac{\alpha+4}{\beta}) \qquad \text{(C-5)}$$

Employing the equation (C-3), this could be rewritten as:

$$\begin{aligned} V_T &= \frac{\pi}{6}\frac{a}{\beta}(SMD/\Gamma_{43})^{\alpha+4}\Gamma(\frac{\alpha+4}{\beta}) \\ &= \frac{\pi}{6} SMD^3 \frac{a}{\beta}\frac{SMD^{\alpha+1}}{\Gamma_{43}{}^{\alpha+4}}\Gamma(\frac{\alpha+4}{\beta}) \\ &= \frac{a}{\beta} V_{SMD}\frac{SMD^{\alpha+1}\Gamma_3{}^{\alpha+4}}{\Gamma_4{}^{\alpha+3}} \end{aligned} \qquad \text{(C-6)}$$

where $\Gamma_3 = \Gamma(\frac{\alpha+3}{\beta})$

$\Gamma_4 = \Gamma(\frac{\alpha+4}{\beta})$

and $V_{SMD} = \frac{\pi}{6} SMD^3$

Thus, the coefficient a could also be rewritten in terms of SMD, as:

$$a = \beta \frac{V_T}{V_{SMD}}\frac{\Gamma_4{}^{\alpha+3}}{\Gamma_3{}^{\alpha+4}}\frac{D^\alpha}{SMD^{\alpha+1}} e^{-(\Gamma_{43} D/SMD)^\beta} \qquad \text{(C-7)}$$

Now the equation (C-1) could be rewritten in terms of V_T and SMD, as:

$$\frac{dN}{dD} = \beta \frac{V_T}{V_{SMD}}\frac{\Gamma_4{}^{\alpha+3}}{\Gamma_3{}^{\alpha+4}}\frac{D^\alpha}{SMD^{\alpha+1}} e^{-(\Gamma_{43} D/SMD)^\beta} \qquad \text{(C-8)}$$

or, in terms of normalised diameter, d = D/SMD, as:

$$\frac{dN}{dd} = \beta \frac{V_T}{V_{SMD}}\frac{\Gamma_4{}^{\alpha+3}}{\Gamma_3{}^{\alpha+4}} d^\alpha e^{-(\Gamma_{43} d)^\beta} \qquad \text{(C-9)}$$

In the present work, V_T is the product of volumetric fuel delivery rate and the fixed time internal between the releases of set of new droplets.

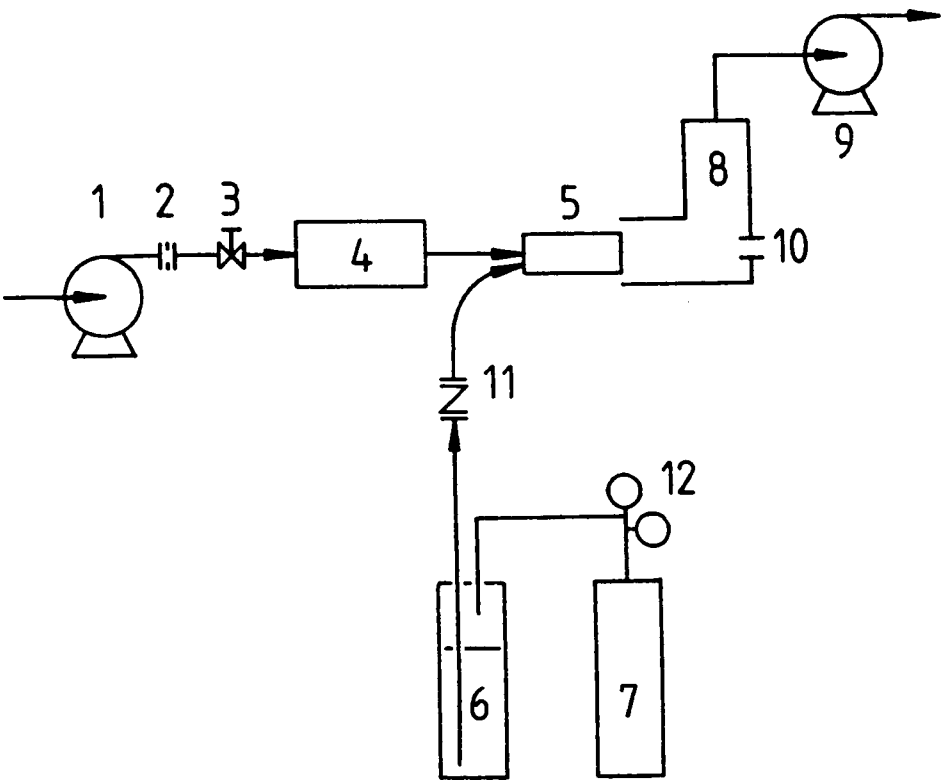

1. Fan Blower; 2. Orifice Flow Metre; 3. Throttle Valve;
4. Air Preheater; 5. Combustor; 6. Fuel Cylinder;
7. N_2 Gas Cylinder; 8. Exhaust Duct; 9. Exhaust Fan;
10. Observation Port; 11. Fuel Flowmeter; 12. Pressure Regulator

Figure 2.1 Test Rig

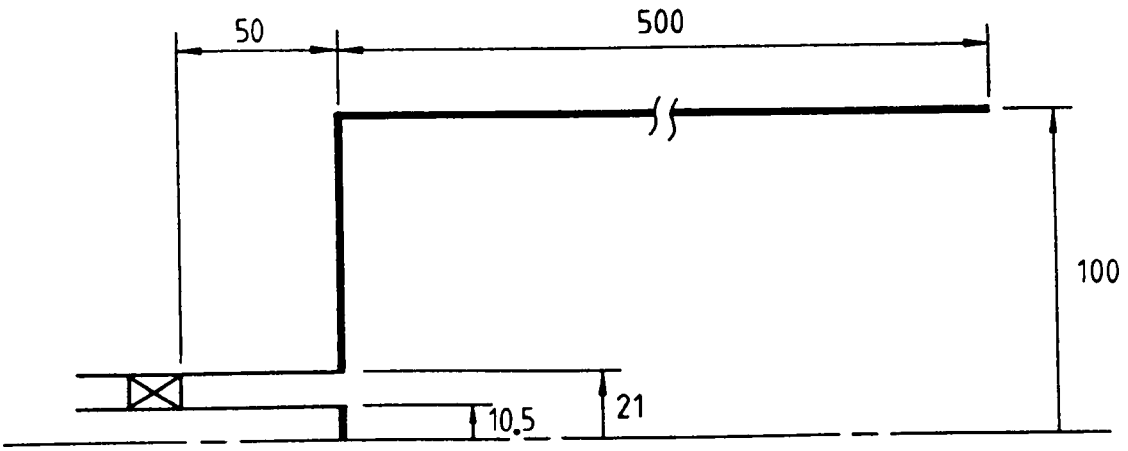

Figure 2.2 Combustor Geometry

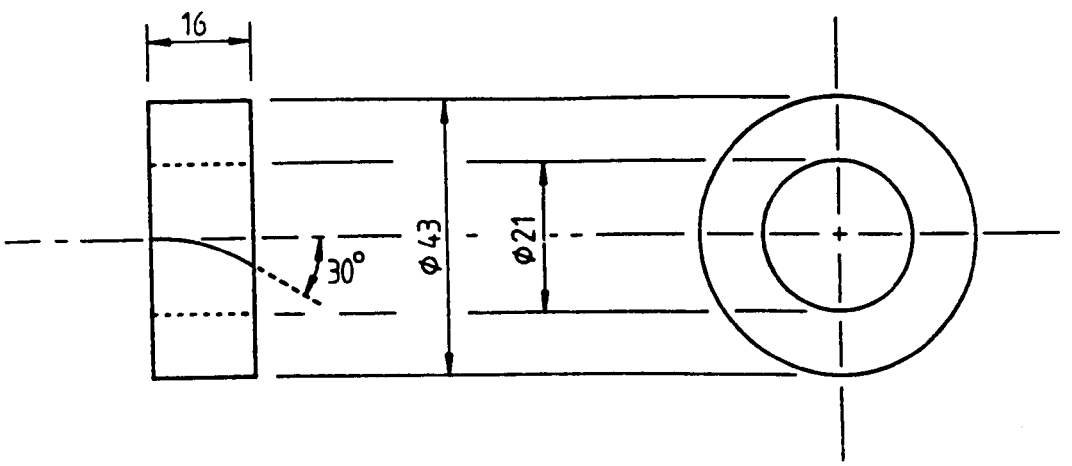

Figure 2.3 Swirler Design

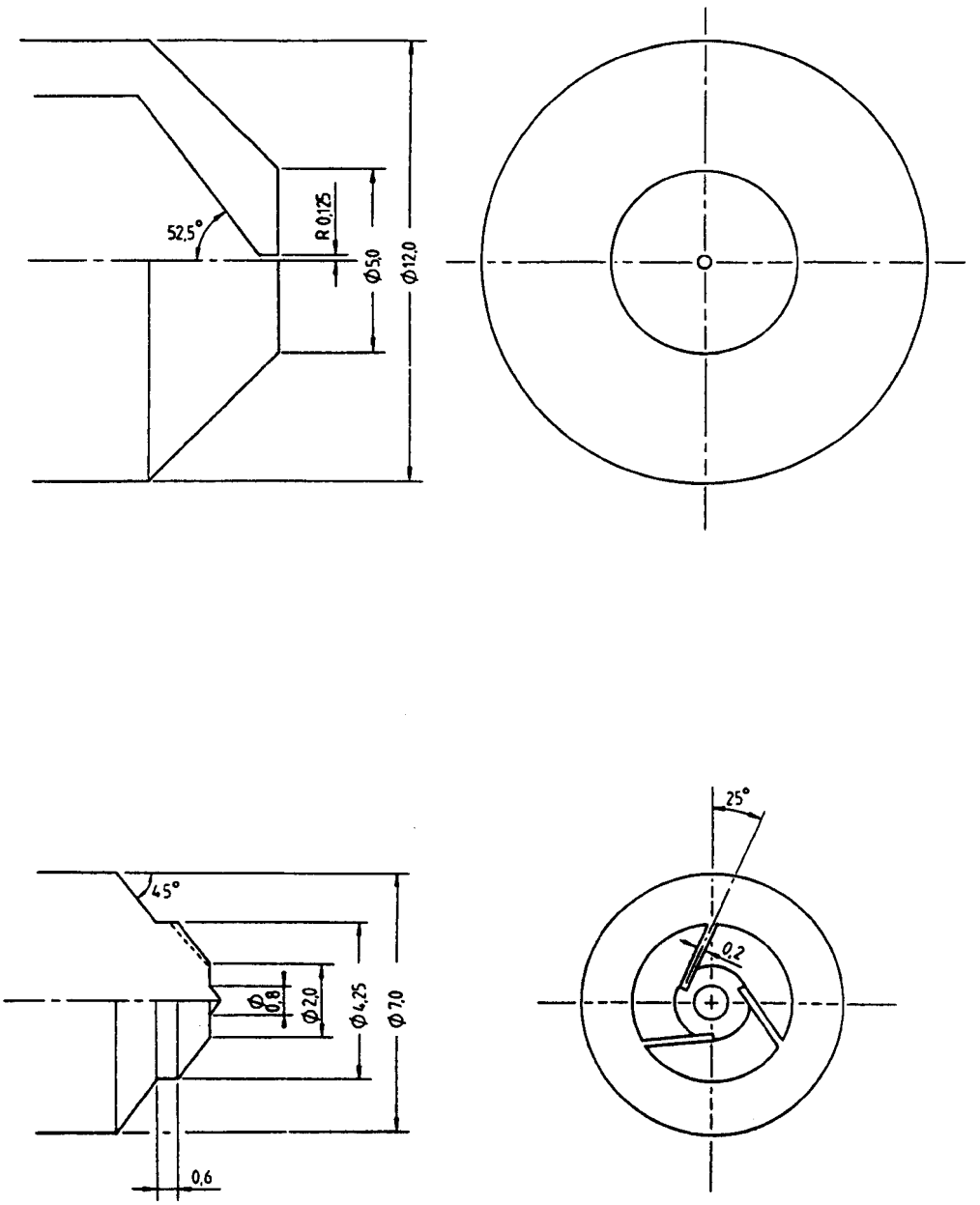

Figure 2.4 Fuel Injection Nozzle

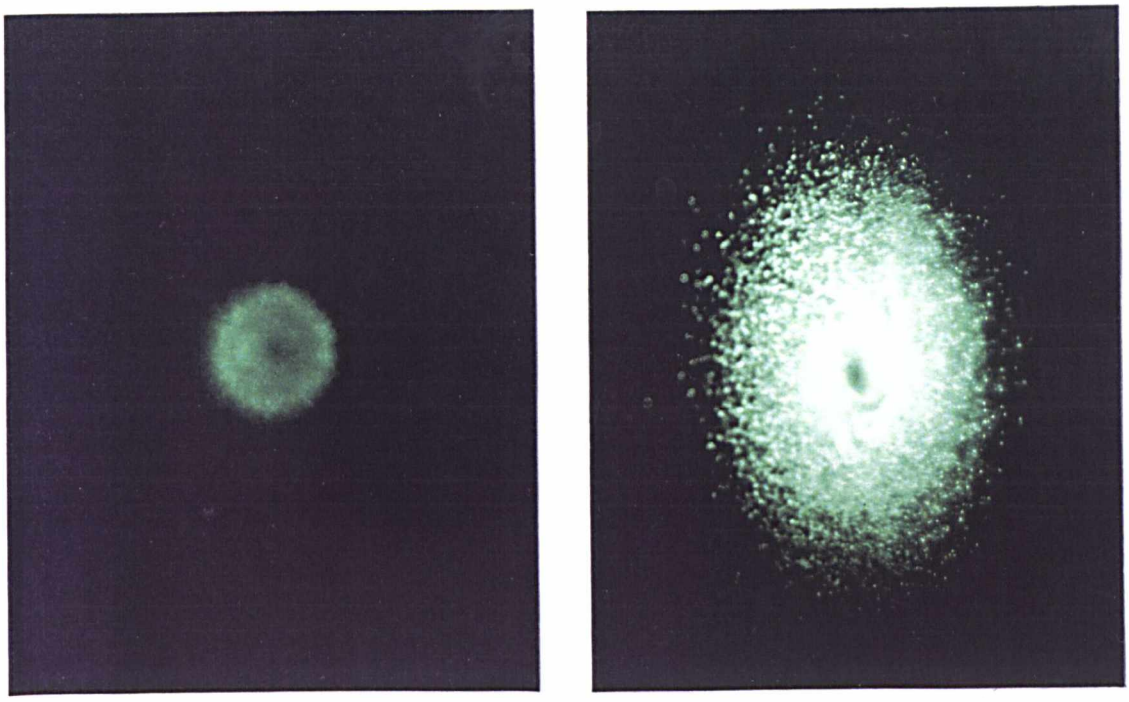

(a) X = 10 mm, AOV ≈ 20° (b) X= 40 mm, AOV ≈ 67°

Figure 2.5 Front Cut View of Spray into Quiescent Air

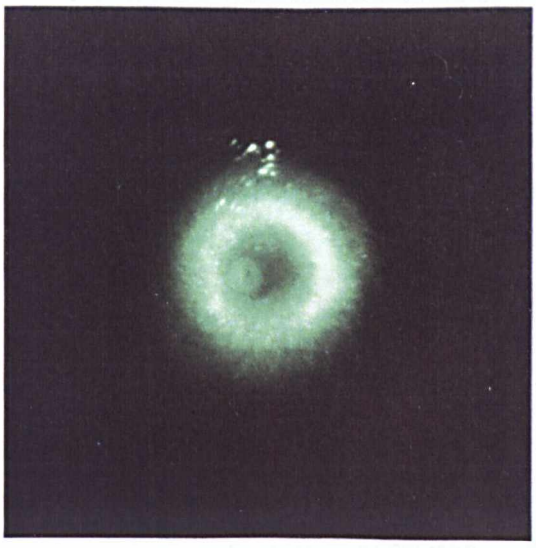

X = 10 mm, AOV ≈ 20°

Figure 2.6 Front Cut View of Spray into Swirling Air

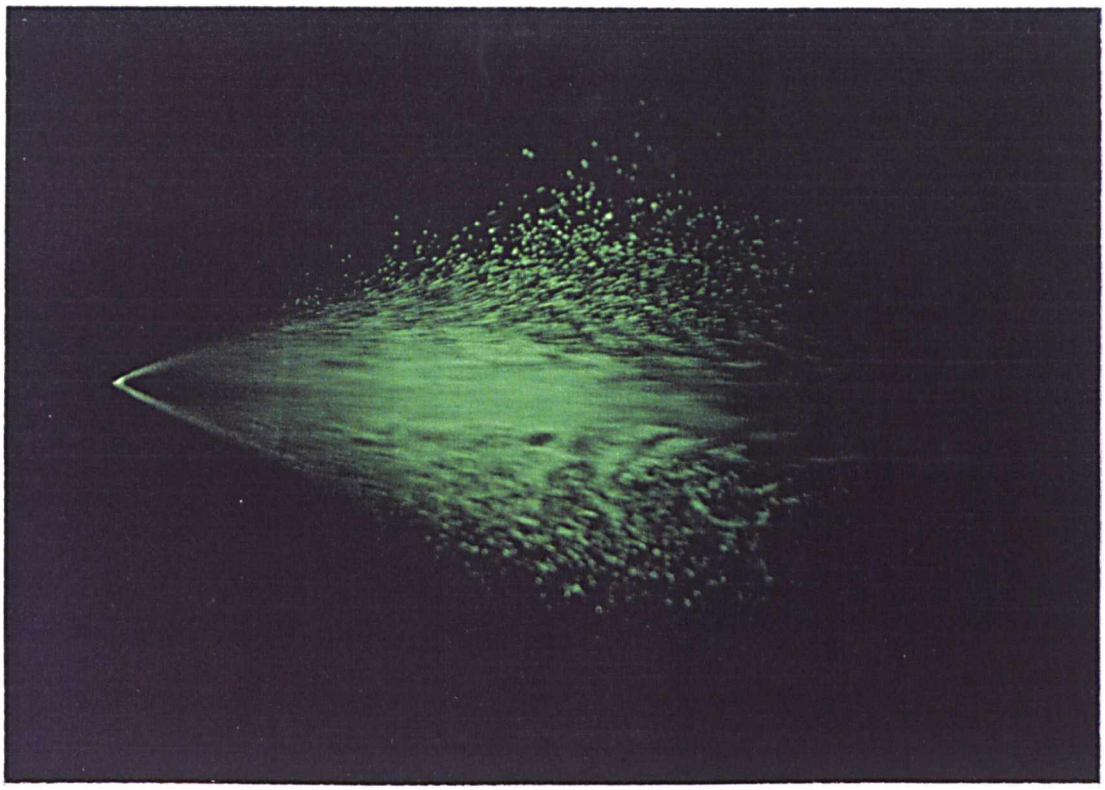

Figure 2.7 Side Cut View of Spray into Quiescent Air

Figure 2.8 Side Cut View of Spray into Swirling Air

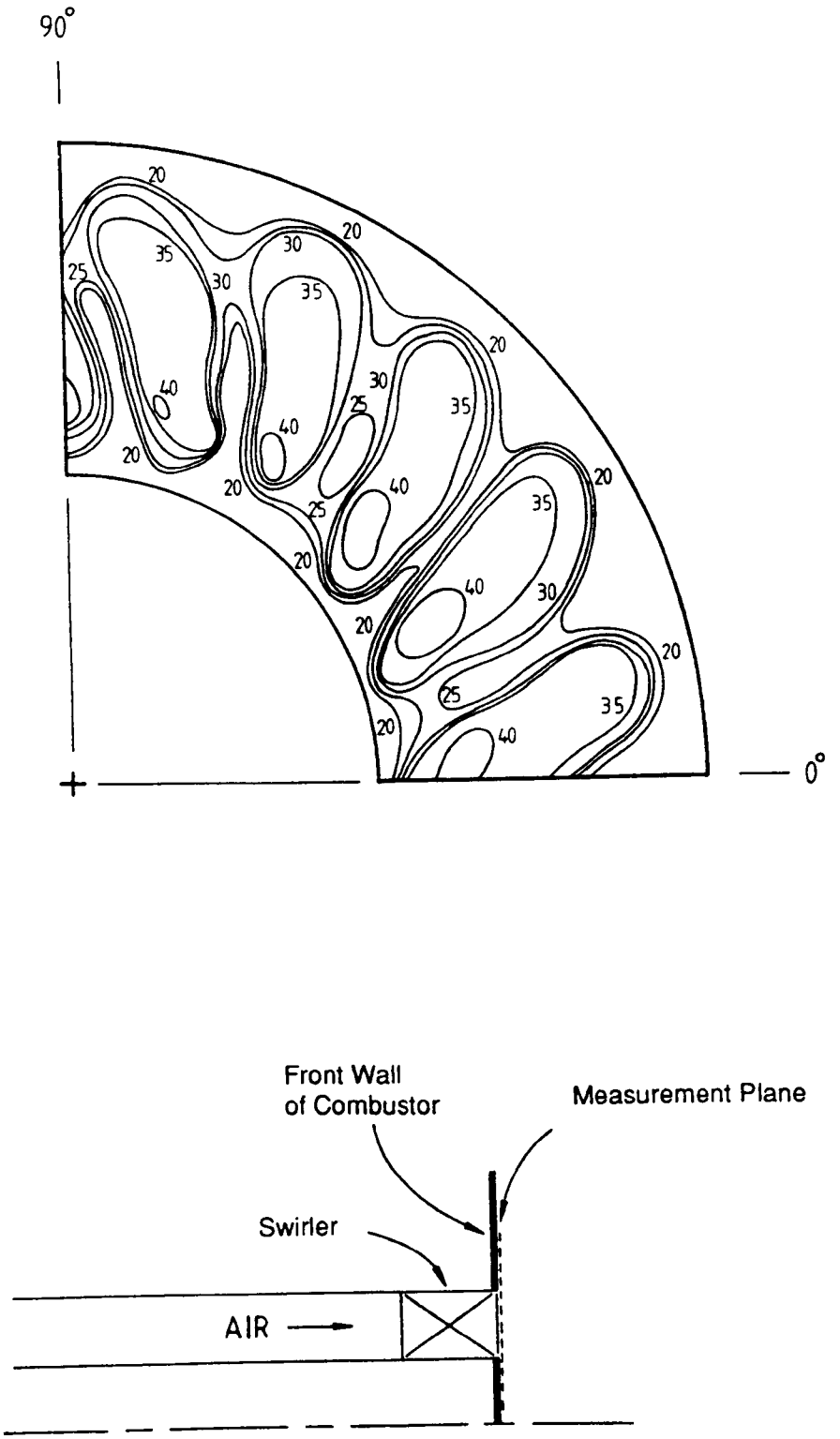

Figure 2.9 Contours of Mean Axial Velocity, Swirler Flush Position

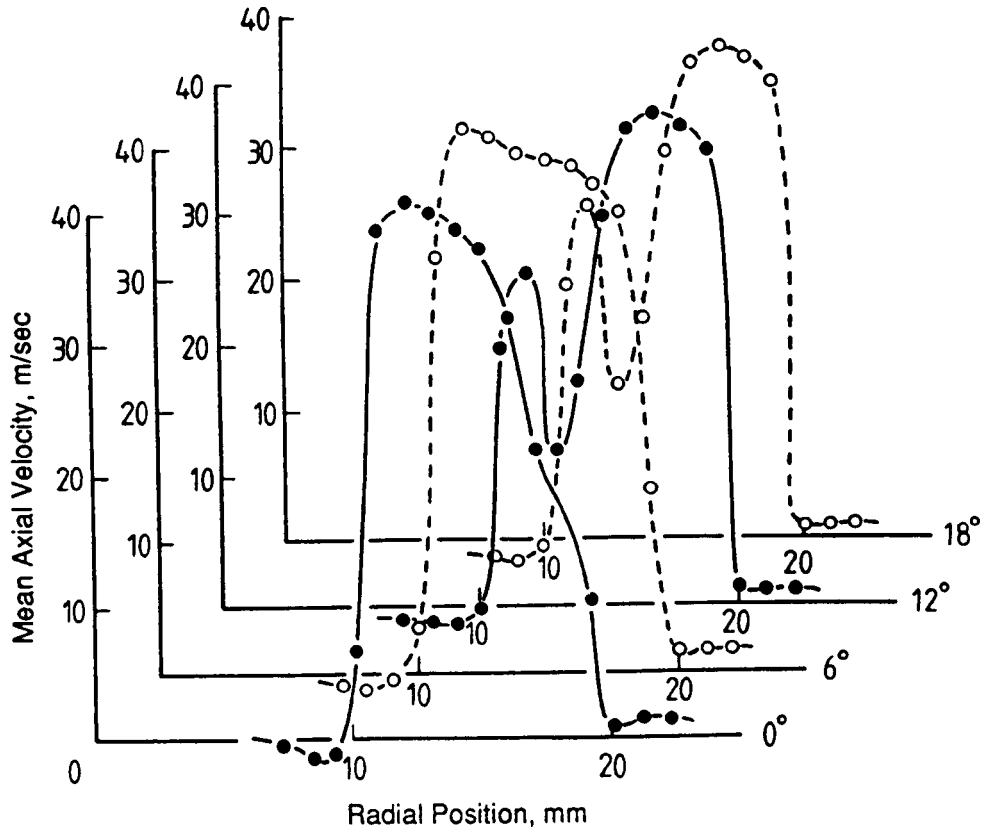

Figure 2.10 Mean Axial Velocity Profiles, Swirler Flush Position

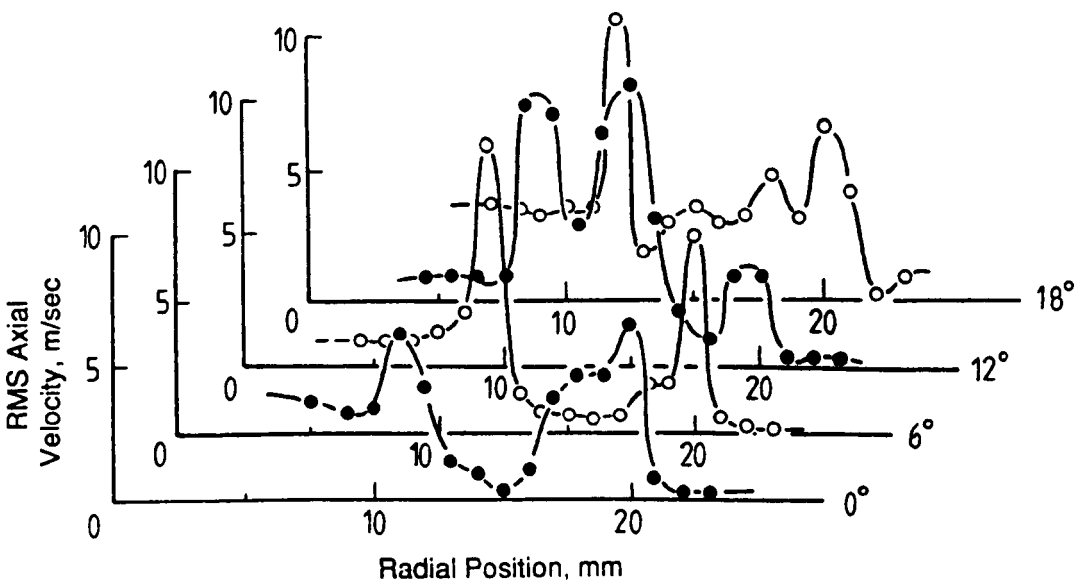

Figure 2.11 RMS Axial Velocity Profiles, Swirler Flush Position

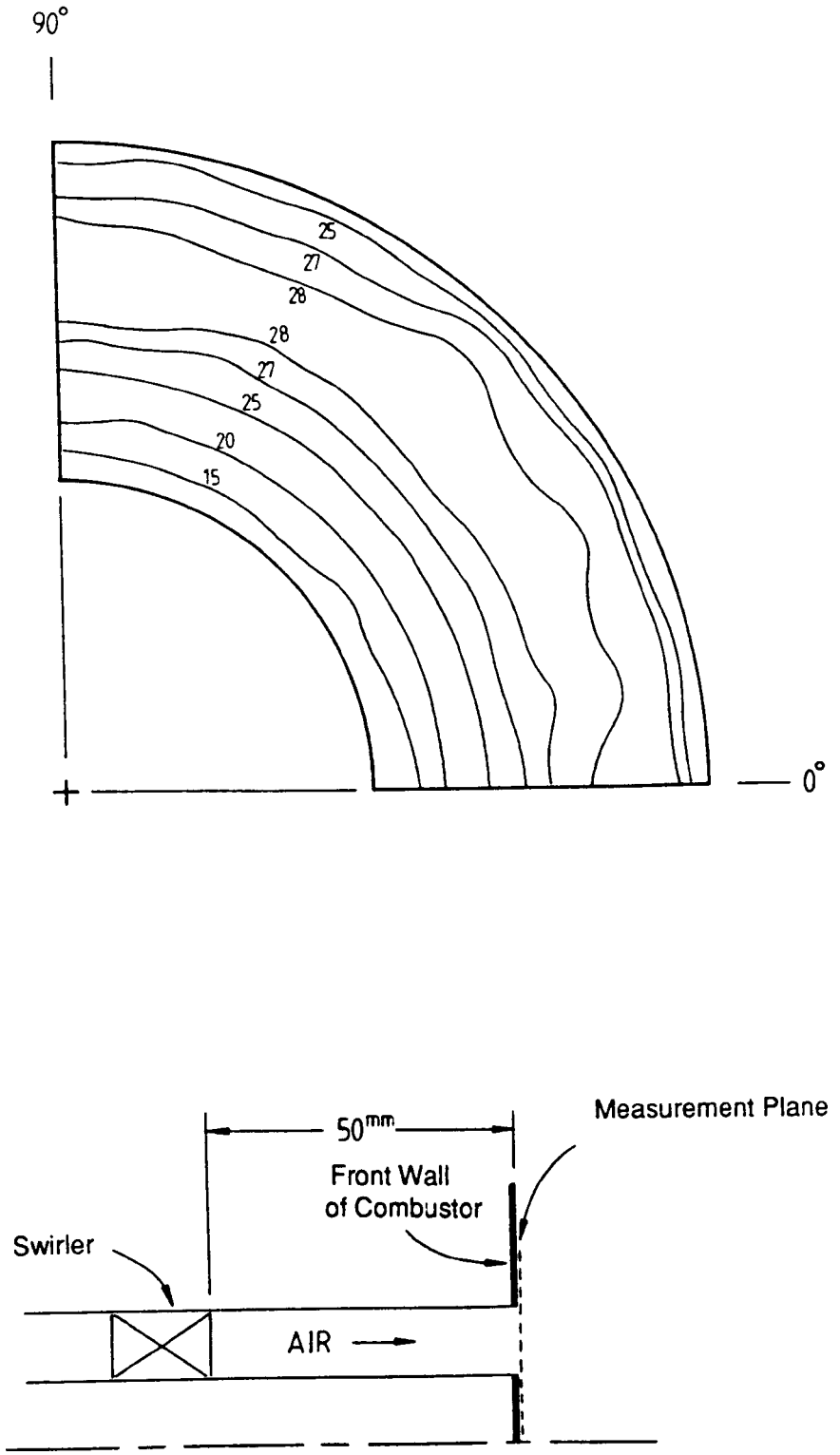

Figure 2.12 Contours of Mean Axial Velocity, Swirler Recessed

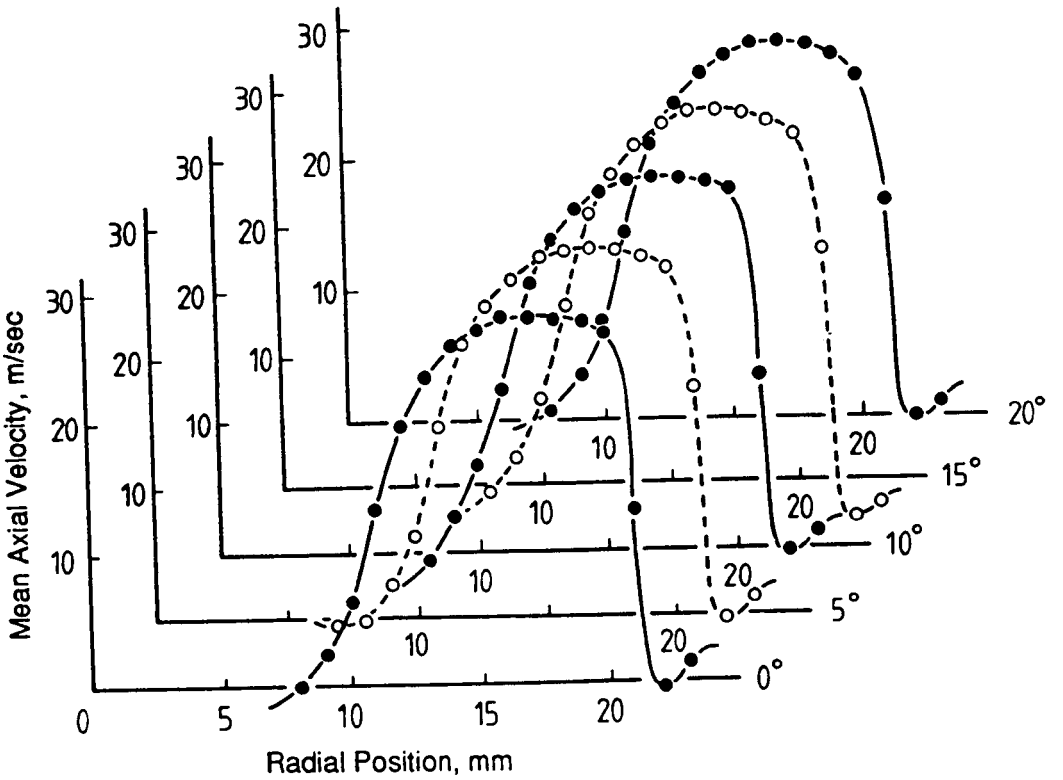

Figure 2.13 Mean Axial Velocity Profiles, Swirler Recessed

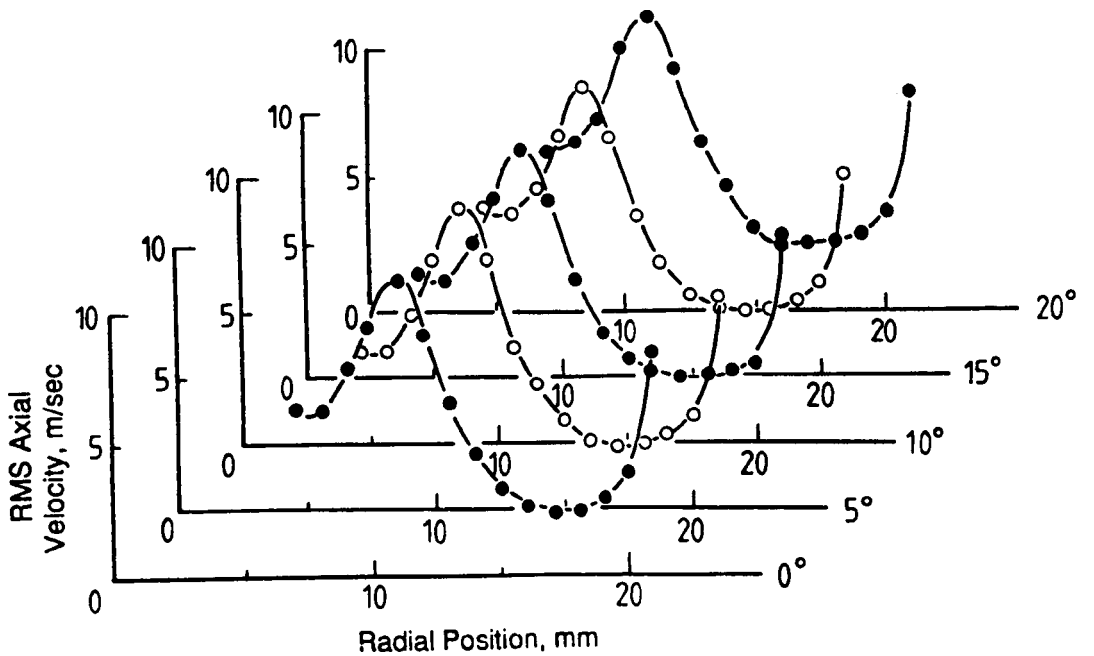

Figure 2.14 RMS Axial Velocity Profiles, Swirler Recessed

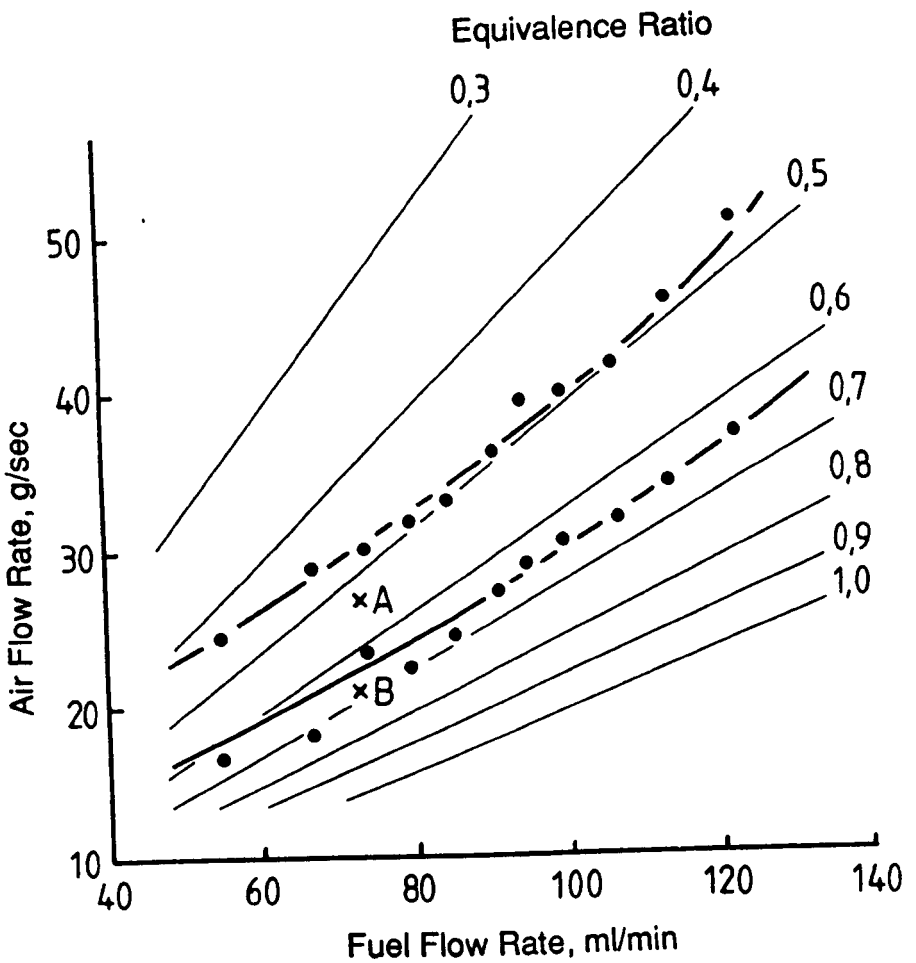

Figure 2.15 Operability of Combustor

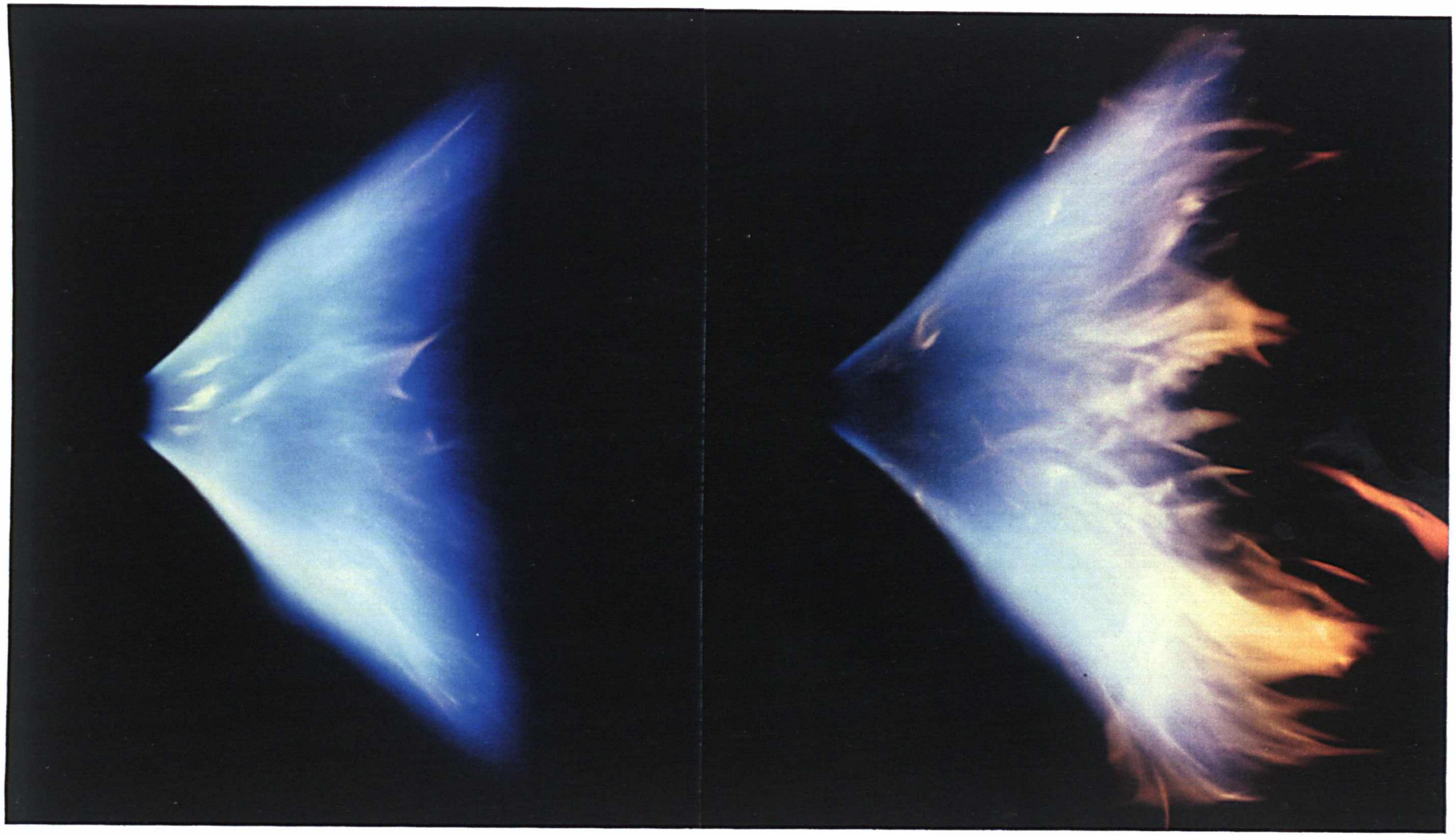

(a) Flame A

(b) Flame B

Figure 2.16 Side View of the Flames

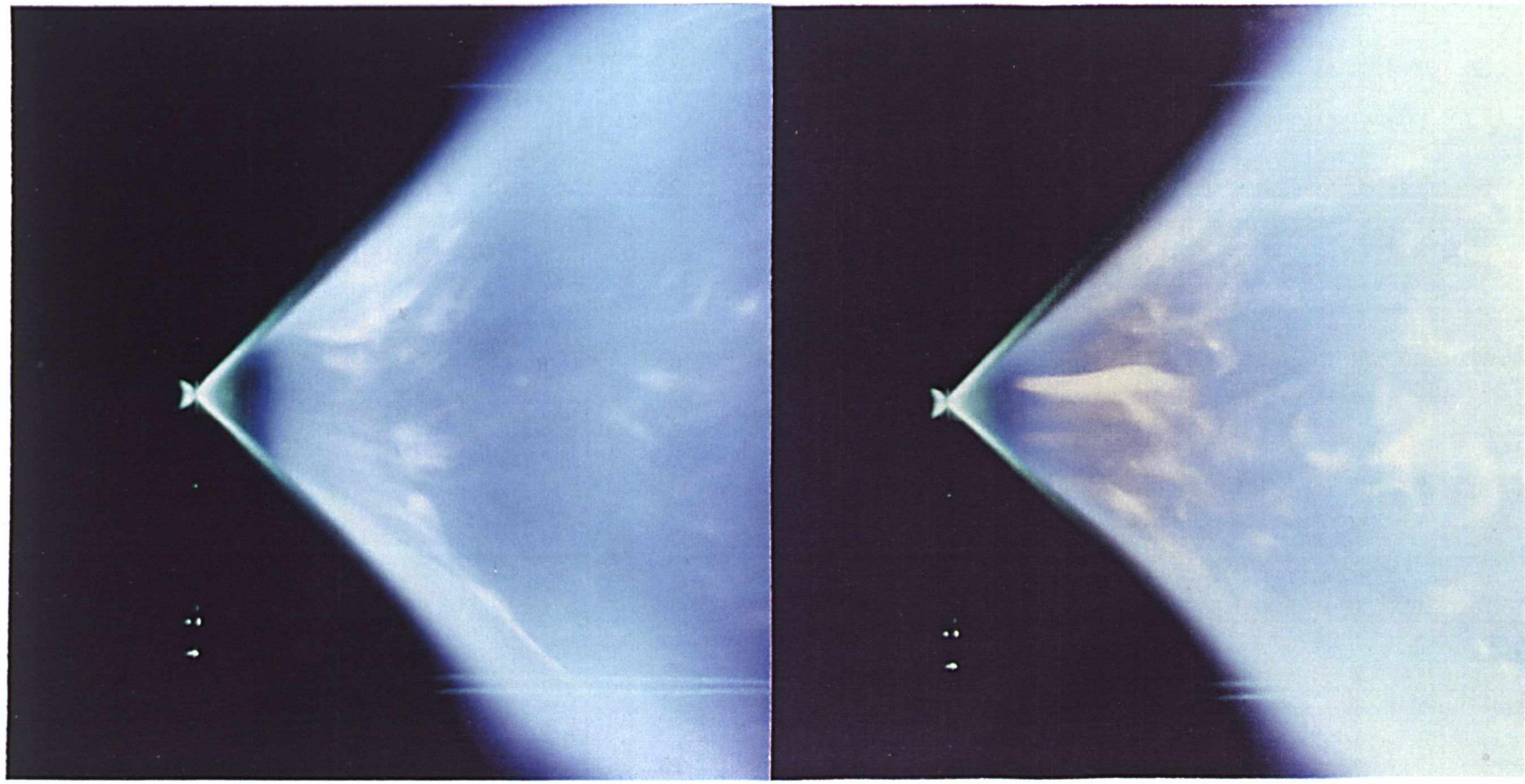

(a) Flame A

(b) Flame B

Figure 2.17 Spray in the Flame, Close to Nozzle

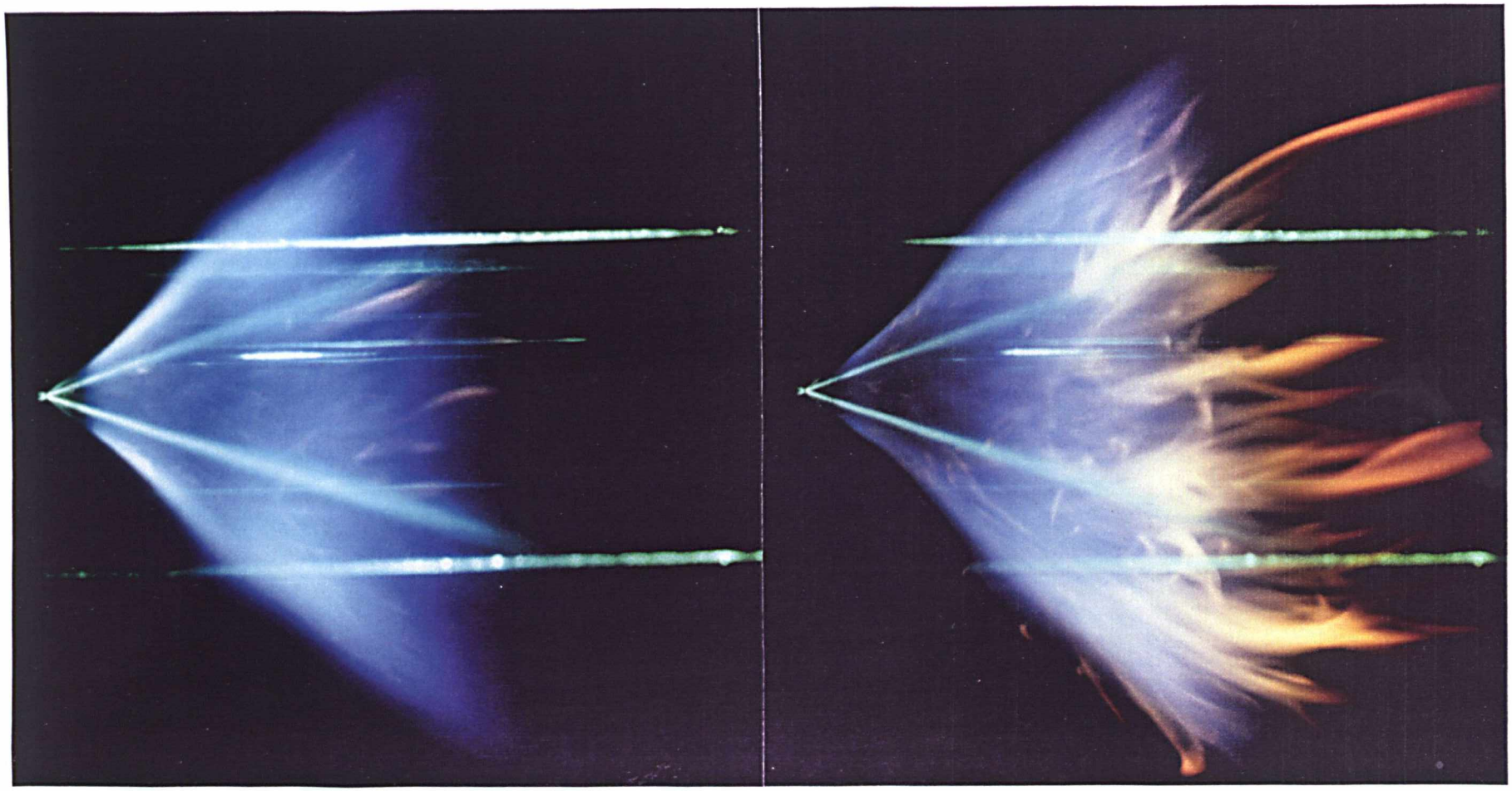

(a) Flame A

(b) Flame B

Figure 2.18 Spray in the Flame, Entire Field

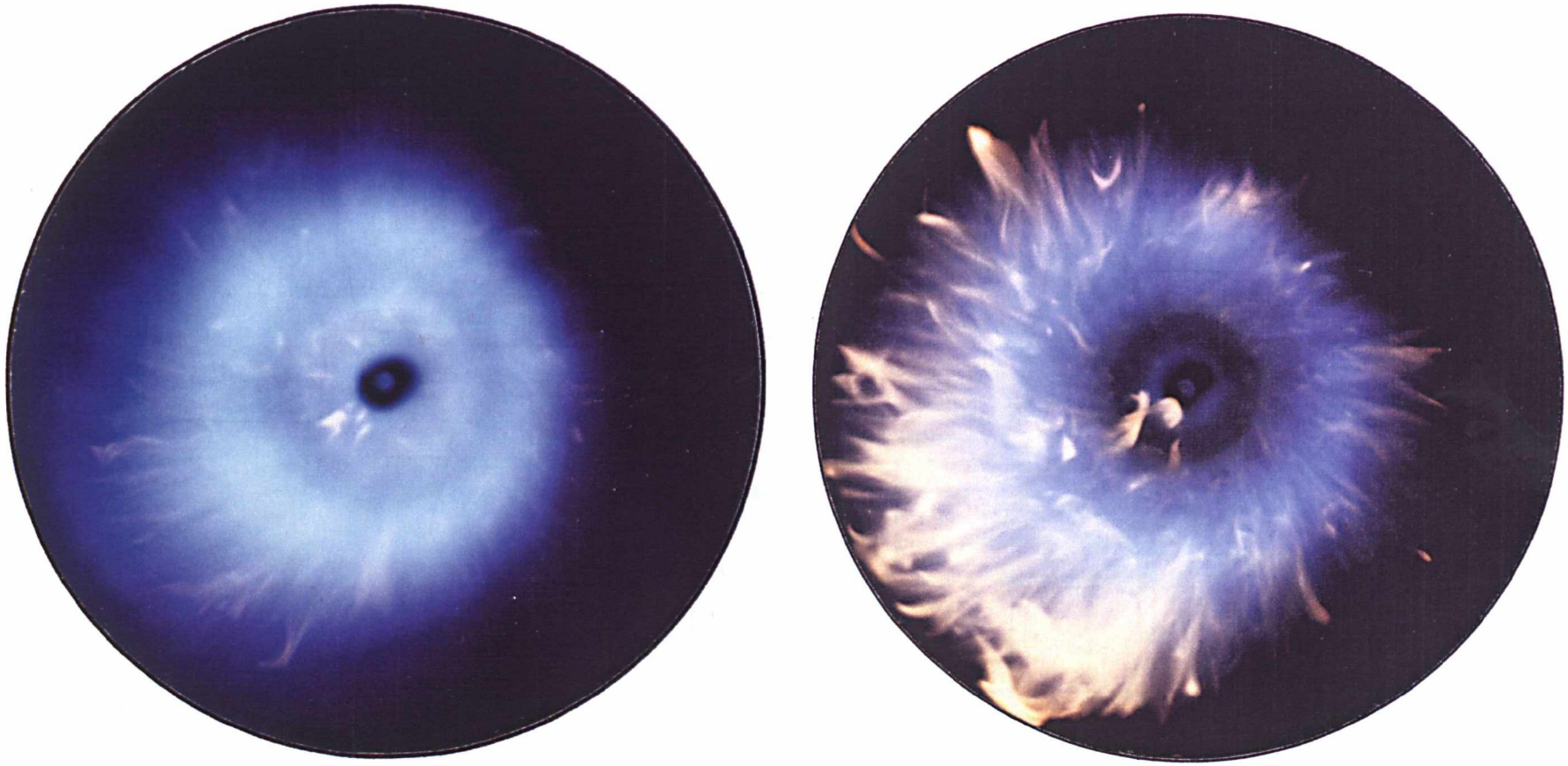

(a) Flame A

(b) Flame B

Figure 2.19 Front View of the Flames

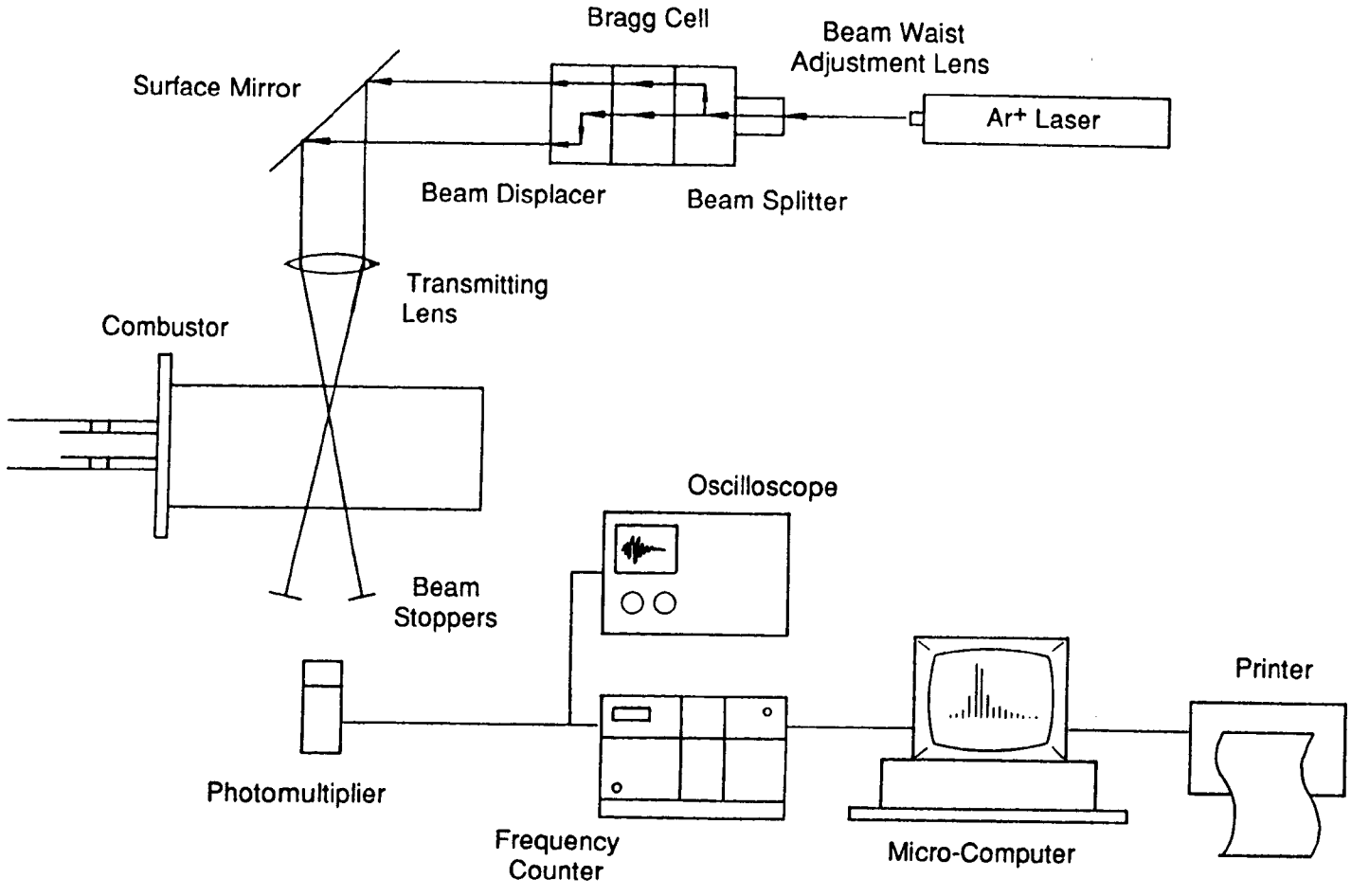

Figure 2.20 Layout of LDV System

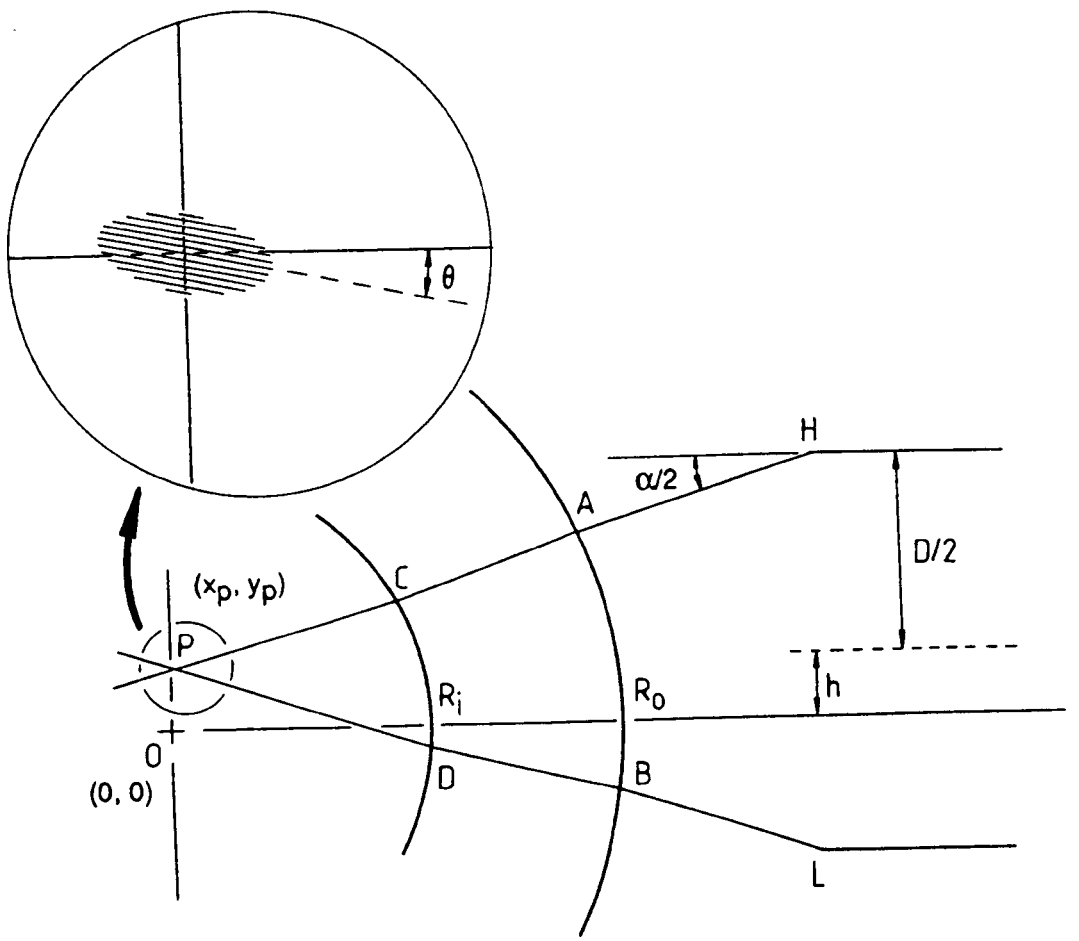

Figure 2.21 Measurement Volume Trajectories
with Optics Arranged for Radial Velocity (continued)

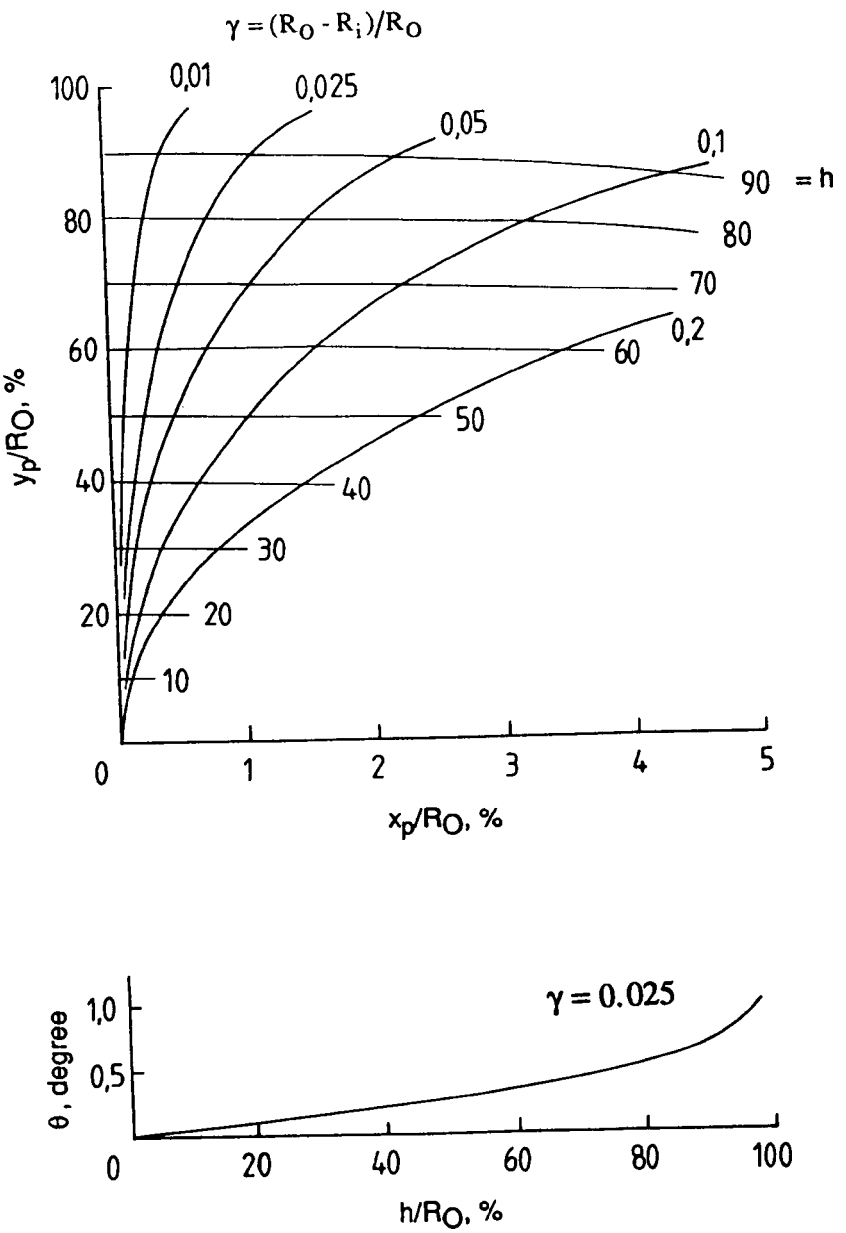

Figure 2.21 Measurement Volume Trajectories with Optics Arranged for Radial Velocity (complete)

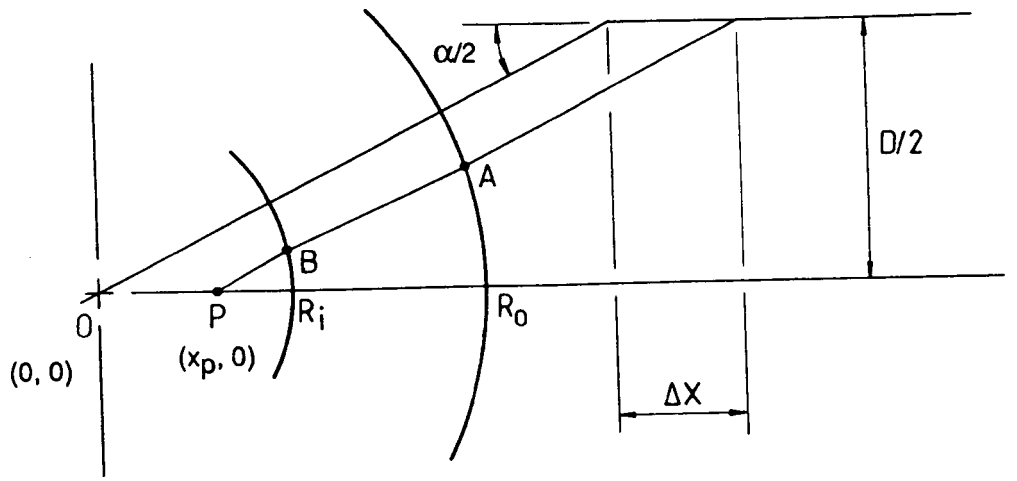

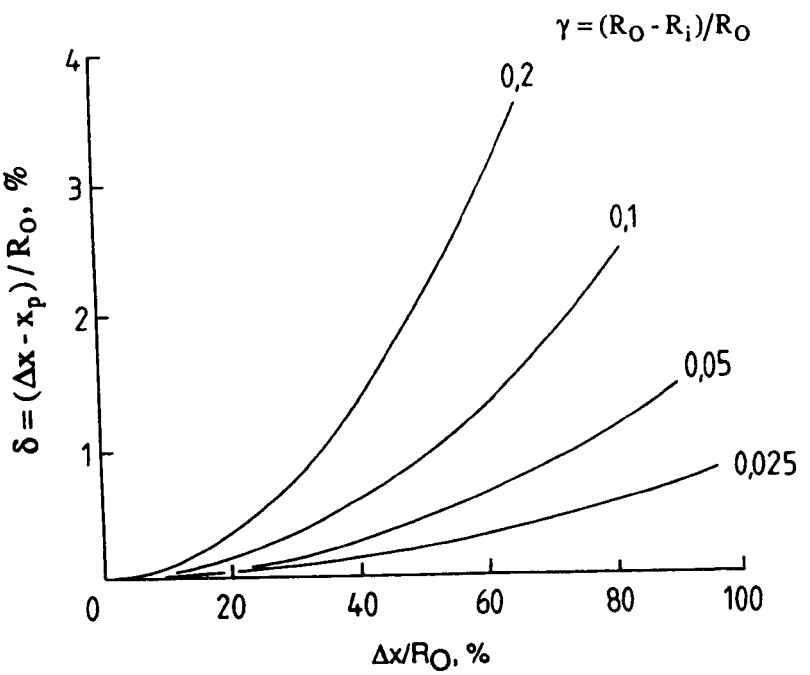

Figure 2.22 Measurement Volume Trajectories
with Optics Arranged for Swirl Velocity

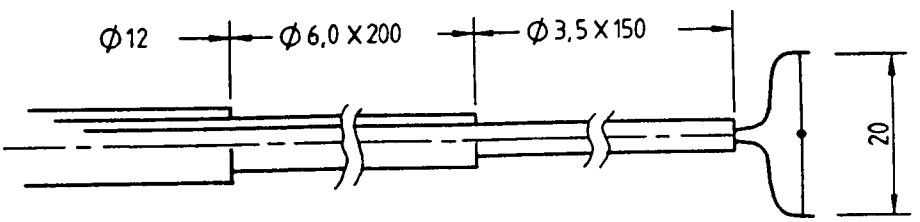

Figure 2.23 Thermocouple Probe Design

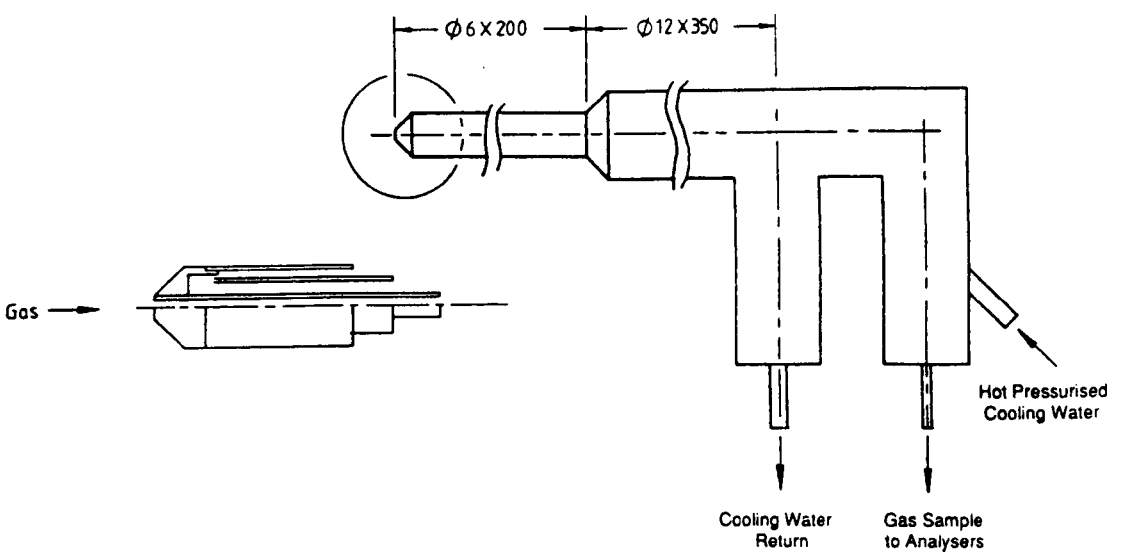

Figure 2.24 Gas Sampling Probe Design

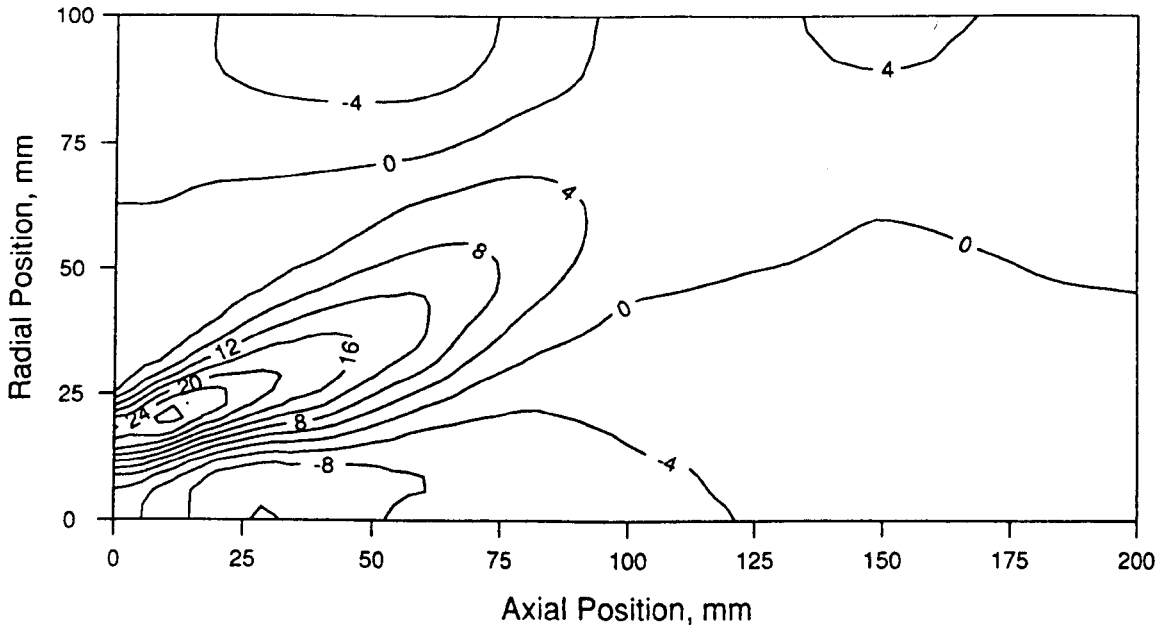

(a) Mean Velocity

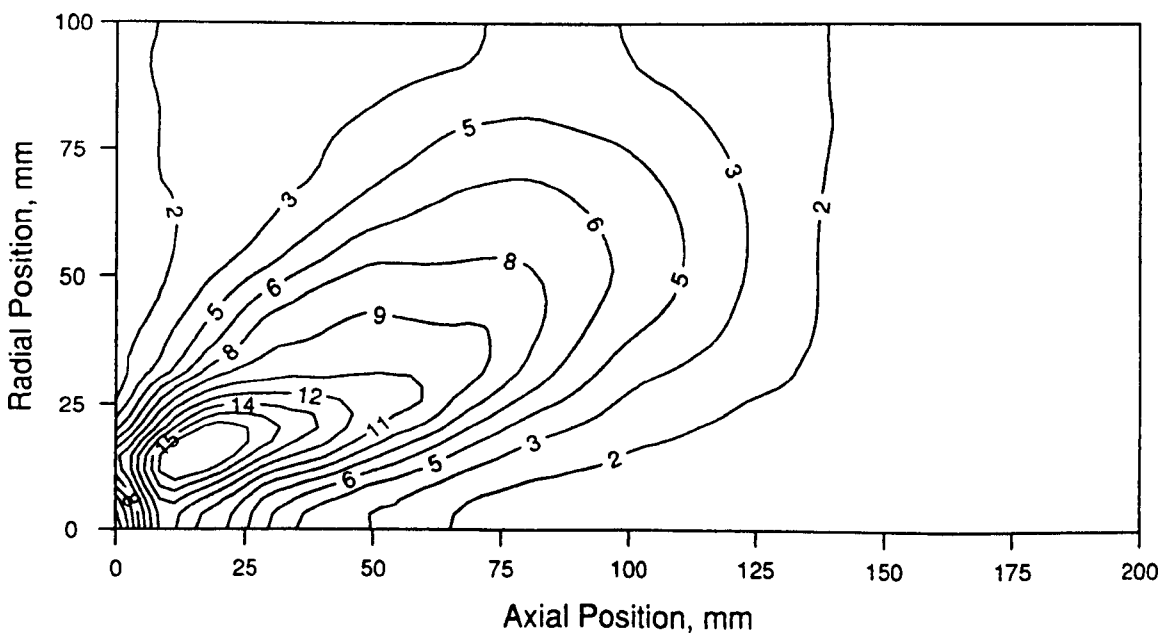

(b) RMS Velocity

Figure 2.25 Axial Velocity Contours, Cold Flow

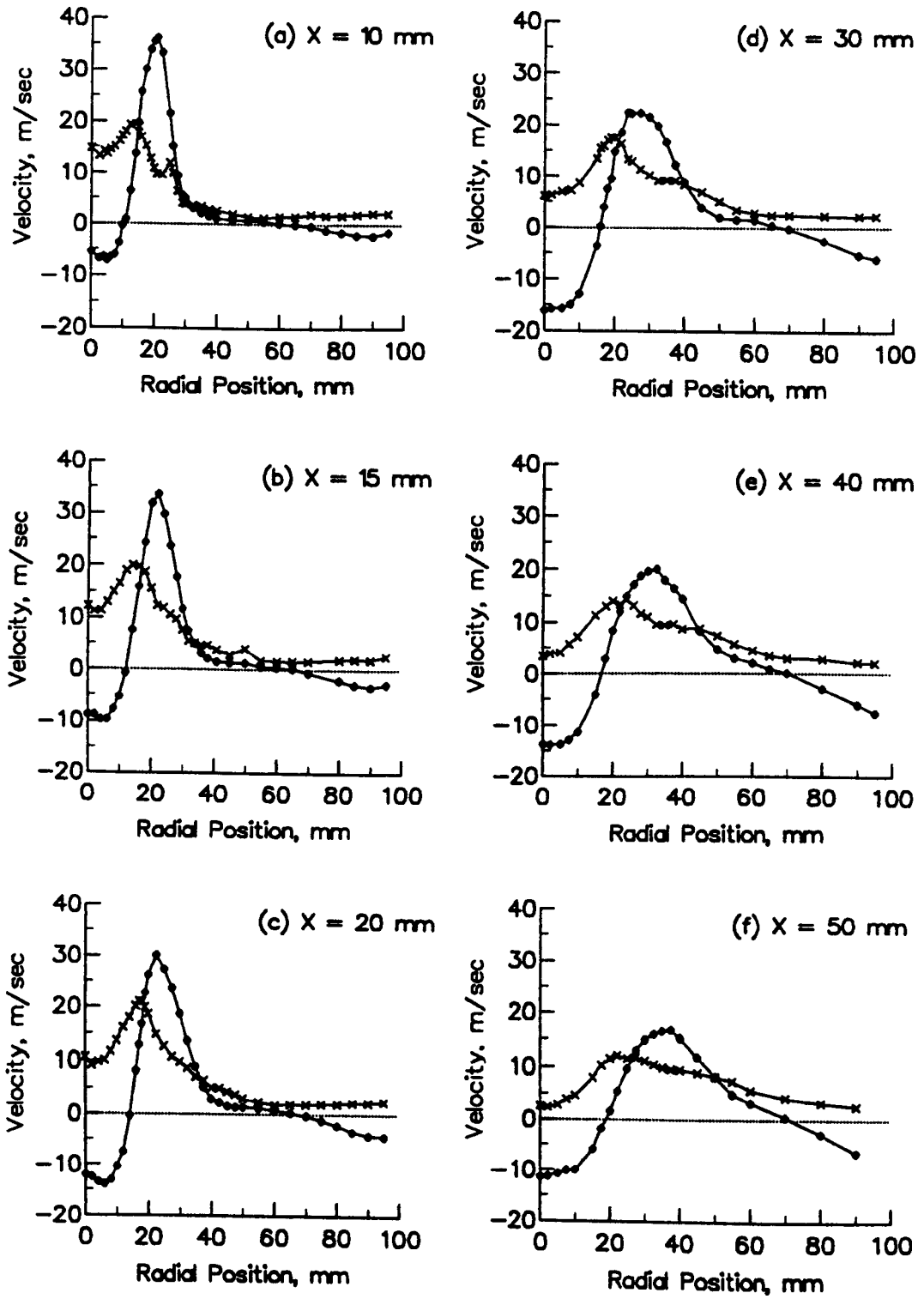

• Mean Velocity
x RMS Velocity

Figure 2.26 Axial Velocity Profiles, Cold Flow (continued)

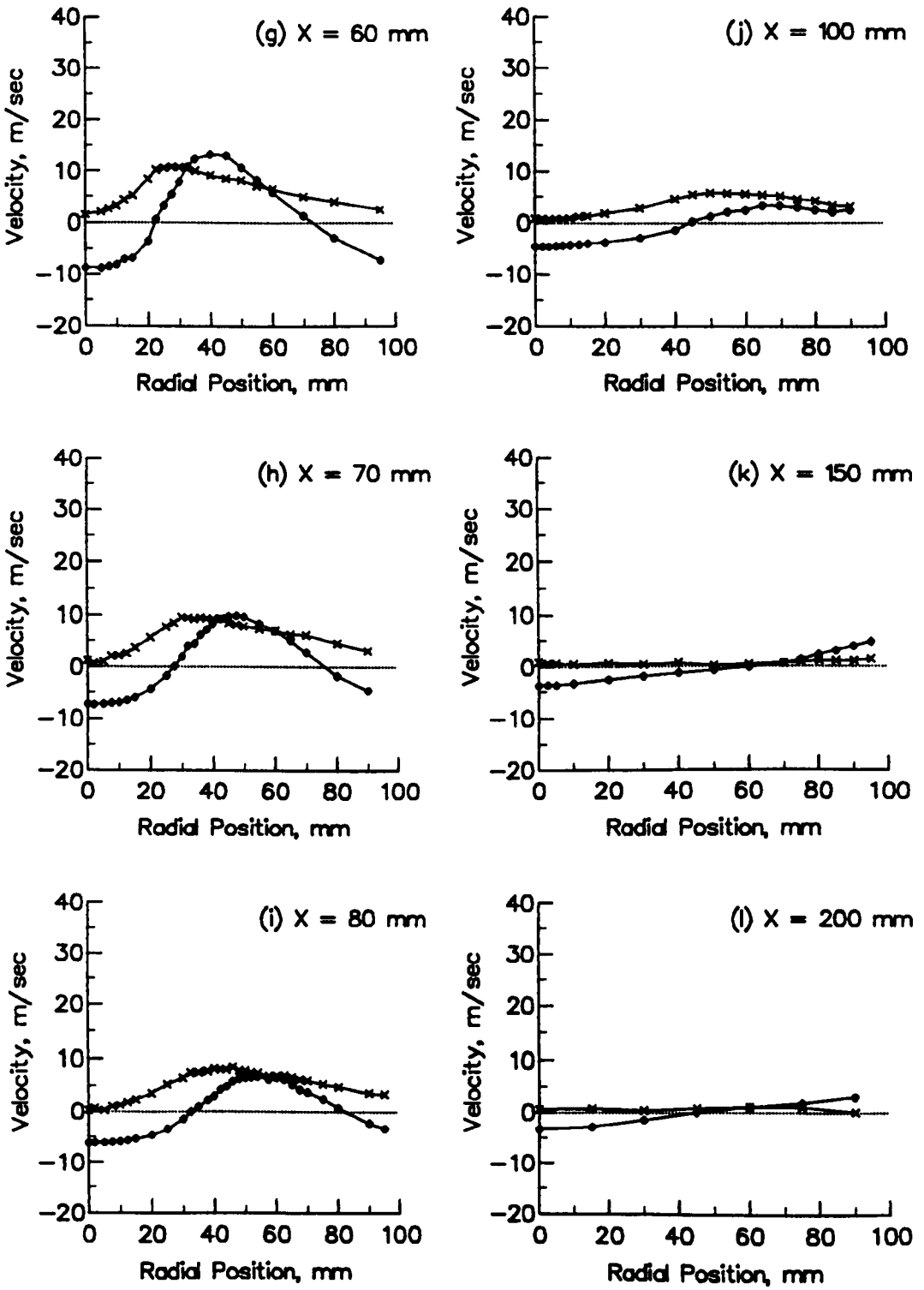

Figure 2.26 Axial Velocity Profiles, Cold Flow (complete)

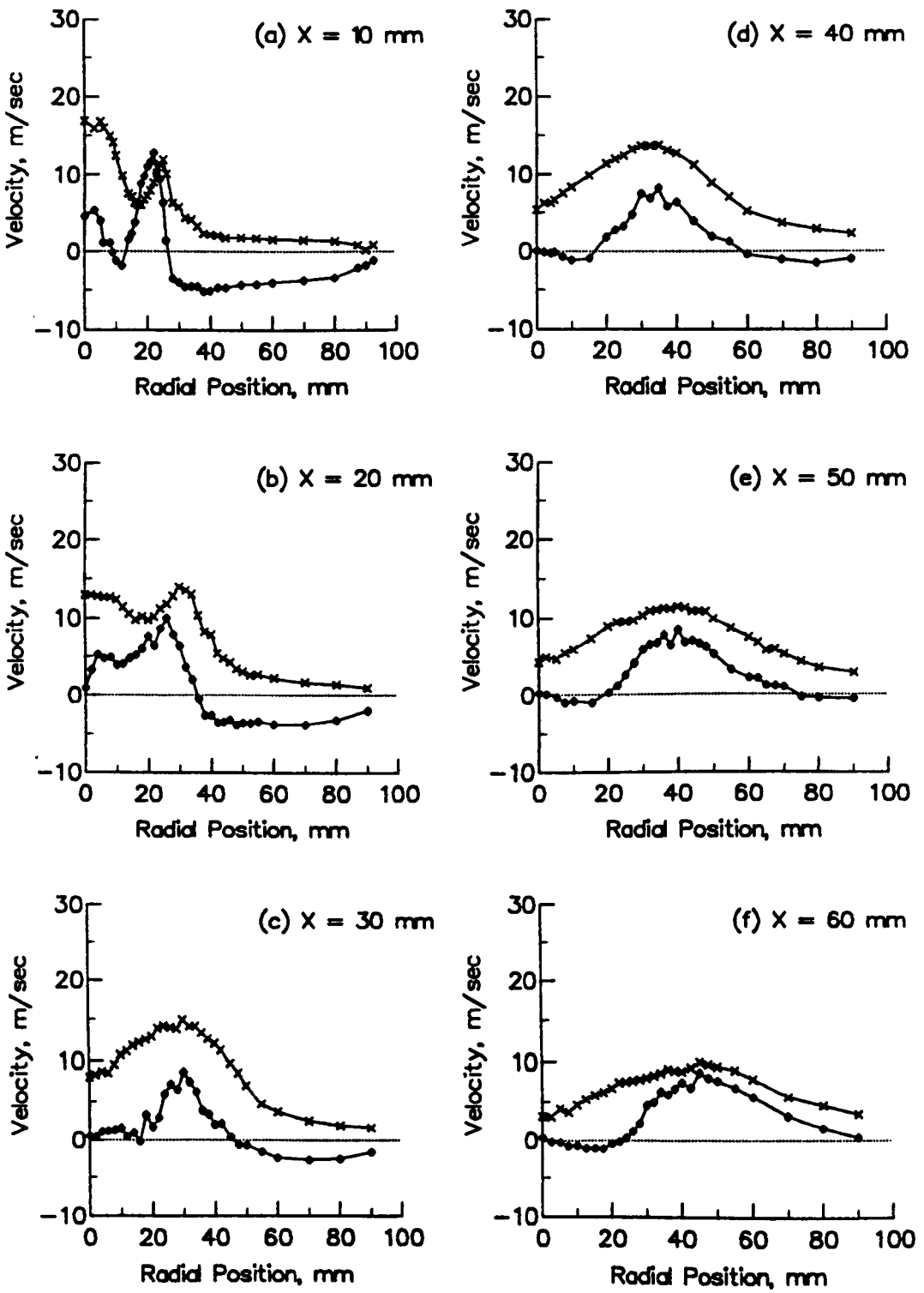

Figure 2.27 Radial Velocity Profiles, Cold Flow (continued)

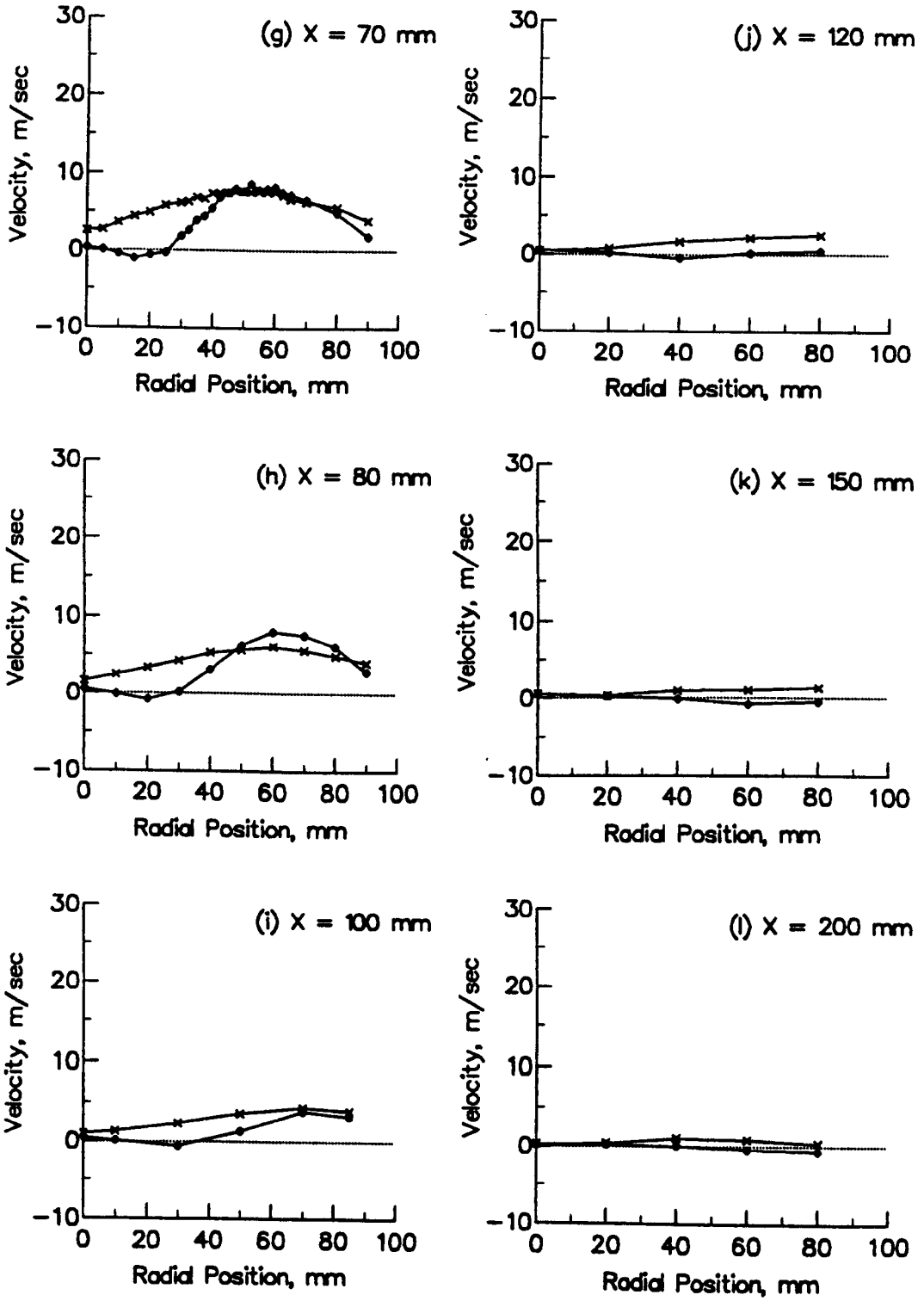

Figure 2.27 Radial Velocity Profiles, Cold Flow (complete)

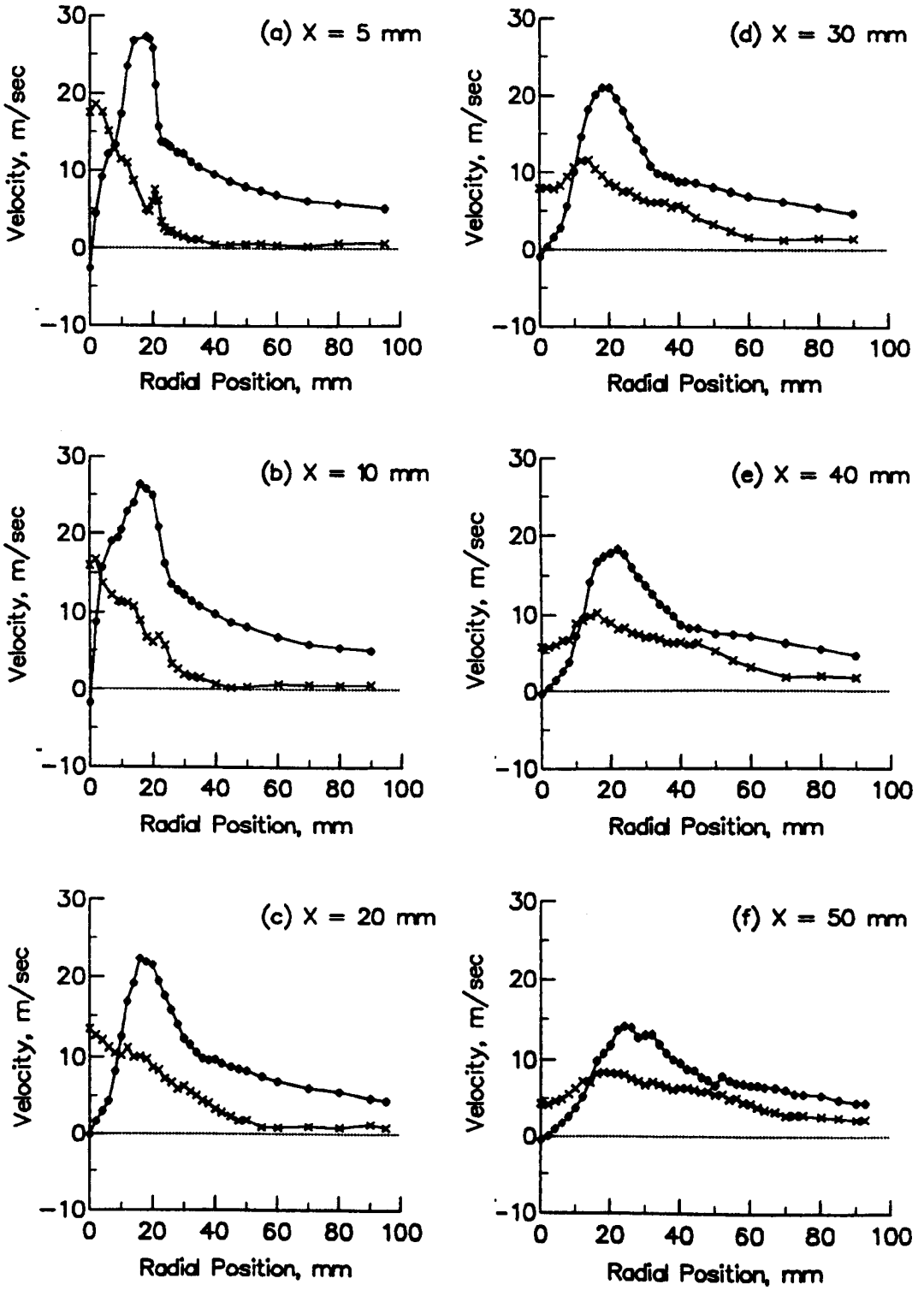

Figure 2.28 Swirl Velocity Profiles, Cold Flow (continued)

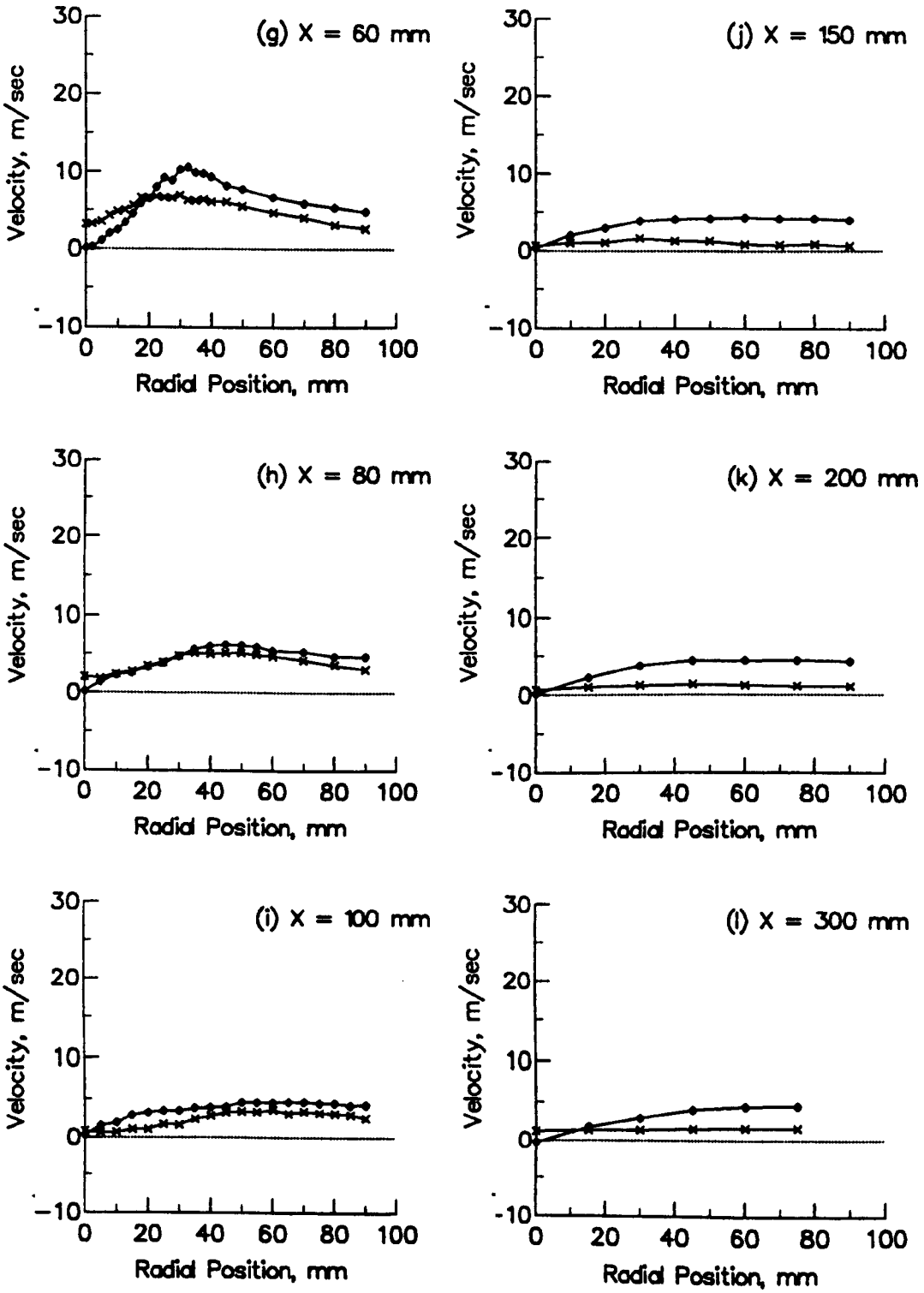

Figure 2.28 Swirl Velocity Profiles, Cold Flow (complete)

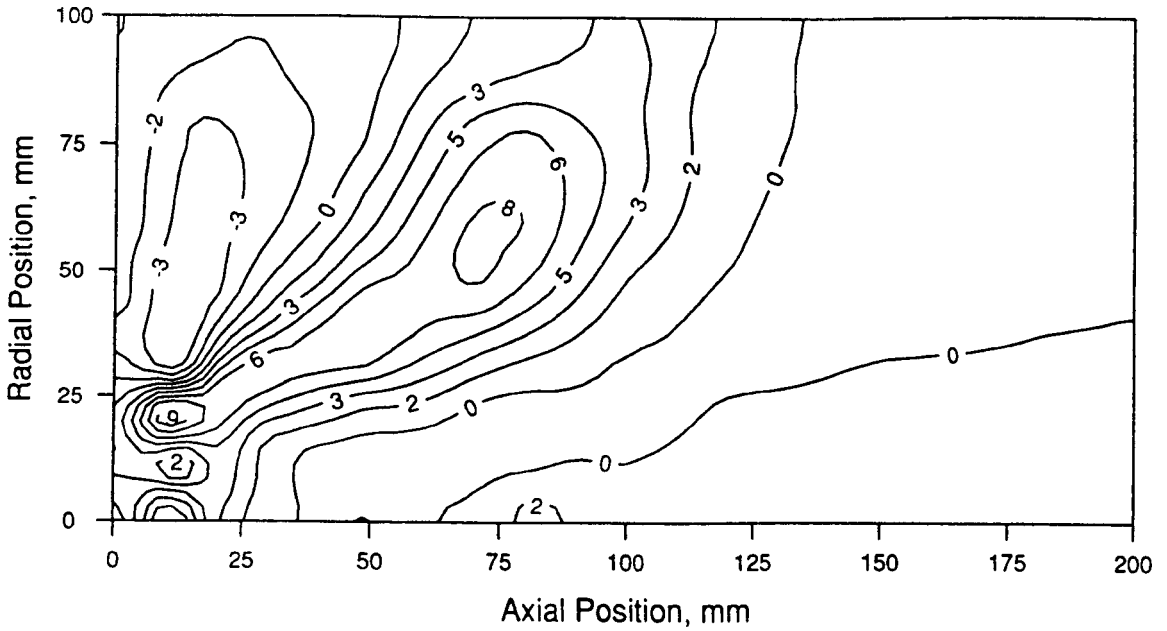

(a) Mean Velocity

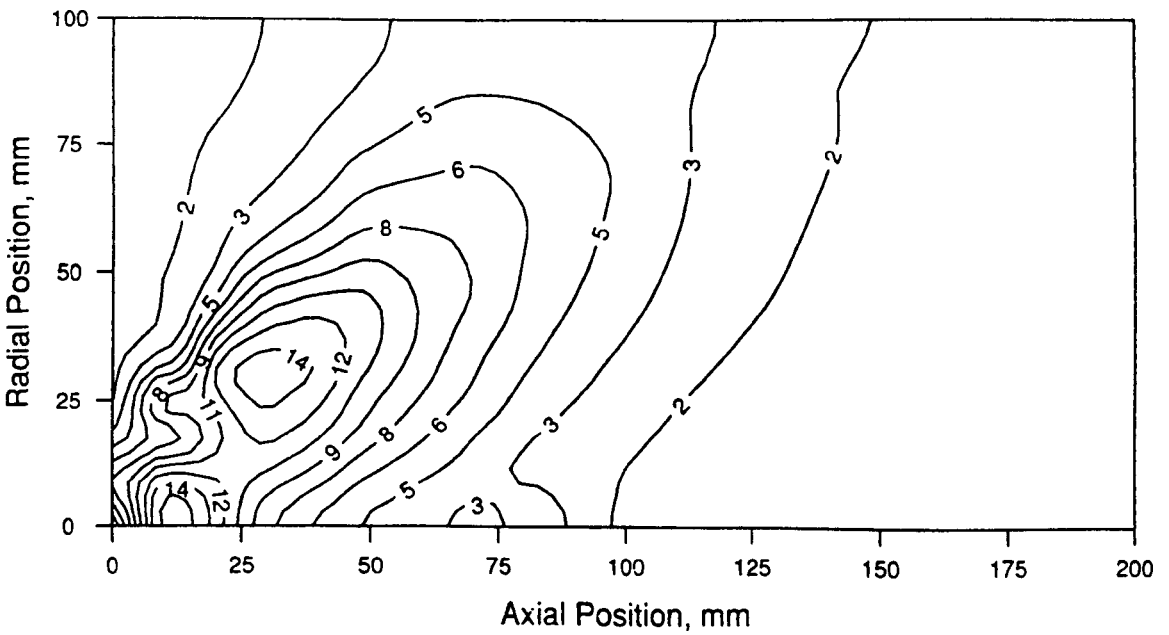

(b) RMS Velocity

Figure 2.29 Contours of Radial Velocities,Cold Flow

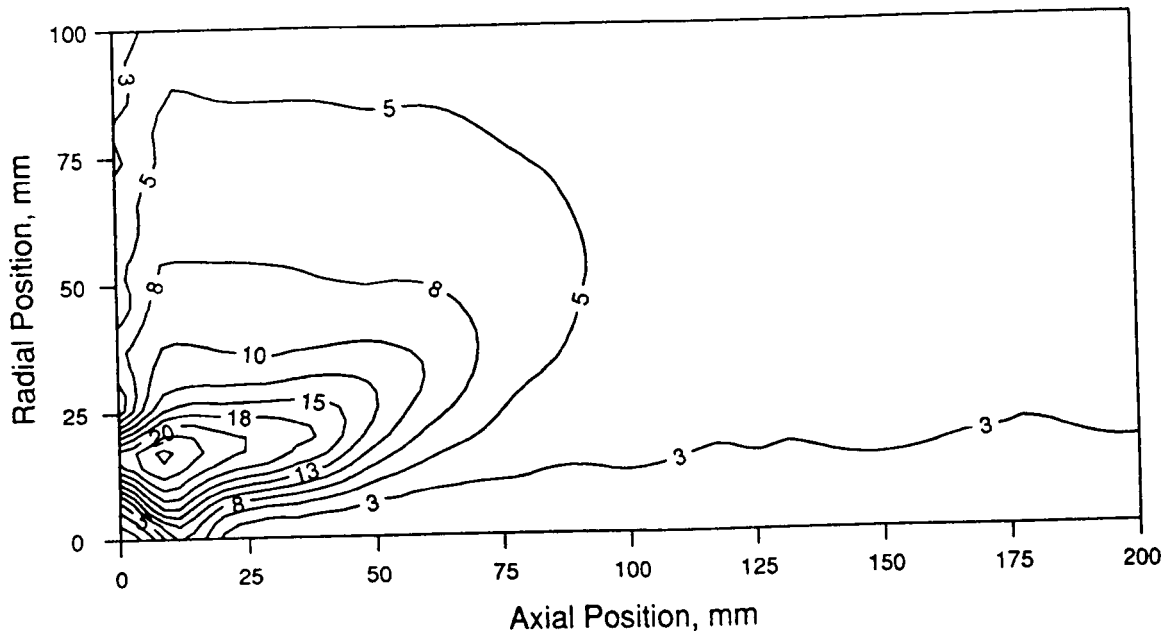

(a) Mean Velocity

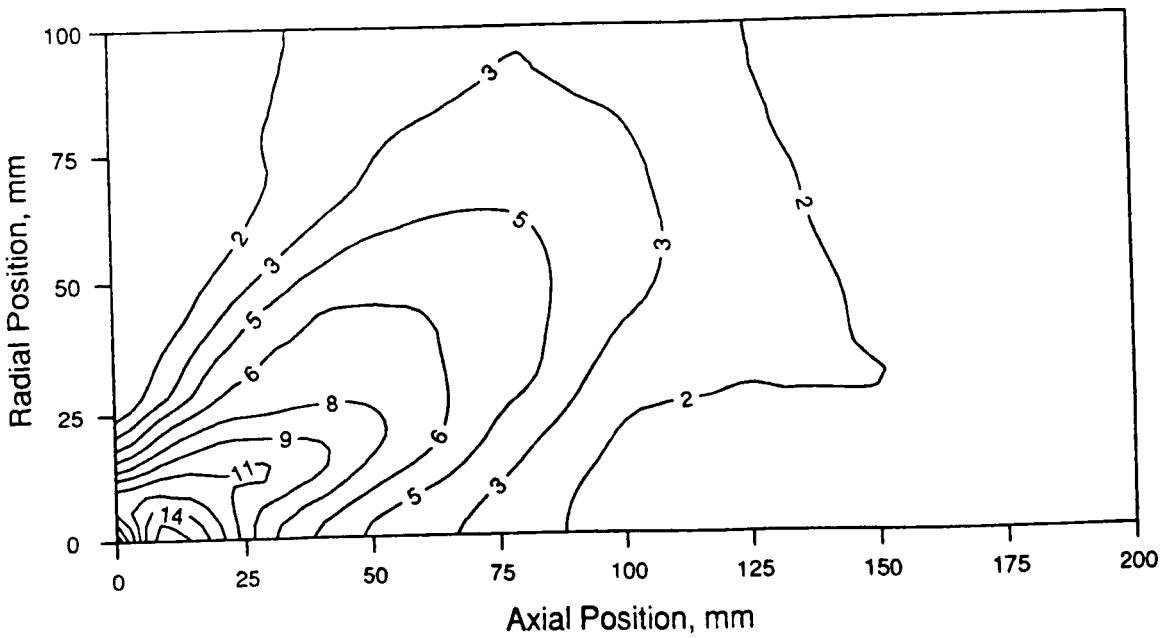

(b) RMS Velocity

Figure 2.30 Contours of Swirl Velocities,Cold Flow

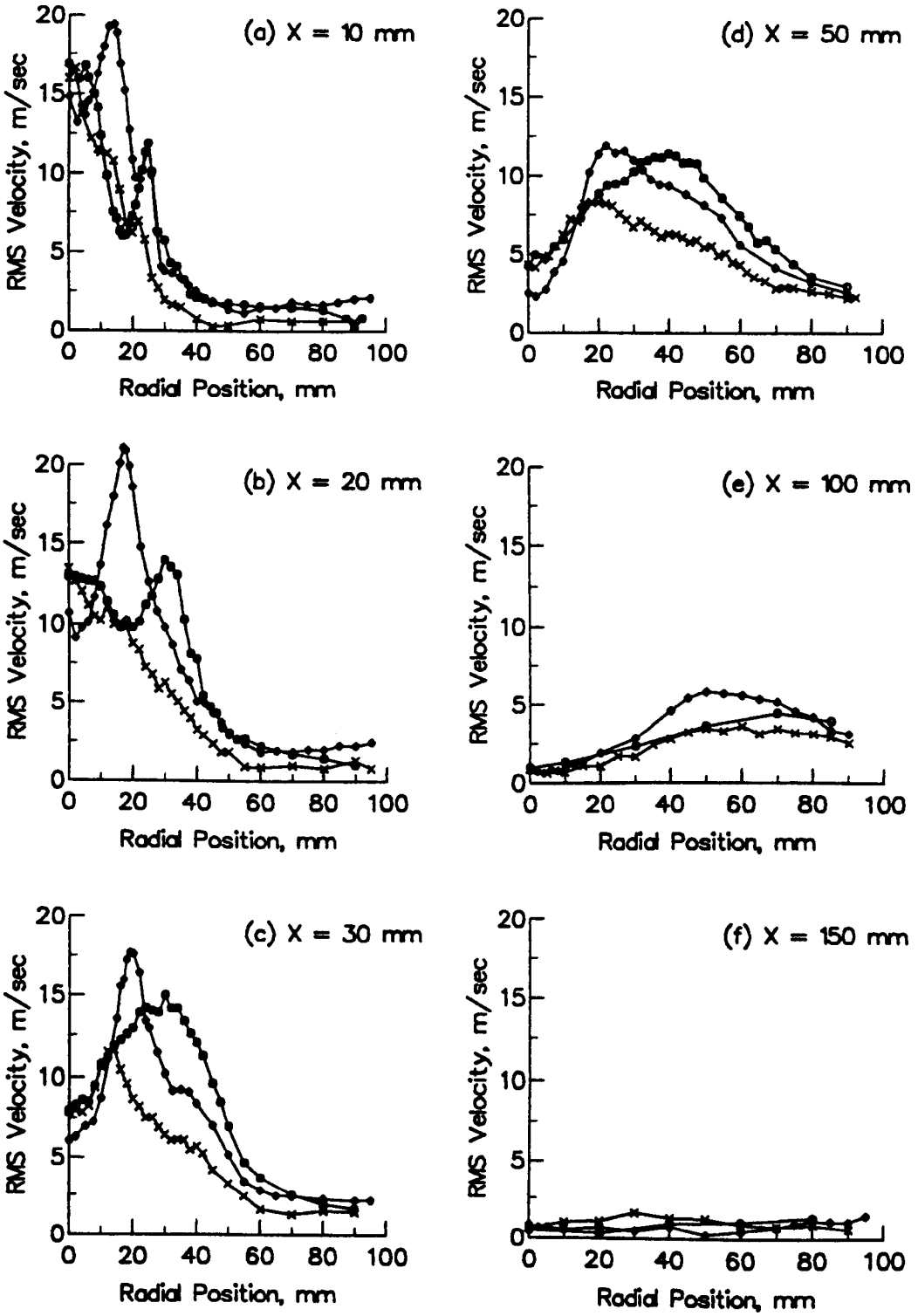

Figure 2.31 Profiles of Three RMS Velocities, Cold Flow

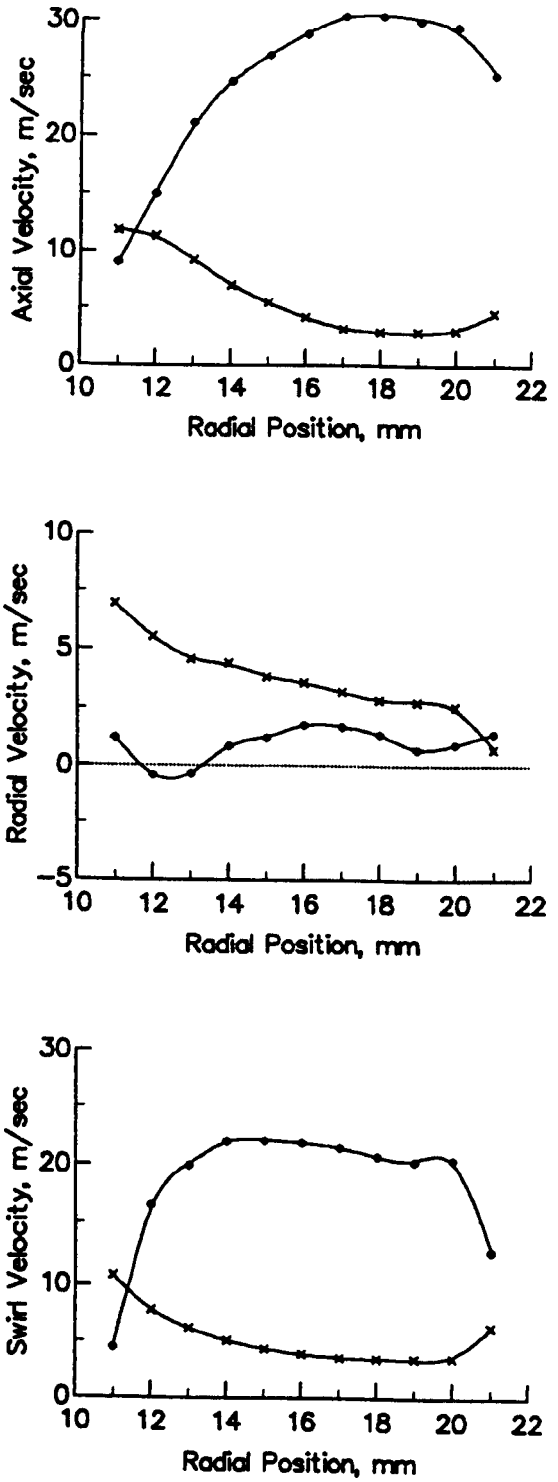

Figure 2.32 Inlet Velocity Profiles, Cold Flow

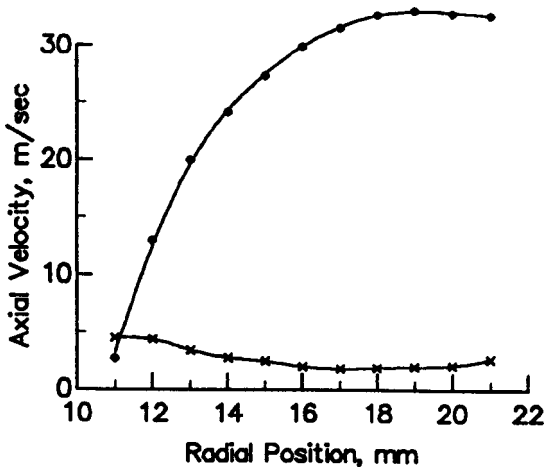

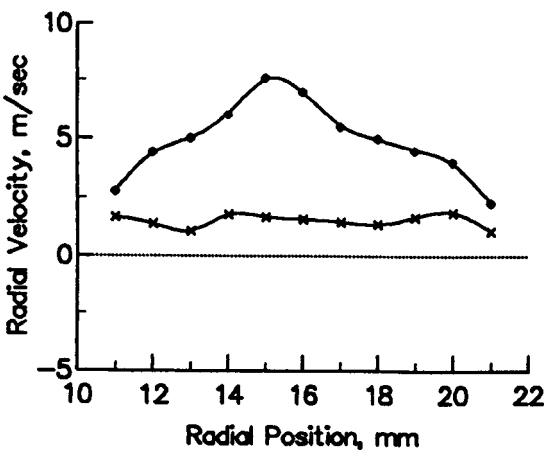

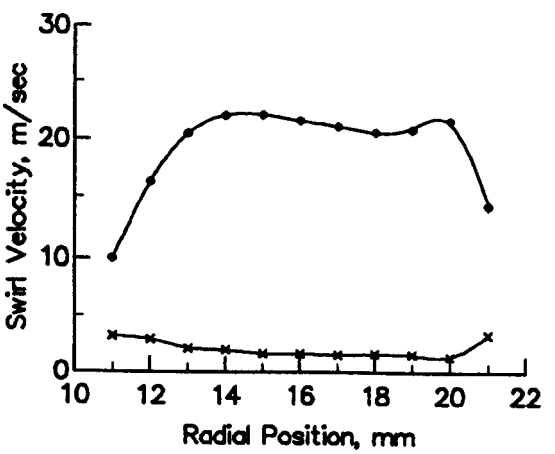

• Mean Velocity
x RMS Velocity

(a) Flame A

Figure 2.33 Inlet Velocity Profiles, Burning Flows (continued)

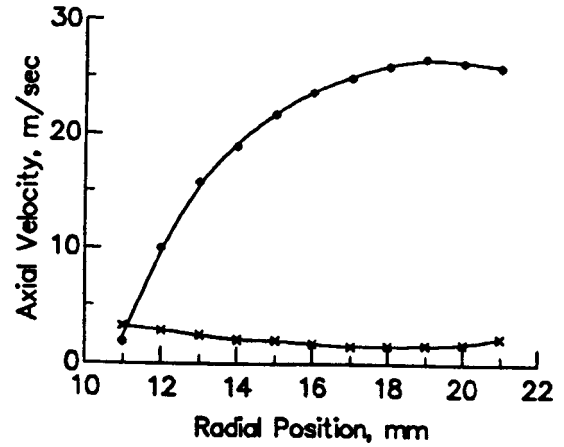

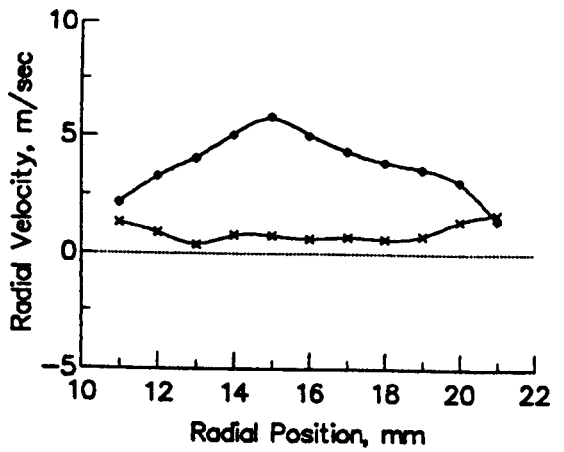

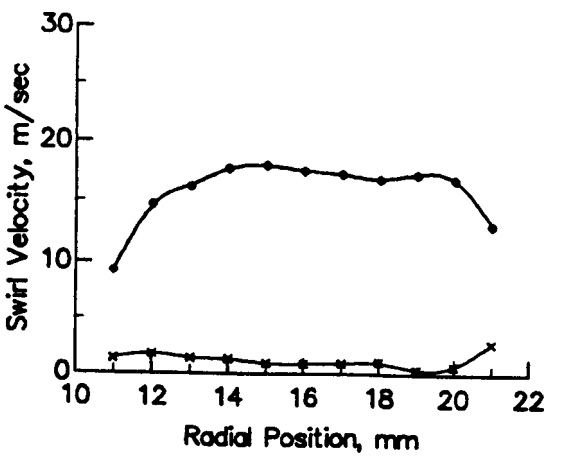

• Mean Velocity
x RMS Velocity

(b) Flame B

Figure 2.33 Inlet Velocity Profiles, Burning Flows (complete)

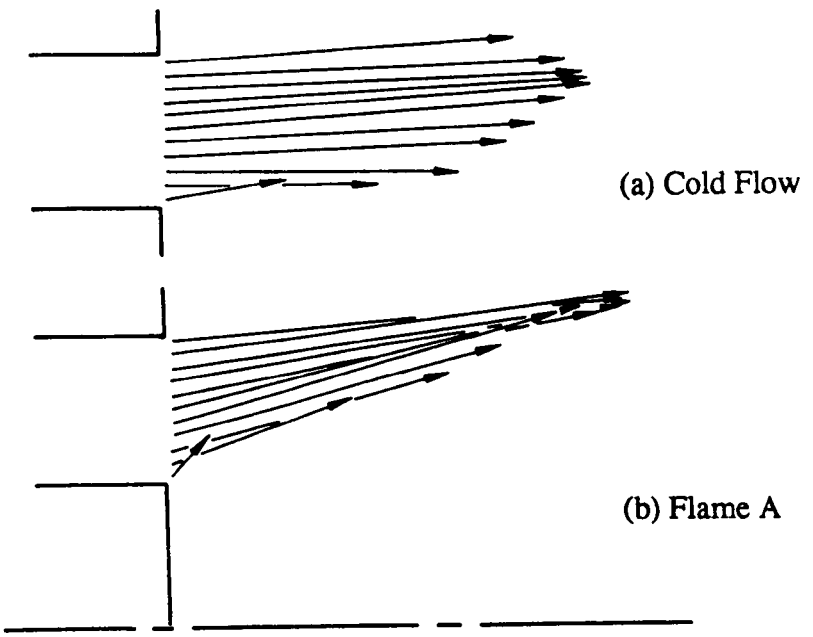

Figure 2.34 Streak Lines at the Inlet in U-V Planes

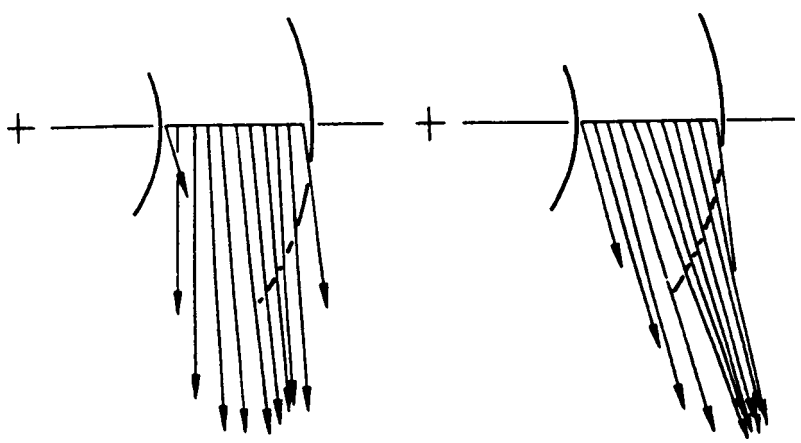

(a) Cold Flow (b) Flame A

Figure 2.35 Streak Lines at the Inlet in U-W Planes

(a) Without Seeding

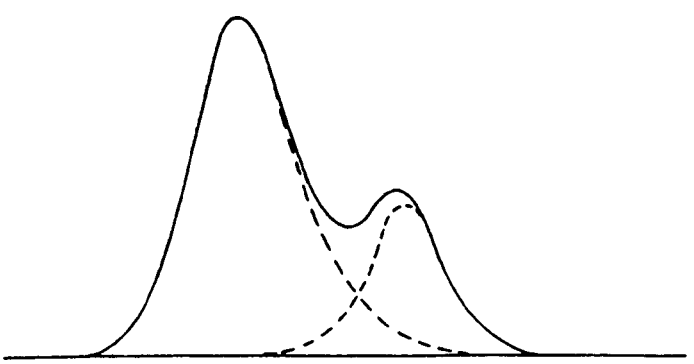

(b) With Seeding

Figure 2.36 Velocity PDF's of Two-Phase Flow

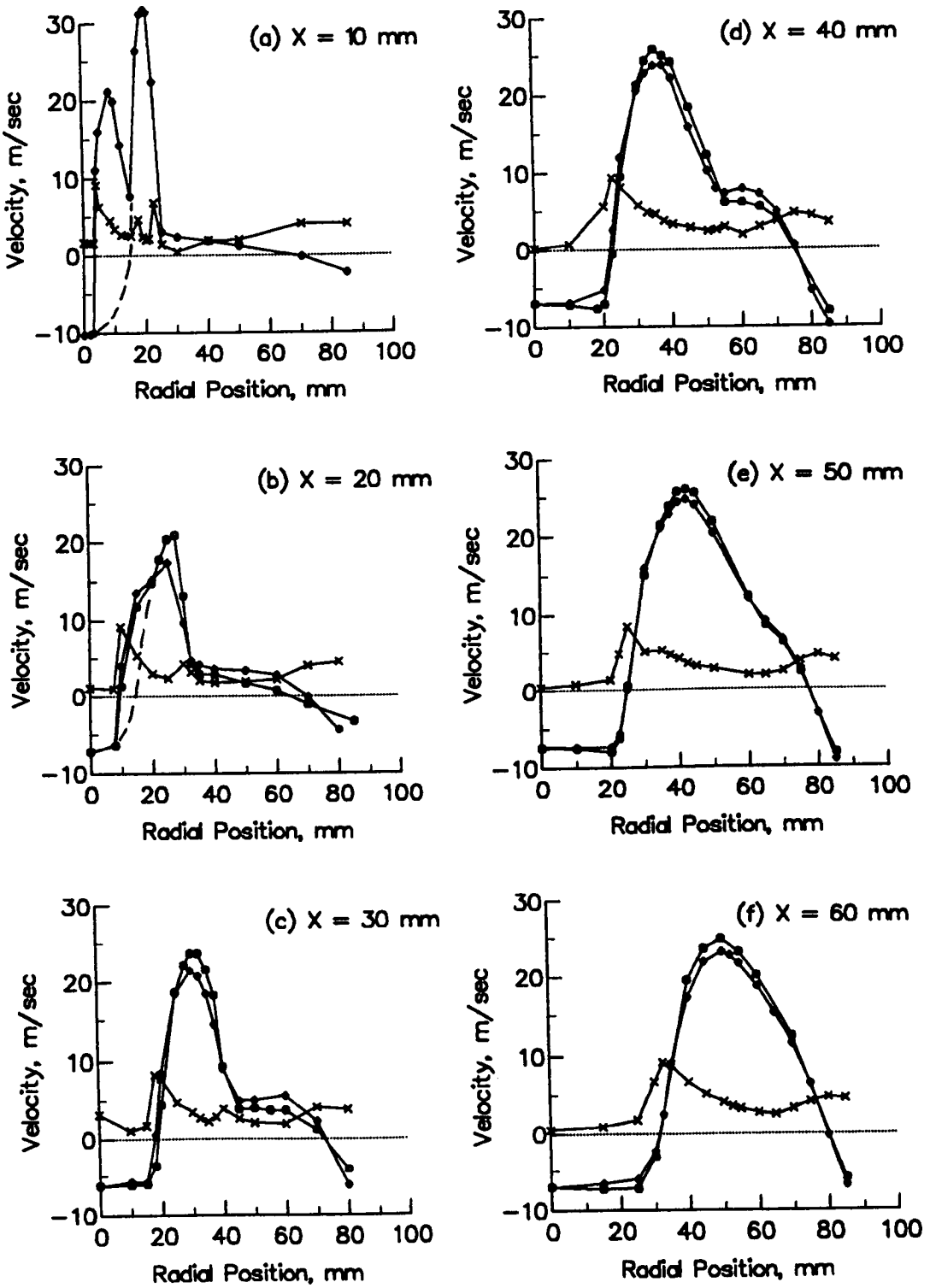

• Mean Velocity, Right Wing
o Mean Velocity, Left Wing
x RMS Velocity

Figure 2.37..Axial Velocity Profiles, Flame A (continued)

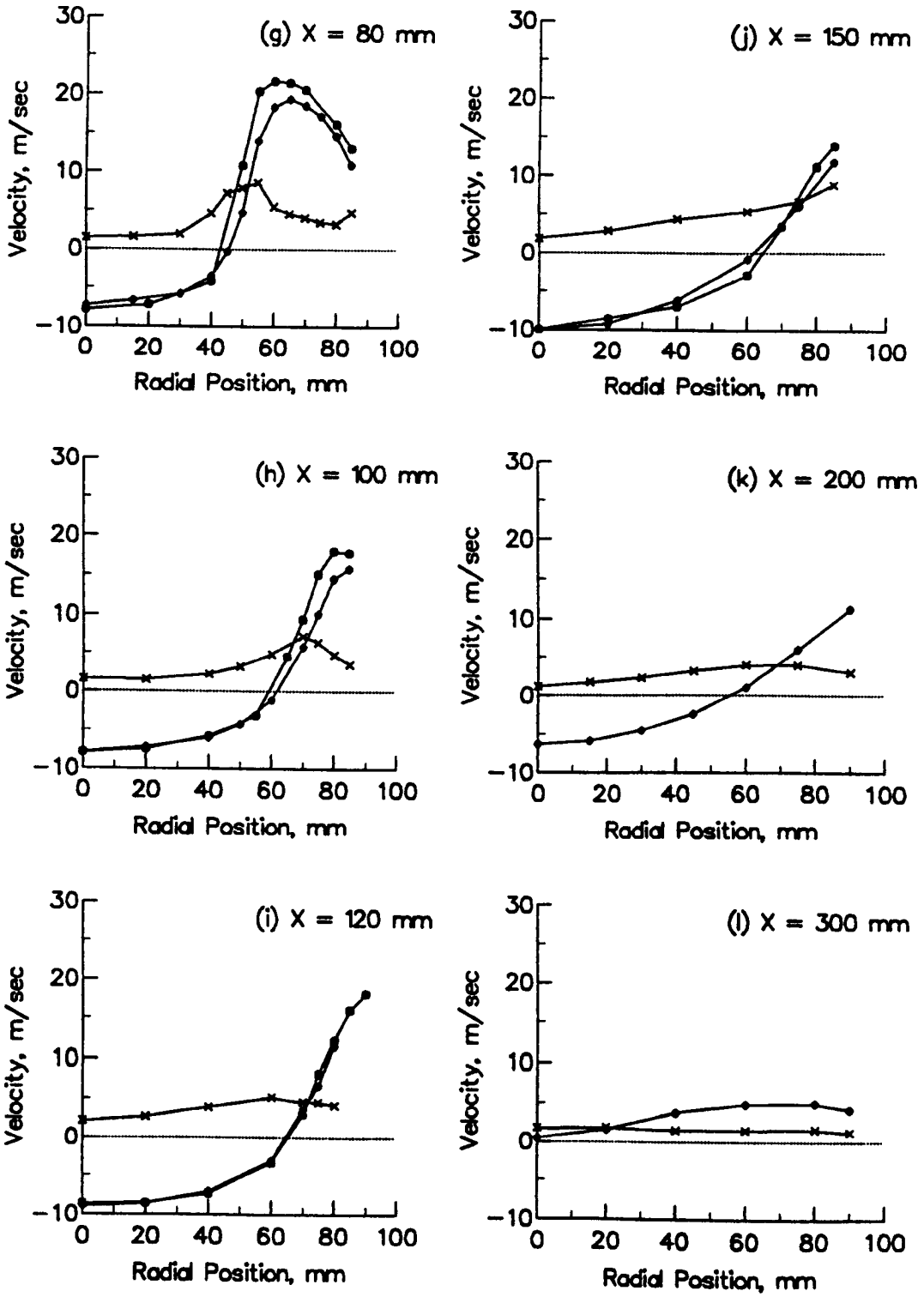

Figure 2.37..Axial Velocity Profiles, Flame A (complete)

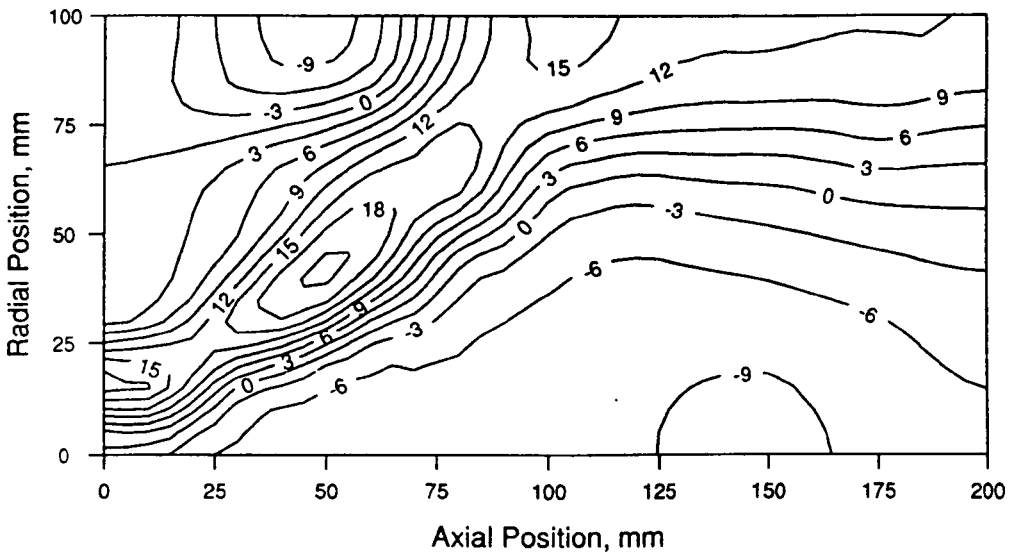

(a) Mean Velocity

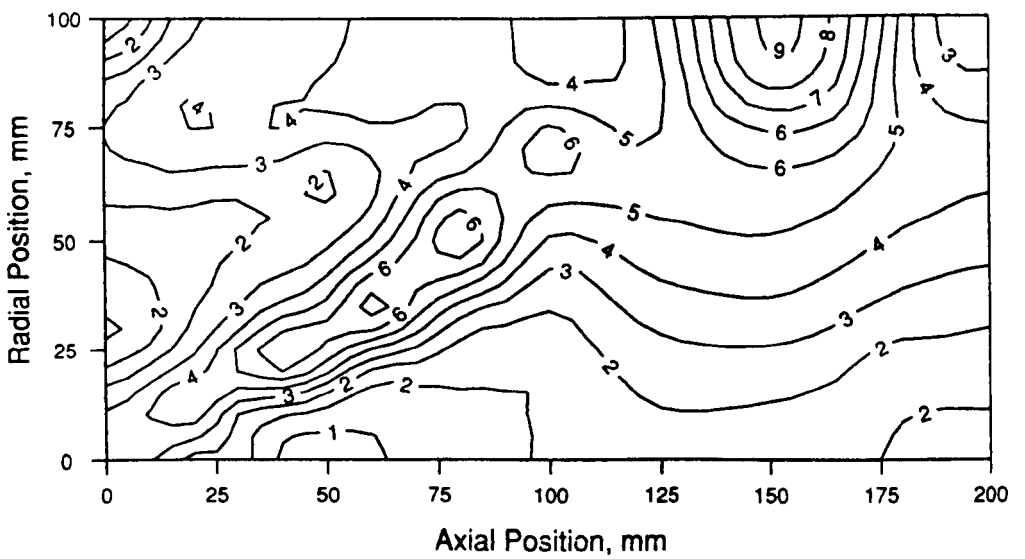

(b) RMS Velocity

Figure 2.38..Contours of Axial Velocity, Flame A

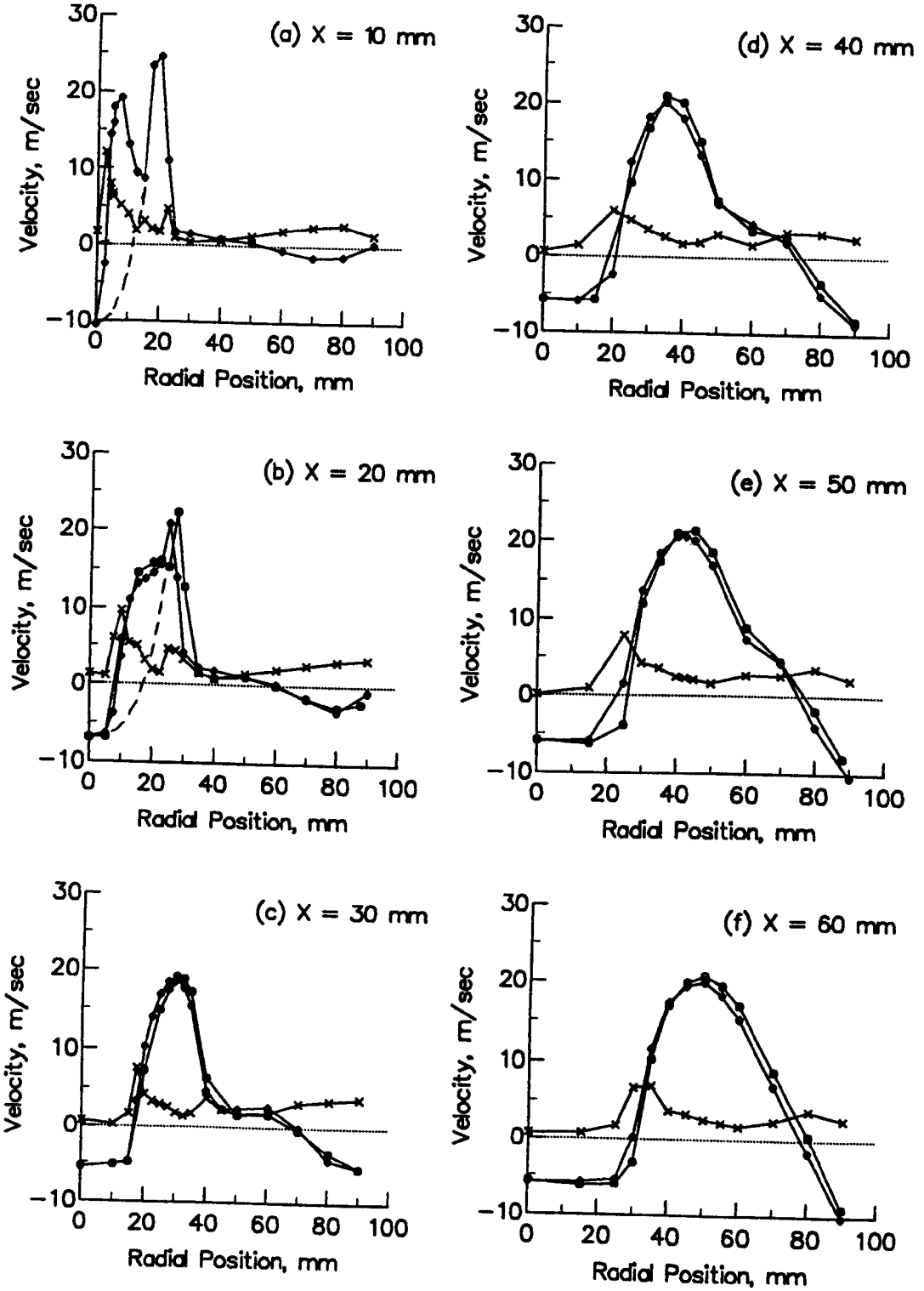

• Mean Velocity, Right Wing
o Mean Velocity, Left Wing
x RMS Velocity

Figure 2.39..Axial Velocity Profiles, Flame B (continued)

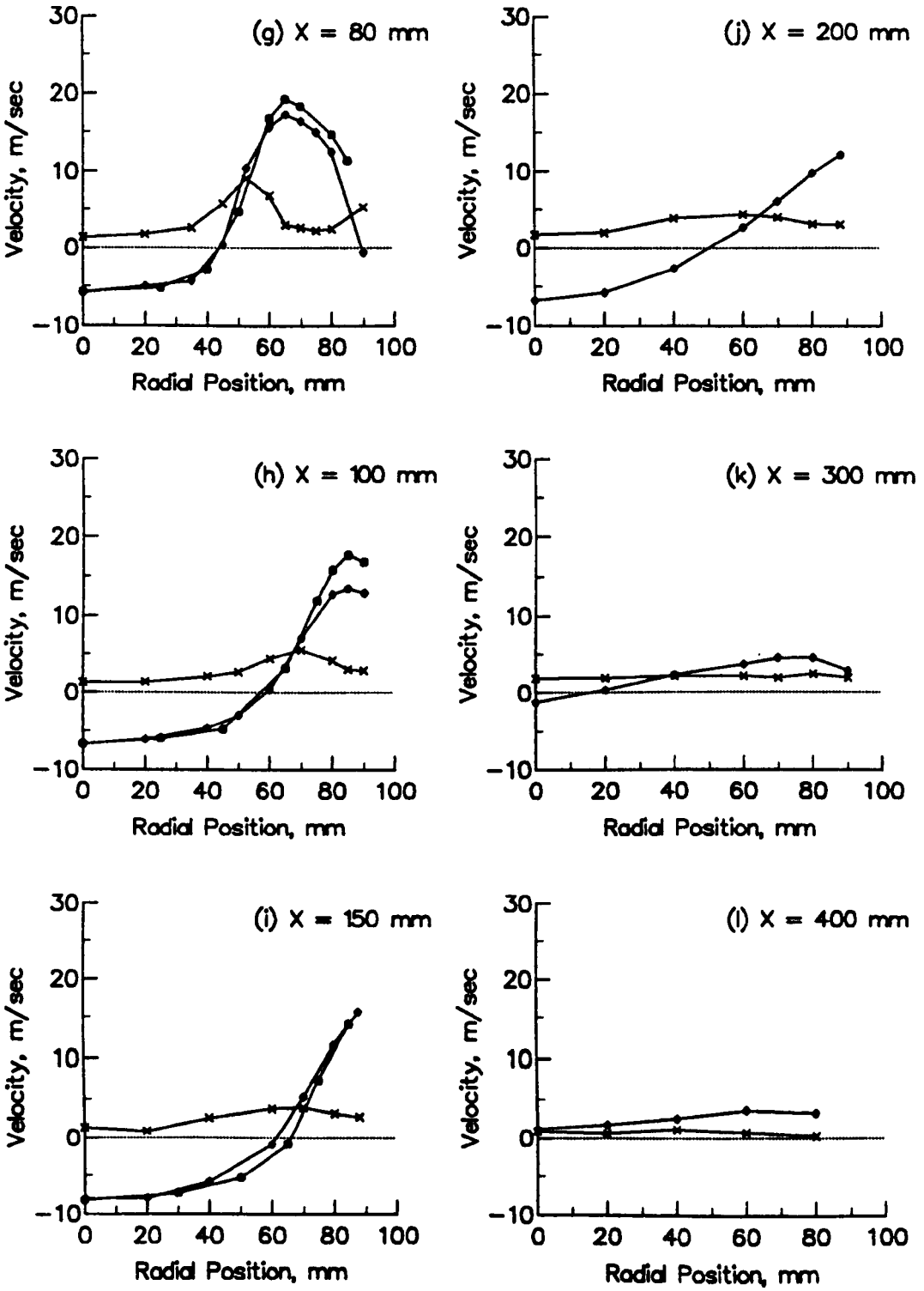

• Mean Velocity, Right Wing
o Mean Velocity, Left Wing
x RMS Velocity

Figure 2.39..Axial Velocity Profiles, Flame B (complete)

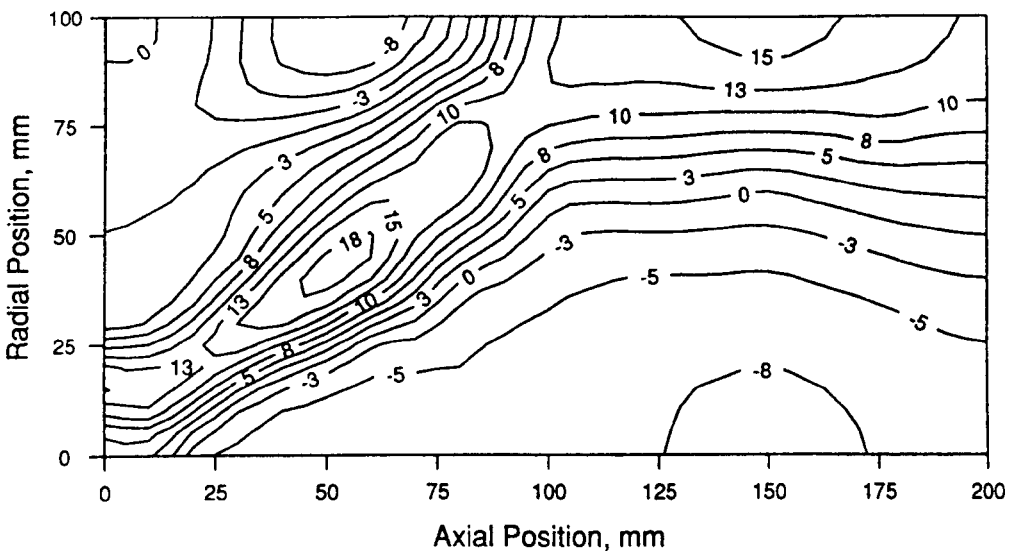

(a) Mean Velocity

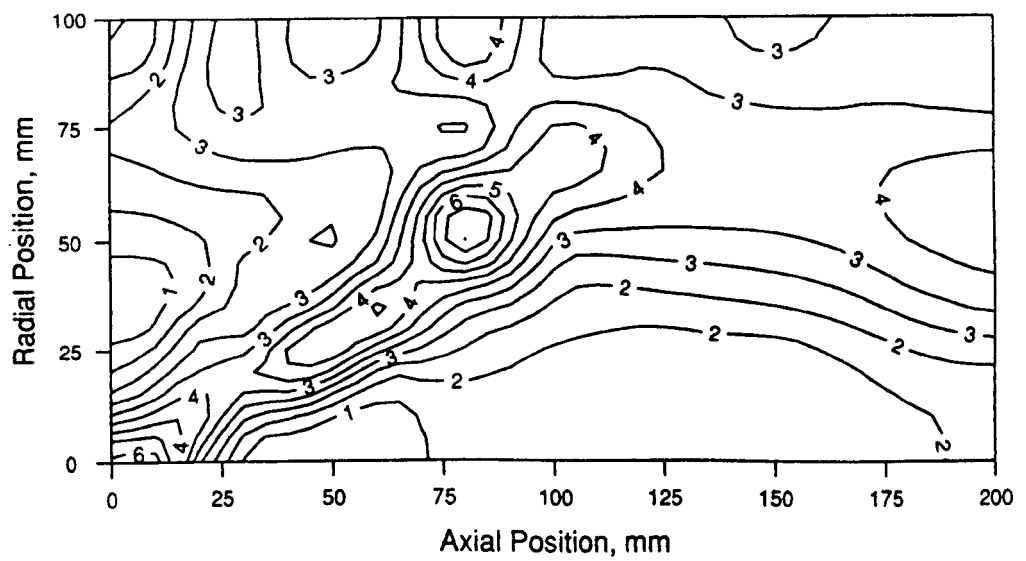

(b) RMS Velocity

Figure 2.40..Contours of Axial Velocity, Flame B

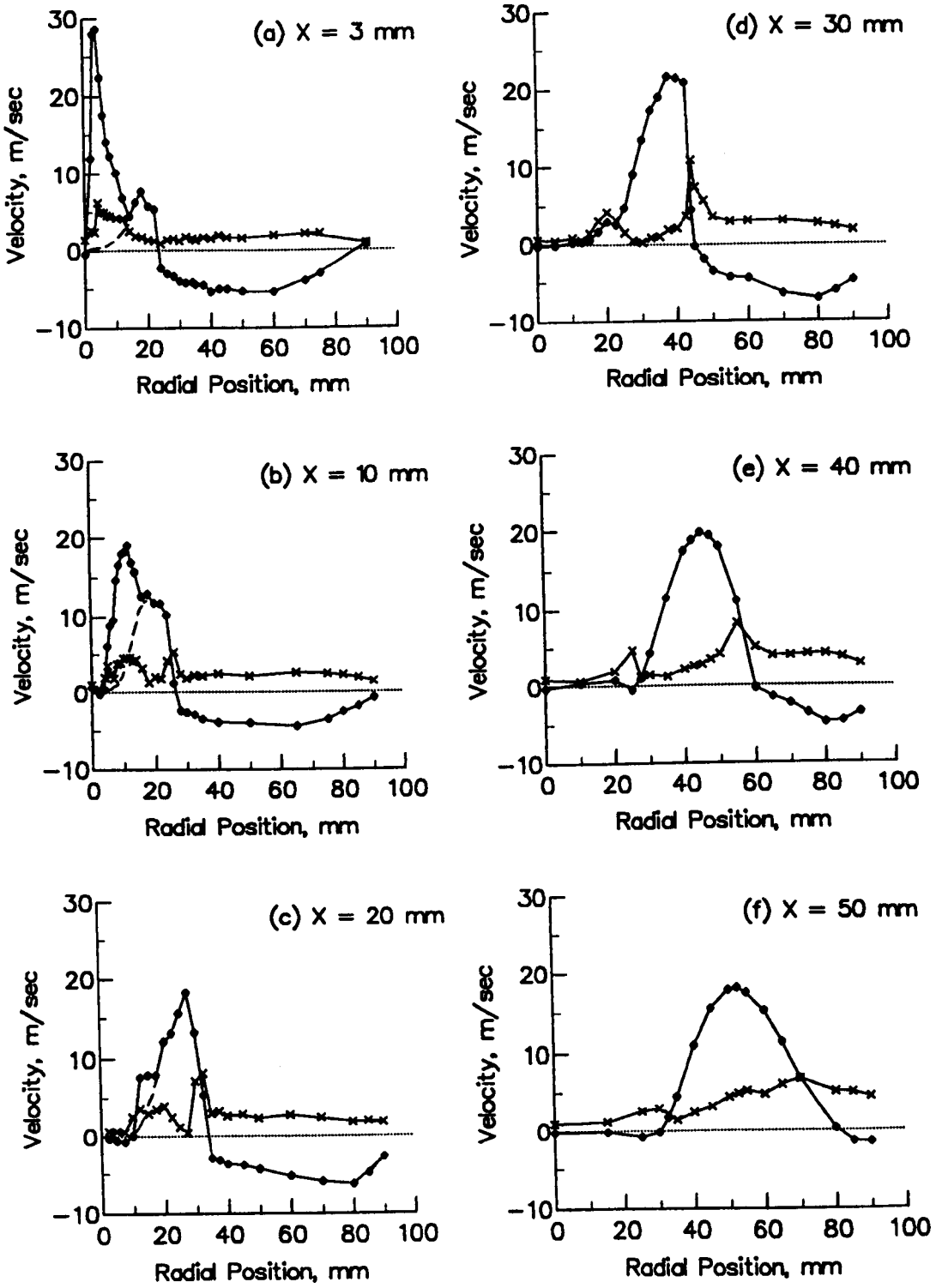

• Mean Velocity
x RMS Velocity

Figure 2.41..Radial Velocity Profiles, Flame A (continued)

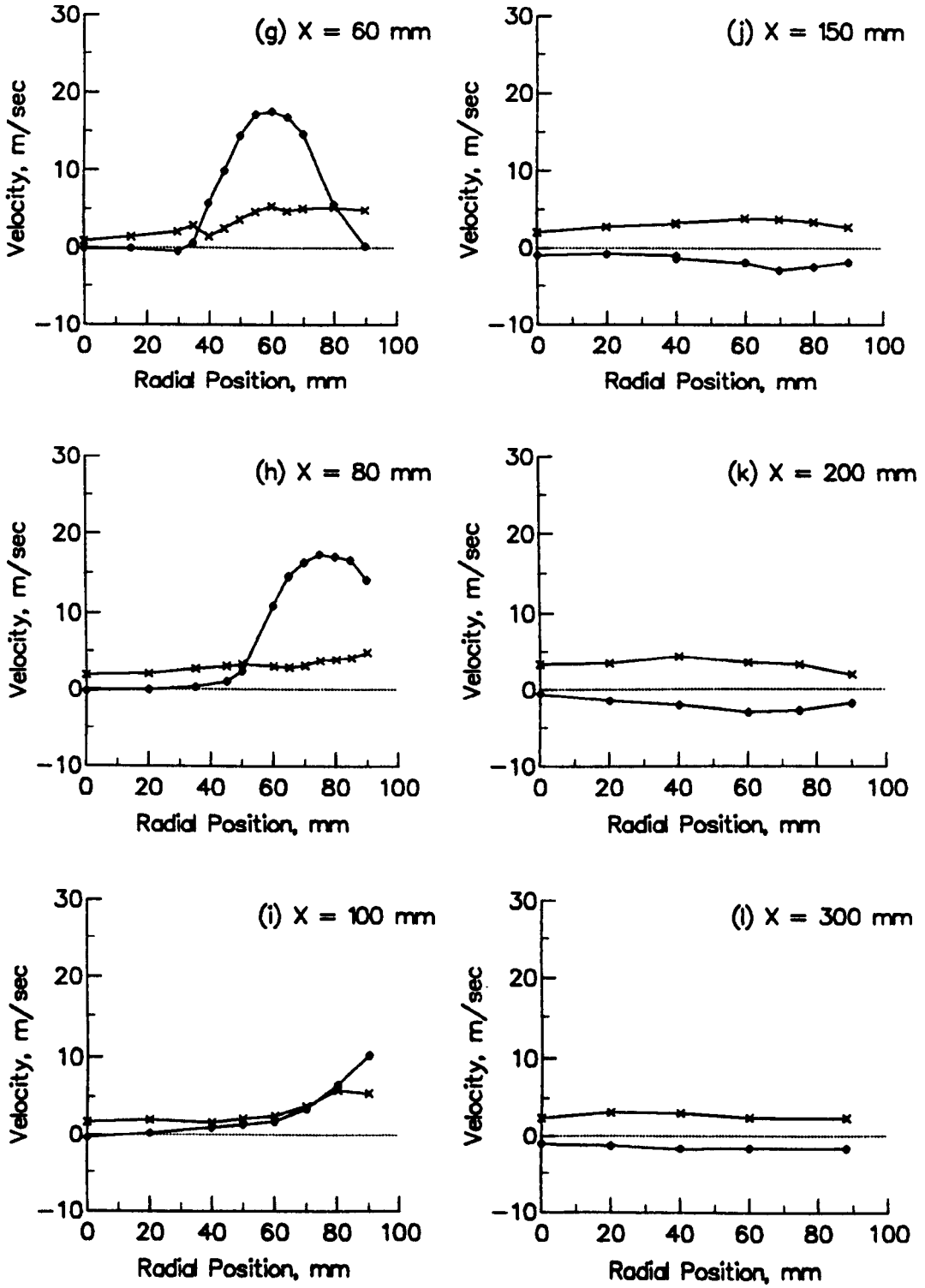

Figure 2.41..Radial Velocity Profiles, Flame A (complete)

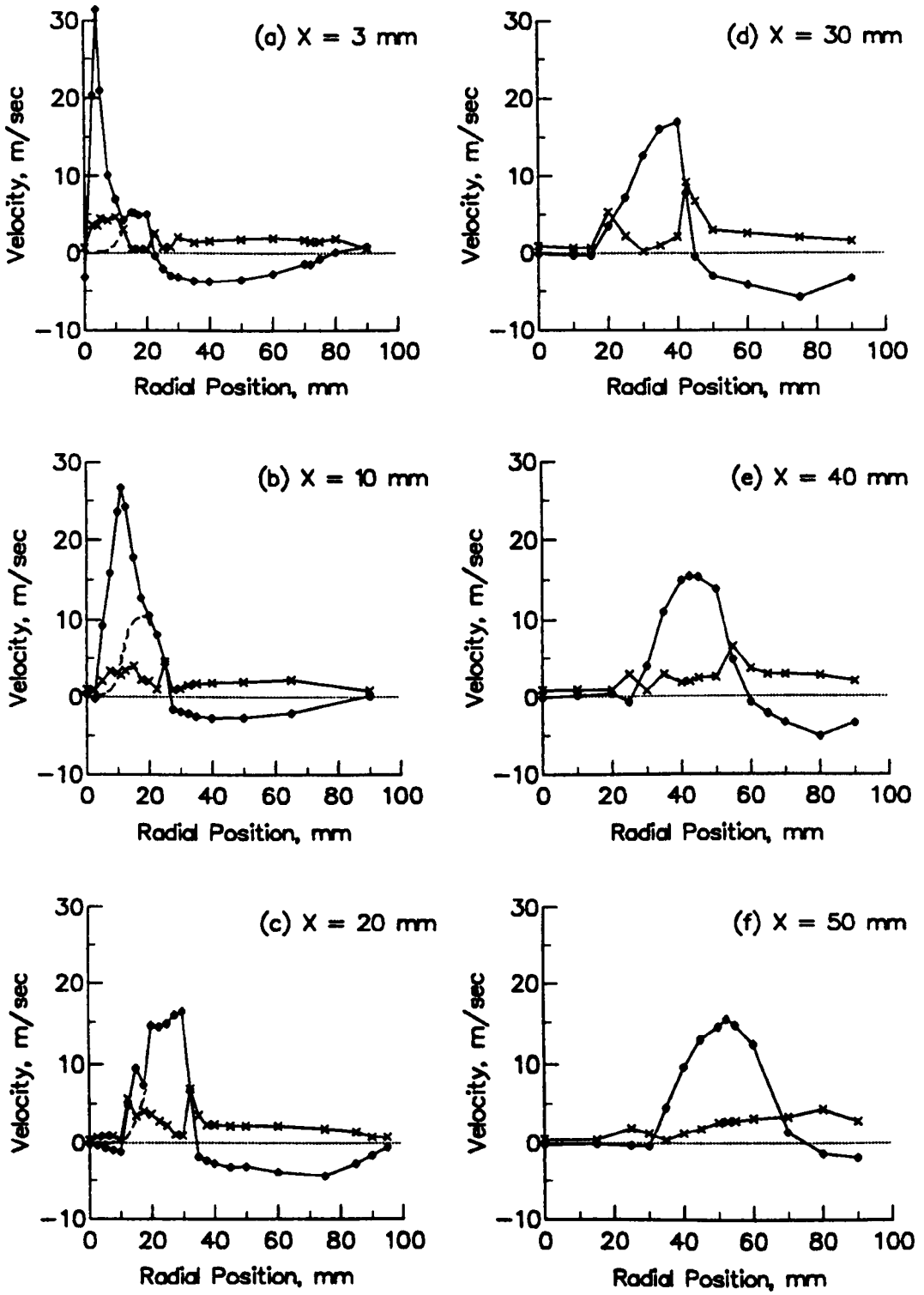

Figure 2.42..Radial Velocity Profiles, Flame B (continued)

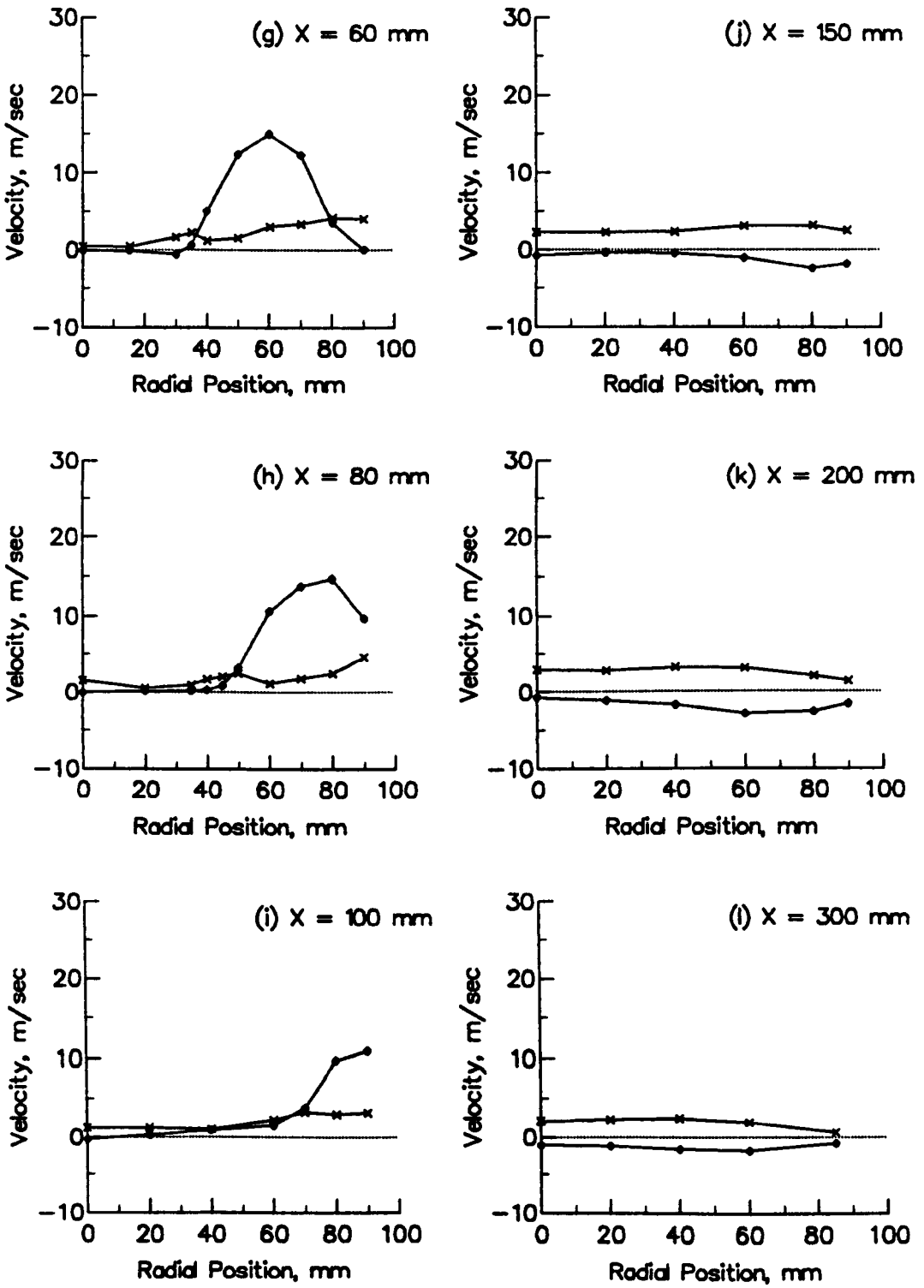

Figure 2.42..Radial Velocity Profiles, Flame B (complete)

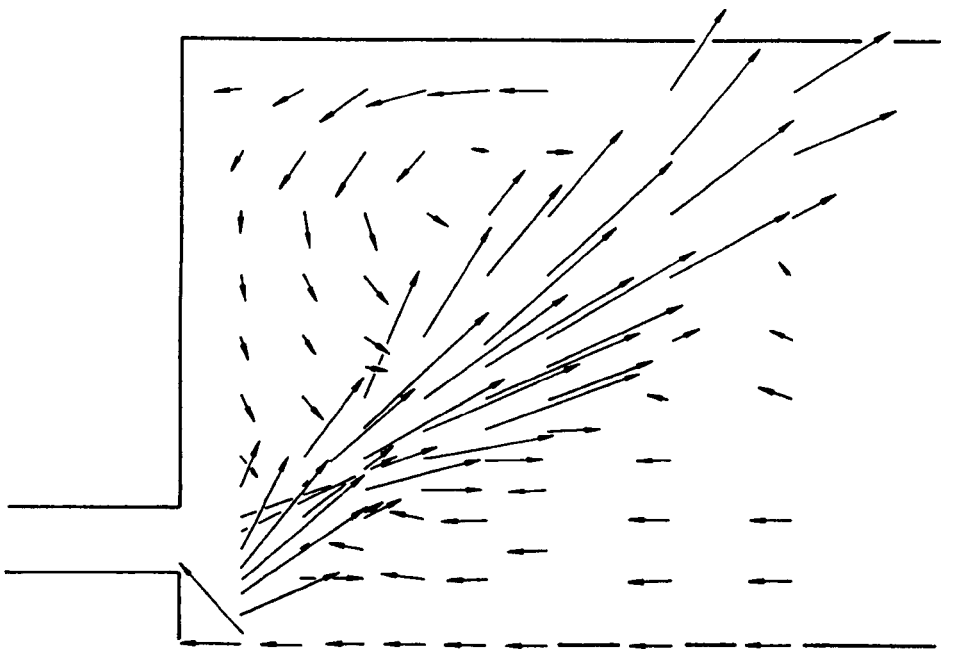

Figure 2.43..Streak Lines in U-V Plane, Flame A

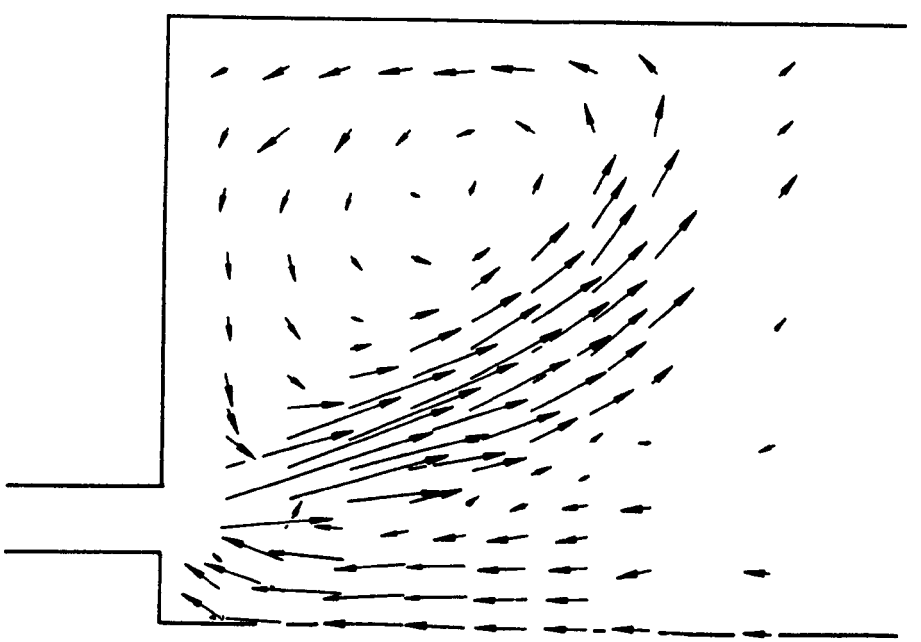

Figure 2.44..Streak Lines in U-V Plane, Cold Flow

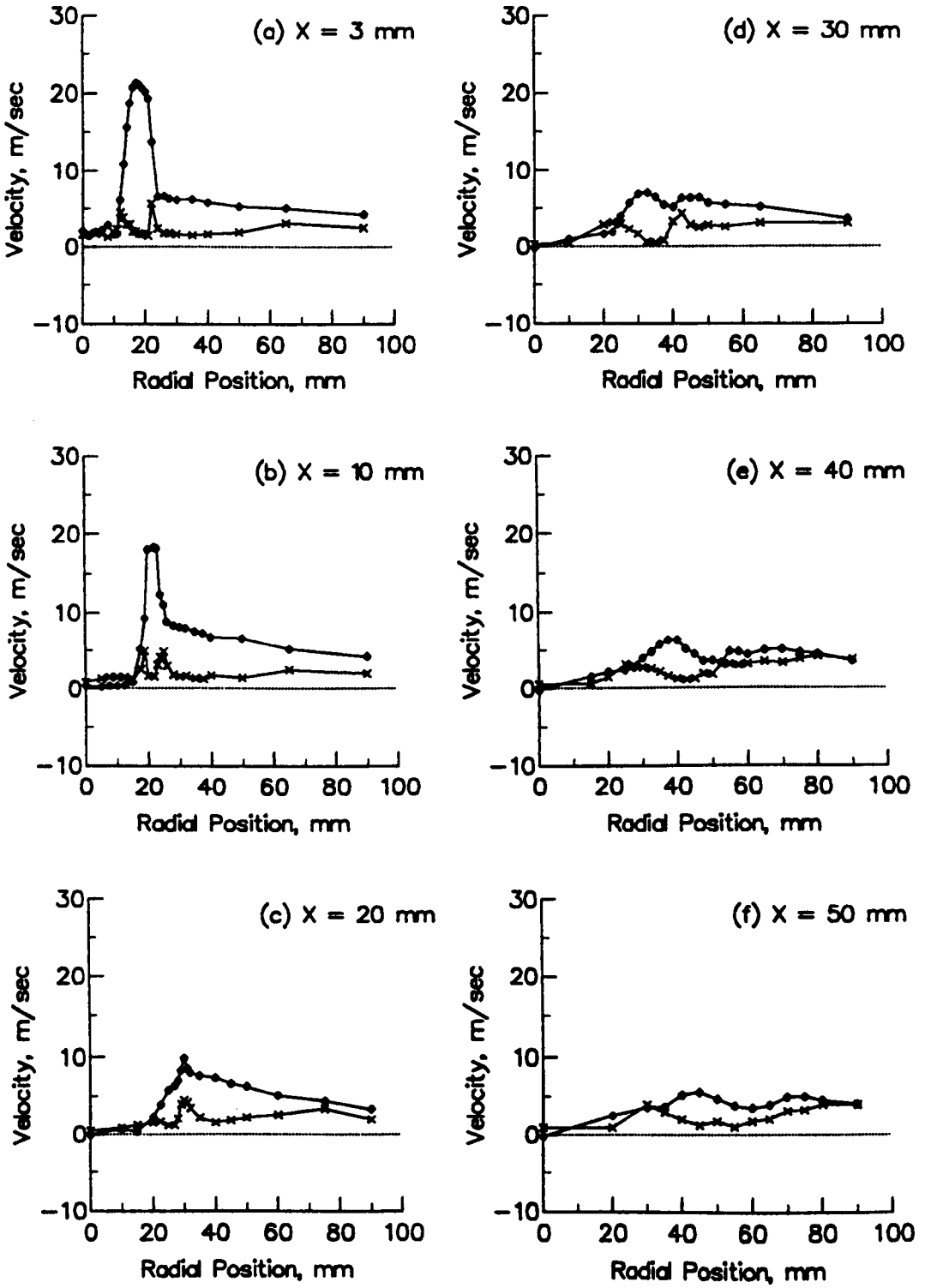

Figure 2.45..Swirl Velocity Profiles, Flame A (continued)

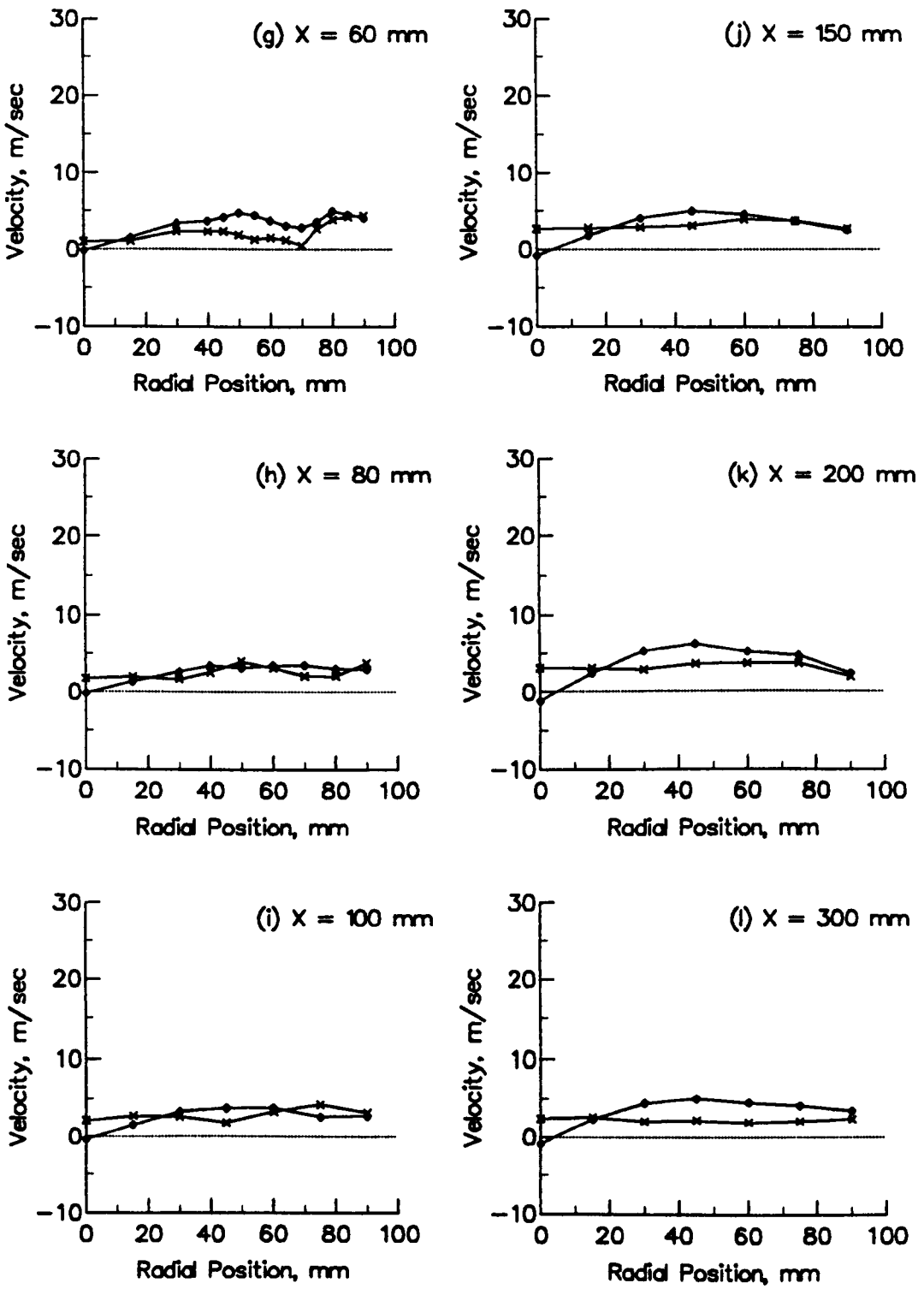

Figure 2.45..Swirl Velocity Profiles, Flame A (complete)

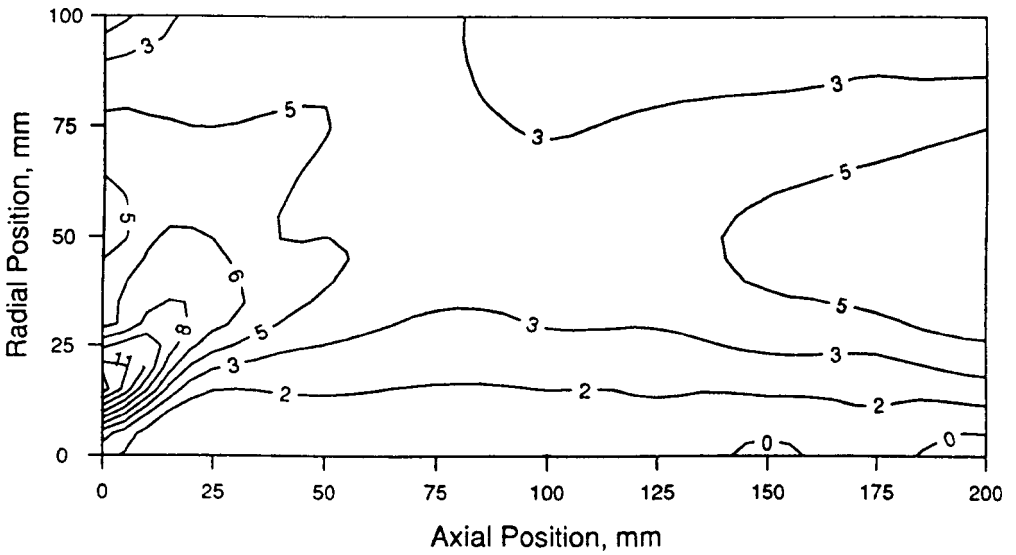

(a) Mean Velocity

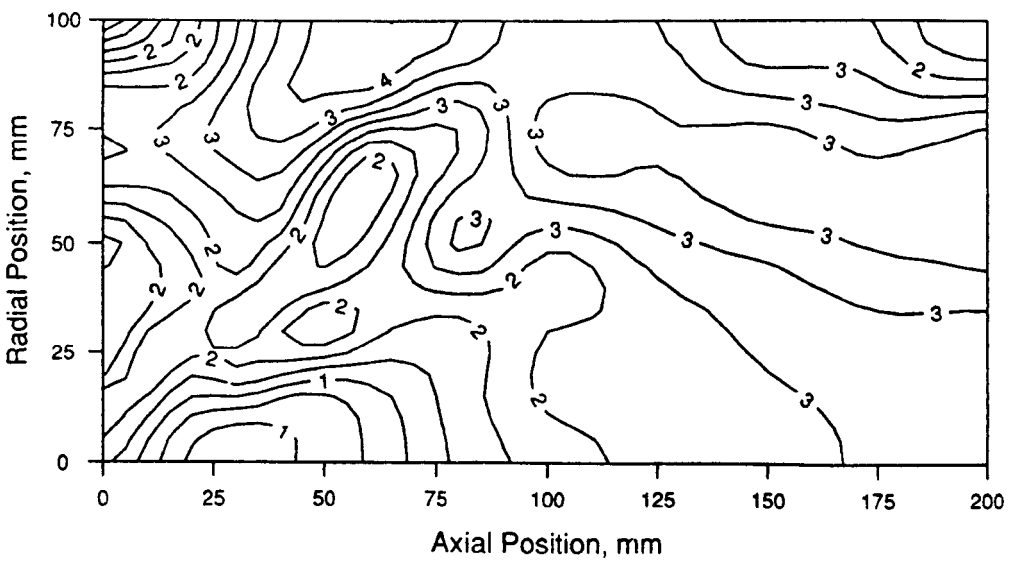

(b) RMS Velocity

Figure 2.46 Contours of Swirl Velocity, Flame A

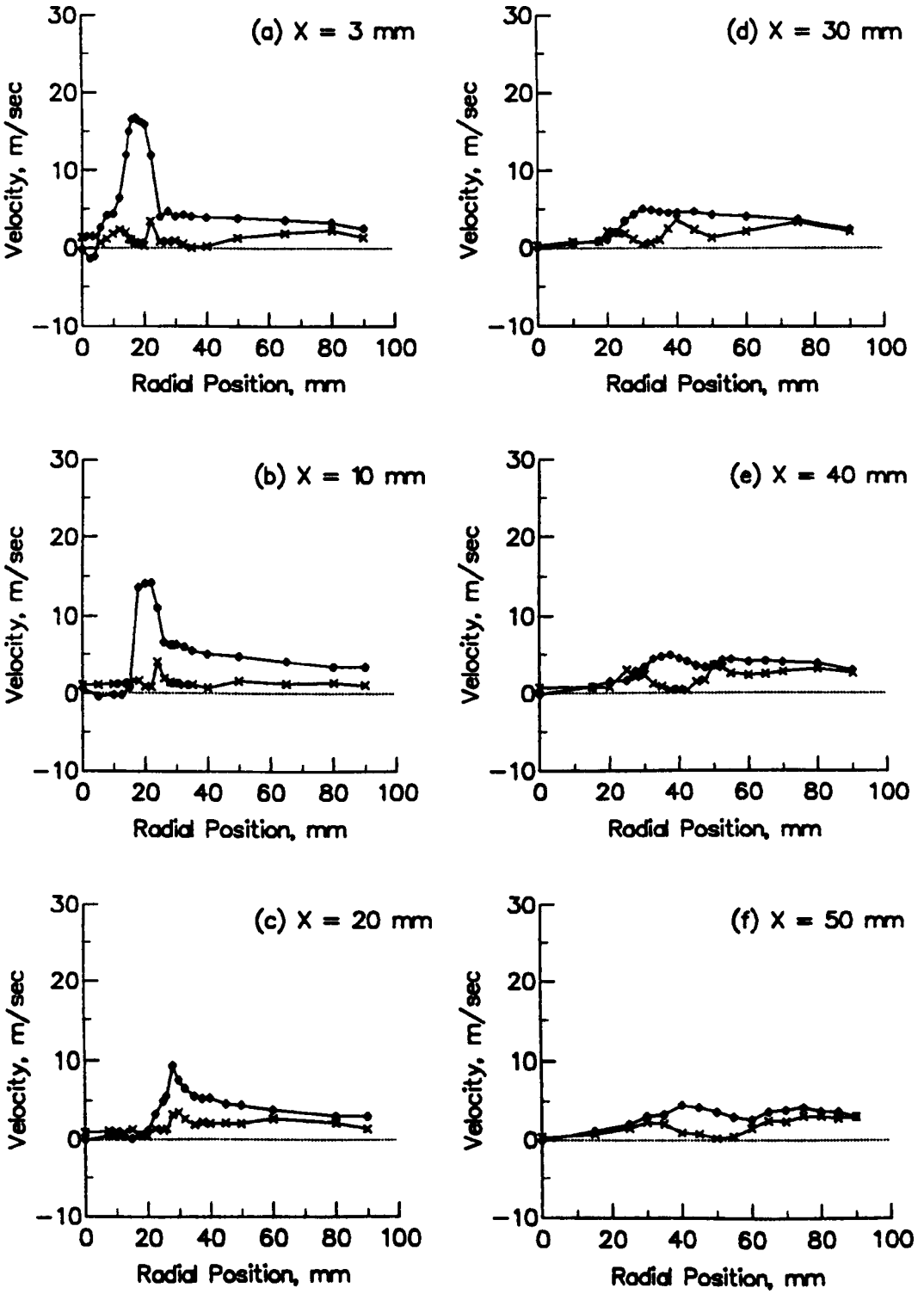

Figure 2.47 Swirl Velocity Profiles, Flame B (continued)

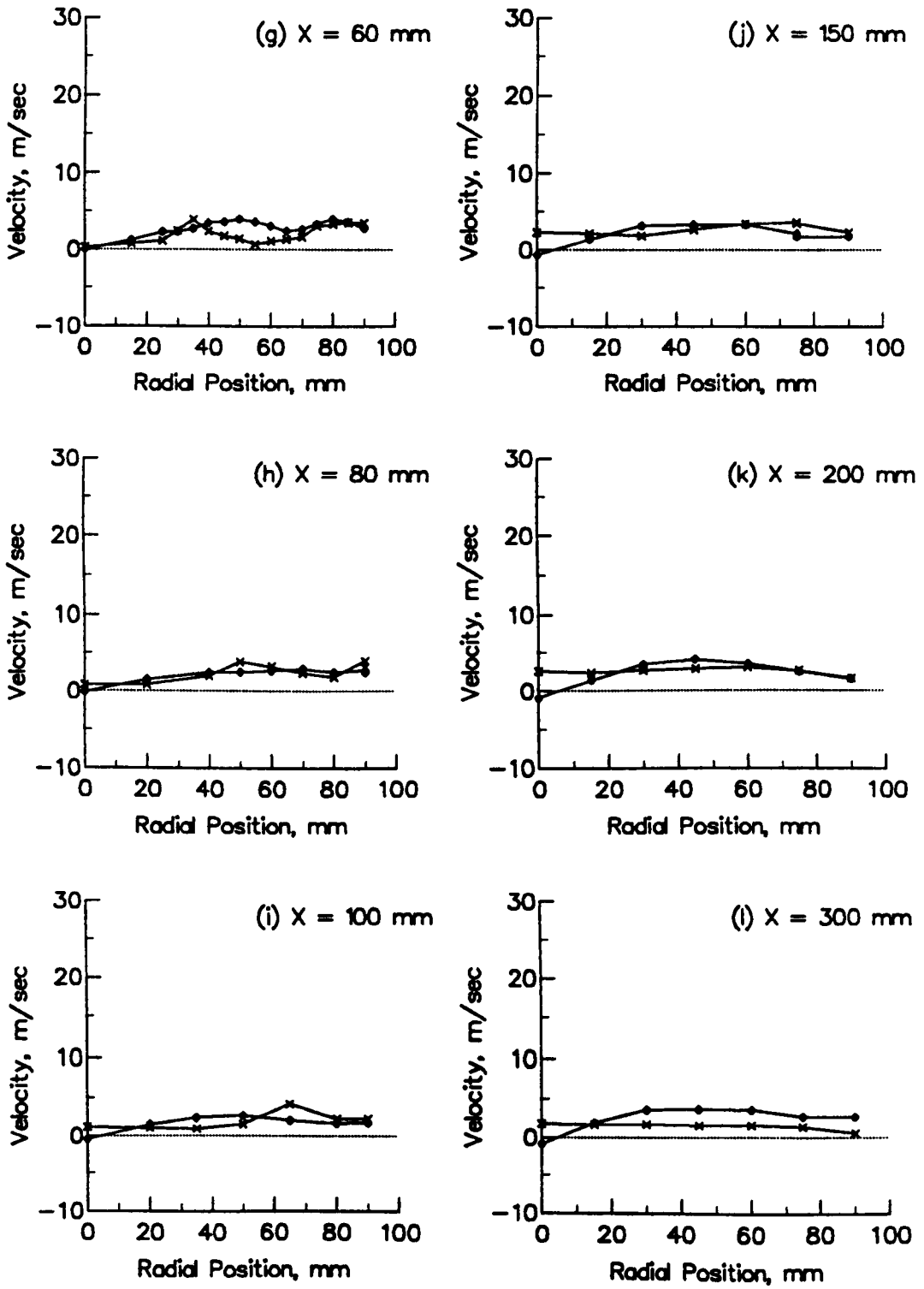

Figure 2.47 Swirl Velocity Profiles, Flame B (complete)

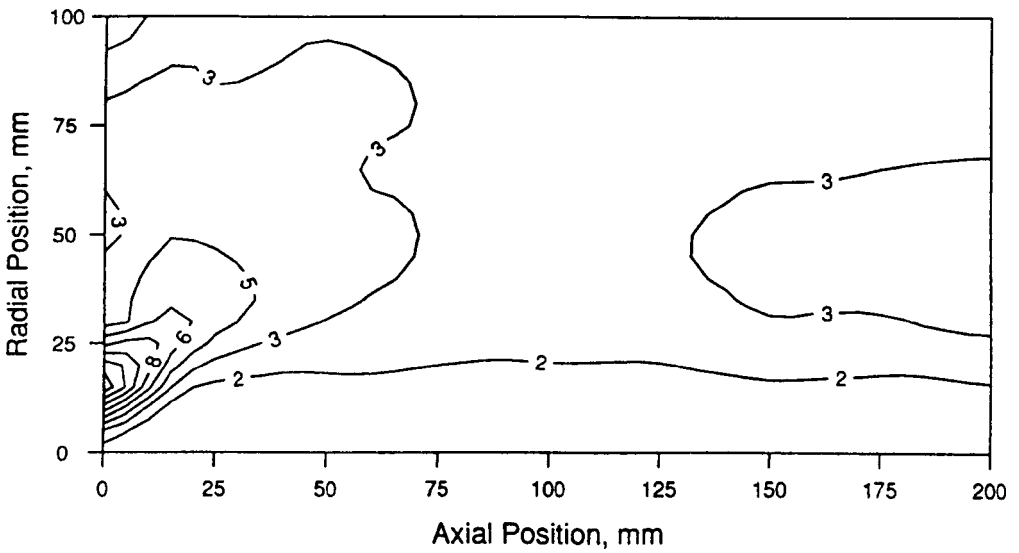

(a) Mean Velocity

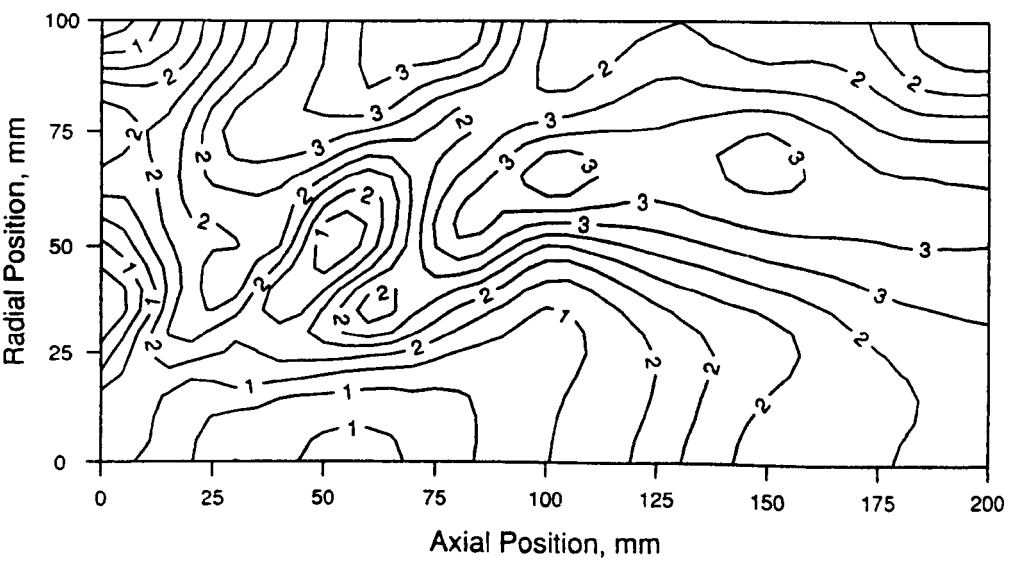

(b) RMS Velocity

Figure 2.48 Contours of Swirl Velocity, Flame B

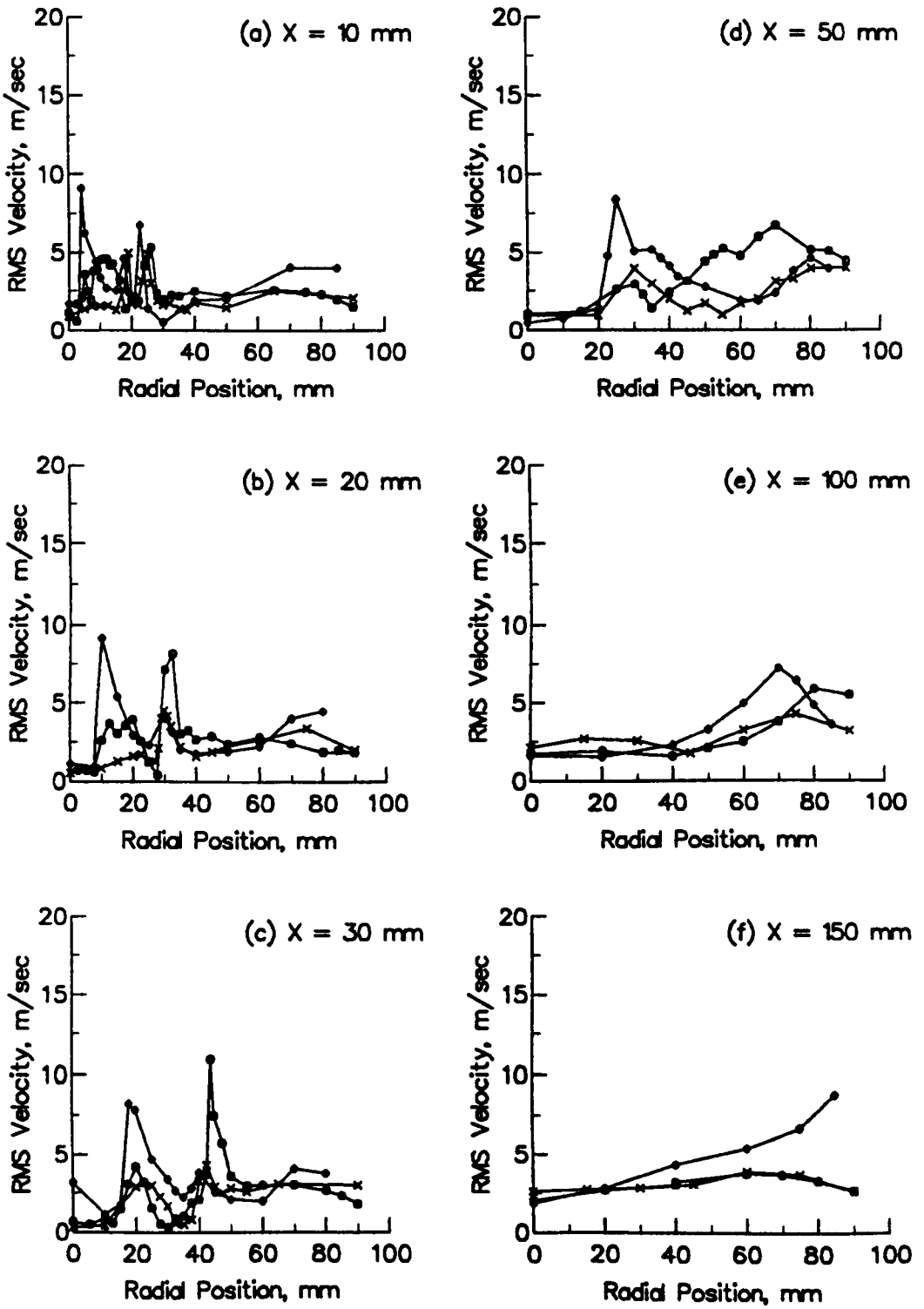

Figure 2.49 Profiles of Three RMS Velocities, Flame A

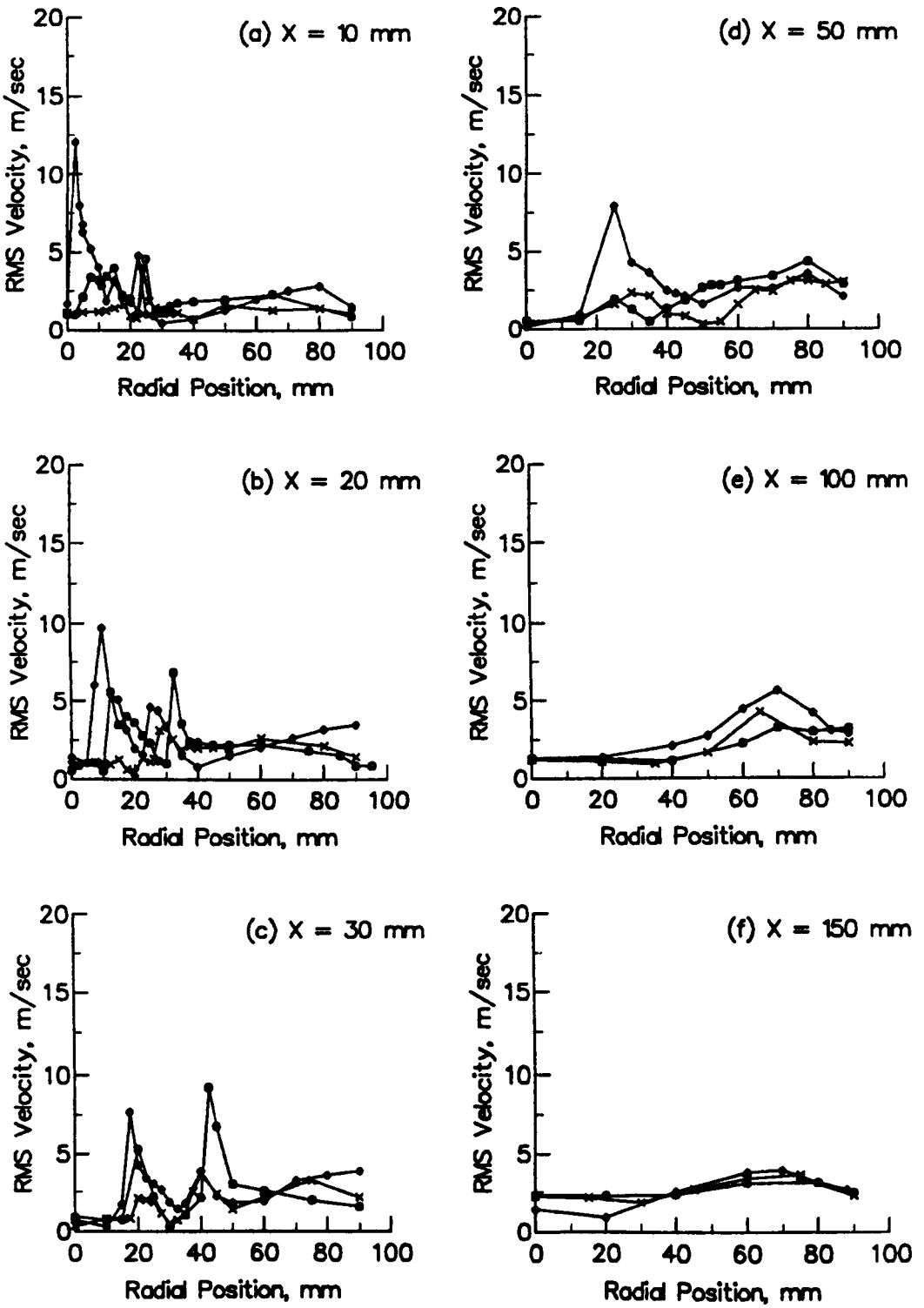

Figure 2.50 Profiles of Three RMS Velocities, Flame B

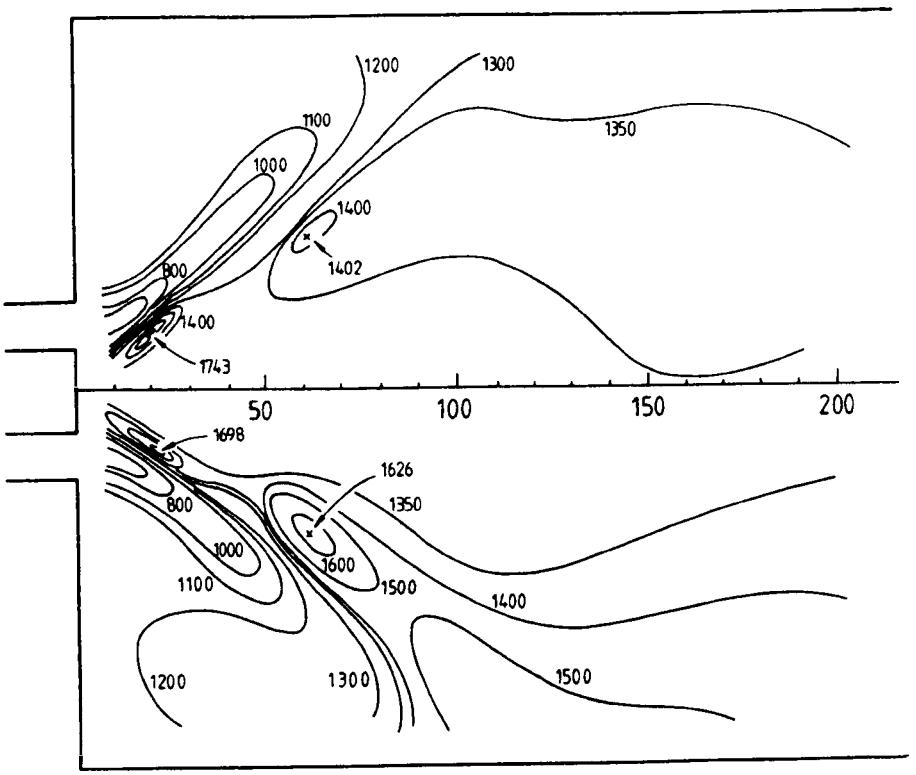

(a) Flame A

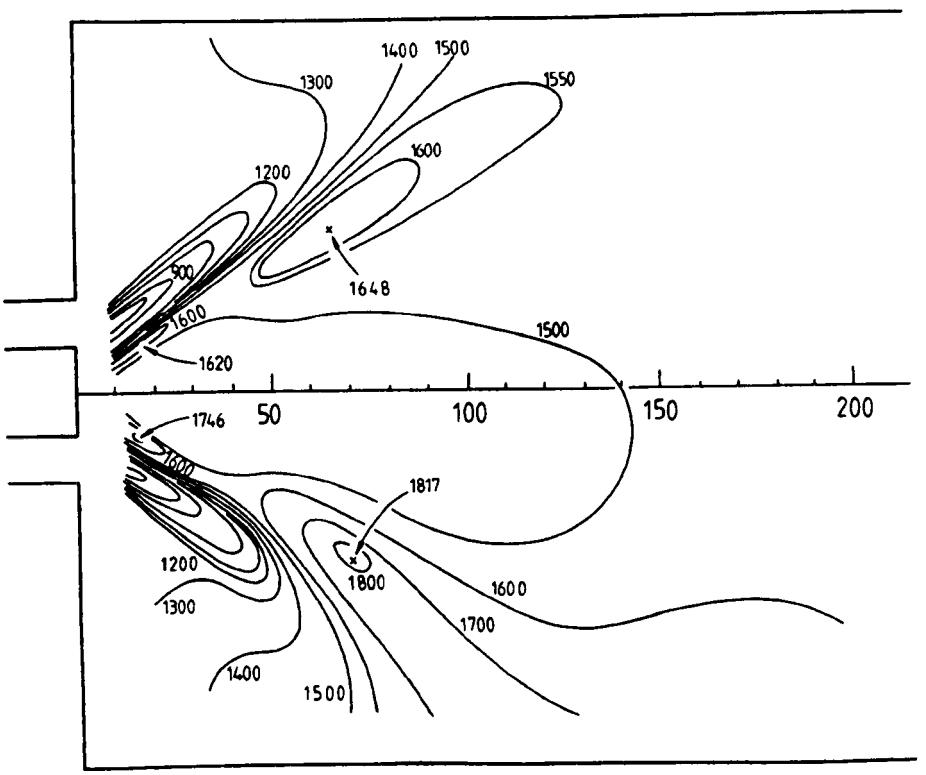

(b) Flame B

Figure 2.51 Contours of Mean Temperature

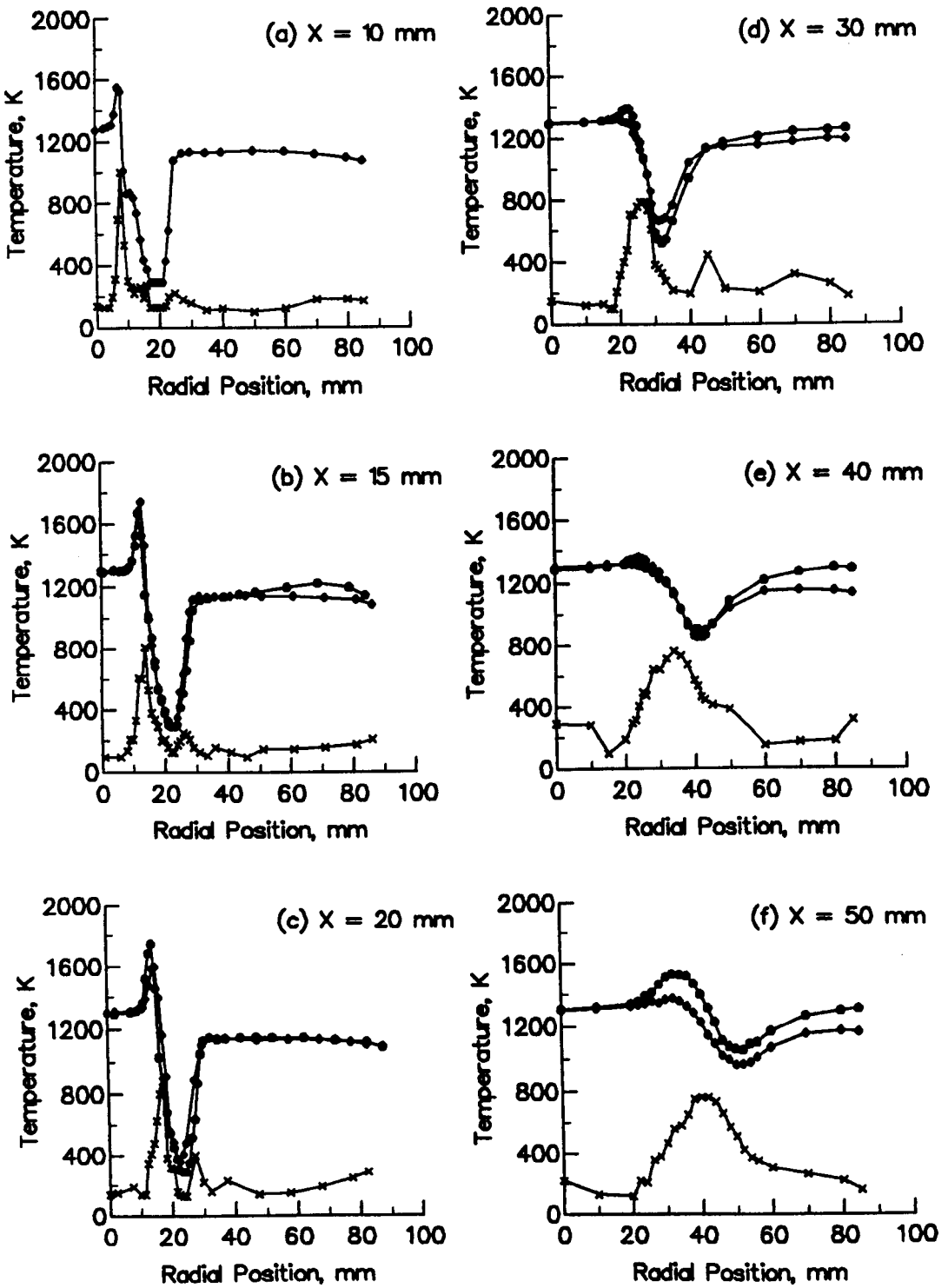

- Mean Temperature , Right Wing
- o Mean Temperature , Left Wing
- x RMS Temperature (x 4)

Figure 2.52 Temperature Profiles, Flame A (continued)

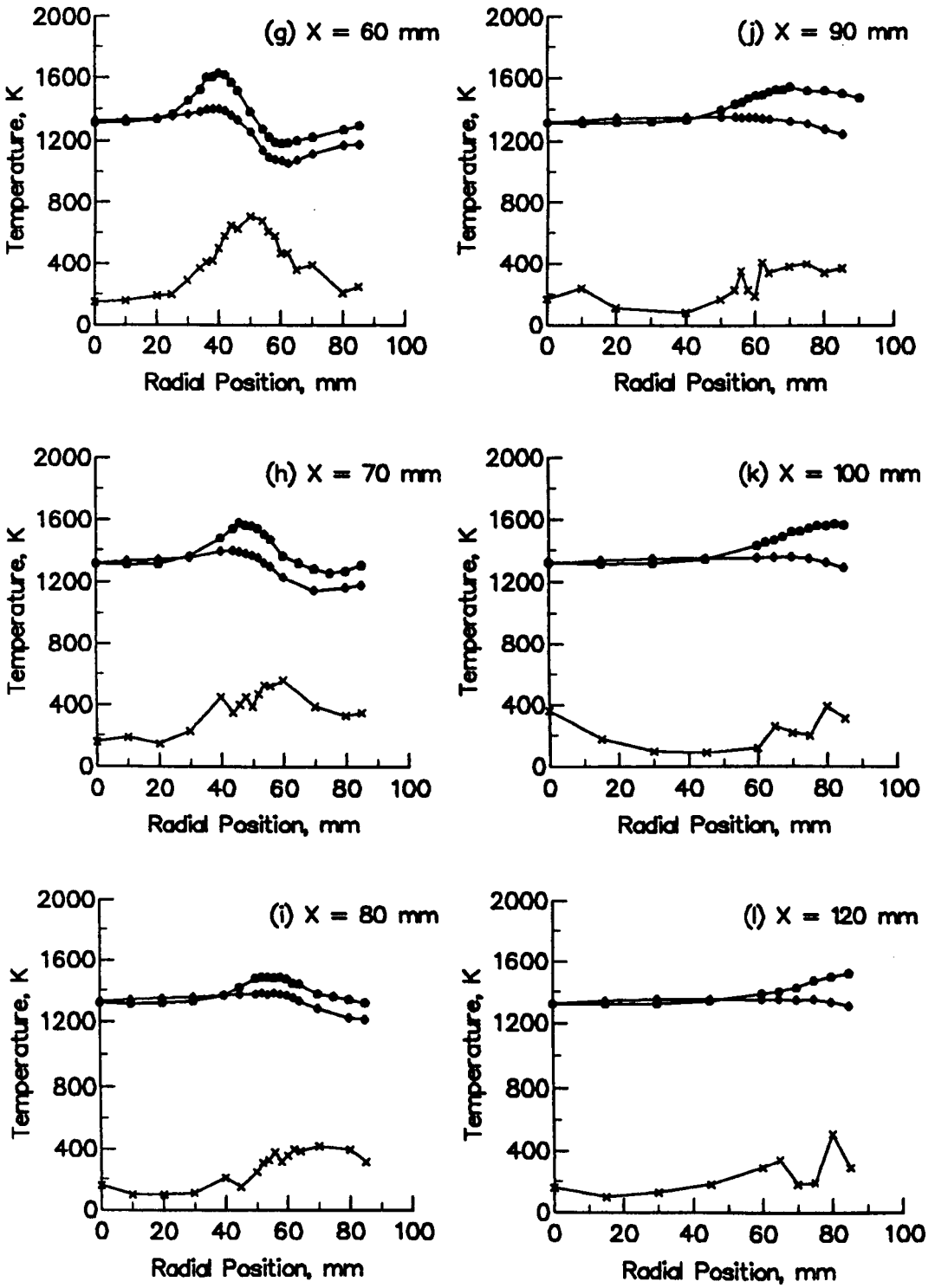

- Mean Temperature , Right Wing
- Mean Temperature , Left Wing
x RMS Temperature (x 4)

Figure 2.52 Temperature Profiles, Flame A (complete)

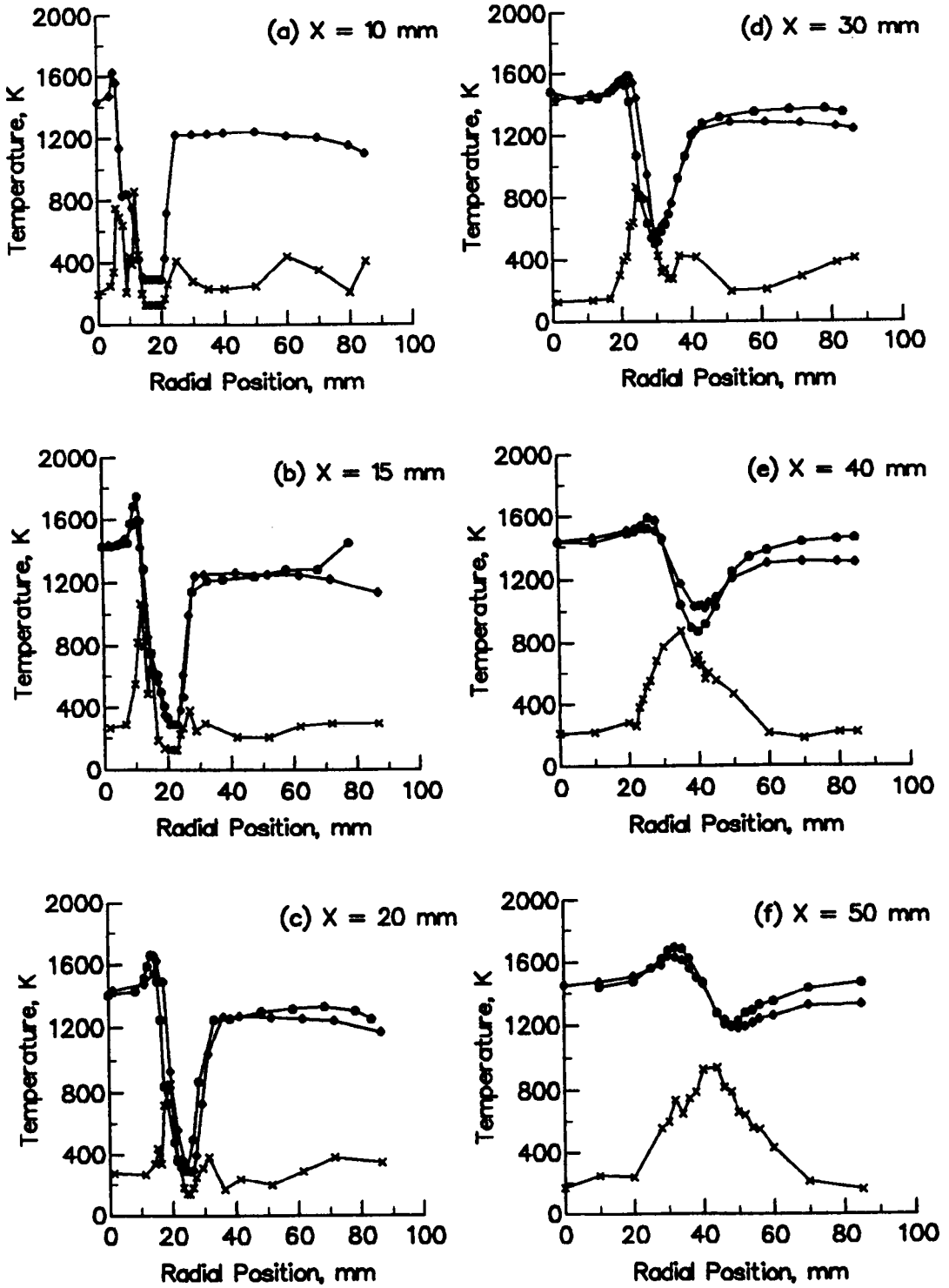

- Mean Temperature , Right Wing
- Mean Temperature , Left Wing
- x RMS Temperature (x 4)

Figure 2.53 Temperature Profiles, Flame B (continued)

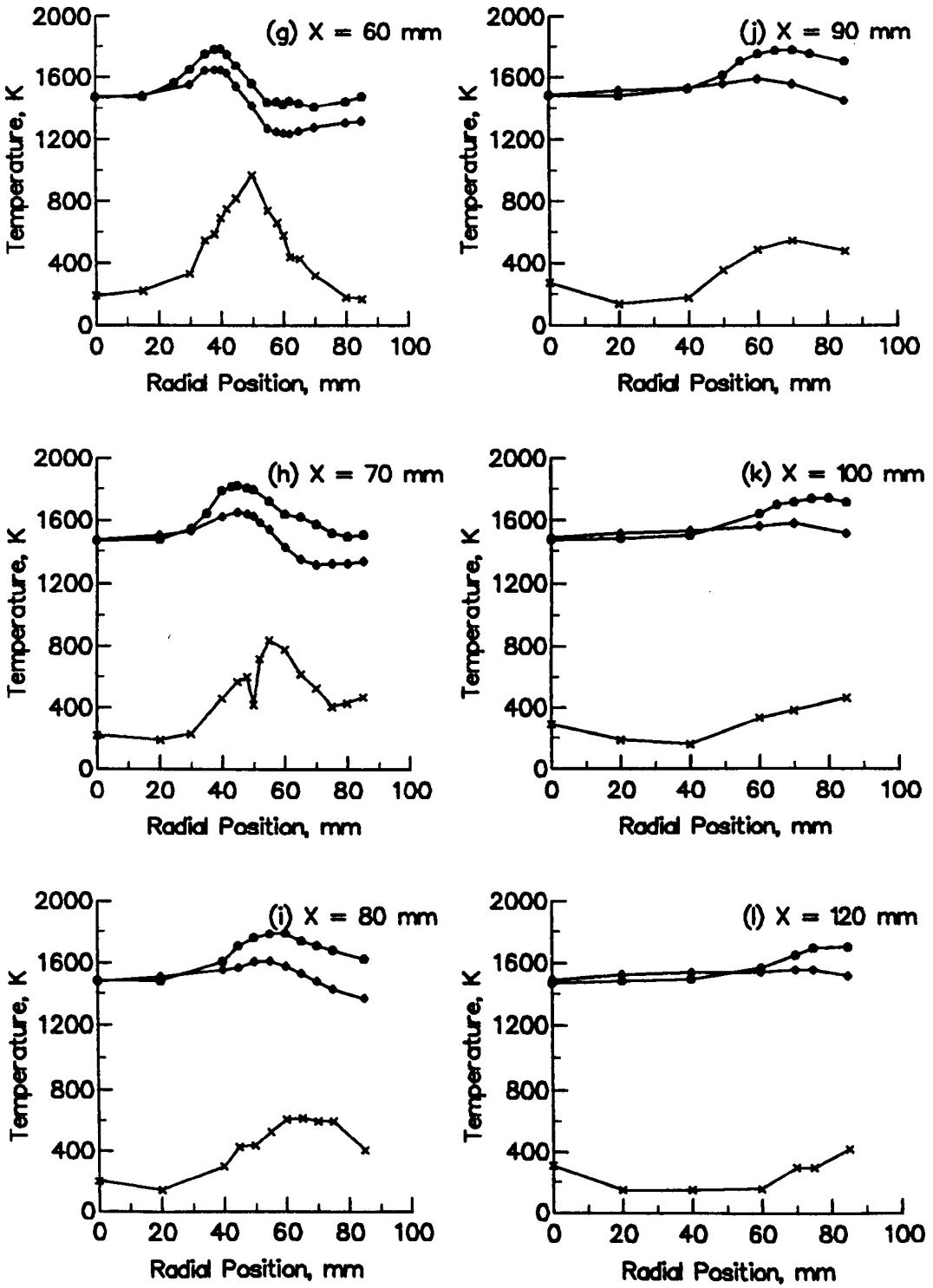

- Mean Temperature , Right Wing
- o Mean Temperature , Left Wing
- x RMS Temperature (x 4)

Figure 2.53 Temperature Profiles, Flame B (complete)

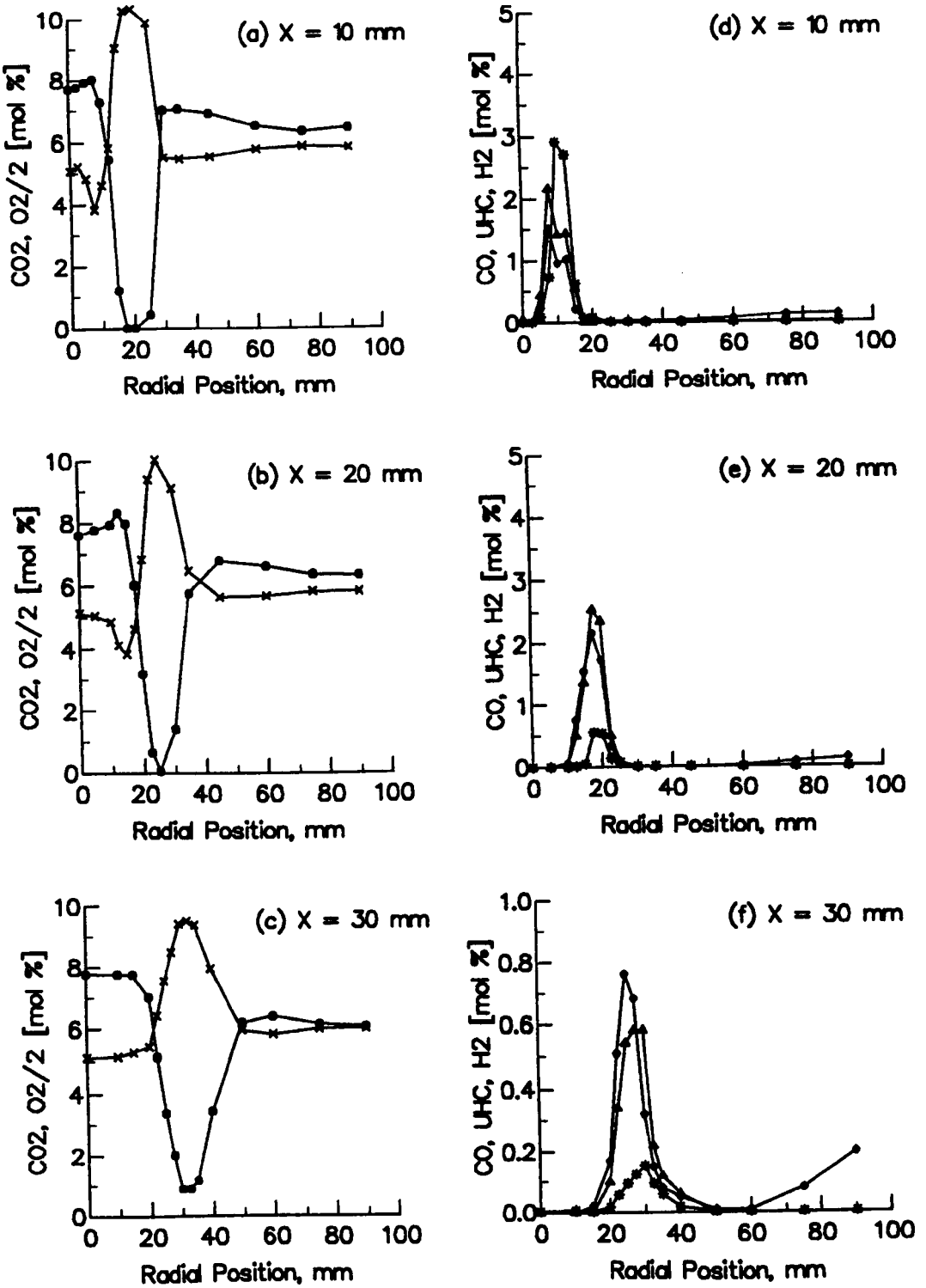

• CO, dry mol %; ○ CO_2, dry mol %; x O_2, dry mol %;
∗ UHC/4, C_{12} equiv. wet mol %; Δ H_2, dry mol %

Figure 2.54 Species Concentration Profiles, Flame A (continued)

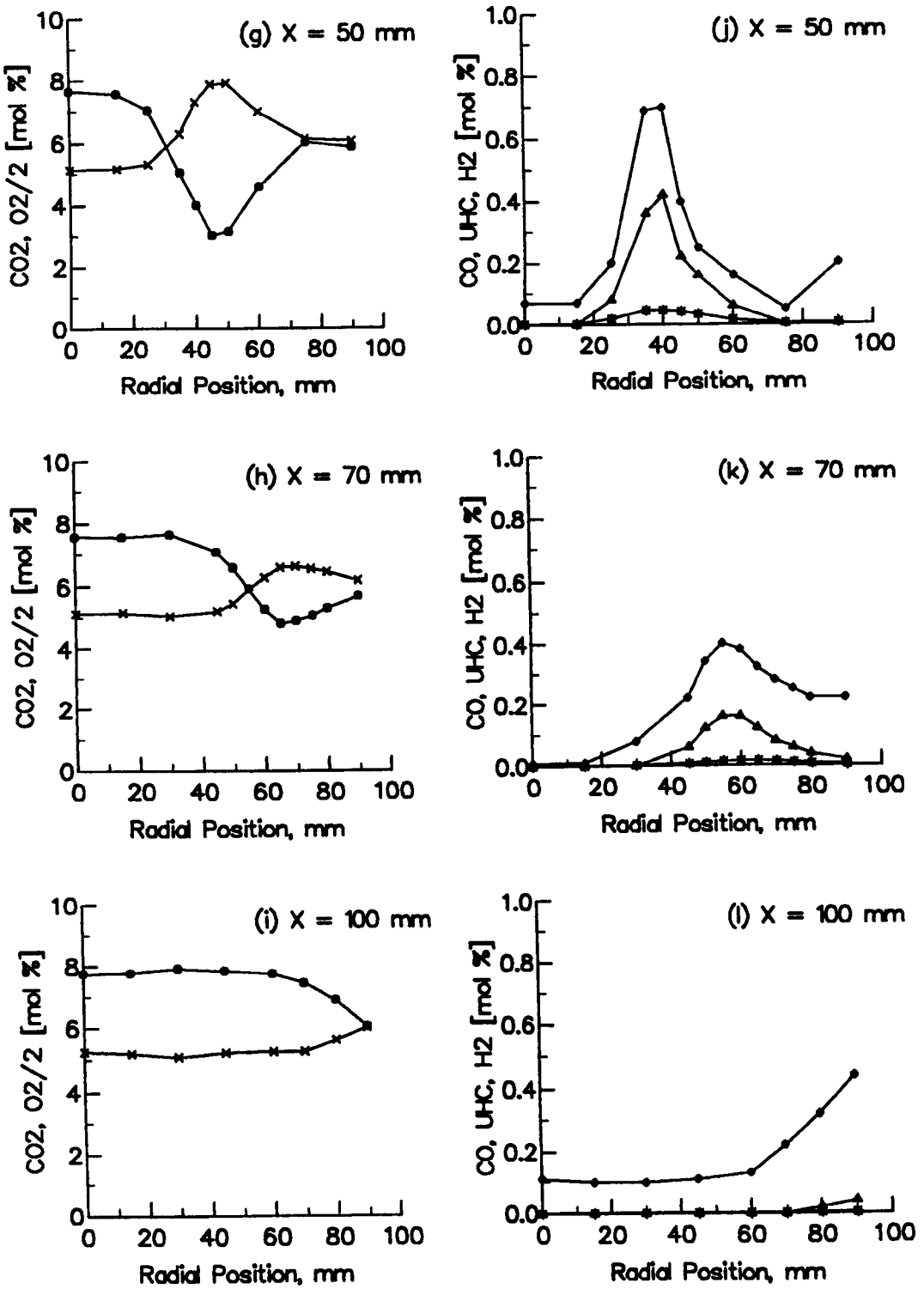

• CO, dry mol %; ○ CO_2, dry mol %; x O_2, dry mol %;
∗ UHC/4, C_{12} equiv. wet mol %; Δ H_2, dry mol %

Figure 2.54 Species Concentration Profiles, Flame A (complete)

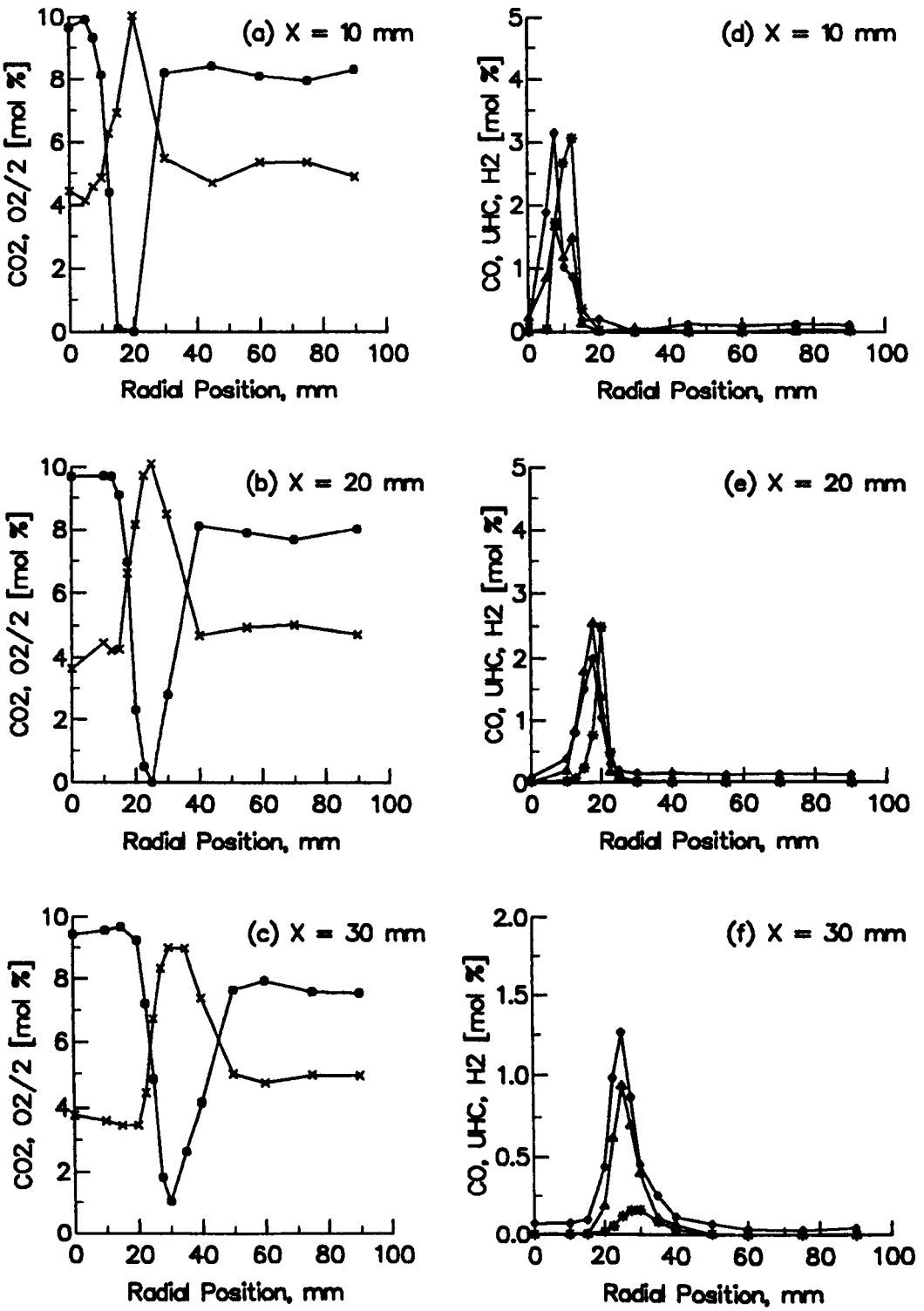

• CO, dry mol %; ○ CO_2, dry mol %; x O_2, dry mol %;
* UHC/4, C_{12} equiv. wet mol %; Δ H_2, dry mol %

Figure 2.55 Species Concentration Profiles, Flame B (continued)

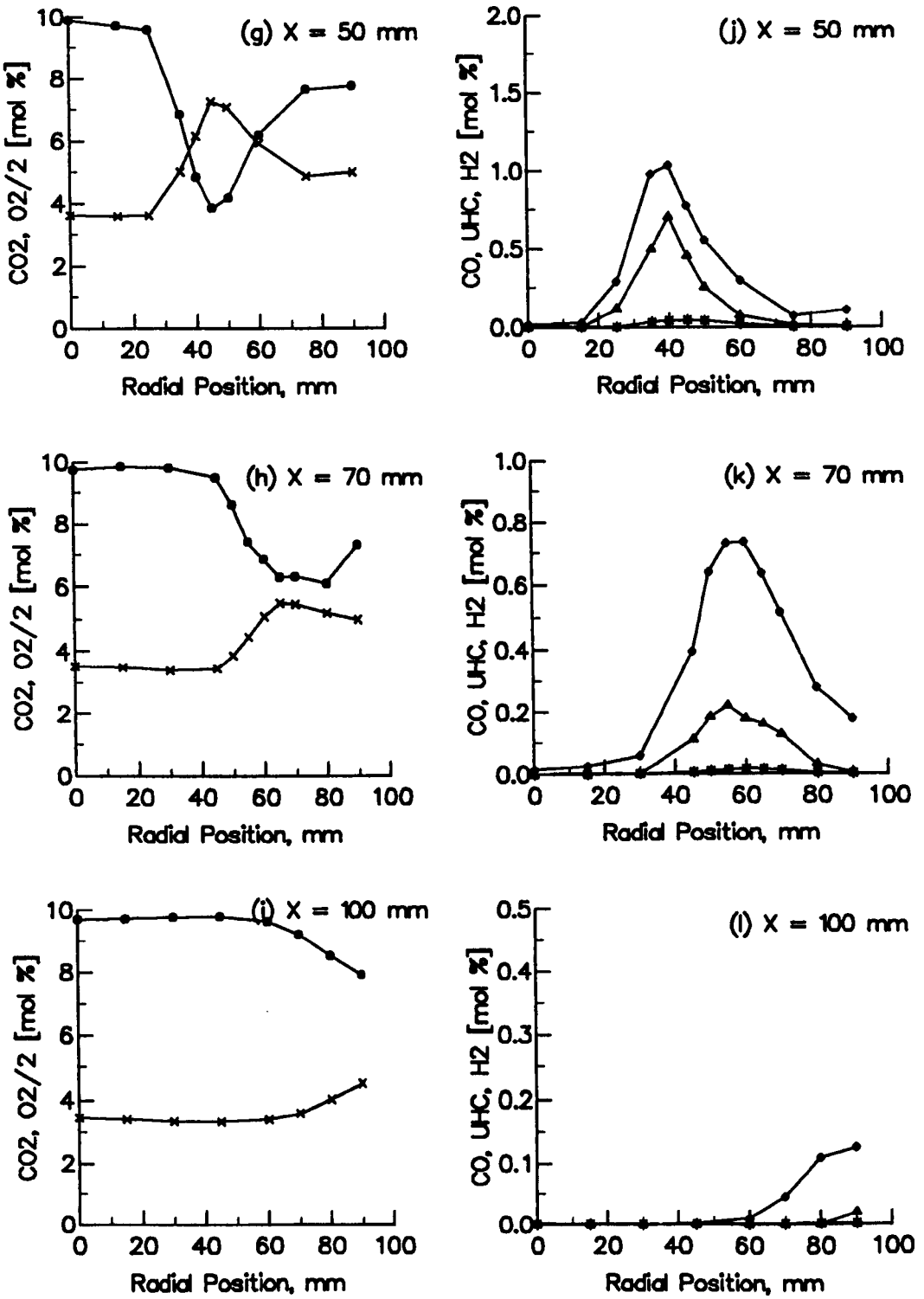

• CO, dry mol %; ○ CO_2, dry mol %; x O_2, dry mol %;
* UHC/4, C_{12} equiv. wet mol %; Δ H_2, dry mol %

Figure 2.55 Species Concentration Profiles, Flame B (complete)

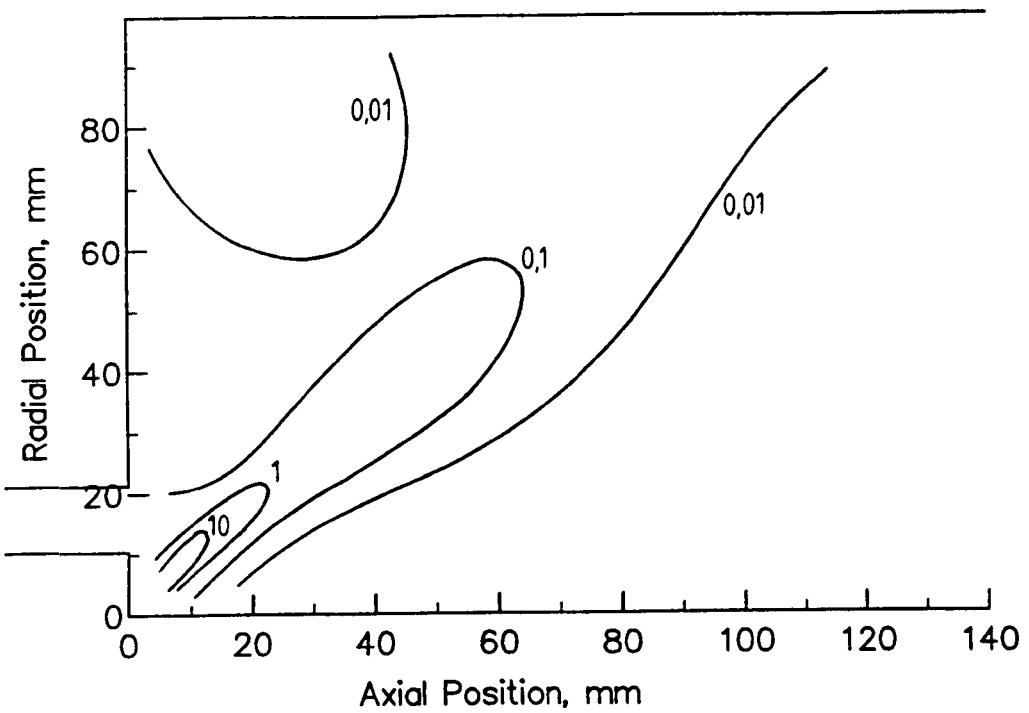

(a) UHC, C_{12} equiv. wet mol %

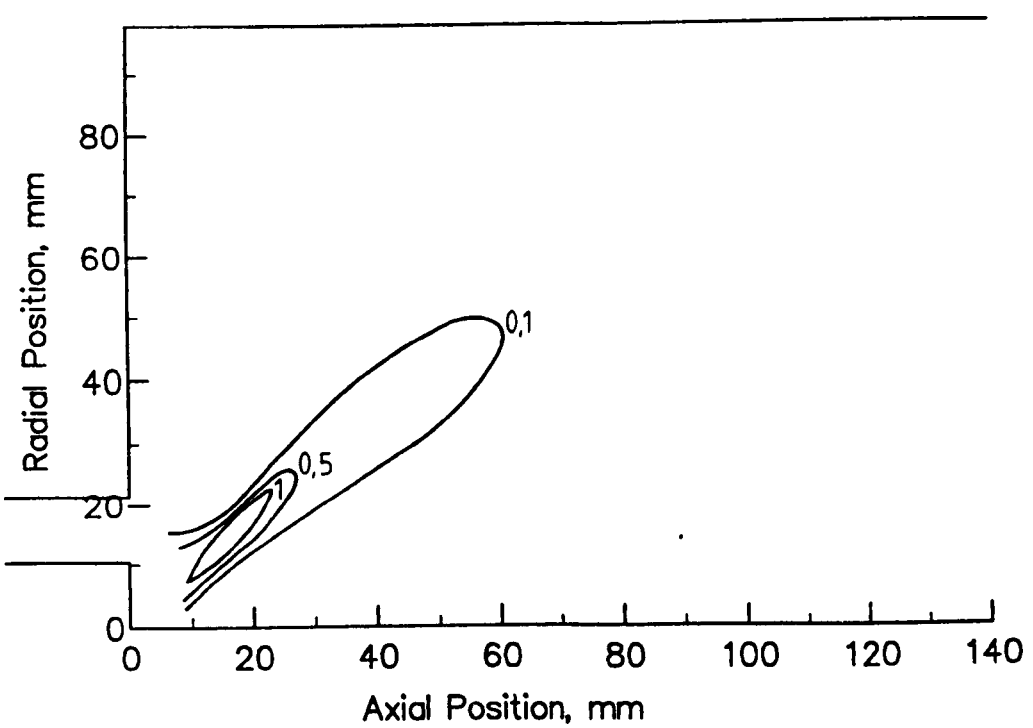

(b) H_2, dry mol %

Figure 2.56 Contours of Species Concentrations, Flame A (continued)

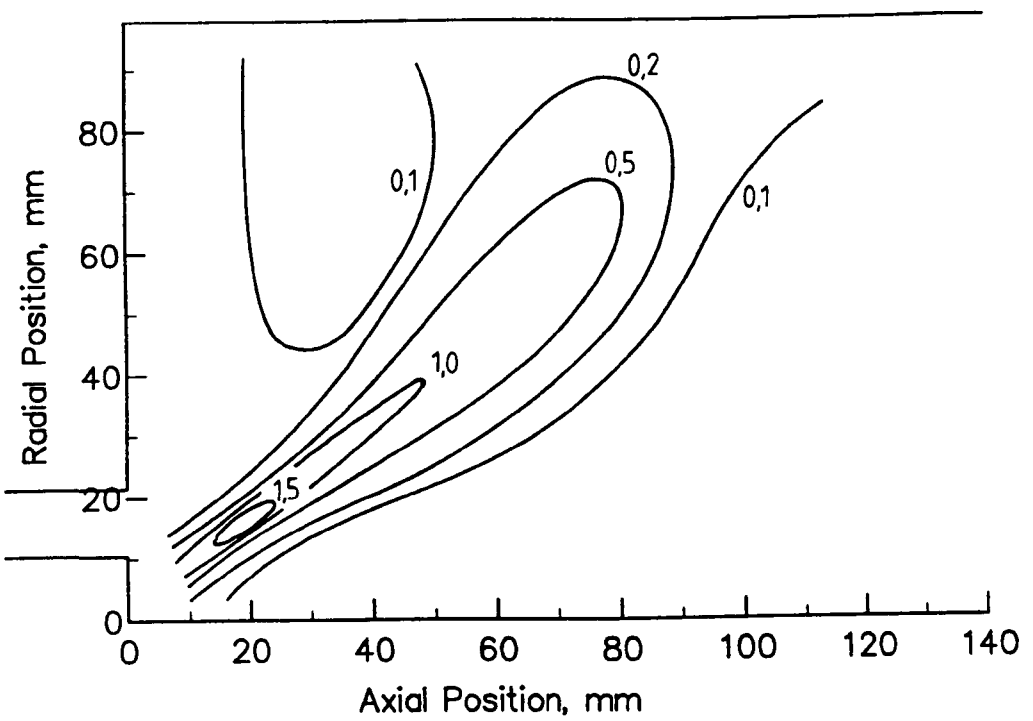

(c) CO, dry mol %

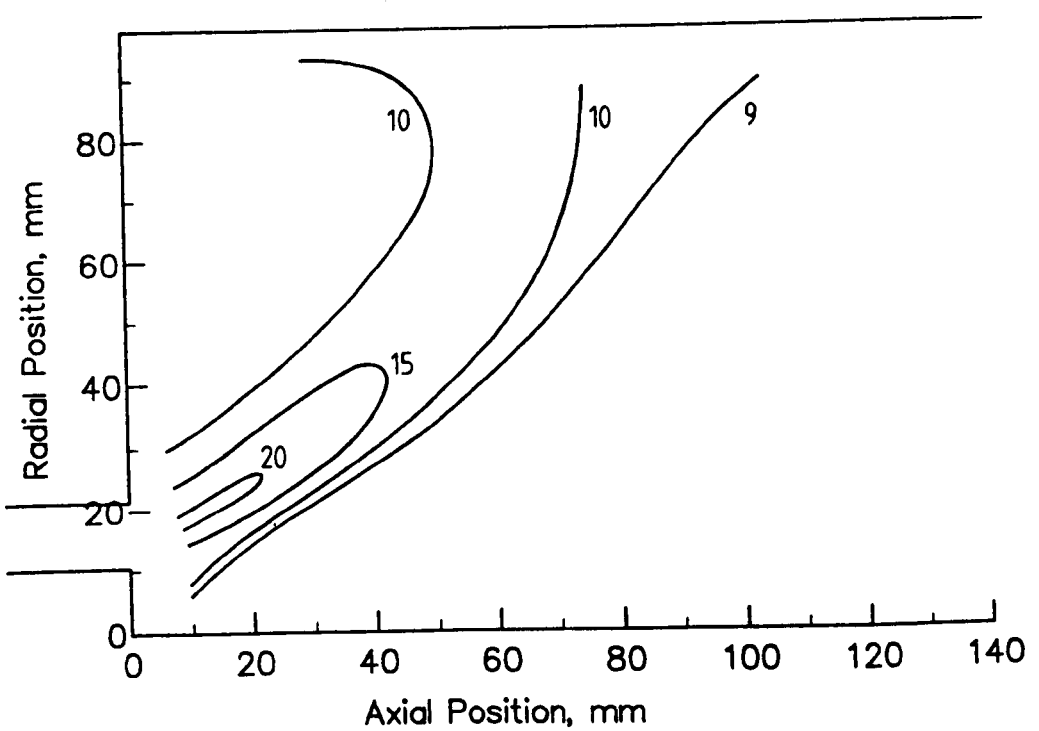

(d) O_2, dry mol %

Figure 2.56 Contours of Species Concentrations, Flame A (complete)

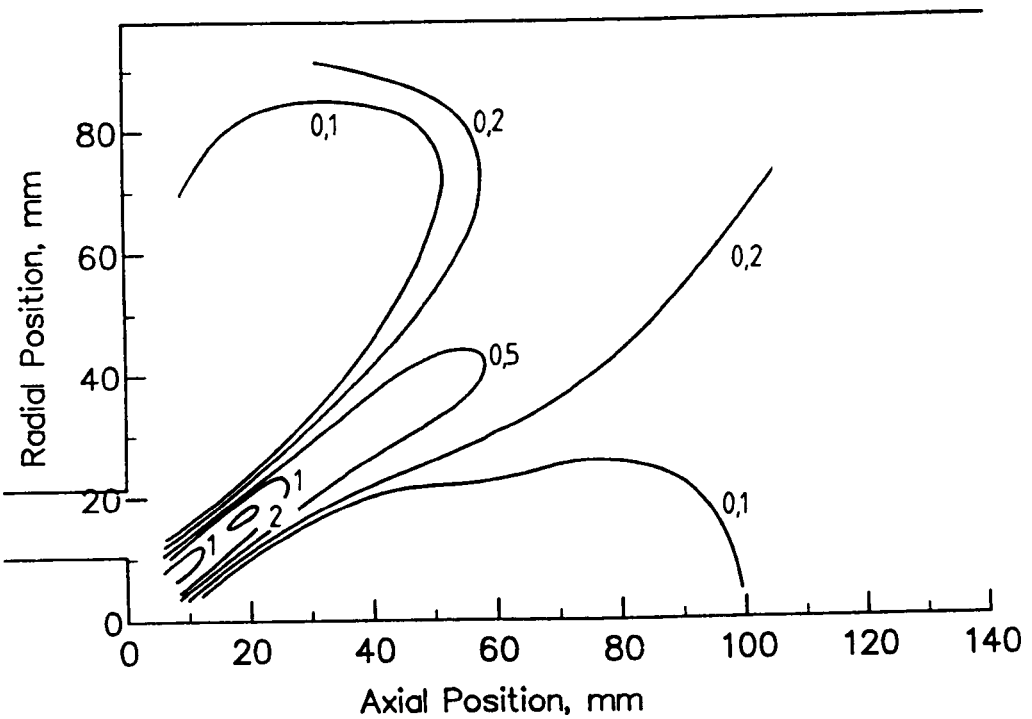

(a) UHC, C_{12} equiv. wet mol %

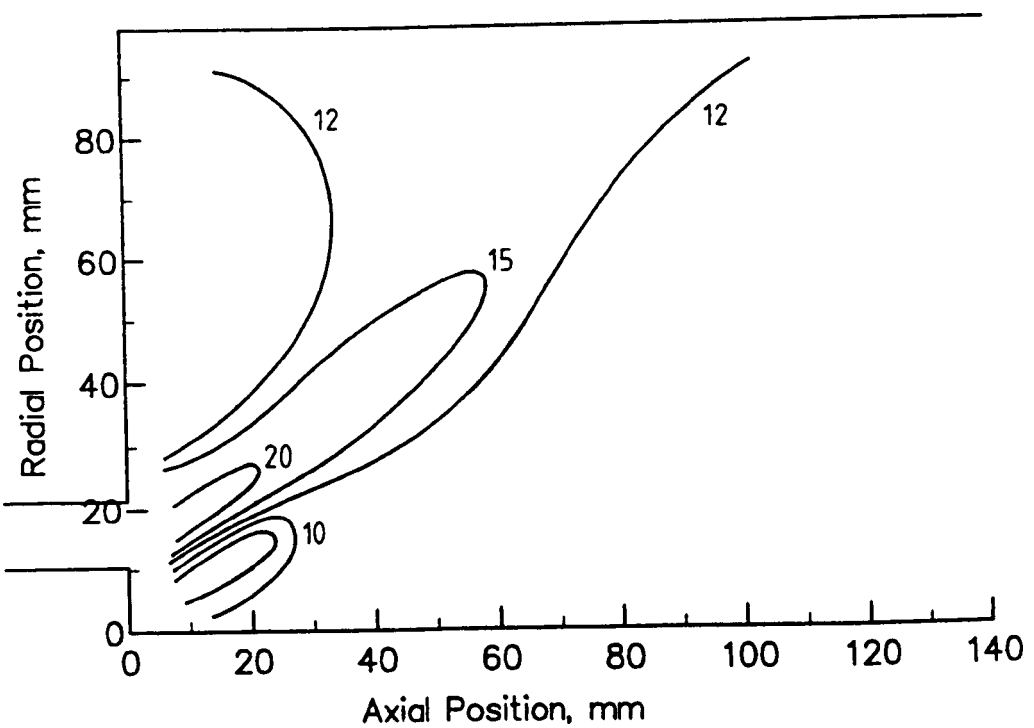

(b) H_2, dry mol %

Figure 2.57 Contours of Species Concentrations, Flame B (continued)

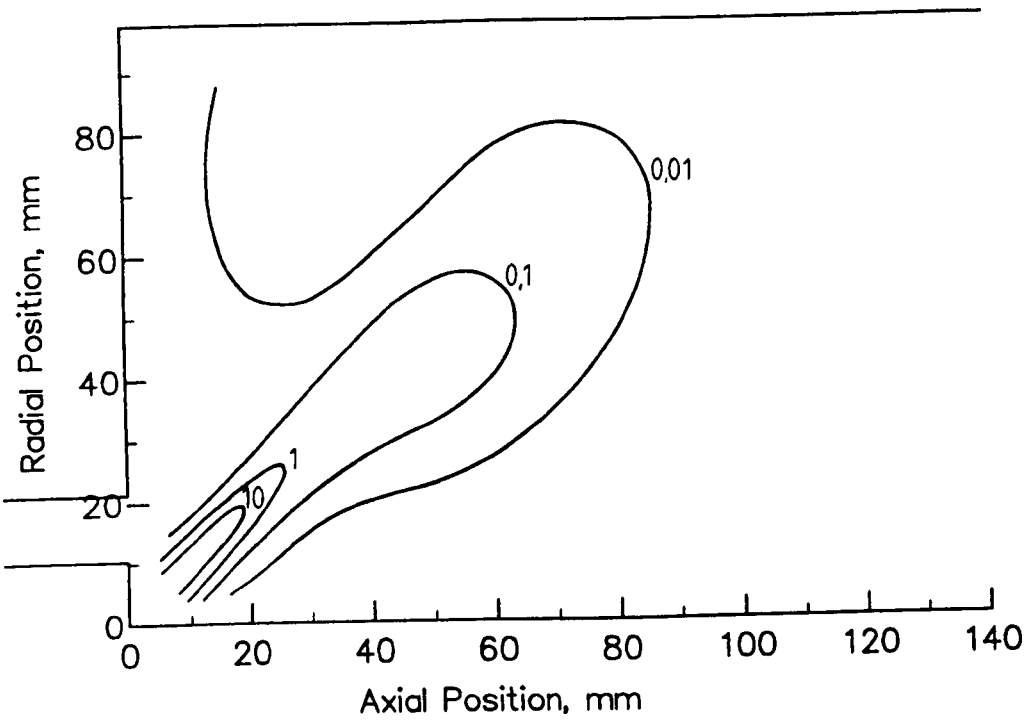

(c) CO, dry mol %

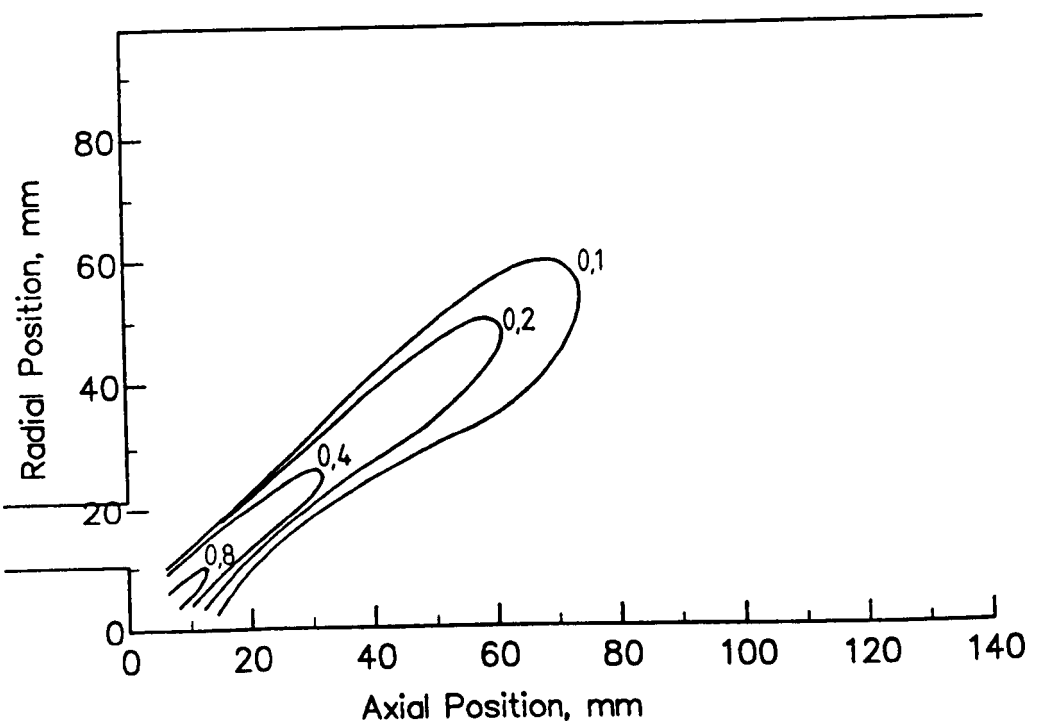

(d) O_2, dry mol %

Figure 2.57 Contours of Species Concentrations, Flame B (complete)

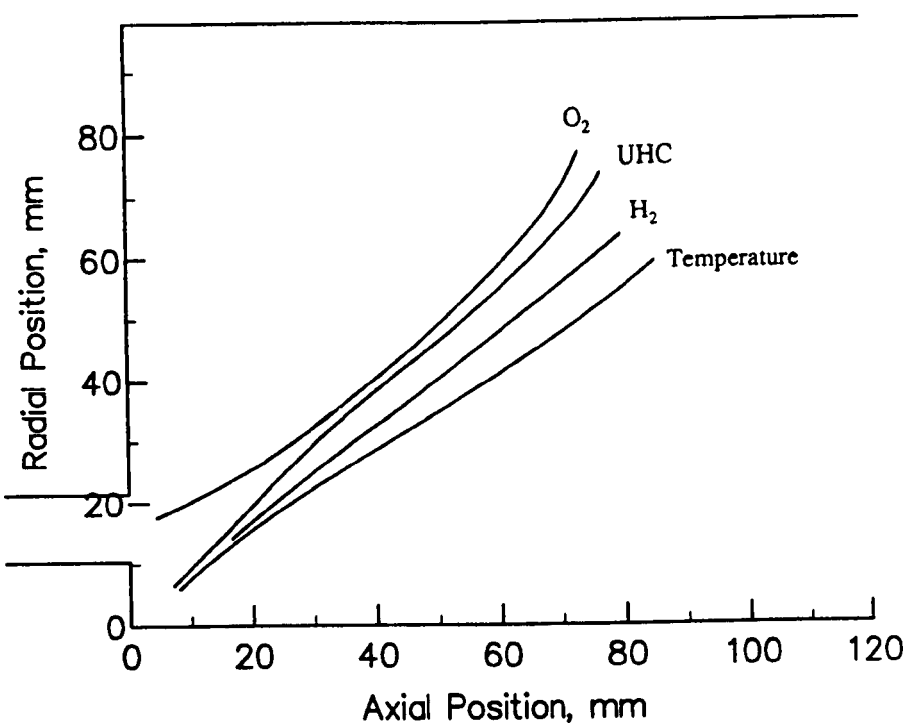

Figure 2.58 Relative Positions of Maxima of Some Properties of Flame A

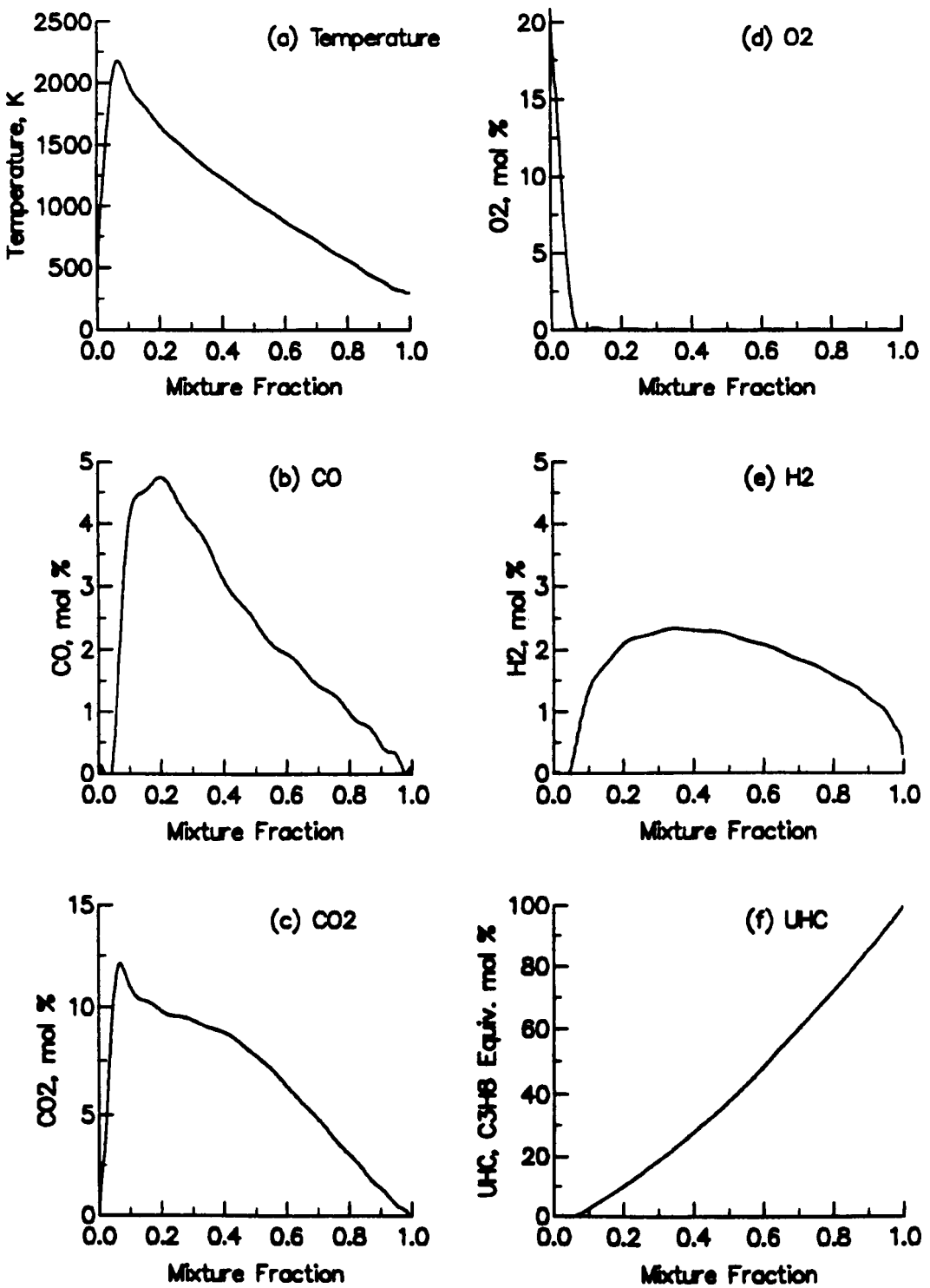

Figure 3.1 Temperature and Species Concentrations versus Mixture Fraction

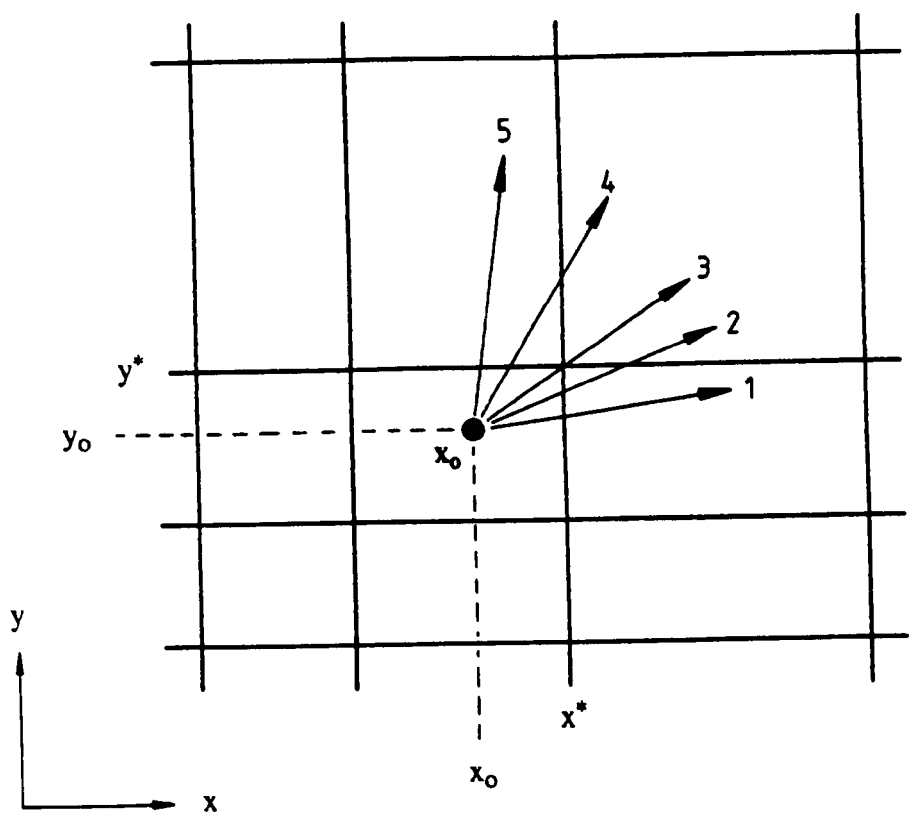

Figure 3.2 Modes of Droplet Translation across the Cell Boundary

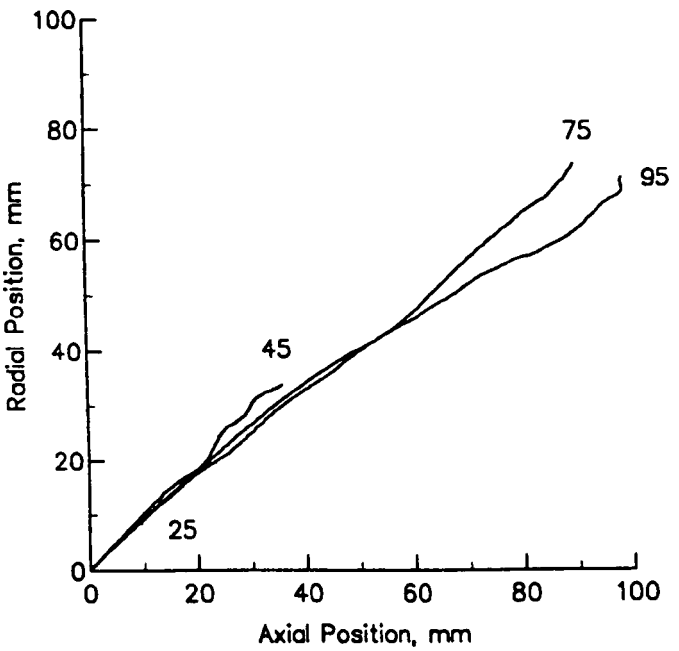

(a) Droplet Trajectories

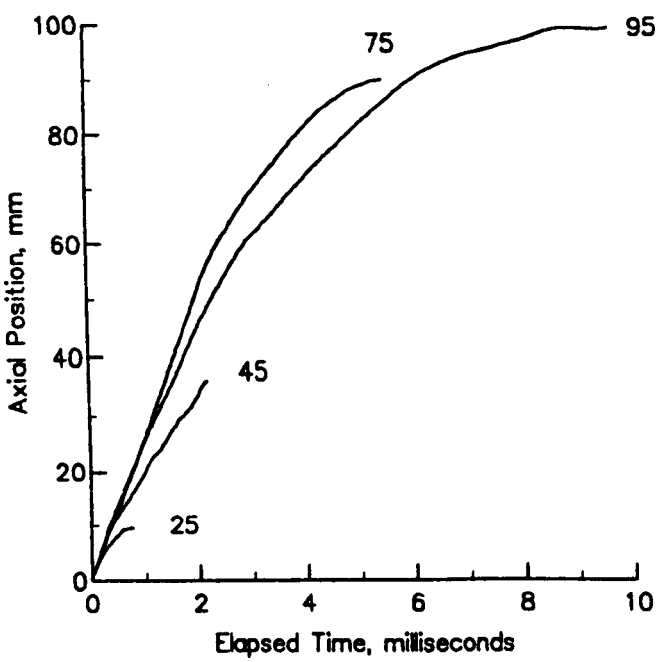

(b) Axial Position of Droplet vs. Elapsed Time

Figure 4.1 Droplet Histories (continued)

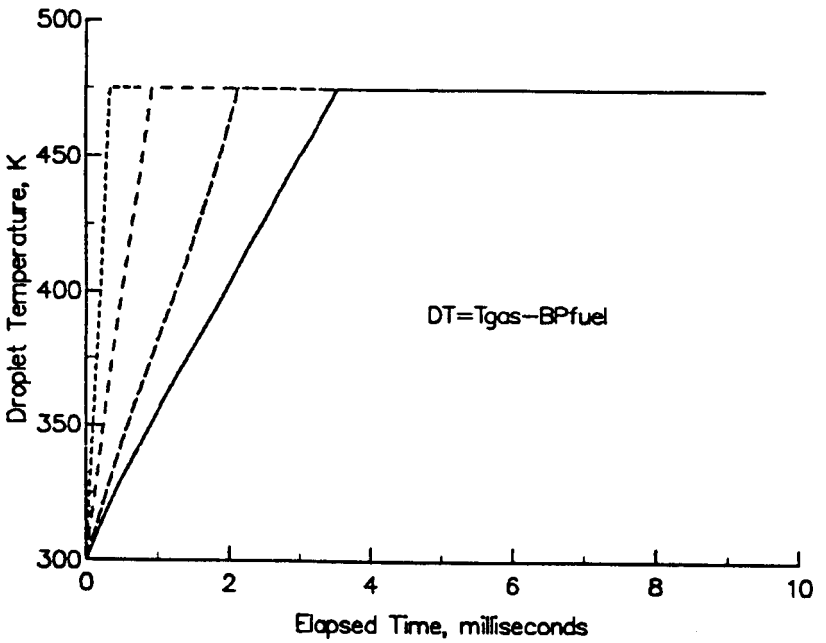

(c) Droplet Temperature Change

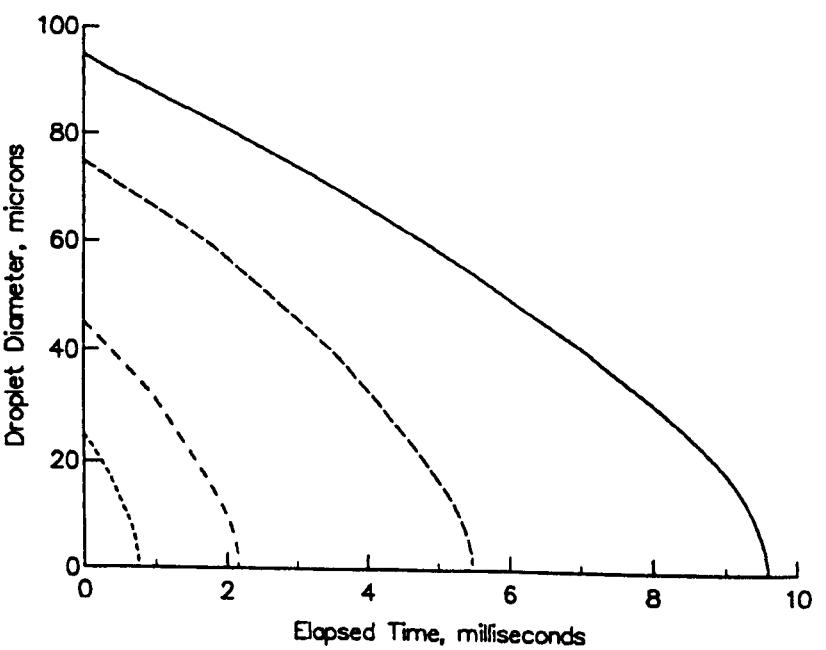

(d) Droplet Size Change

Figure 4.1 Droplet Histories (complete)

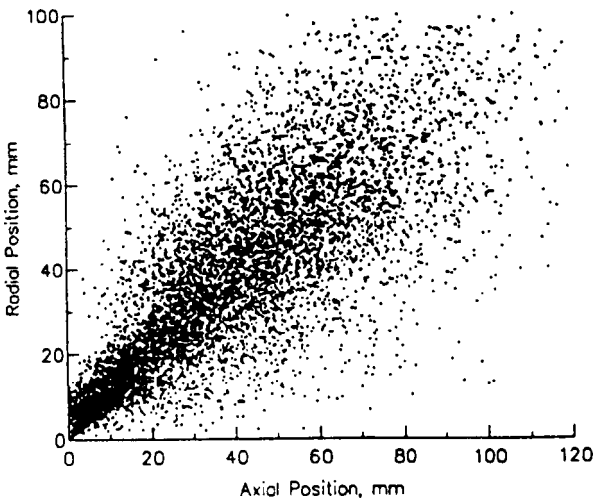

Figure 4.2 Side Cut View of Spray

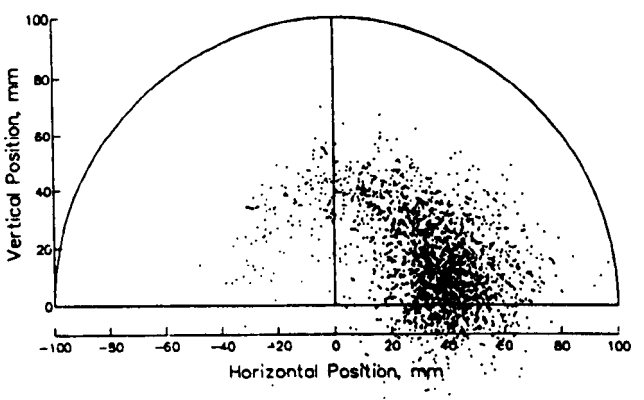

Figure 4.3 Front Cut View of Spray at X= 50 mm

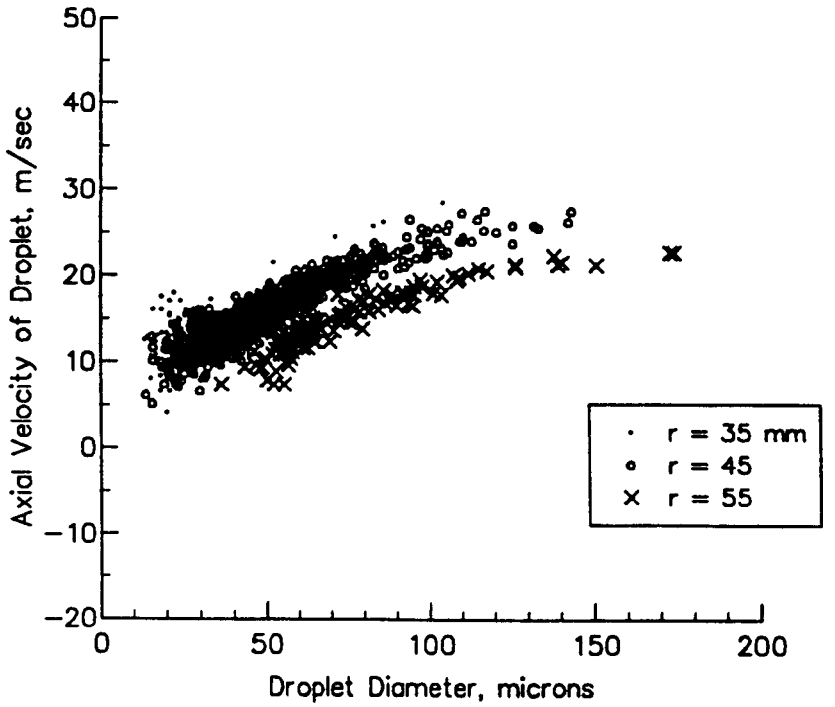

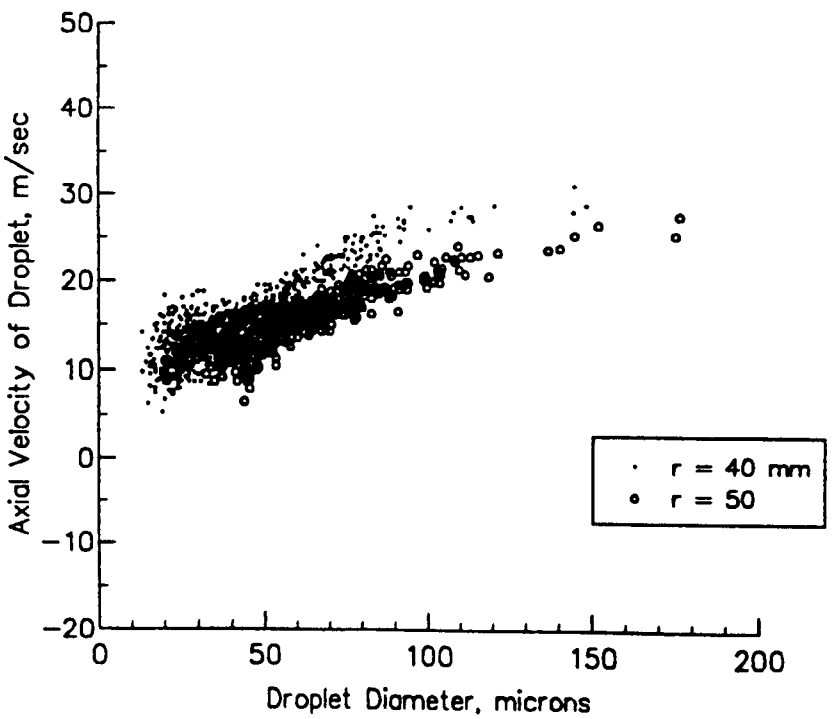

Figure 4.4 Droplet Size-Velocity Correlation at X = 50 mm

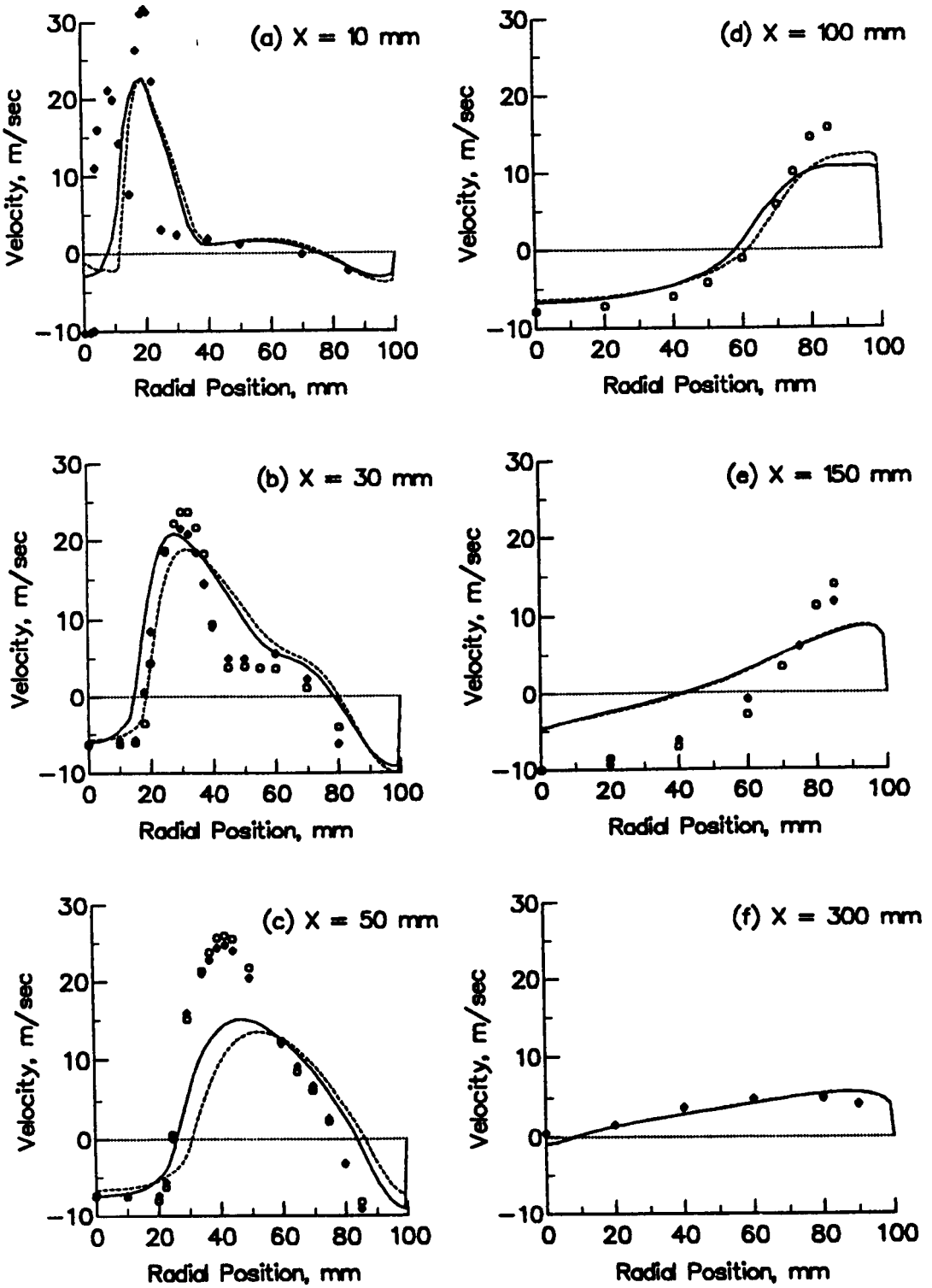

Figure 4.5 Effect of Specification of Inlet Boundary Condition on Axial Velocity Prediction

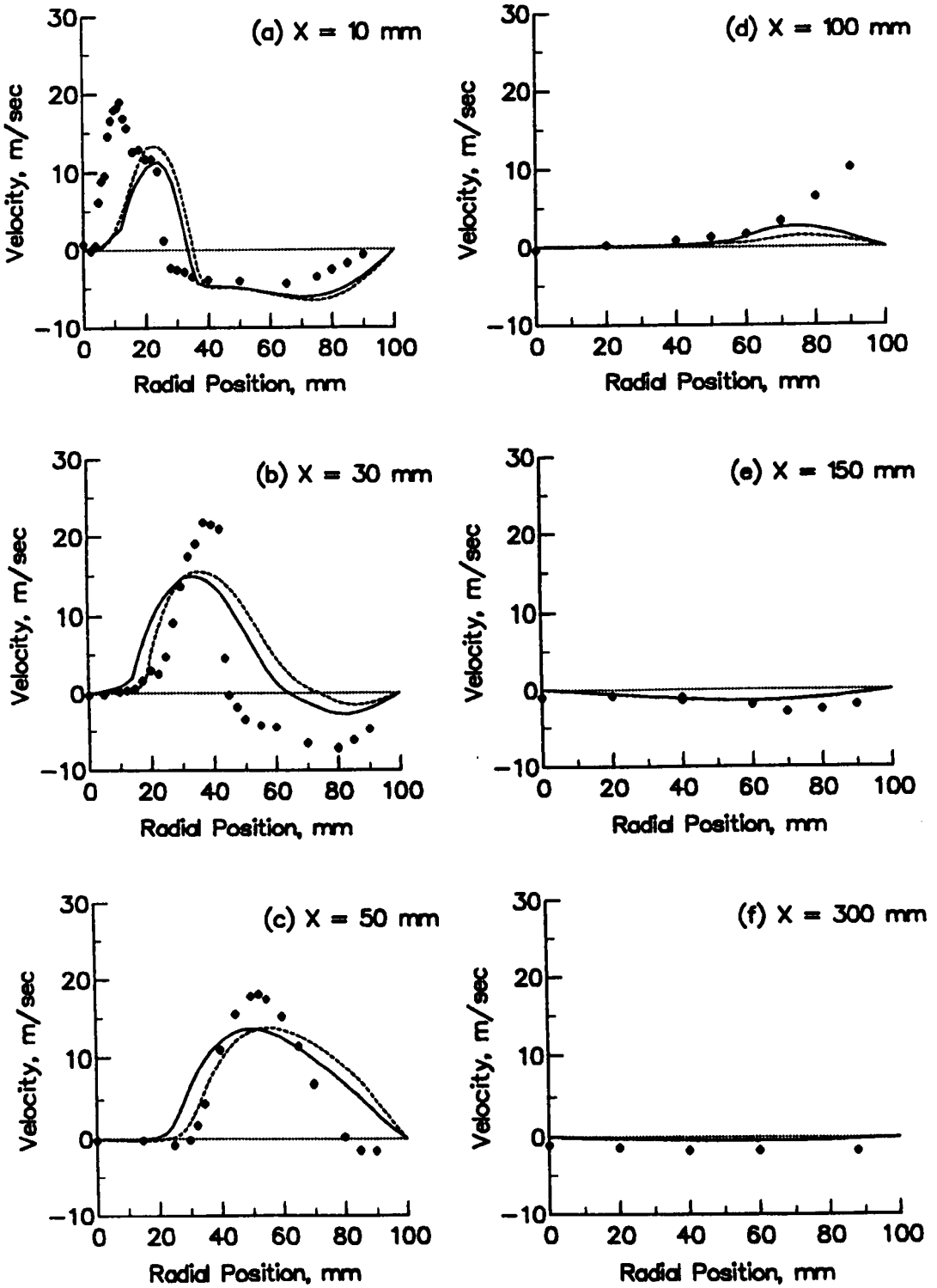

Figure 4.6 Effect of Specification of Inlet Boundary Condition on Radial Velocity Prediction

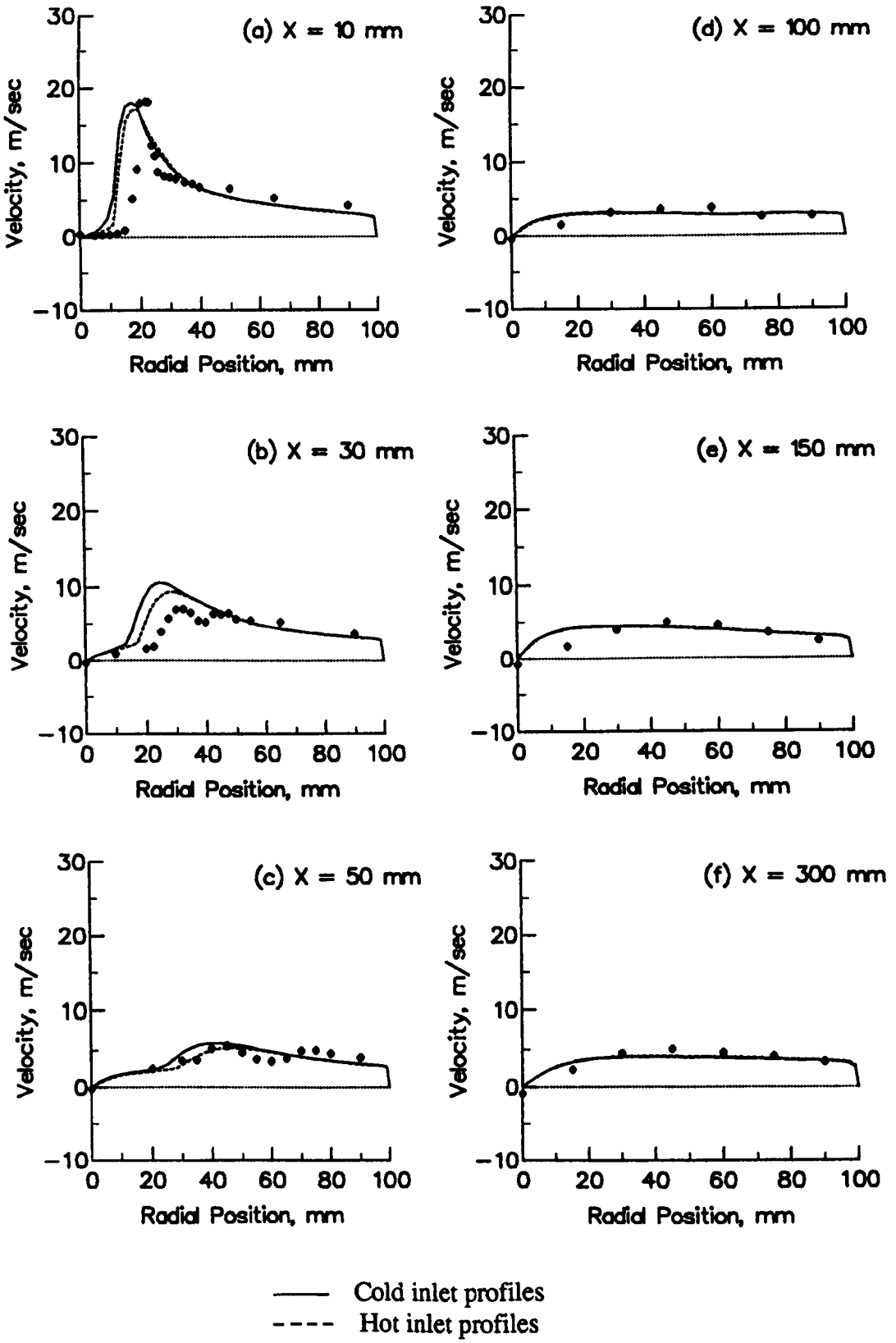

Figure 4.7 Effect of Specification of Inlet Boundary Condition on Swirl Velocity Prediction

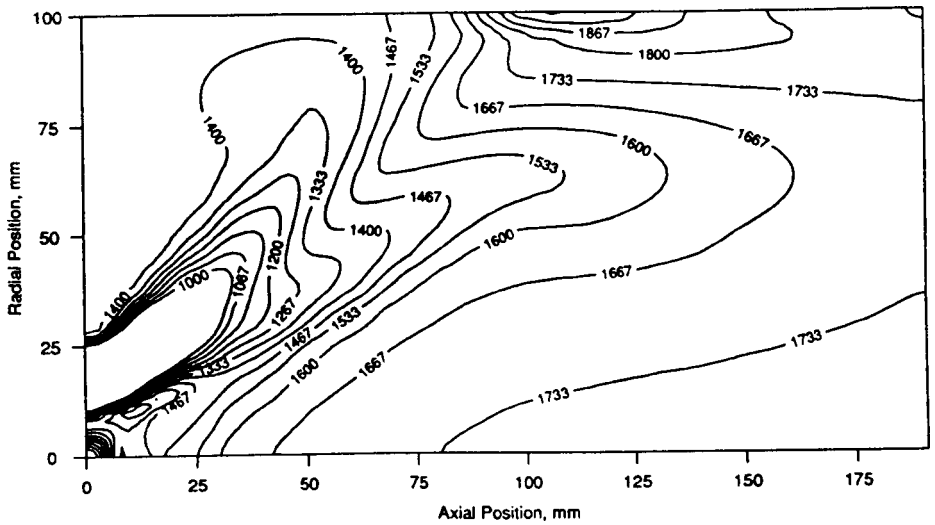

(a) SMD = 90 μm

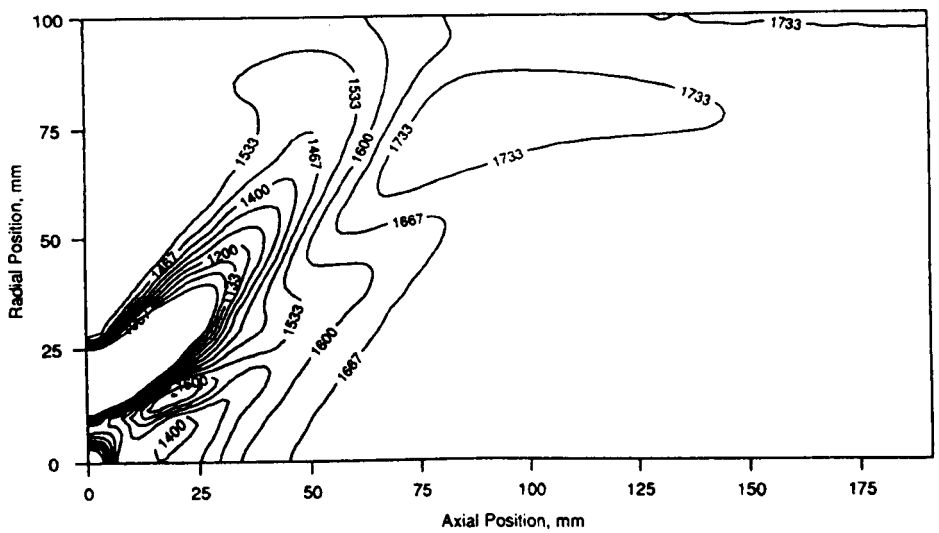

(b) SMD = 70 μm

Figure 4.8 Effect of Change in SMD, in Terms of Mean Temperature (continued)

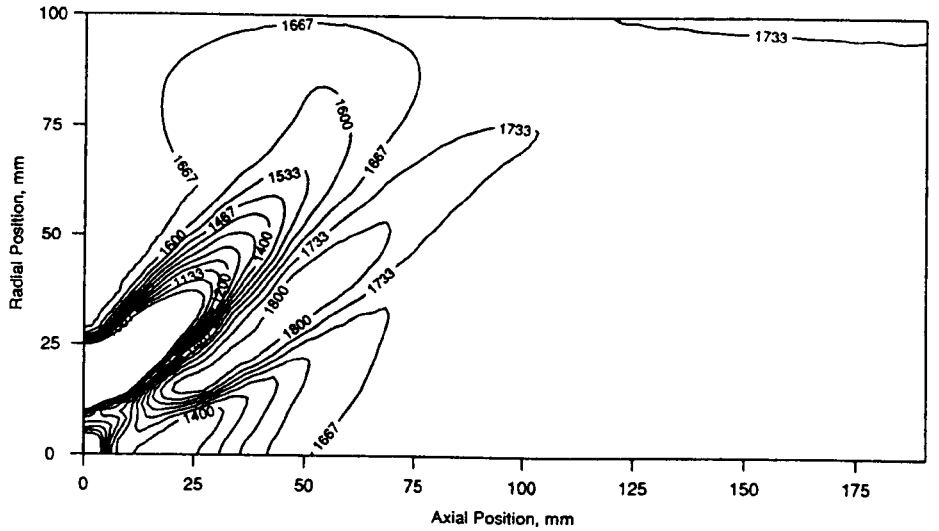

(a) SMD = 50 μm

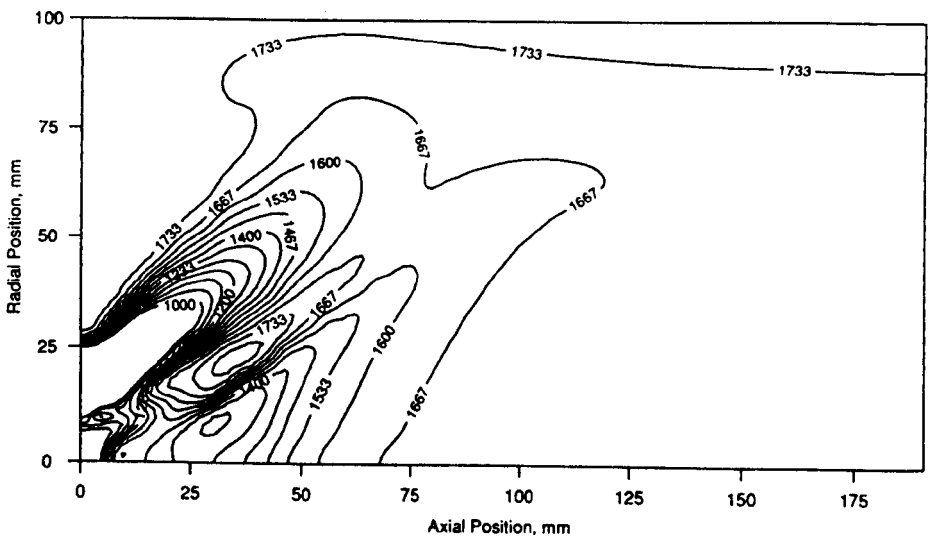

(b) SMD = 30 μm

Figure 4.8 Effect of Change in SMD, in Terms of Mean Temperature (complete)

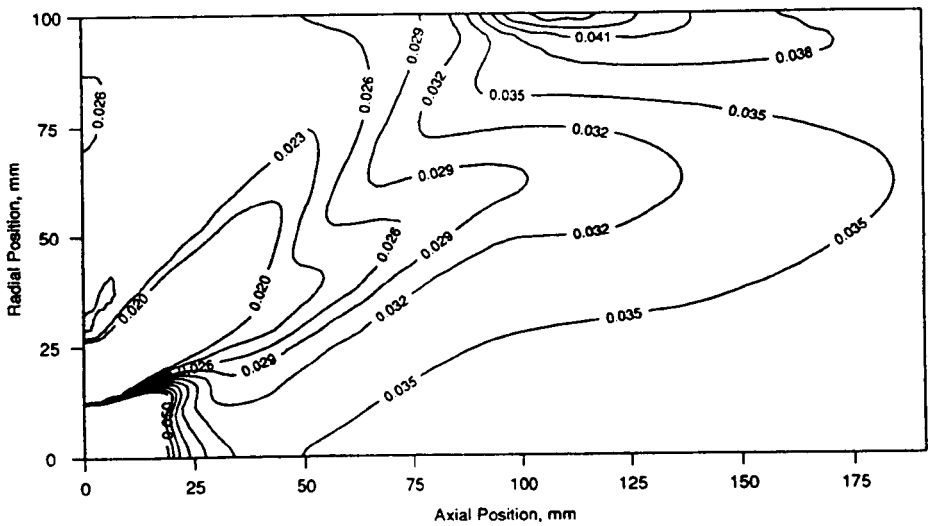

(a) SMD = 90 μm

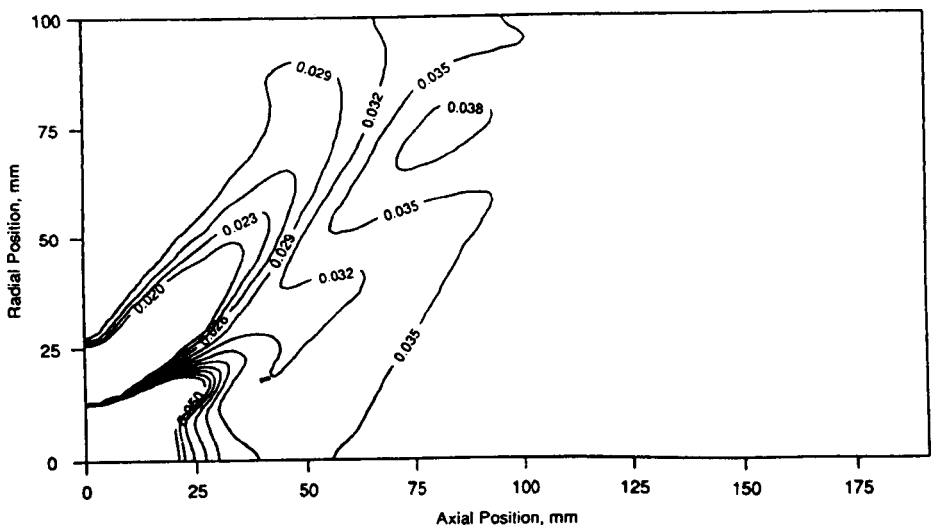

(b) SMD = 70 μm

Figure 4.9 Effect of Change in SMD, in Terms of Mixture Fraction (continued)

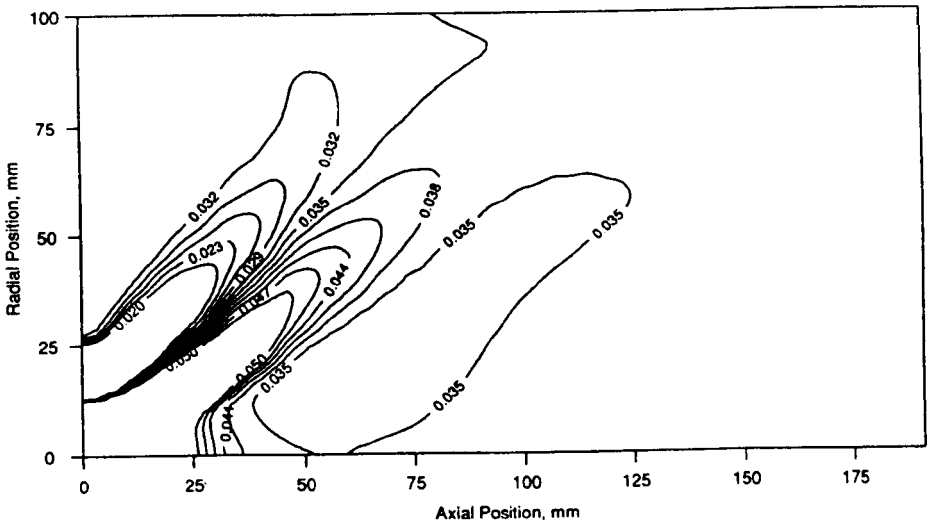

(a) SMD = 50 μm

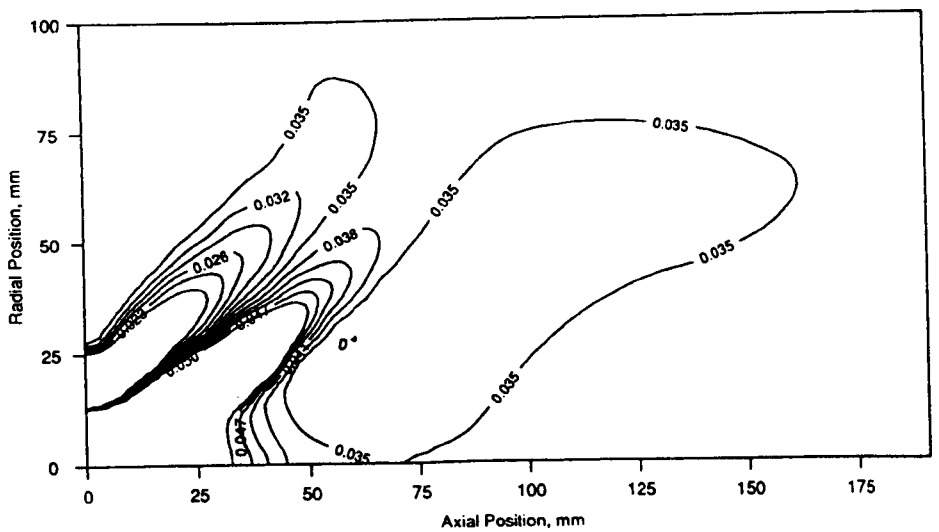

(b) SMD = 30 μm

Figure 4.9 Effect of Change in SMD, in Terms of Mixture Fraction (complete)

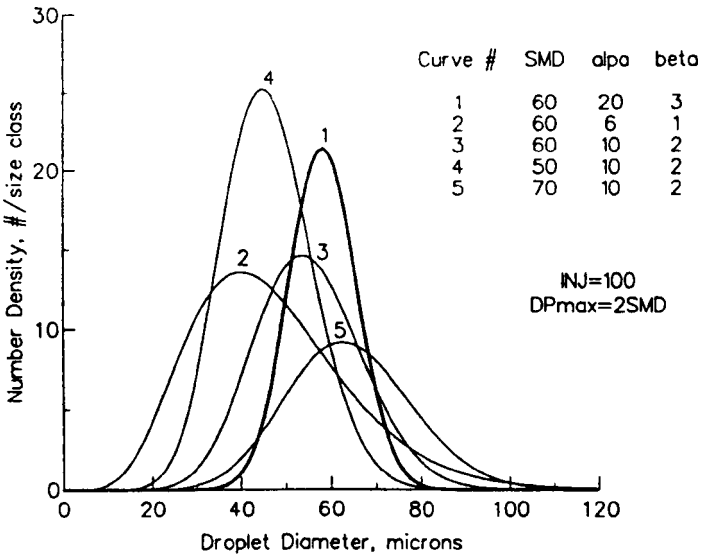

(a) Droplet Size Distributions Tested

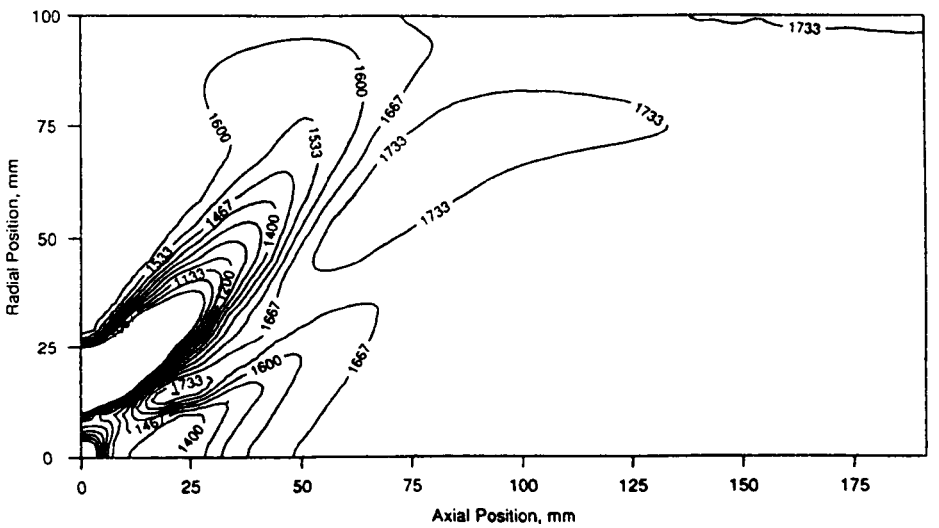

(b) Curve 1

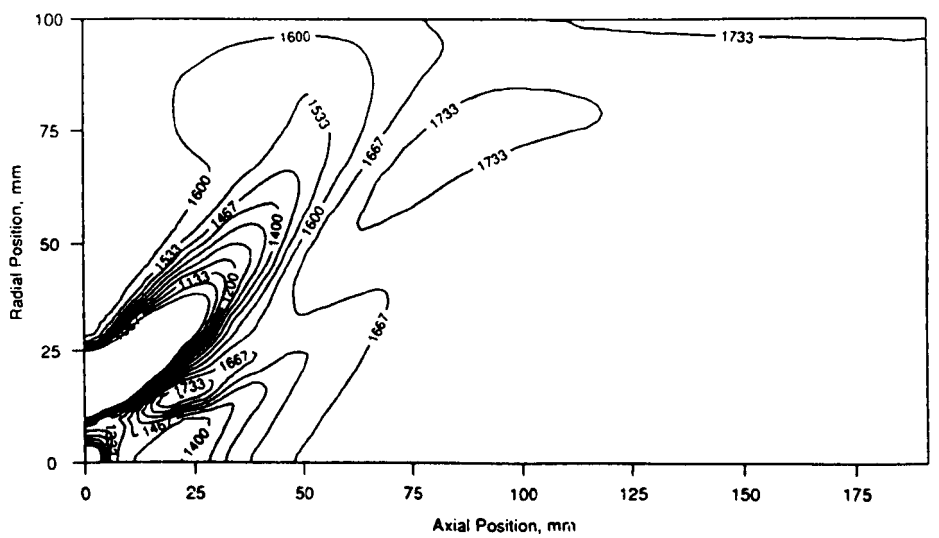

(c) Curve 3

Figure 4.10 Effect of Change in DSD, in Terms of Mean Temperature (continued)

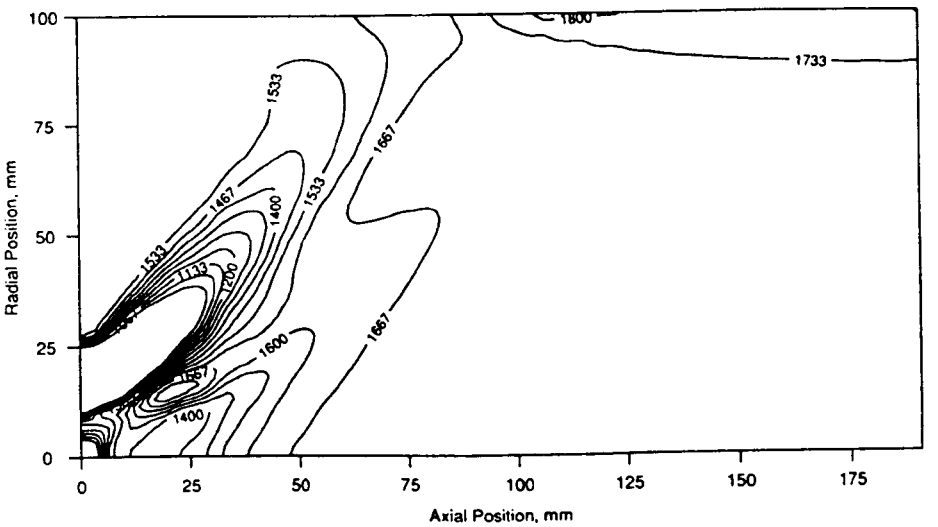

(d) Curve 2

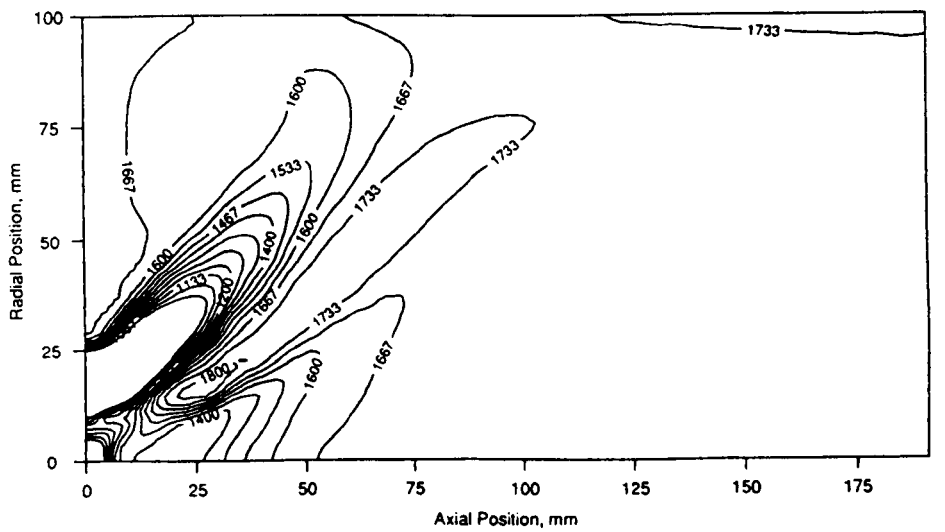

(e) Curve 4

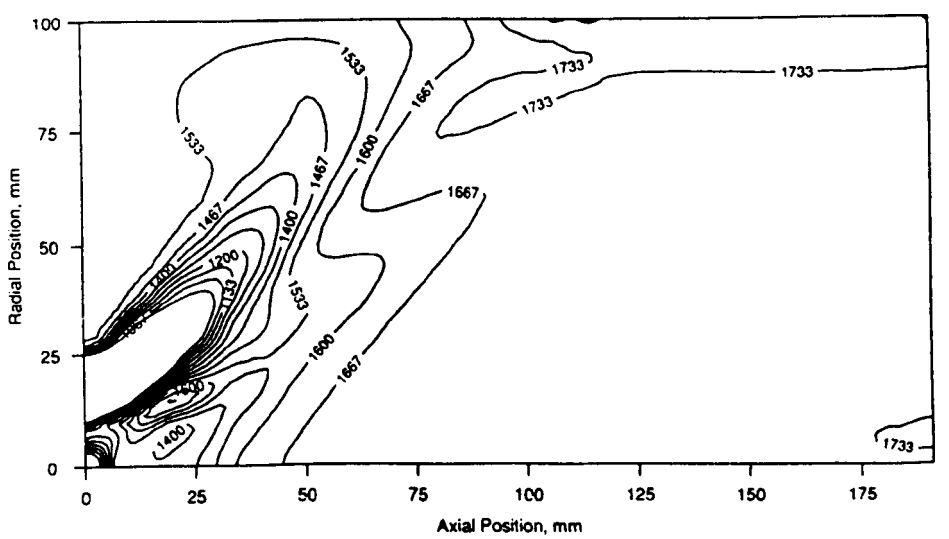

(f) Curve 5

Figure 4.10 Effect of Change in DSD, in Terms of Mean Temperature (complete)

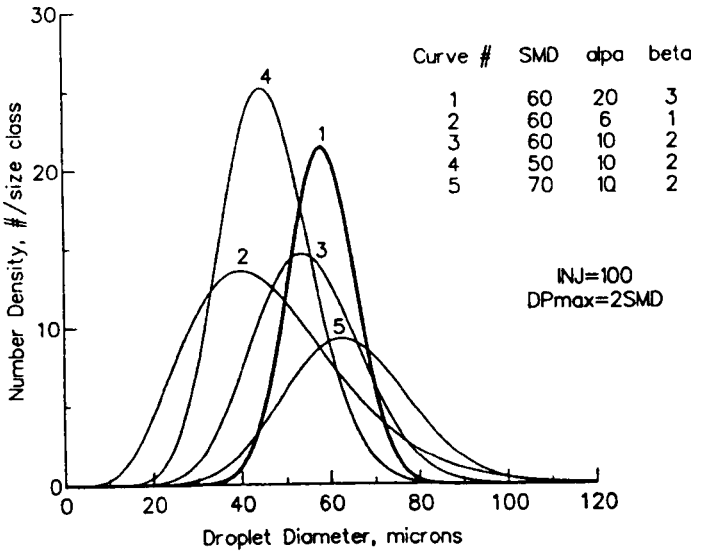

(a) Droplet Size Distributions Tested

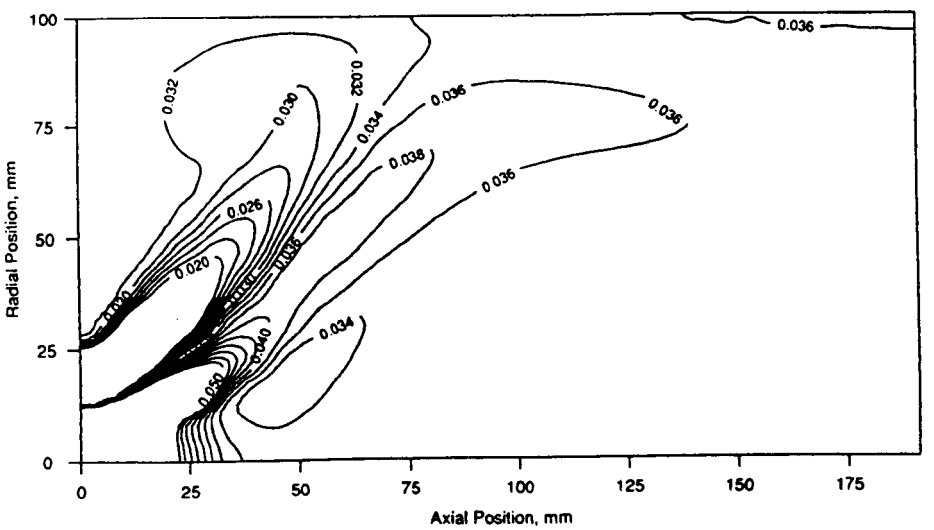

(b) Curve 1

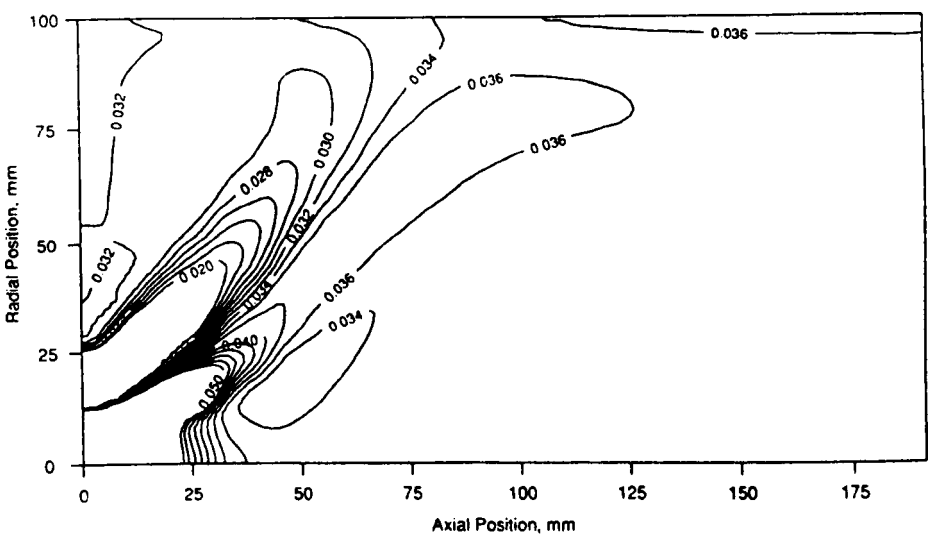

(c) Curve 3

Figure 4.11 Effect of Change in DSD, in Terms of Mixture Fraction (continued)

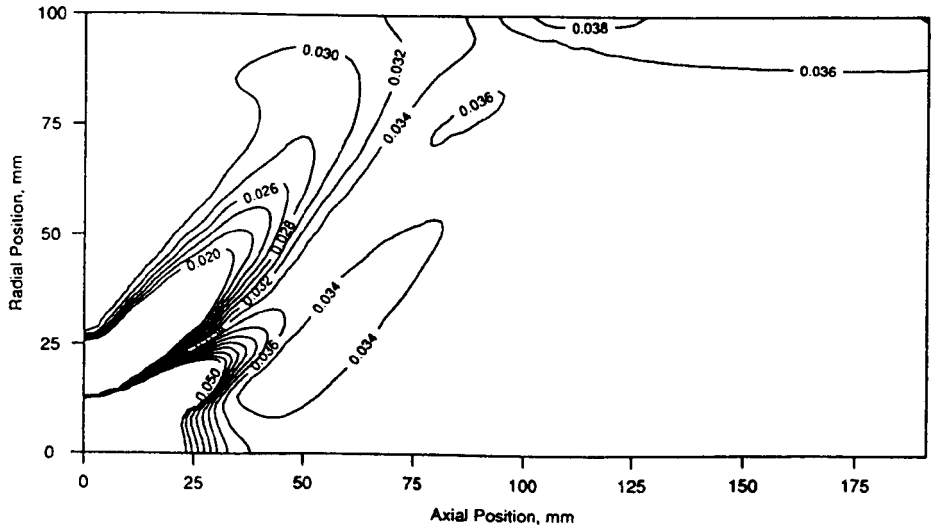

(d) Curve 2

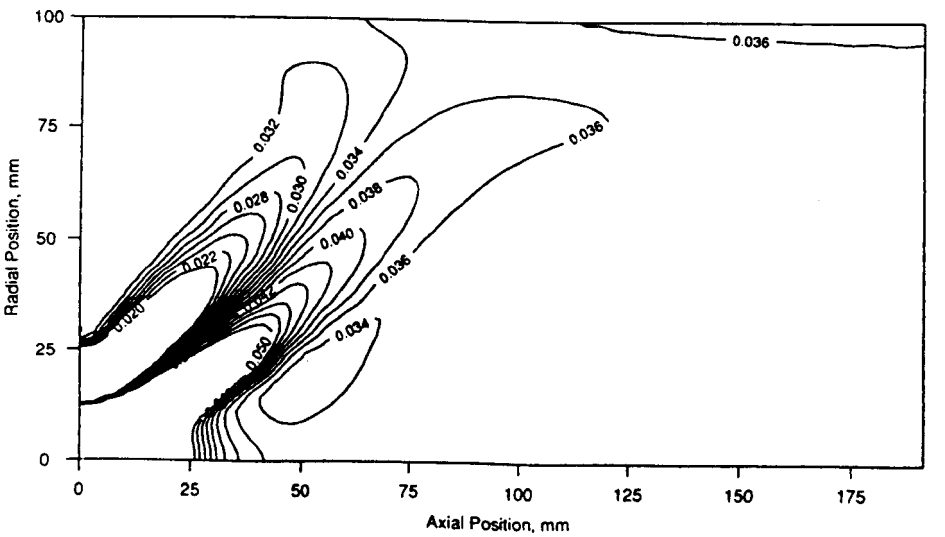

(e) Curve 4

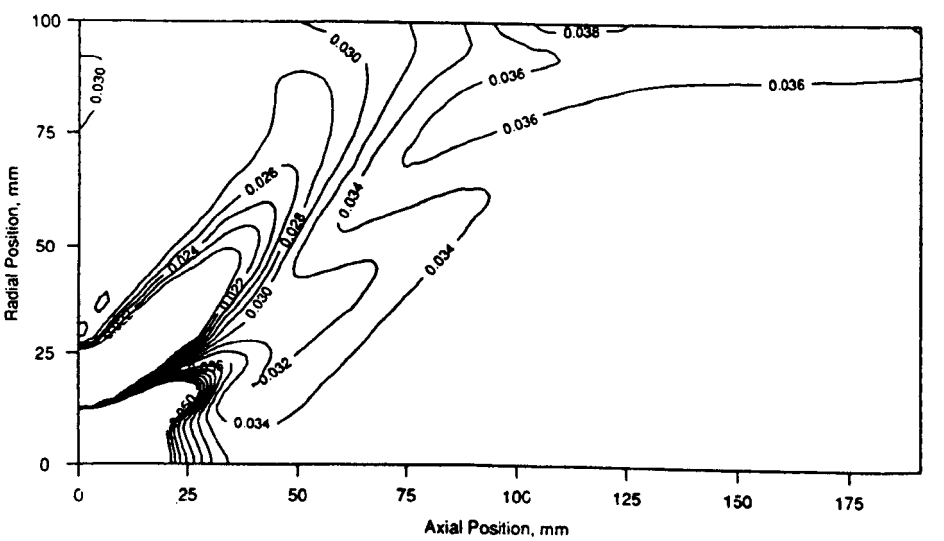

(f) Curve 5

Figure 4.11 Effect of Change in DSD, in Terms of Mixture Fraction (complete)

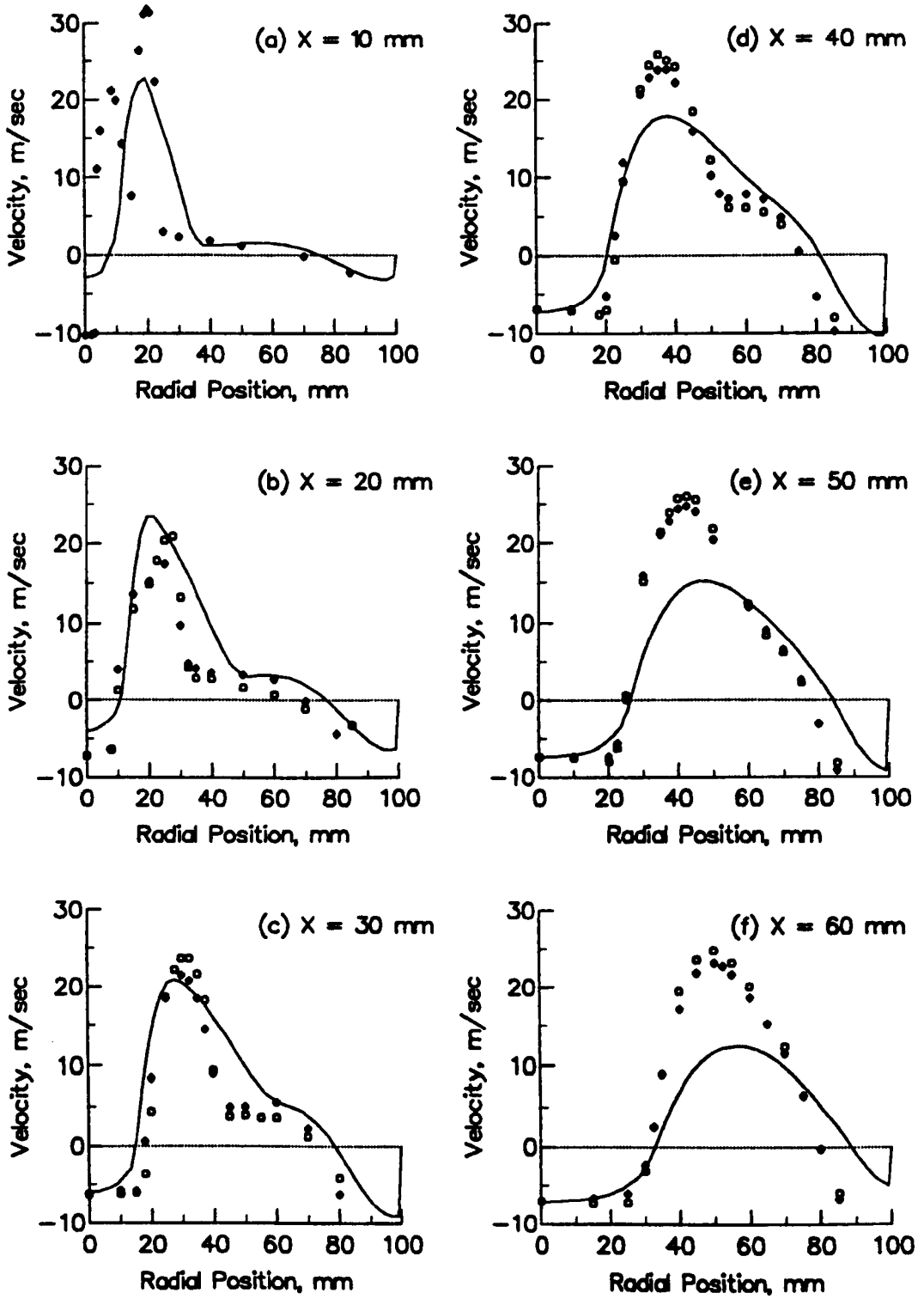

Figure 4.12 Mean Axial Velocities (continued)

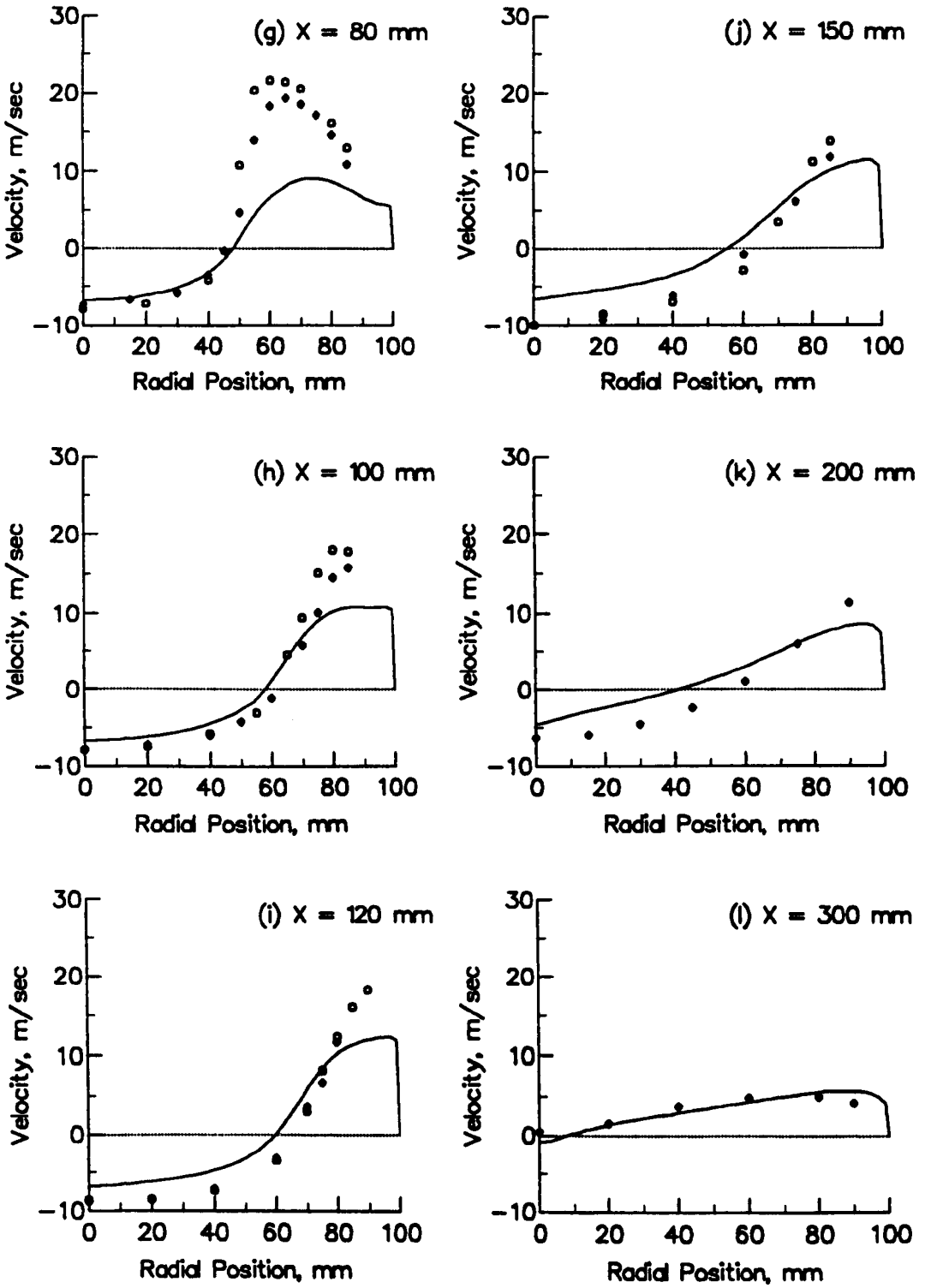

Figure 4.12 Mean Axial Velocities (complete)

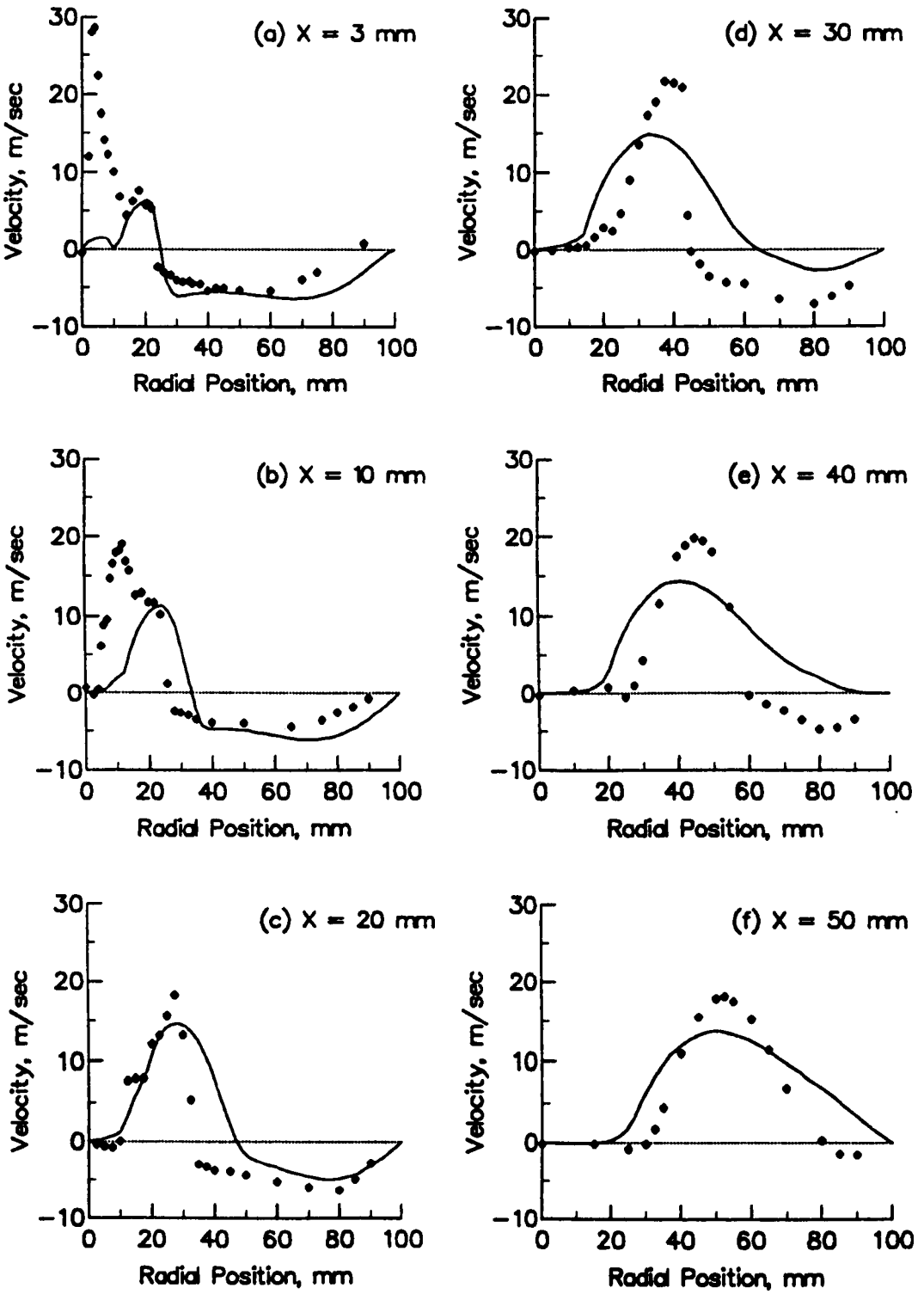

Figure 4.13 Mean Radial Velocities (continued)

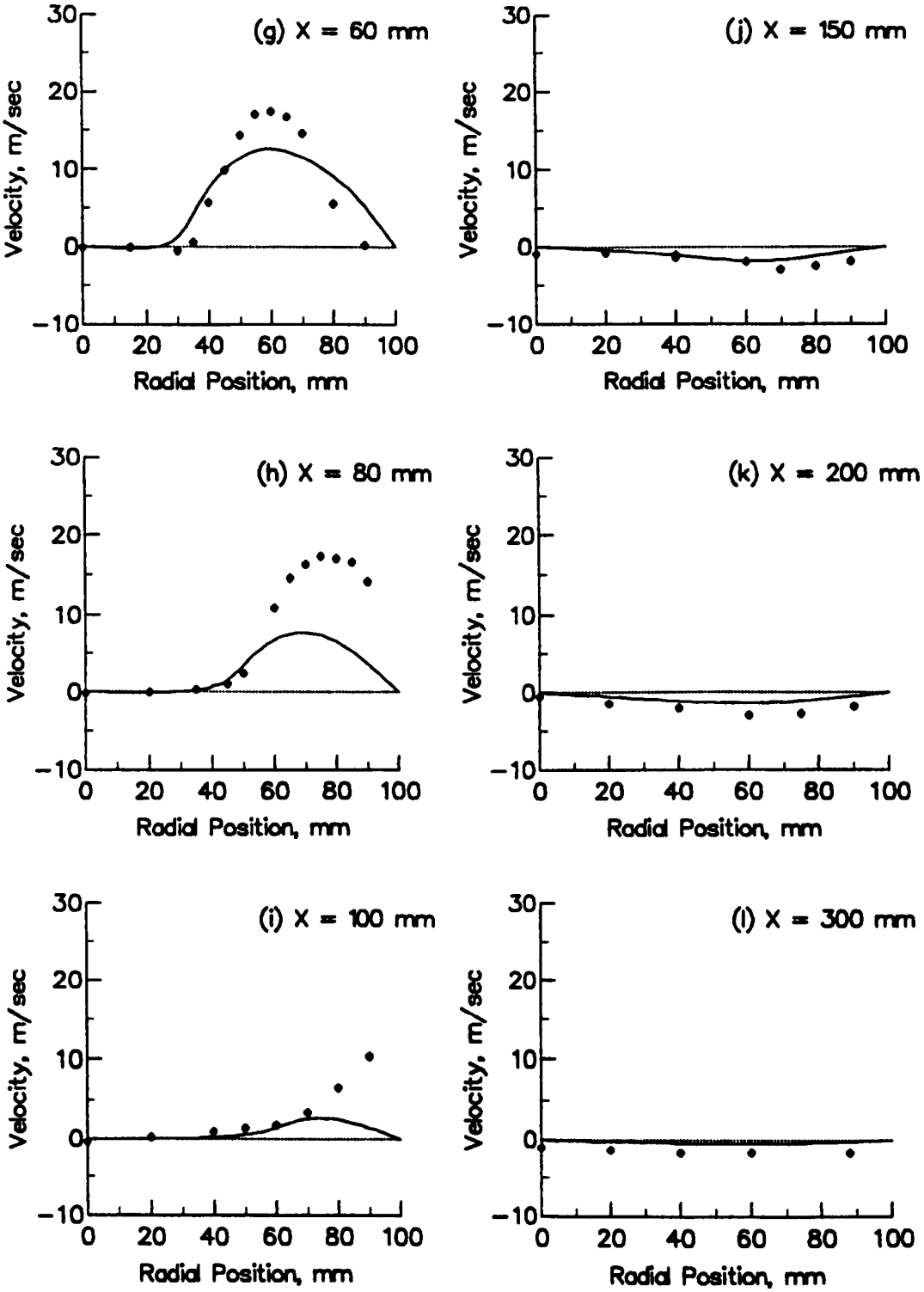

Figure 4.13 Mean Radial Velocities (complete)

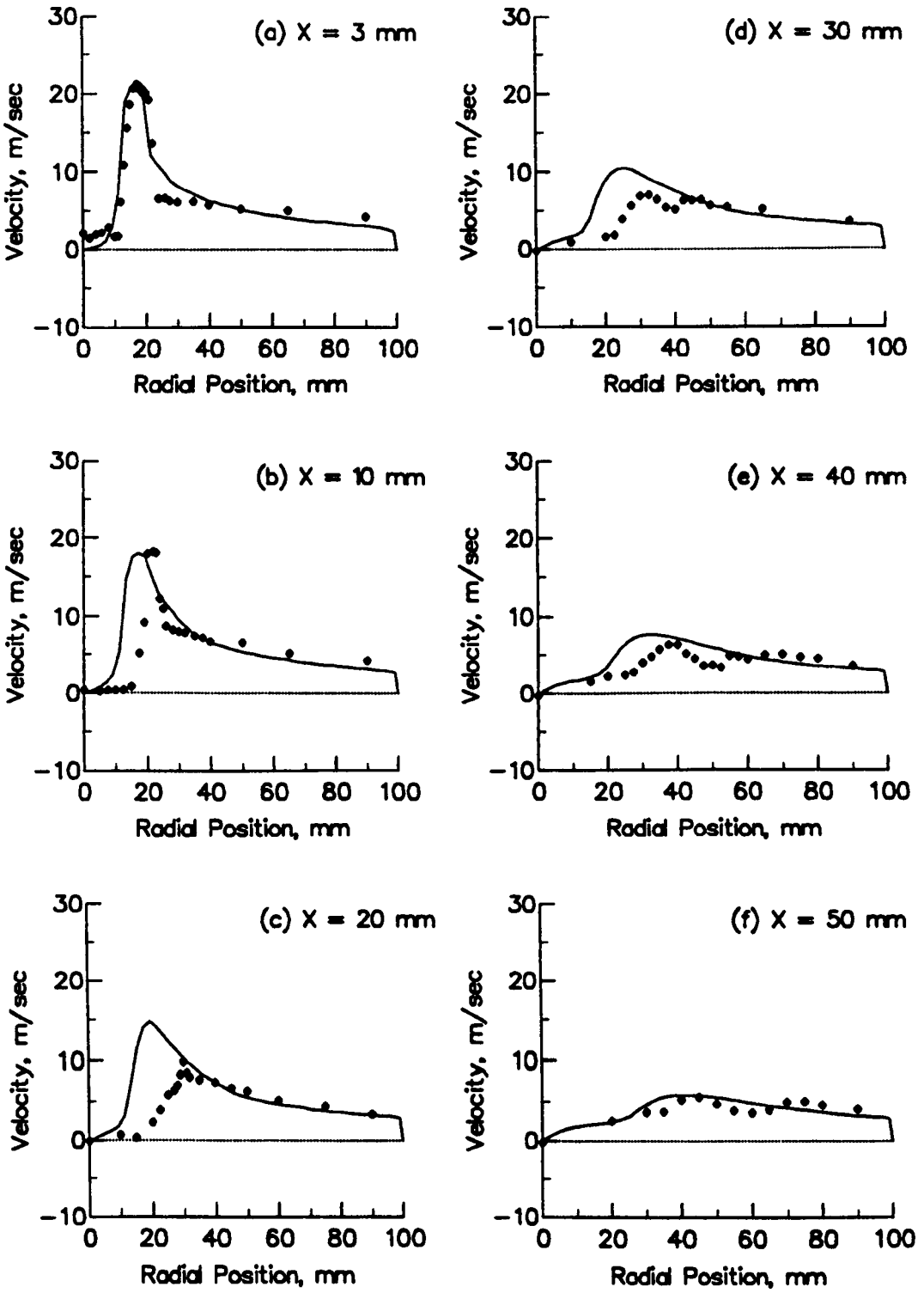

Figure 4.14 Mean Swirl Velocities (continued)

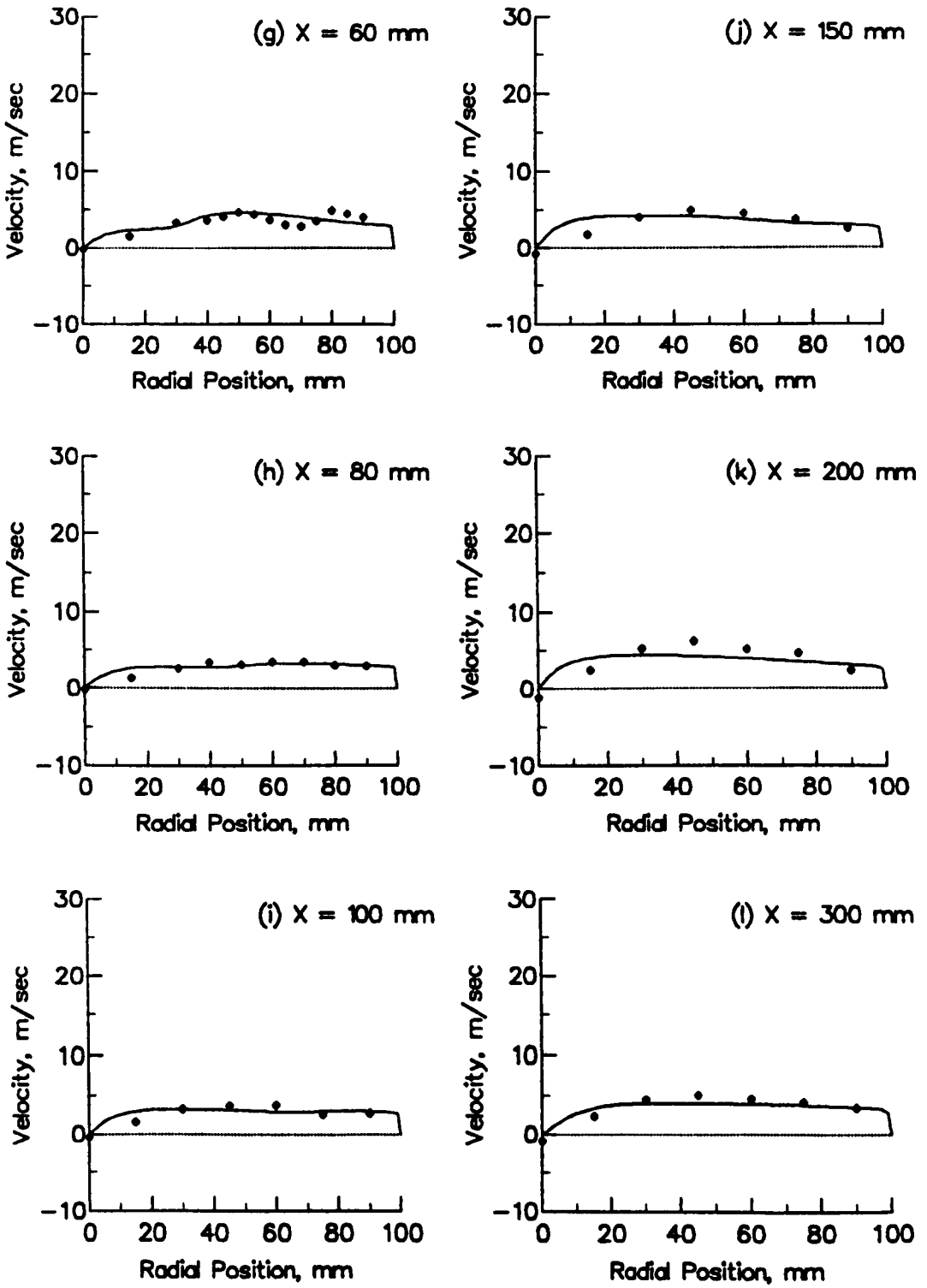

Figure 4.14 Mean Swirl Velocities (complete)

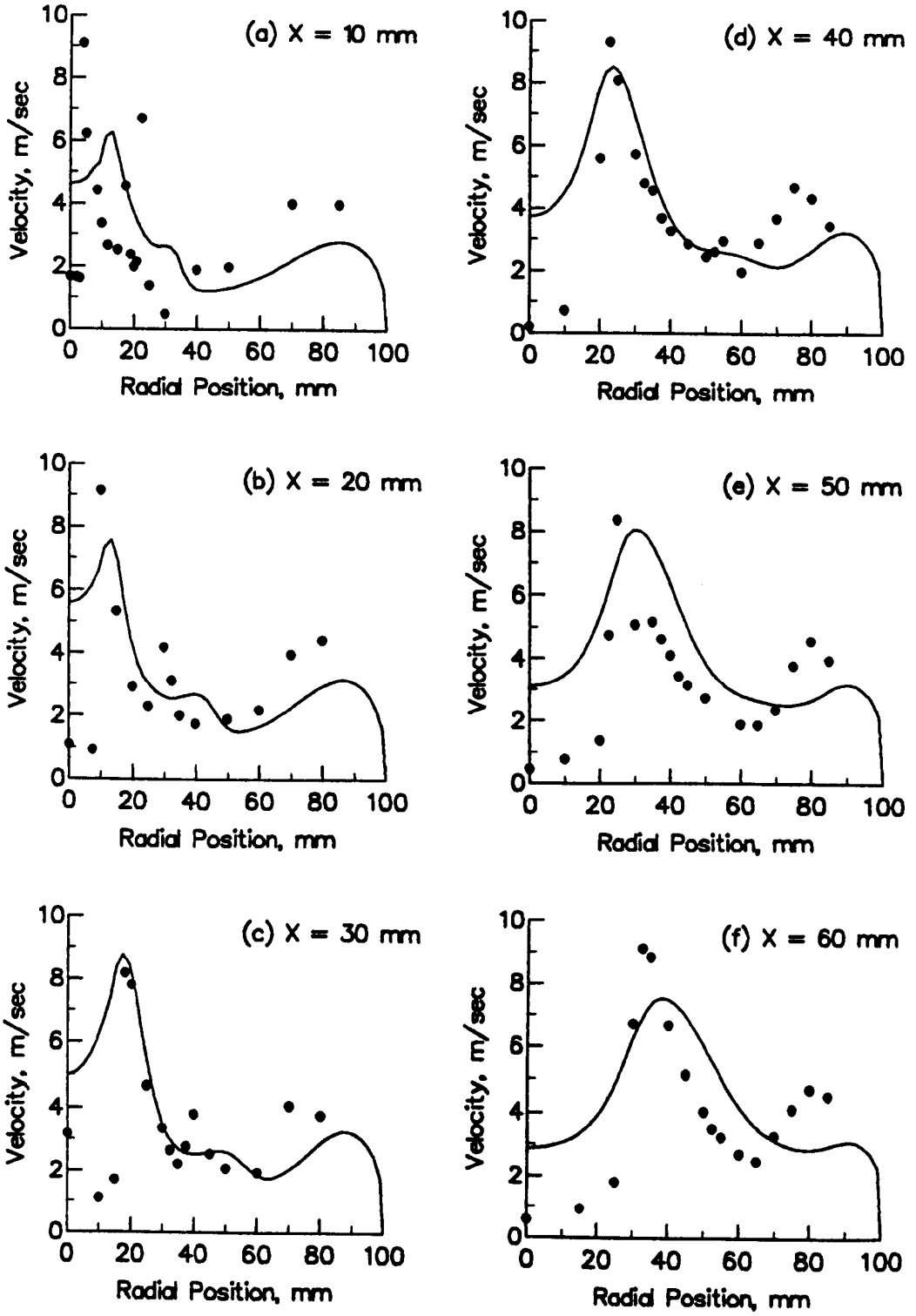

Figure 4.15 RMS Axial Velocities (continued)

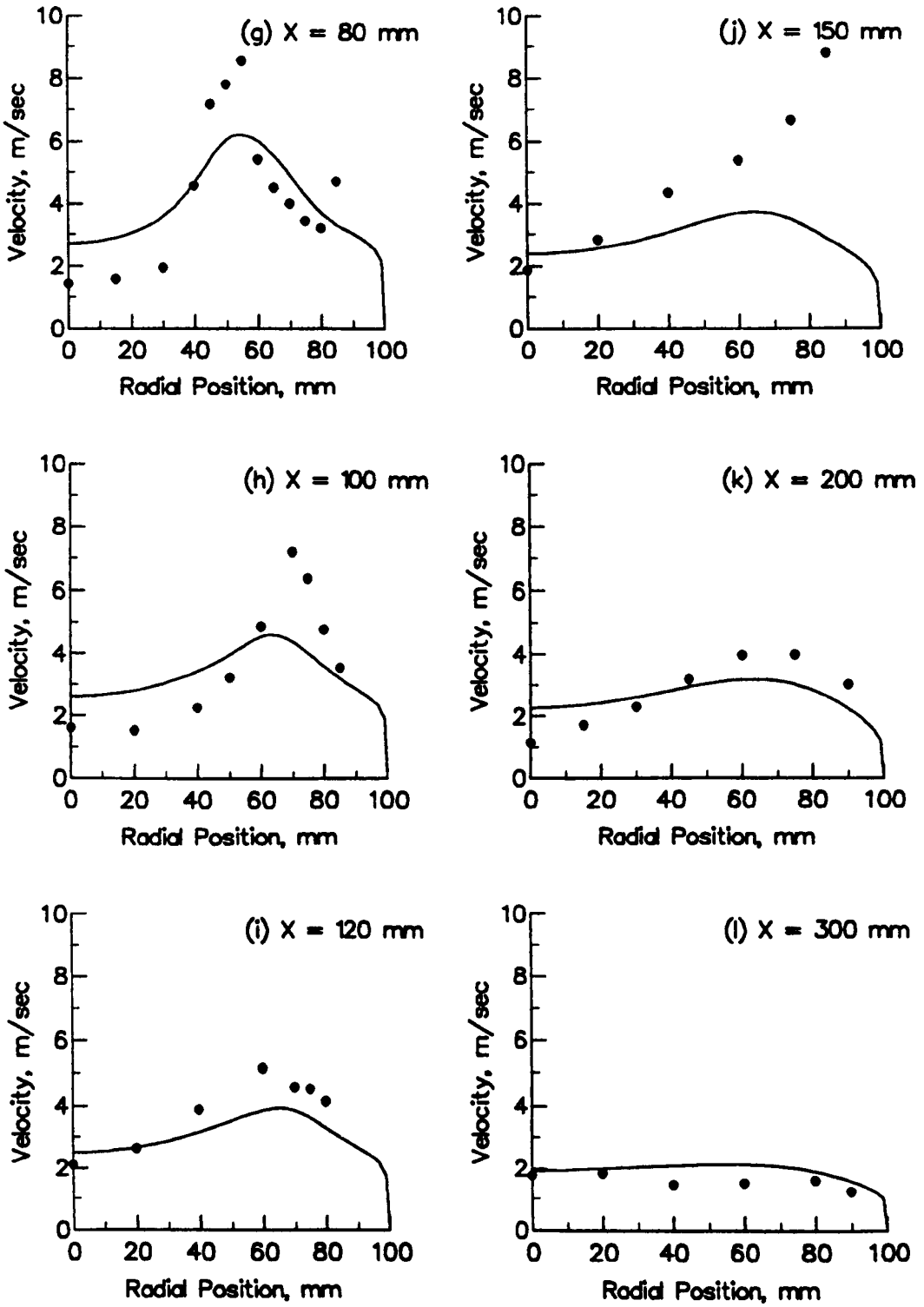

Figure 4.15 RMS Axial Velocities (complete)

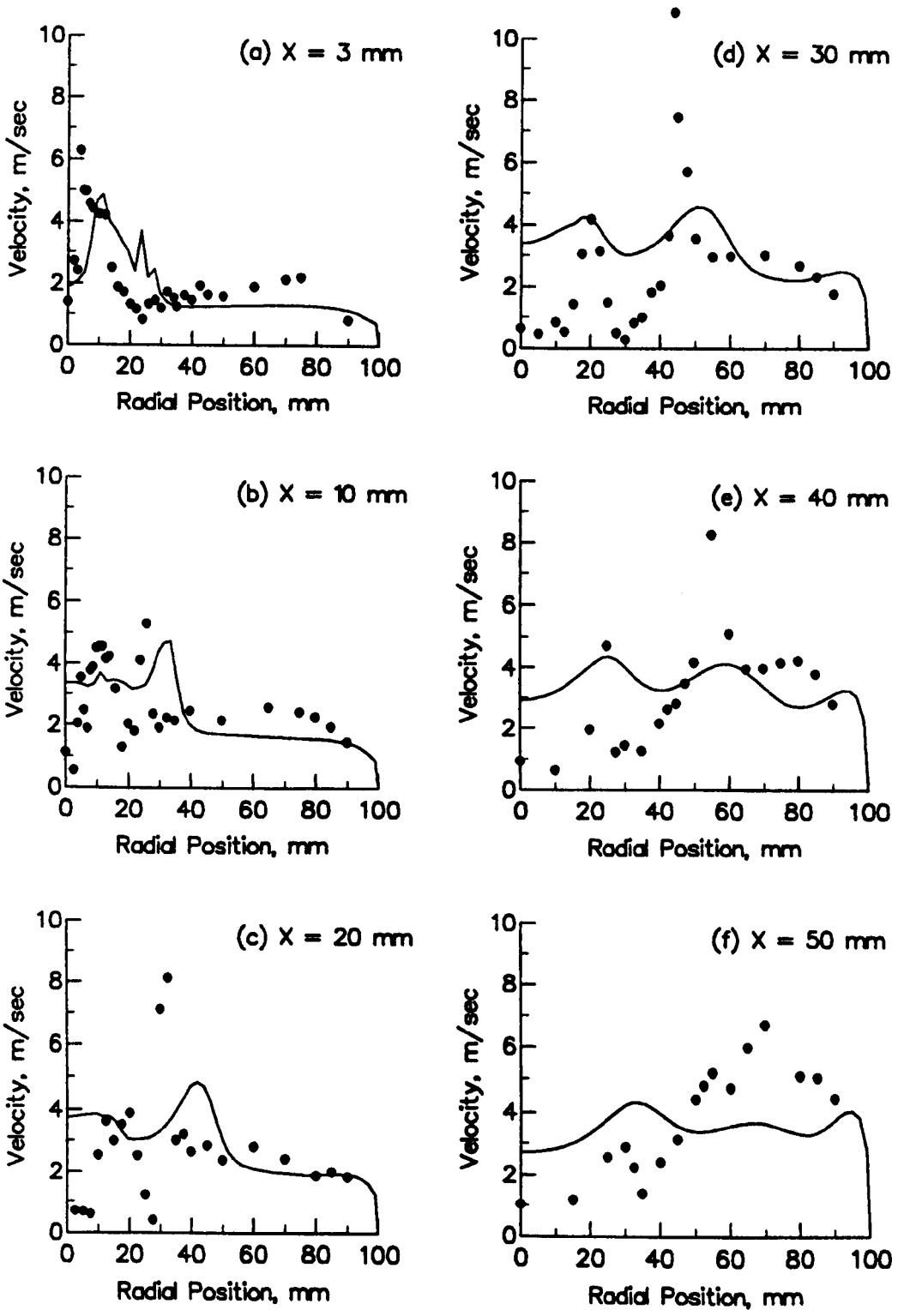

Figure 4.16 RMS Radial Velocities (continued)

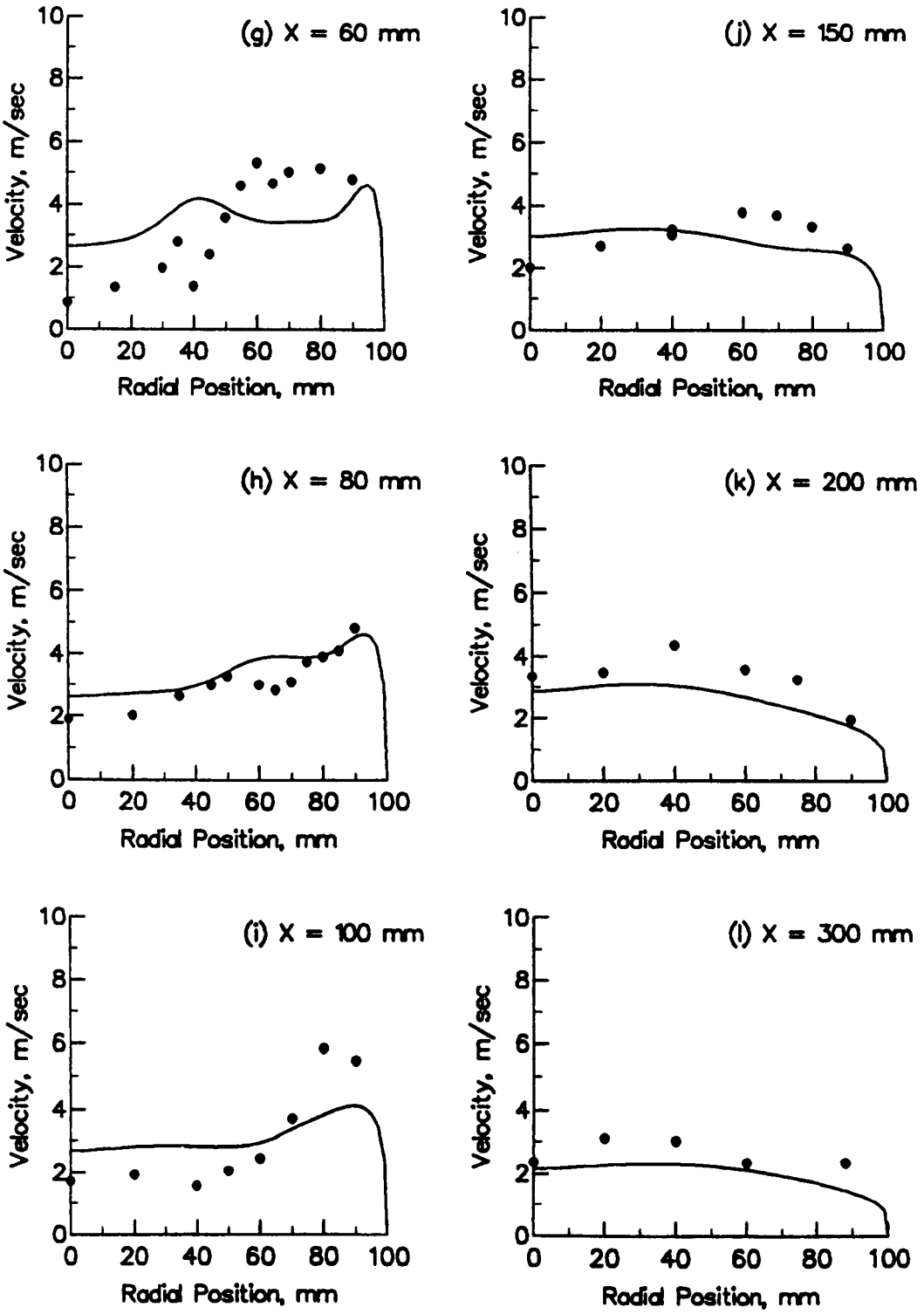

Figure 4.16 RMS Radial Velocities (complete)

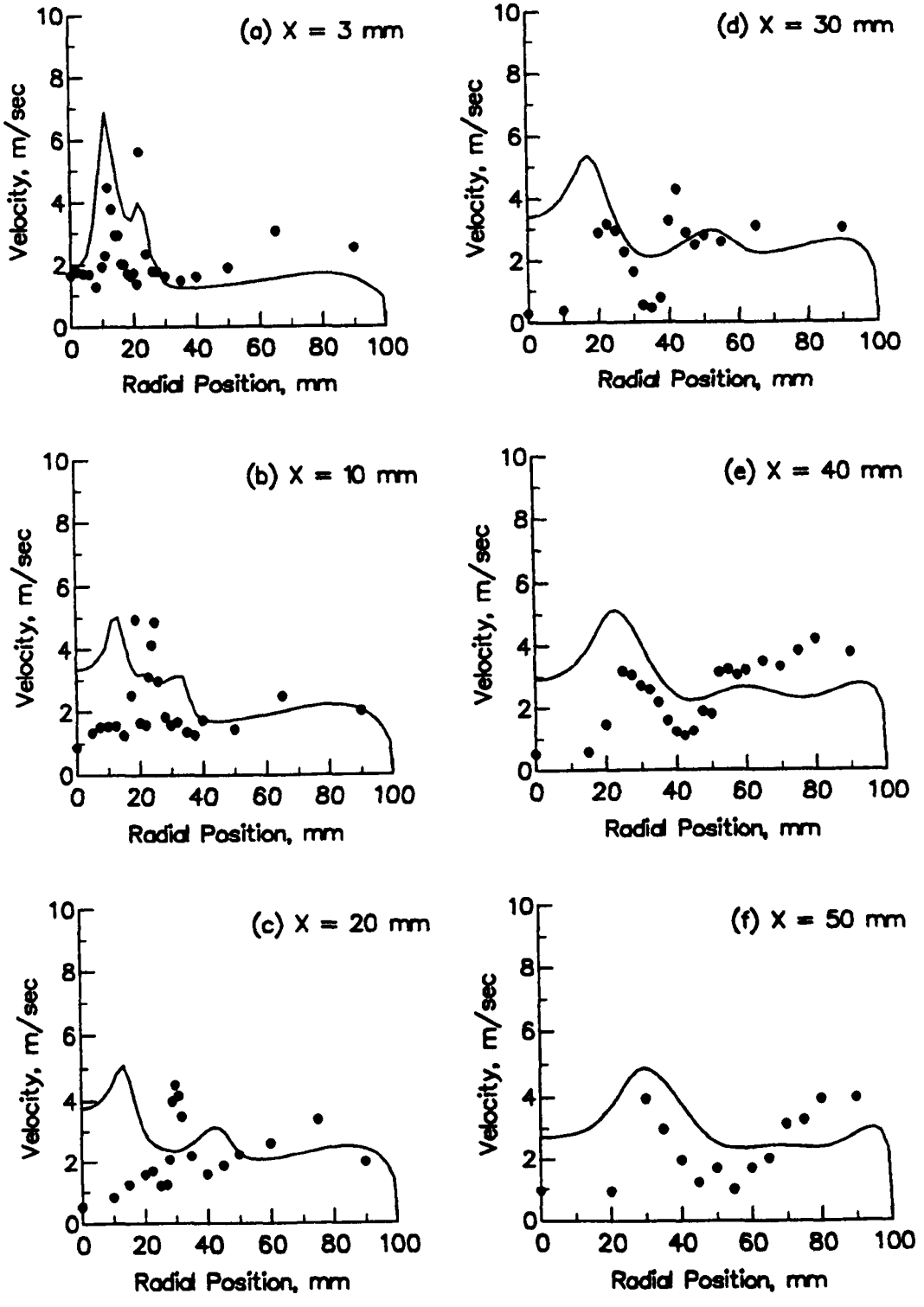

Figure 4.17 RMS Swirl Velocities (continued)

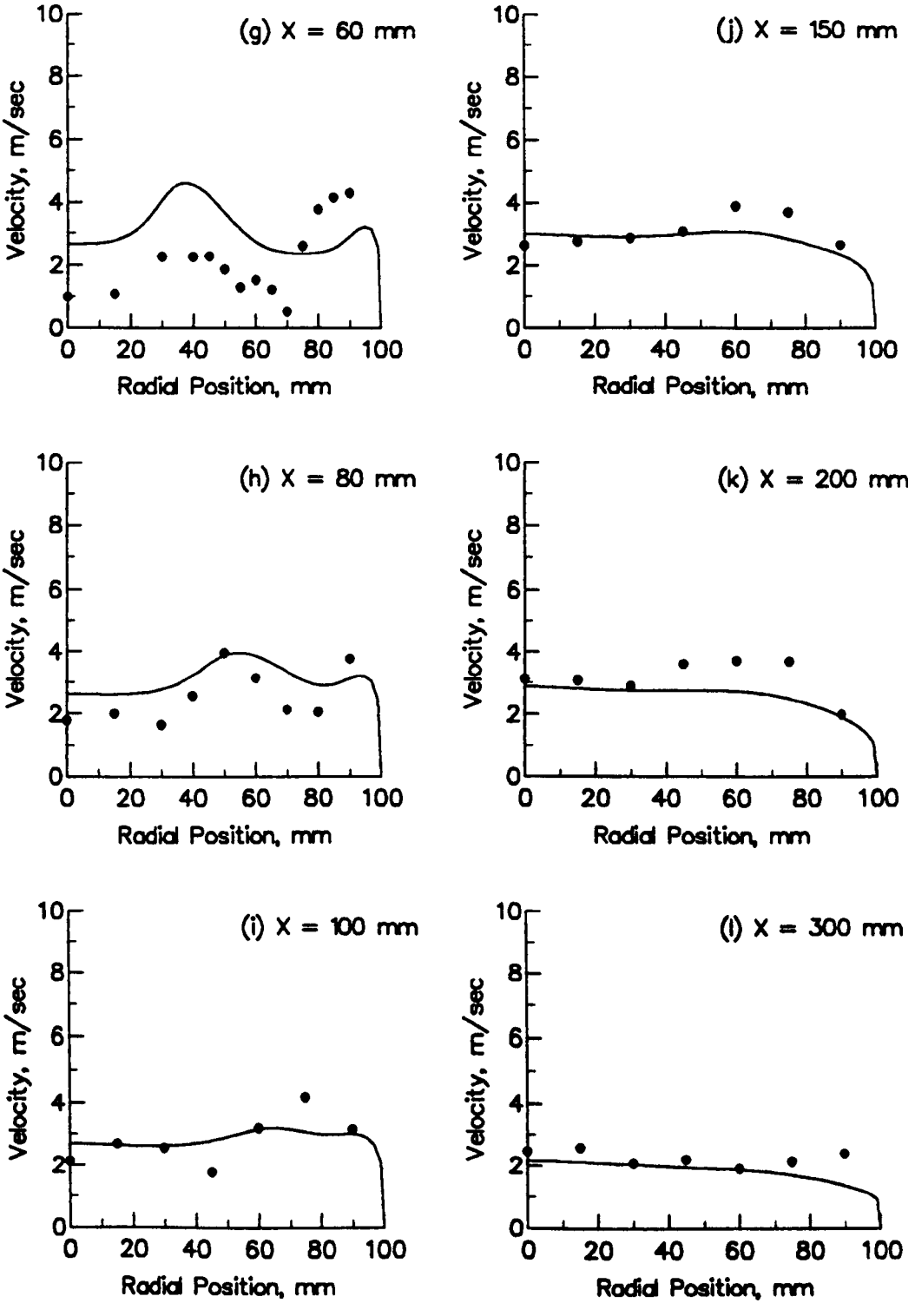

Figure 4.17 RMS Swirl Velocities (complete)

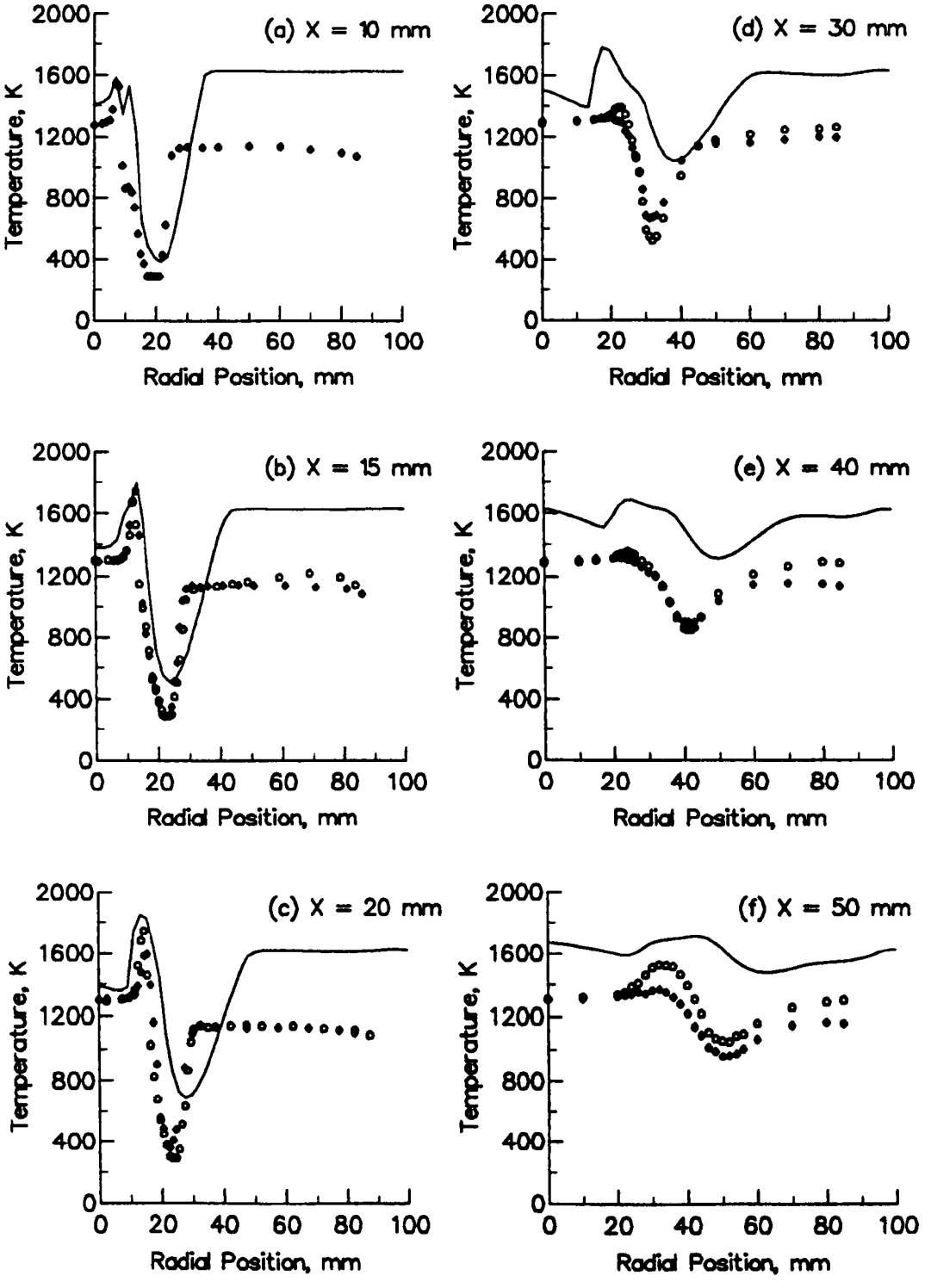

Figure 4.18 Mean Temperature Profiles (continued)

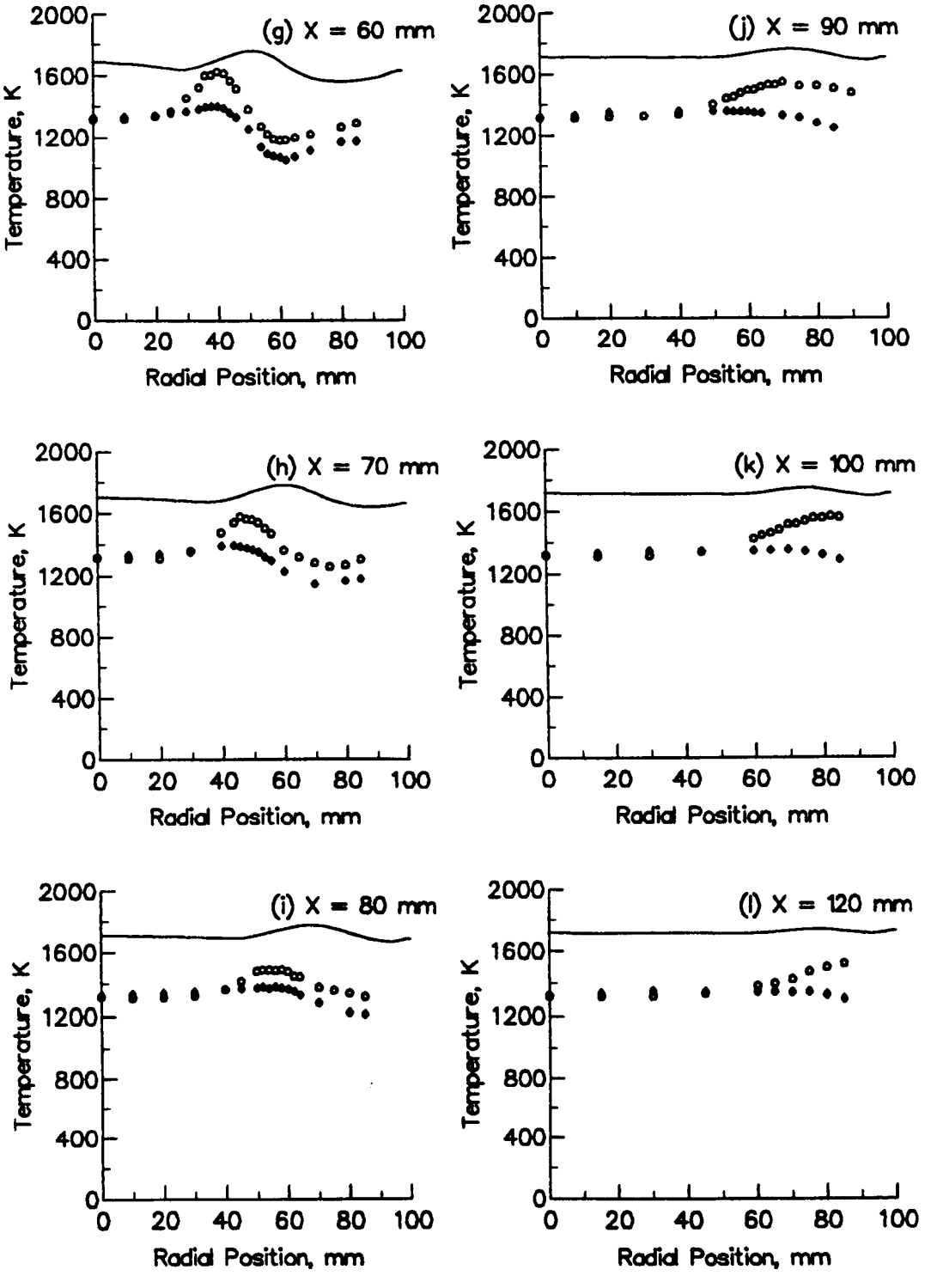

Figure 4.18 Mean Temperature Profiles (complete)

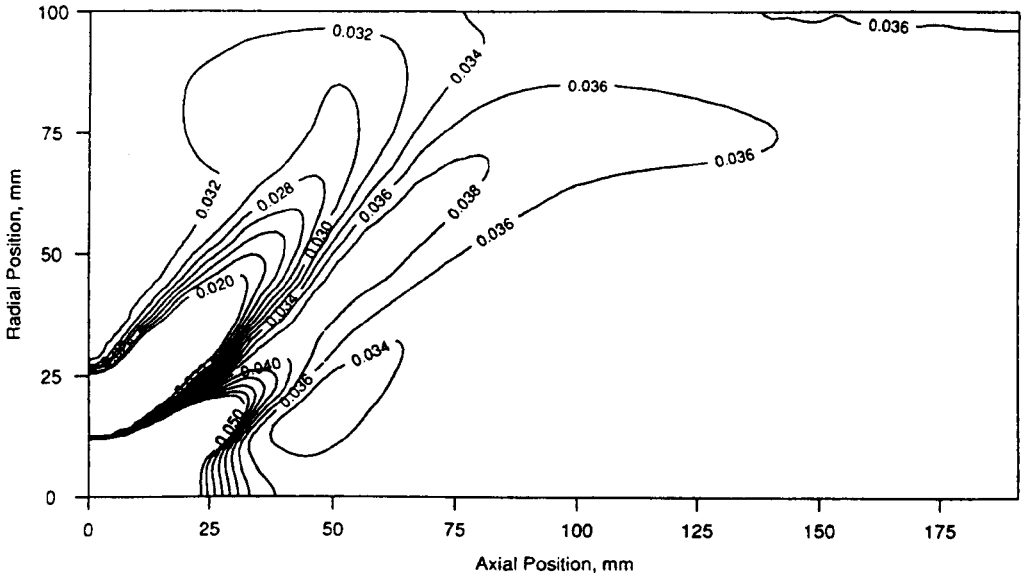

Figure 4.19 Mean Temperature Contours

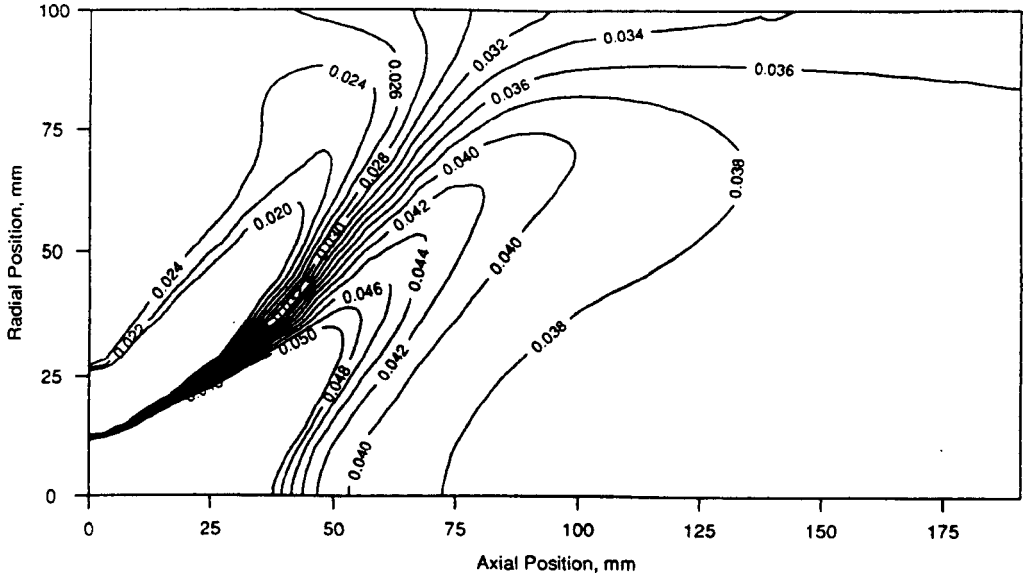

Figure 4.20 Mean Temperature Contours, with k-ε Model for Turbulence

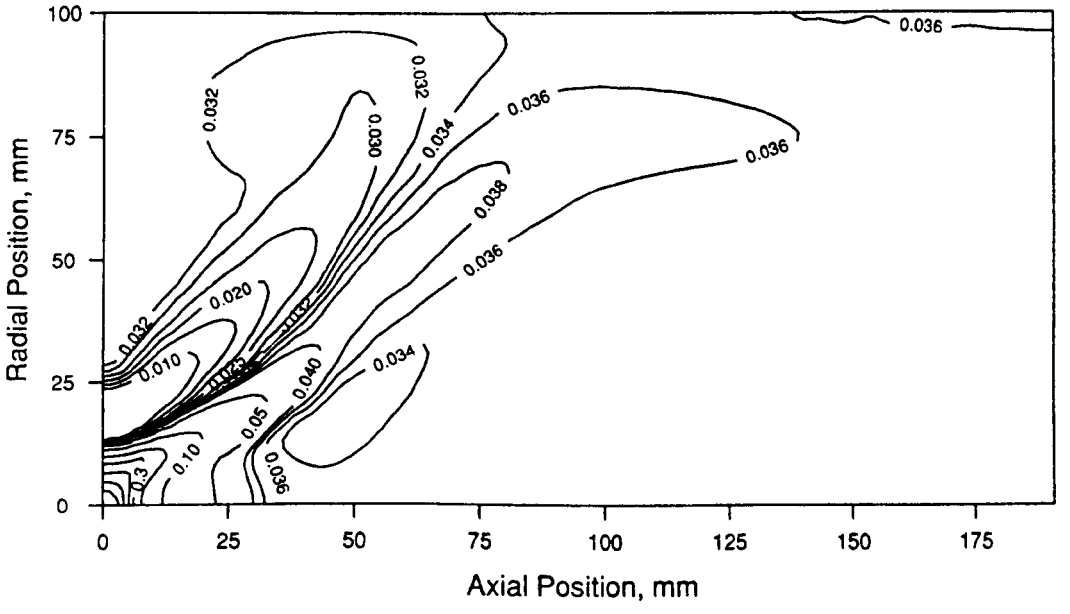

Figure 4.21 Mixture Fraction Contours

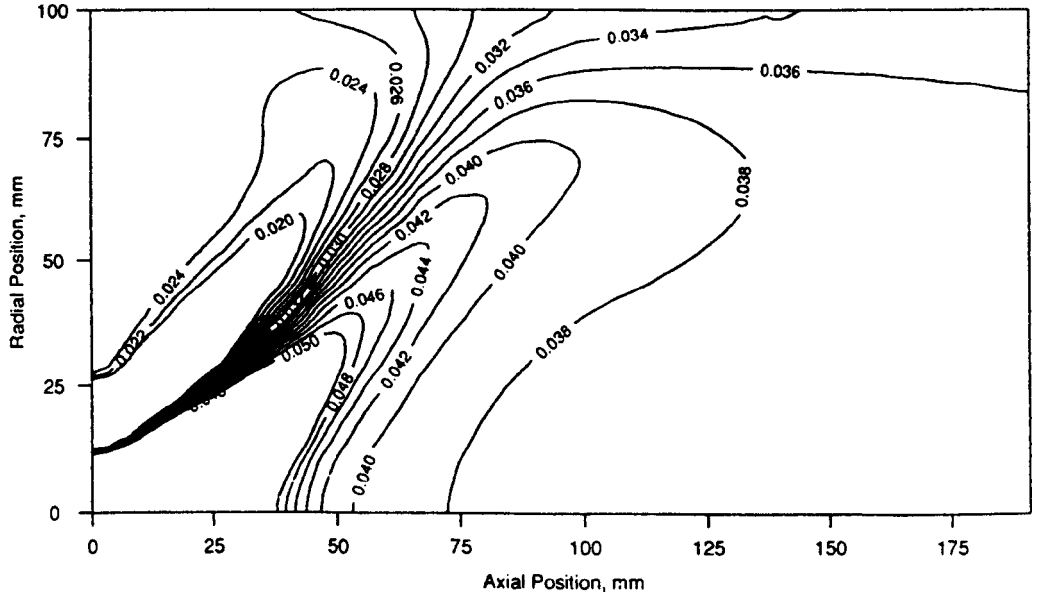

Figure 4.22 Mixture Fraction Contours, with k-ε Model for Turbulence

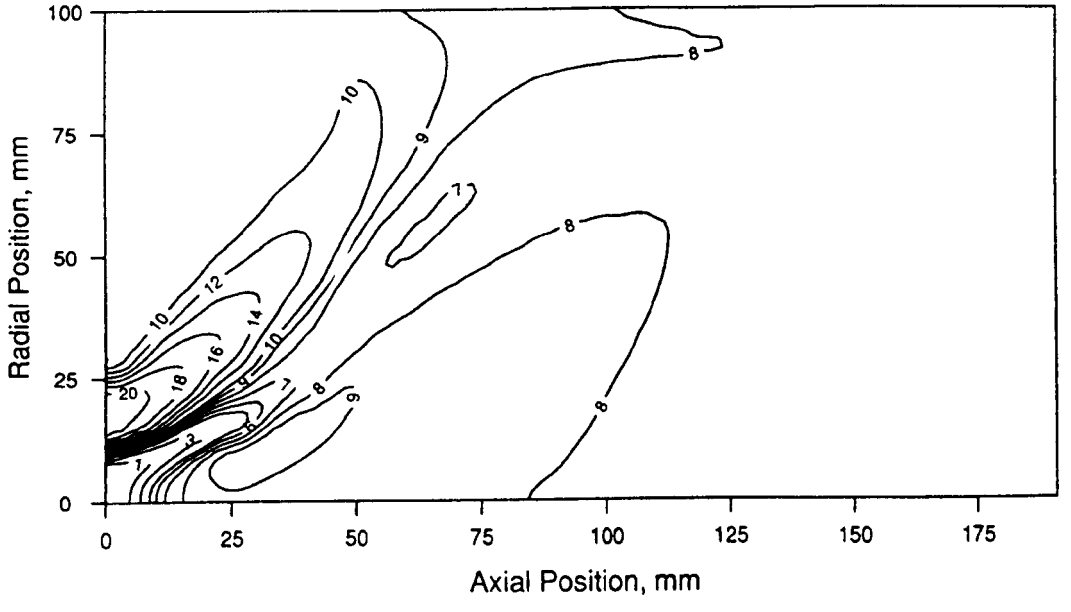

(a) O_2, dry mol %

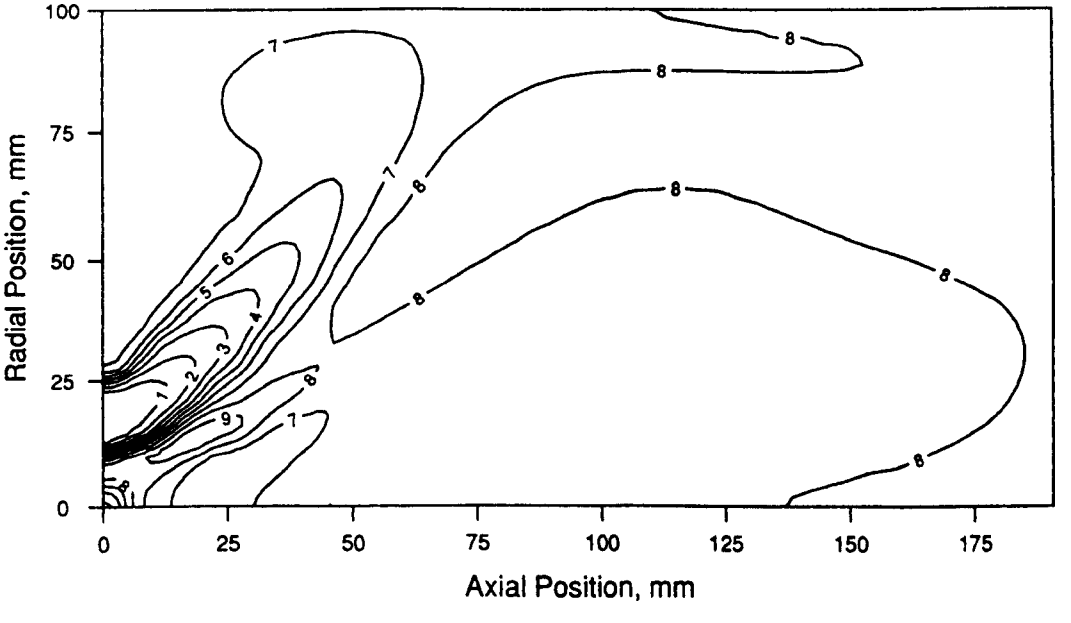

(b) CO_2, dry mol %

Figure 4.23 Contours of Species Concentrations Predicted (continued)

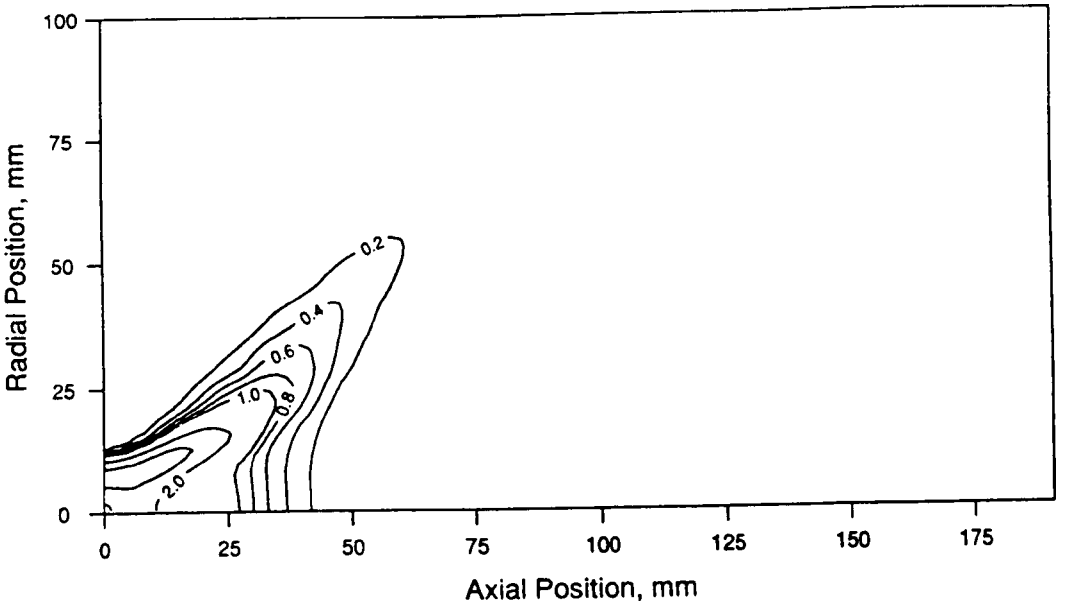

(c) CO, dry mol %

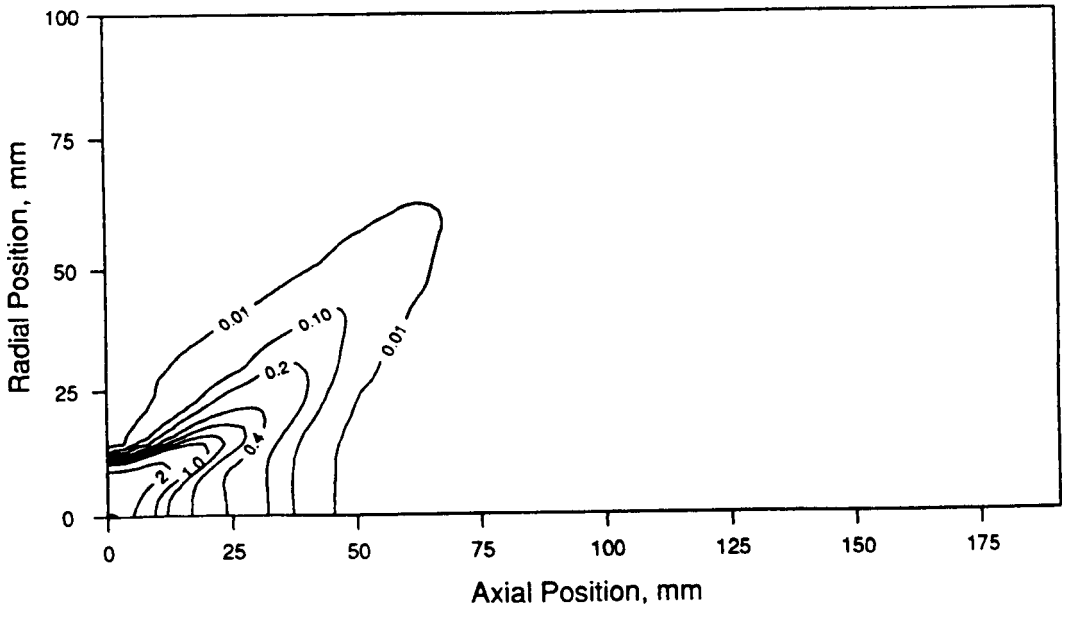

(d) H_2, dry mol %

Figure 4.23 Contours of Species Concentrations Predicted (continued)

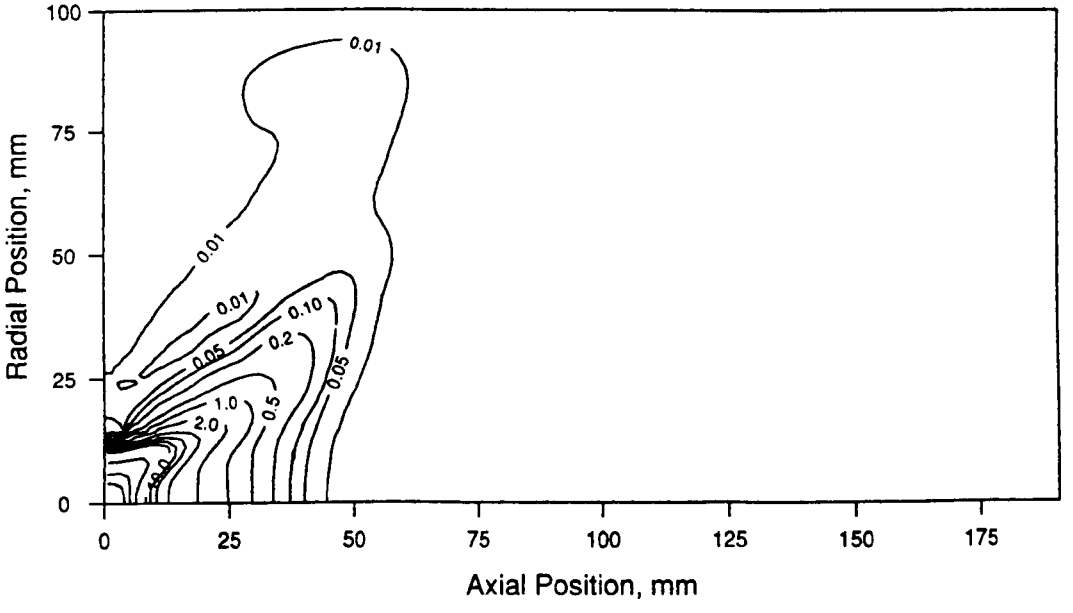

(e) UHC, C_{12} equiv. wet mol %

Figure 4.23 Contours of Species Concentrations Predicted (complete)

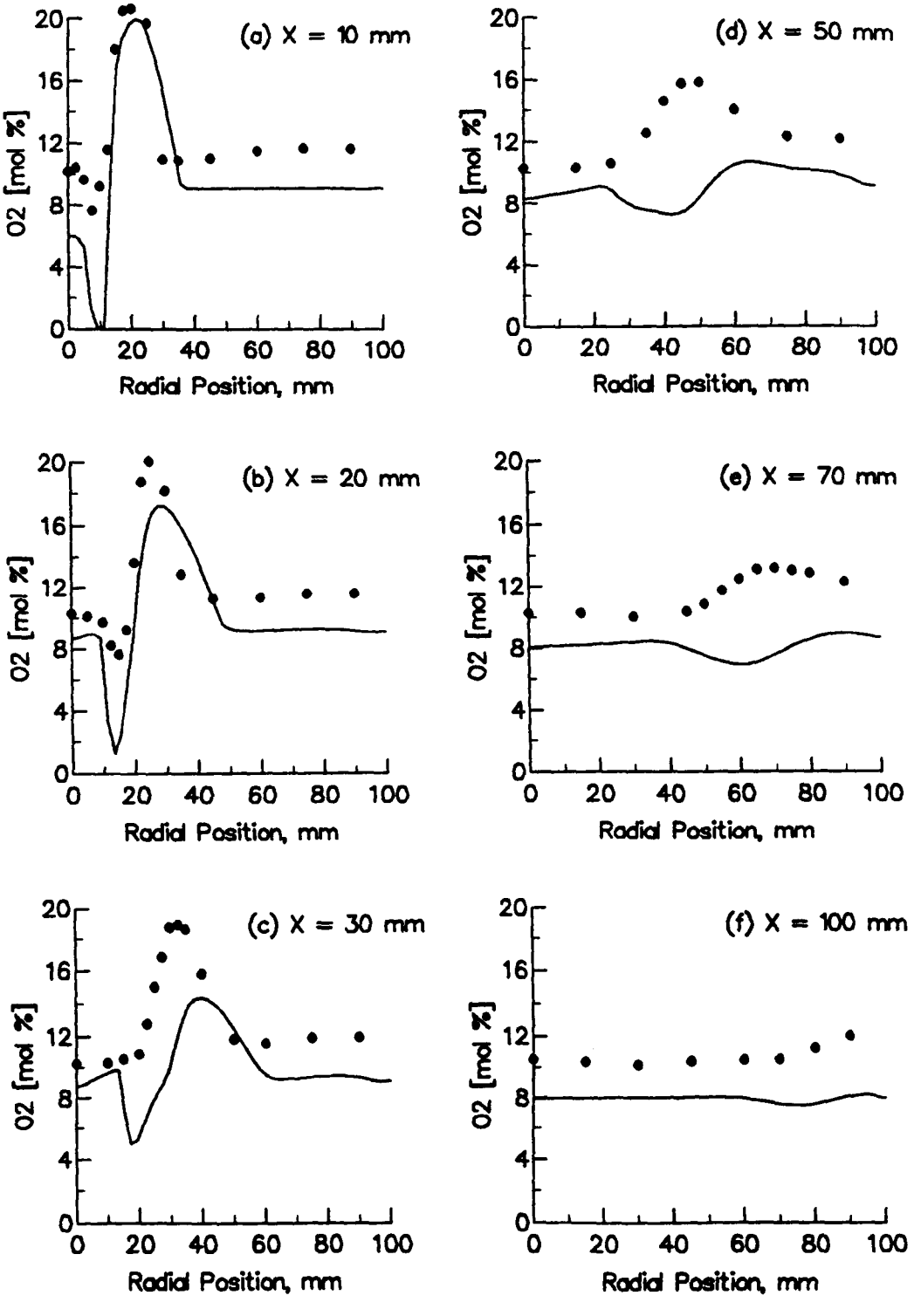

Figure 4.24 O_2 Concentration Profiles

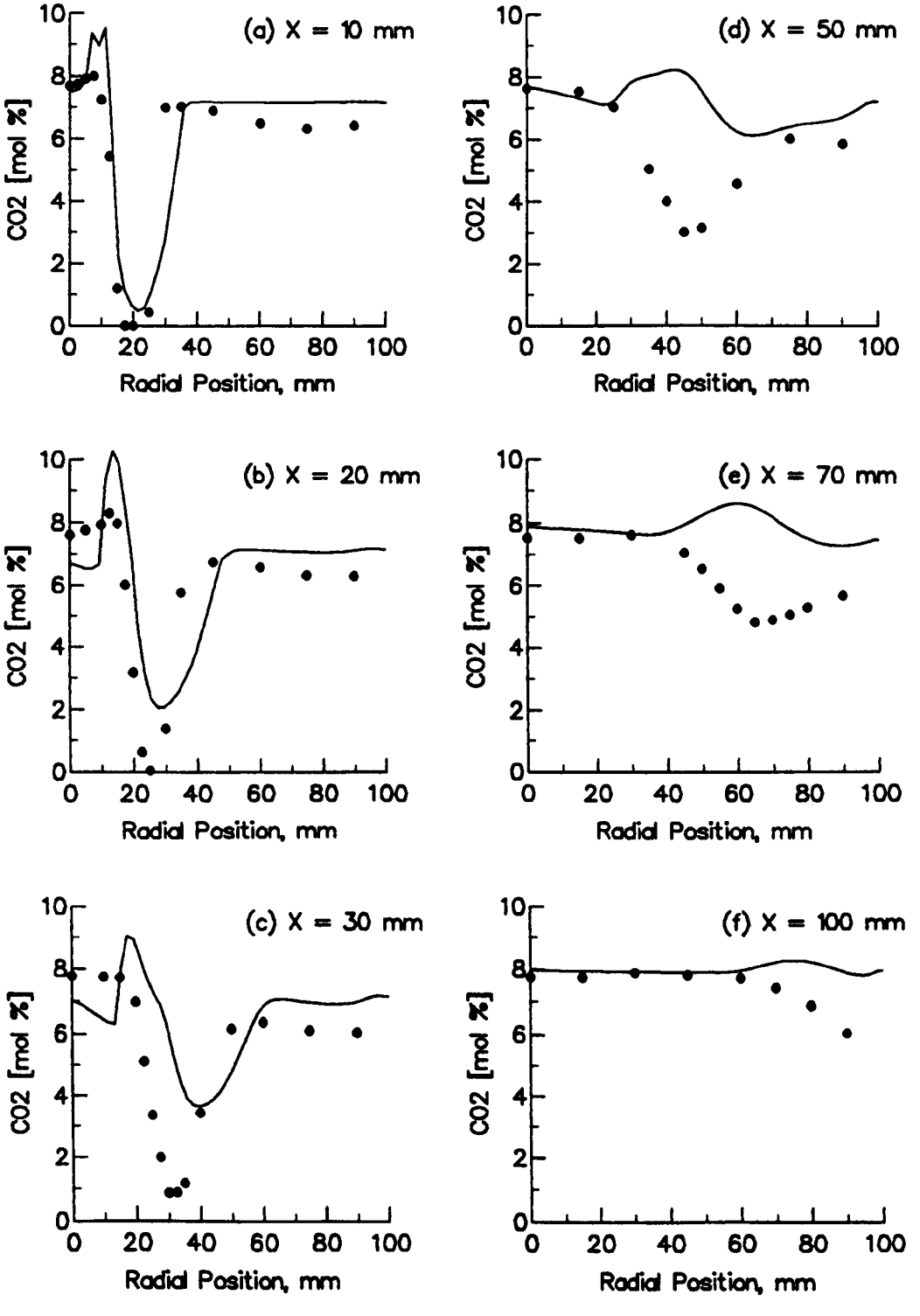

Figure 4.25 CO_2 Concentration Profiles

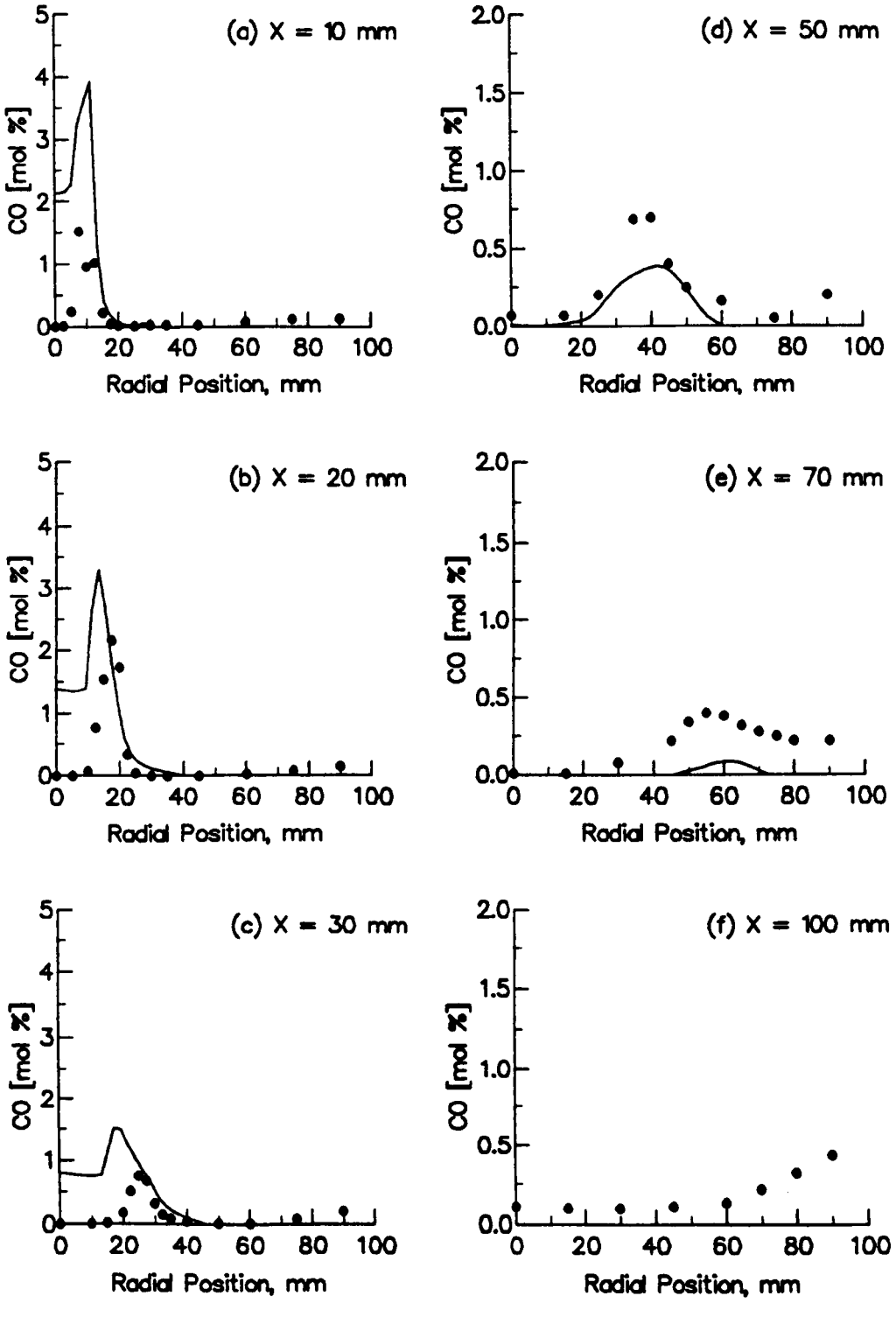

Figure 4.26 CO Concentration Profiles

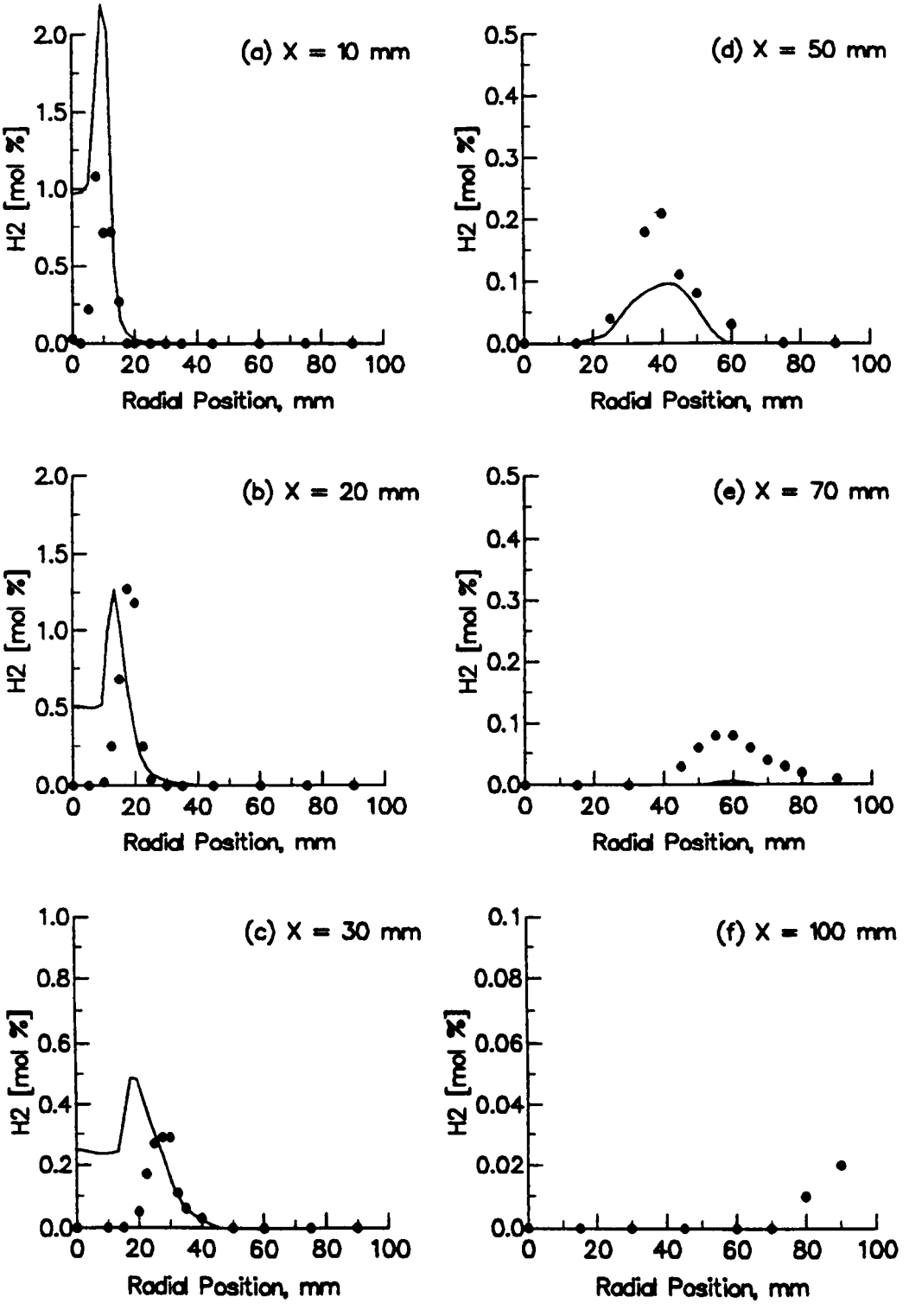

Figure 4.27 H_2 Concentration Profiles

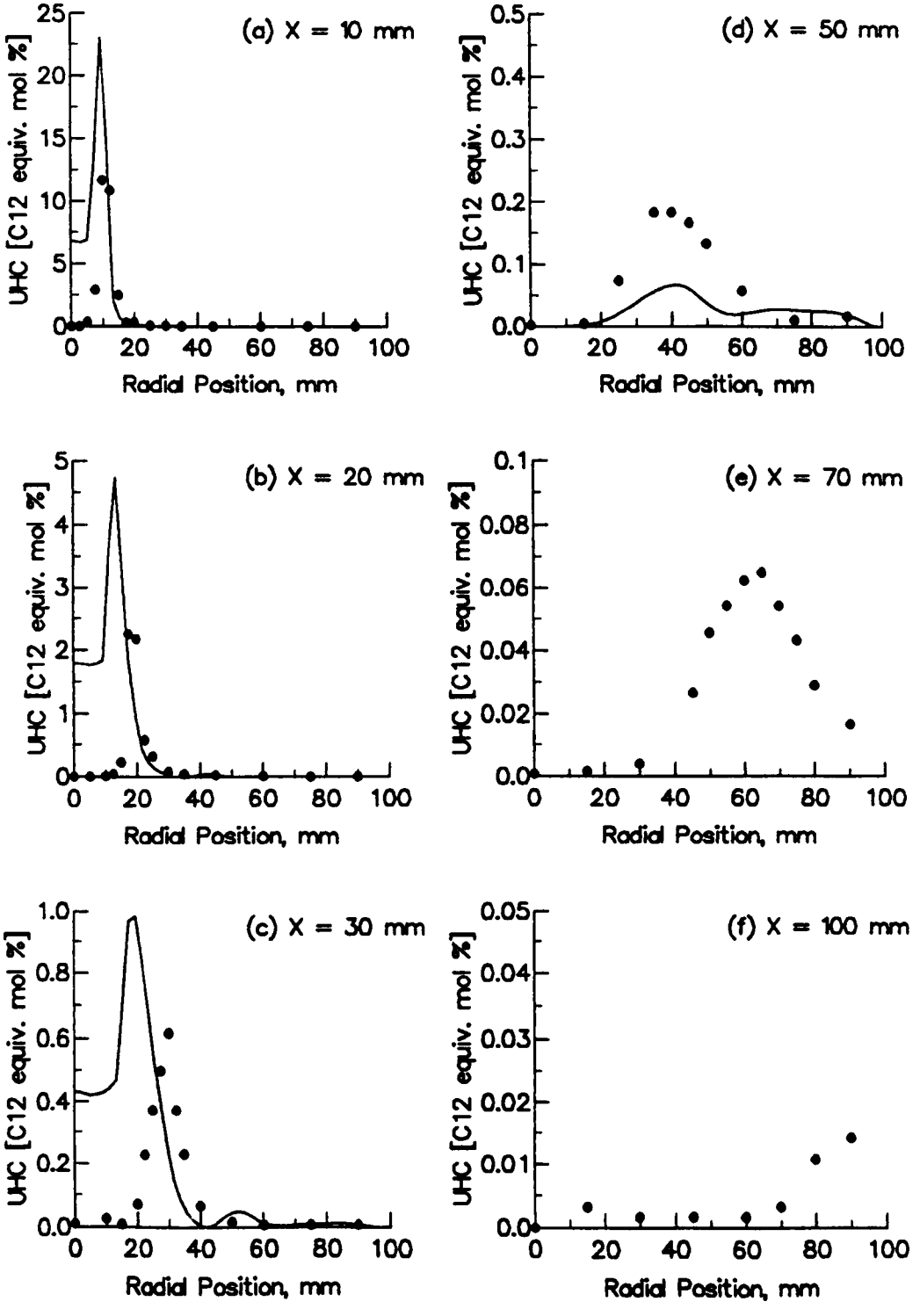

Figure 4.28 UHC Concentration Profiles